HENRY

Hydraulic Engineering Repository

Ein Service der Bundesanstalt für Wasserbau

Bergholz, Katharina

An extended bounding surface model for the application to general stress paths in sand

Mitteilungen

TECHNISCHE UNIVERSITÄT DRESDEN

Institut für Geotechnik

MITTEILUNGEN
HEFT 26

An extended bounding surface model for the application to general stress paths in sand

Ein erweitertes Bounding Surface Modell für die Anwendung auf allgemeine Spannungspfade im Sand

von
Katharina Bergholz

DRESDEN 2020

Abstract

The prediction of settlements in infrastructural design puts high demands on the numerical analysis of the subsoil and the associated constitutive model: complex installation processes and the repetitive character of live loads pose considerable challenges. Although in this context the main focus is on the analytical requirements of a geotechnical problem in order to realistically capture soil behaviour, the needs of engineering practice should not be neglected in constitutive modelling. Along these lines, a new soil model for non-cohesive soils has been developed in the theoretical framework of elastoplasticity.

Based on the concept of bounding surface plasticity according to Manzari and Dafalias [MD97], soil properties such as strength, stiffness and dilatancy depend on the distance between the current stress state and a corresponding model surface in stress space. This way the multi surface model correctly reproduces elementary behavioural patterns of soil, including for example shear related phenomena such as hardening/softening, contraction/dilation and attainment of critical state (constant volume shear strength). Moreover, the model captures the state dependence of soil behaviour (barotropy and pycnotropy). Thus, with only one set of material parameters, the mechanical behaviour of a wide range of initial soil states with respect to stress and void ratio can be simulated (unified modelling). The kinematic hardening mechanism of the conical yield surface contributes to a realistic stiffness evolution in un- and reloading and is hence essential for stress or strain accumulation due to load reversals.

Since the chosen modelling framework is suitable for further development, the original formulation has been extended to adapt the model to the defined needs. In order to adequately simulate geotechnically relevant stress paths of low and higher complexity, first of all, a cap shaped yield surface was added to allow for plastic straining not only in shear, but also in con-

stant stress ratio loading (e. g. isotropic or oedometric compression). When it comes to stress paths of unconventional orientation, to load reversals or composed stress paths with changes in loading direction, a supplementary stiffness increase at small strains and its subsequent strain dependent degradation have proven valuable. Furthermore, an additional mechanism accounts for a regressive accumulation of stresses or strains with increasing number of load cycles (in terms of dissipated energy).

In view of its suitability for practical use, all model extensions are structured in a modular fashion, so that the complexity of the model (and hence the amount of parameters) can be adapted to the complexity of the geotechnical problem by activating or deactivating certain features. Most model parameters can be determined by conventional laboratory testing. An internal routine optionally facilitates the parameter choice by calibrating certain bounding surface related parameters from an alternative user input, which is more oriented towards experimental outcome.

Since a good understanding of a material model is crucial for its reasonable and responsible use, the present thesis aims at offering a sound documentation. Thus, the first part gives an outline of the underlying bounding surface concept and describes the innovations on the constitutive level with reference to theoretical considerations. It is followed by a detailed analysis of capabilities and limitations of the extended model. The next part is dedicated to the numerical implementation of the soil model and its calibration procedure on the basis of laboratory test results. Moreover, the embedded calibration routine including the applied optimisation algorithm is presented. The subsequent section serves model validation: by means of element test simulations, generation of response envelopes as well as the reproduction of more general (e. g. composed) stress paths the performance of the extended bounding surface model is demonstrated. Finally, the last chapter draws conclusions and discloses potential future perspectives.

Zusammenfassung

Die Prognose von Setzungen für die Bemessung von Infrastrukturbauwerken stellt hohe Anforderungen an die numerische Untersuchung des Baugrunds und das damit verbundene Stoffgesetz: komplexe Herstellungsprozesse und zyklisch wiederkehrende Verkehrslasten stellen beachtliche Herausforderungen dar. Während das Hauptaugenmerk zumeist auf der realitätsnahen Abbildung des Bodenverhaltens liegt und damit die analytischen Anforderungen des geotechnischen Problems im Fokus stehen, sollten die Bedürfnisse der Ingenieurspraxis in der Stoffgesetzmodellierung nicht außer Acht gelassen werden. In diesem Sinne wurde im Rahmen der Elastoplastizität ein neues Materialmodell für nichtbindige Böden entwickelt.

Auf dem Konzept der Bounding Surface Plastizität nach Manzari und Dafalias [MD97] beruhend, sind Eigenschaften wie Festigkeit, Steifigkeit und Dilatanz Funktion des Abstands zwischen aktuellem Spannungszustand und einer zugeordneten Modellfläche im Spannungsraum. Auf diese Weise bildet das Mehrflächenmodell fundamentale Verhaltensmuster von Boden korrekt ab, einschließlich beispielsweise scherbezogener Phänomene wie Ver- und Entfestigung, Kontraktanz und Dilatanz oder das Erreichen des kritischen Zustands (Scherfestigkeit bei konstantem Volumen). Des Weiteren erfasst das Modell die Zustandsabhängigkeit des Bodenverhaltens (Barotropie und Pyknotropie). So kann mit nur einem Parametersatz das mechanische Verhalten einer großen Spannweite unterschiedlicher Anfangszustände hinsichtlich Spannung und Lagerungsdichte simuliert werden. Der kinematische Verfestigungsmechanismus der konusförmigen Fließfläche trägt bei Ent- und Wiederbelastungen zu einer realistischeren Steifigkeitsentwicklung bei und ist damit von essenzieller Bedeutung für die Akkumulation von Spannungen oder Verformungen infolge von Lastwechseln.

Da sich der gewählte konstitutive Rahmen für Weiterentwicklungen eignet, wurde die ursprüngliche Formulierung des Stoffgesetzes erweitert, um das

Modell an die definierten Anforderungen anzupassen. Um geotechnisch relevante Spannungspfade niedriger und höherer Komplexität adäquat reproduzieren zu können, wurde zunächst eine kappenförmige Fließfläche ergänzt. So können irreversible Verformungen nicht nur bei Scherung, sondern auch bei Belastungen ohne Änderung des Spannungsverhältnisses, wie z. B. bei isotroper oder ödometrischer Kompression, auftreten. Bei Spannungspfaden ungewöhnlicher Orientierung, bei Lastwechseln oder zusammengesetzten Spannungspfaden mit Änderung der Belastungsrichtung hat sich eine erhöhte Steifigkeit bei kleinen Dehnungen mit anschließendem dehnungsabhängigen Abfall als nützlich erwiesen. Darüber hinaus berücksichtigt ein zusätzlicher Mechanismus die rückläufige Akkumulation von Spannung oder Verformung mit zunehmender Zyklenanzahl (mittels dissipierter Energie).

Im Hinblick auf die Eignung des Stoffgesetzes für die Praxis ist das Modell modular aufgebaut. So kann die Komplexität des Modells (und damit die Anzahl der Parameter) durch Ein- und Ausschalten bestimmter Erweiterungen an die Komplexität des geotechnischen Problems angepasst werden. Die Mehrzahl der Modellparameter wird mit Hilfe konventioneller Laborversuche bestimmt. Eine interne Routine erleichtert durch die Kalibrierung bestimmter Bounding Surface bezogener Größen anhand eines alternativen, stärker an Versuchsergebnissen orientierten User-Inputs bei Bedarf die Parameterwahl.

Da die Kenntnis eines Stoffgesetzes entscheidend ist für dessen vernünftigen und verantwortungsvollen Einsatz, soll die vorliegende Arbeit eine fundierte und umfassende Dokumentation bieten. Der erste Teil vermittelt daher zunächst einen Überblick über das zugrunde liegende Bounding Surface Konzept und beschreibt die Neuerungen auf konstitutiver Ebene mit Bezug auf theoretische Hintergründe. Er wird gefolgt von einer detaillierten Darlegung von Potenzialen und Einschränkungen für die Nutzung des erweiterten Modells. Der nächste Abschnitt widmet sich der numerischen Implementierung des Stoffgesetzes und seiner Kalibrierung auf Basis von Versuchsergebnissen. Des Weiteren wird die Kalibrierungsroutine einschließlich des verwendeten Optimierungsalgorithmus präsentiert. Der nachfolgende Teil dient der Modellvalidierung: durch die Simulation von Elementversuchen, die Erzeugung von Antwortellipsen sowie die Abbildung allgemeinerer (beispielsweise zusammengesetzter) Spannungspfade wird die Leistungsfähigkeit des erweiterten Bounding Surface Modells demonstriert. Abschließend werden Schlussfolgerungen gezogen und potenzielle Perspektiven aufgezeigt.

Vorwort des Herausgebers

Die Entwicklung von Stoffmodellen für Boden ist längst nicht abgeschlossen. Obwohl das mechanische Bodenverhalten für monotone Belastungspfade mit mehreren Stoffmodellen zufriedenstellend wiedergegeben werden kann, ist die konstitutive Abbildung des Bodenverhaltens bei mehreren Belastungszyklen bzw. bei zusammengesetzten Spannungspfaden immer noch problematisch.

Frau Bergholz hat sich in ihrer Dissertation das Ziel gesetzt, ein Stoffmodell für allgemeine Spannungspfade einschließlich zyklischer Belastung zu entwickeln. Dabei hat sie als Grundlage ein bestehendes elastoplastisches (sog. bounding surface) Modell genommen und mit einigen wesentlichen Modifikationen seine Leistung verbessert. Die Komplexität des Modells wurde dadurch nicht unwesentlich erhöht, was auch die Modellkalibrierung betrifft. Es ist zu begrüßen, dass Frau Bergholz die Bestimmung der Stoffparameter detailliert analysiert und in einer semiautomatischen Prozedur erfasst hat. Das mit ihrem Modell abgebildete Elementverhalten ist vielversprechend und es ist zu hoffen, dass nach einer numerischen Implementierung in ein FE-Programm die Simulationen neue Einblicke in das Verhalten von geotechnischen Bauwerken ermöglichen.

Frau Bergholz hat ihre Dissertation im Rahmen eines Kooperationsvertrags mit der Bundesanstalt für Wasserbau in Karlsruhe als externe Doktorandin vorbereitet. Es ist zu würdigen, dass ein solches theoretisches Thema durch die BAW unterstützt wurde und dass Frau Bergholz neben ihren hauptberuflichen Verpflichtungen die anspruchsvolle Modellentwicklung in der hier dargestellten Tiefe erreicht hat. Ihre kritische Auseinandersetzung mit allen Modelldetails hat zu zahlreichen gemeinsamen Fachdiskussionen geführt, die ich sehr geschätzt habe.

Ivo Herle

Vorwort des Verfassers

Als ich 2009 zur Bundesanstalt für Wasserbau (BAW) kam, war mein Weg in Richtung Forschung noch nicht vorgezeichnet. Nach einigen Jahren wertvoller Projektarbeit wurde mir angeboten, ein bestehendes FuE-Projekt wiederaufzunehmen, in dem es um die Modellierung zyklischer Belastungen von Schleusen in nichtbindigen Böden ging. Dieses Forschungsprojekt gab mir die Gelegenheit mich – über den Stand der Technik hinaus – mit numerischer Modellierung zu beschäftigen und meine Kenntnisse in der Stoffgesetzentwicklung zu vertiefen. Daher möchte ich der BAW – vertreten durch Markus Herten und Michael Heibaum – meine aufrichtige Dankbarkeit aussprechen, die mir dieses Forschungsvorhaben anvertraut und für ausgezeichnete Arbeitsbedingungen gesorgt haben. Markus hielt mir den Rücken frei, solange er konnte – selbst wenn ich zum wiederholten Male den Zeitplan über den Haufen geworfen hatte. Ich möchte auch all den anderen Kollegen der BAW danken, die mich in diesen Jahren des Forschens und Schreibens begleitet haben, indem sie Interesse an dem zeigten, was ich tat, aus einer eher praktischen Perspektive einen Blick auf meine Ergebnisse warfen, Korrektur lasen oder einfach die Mittagspausen mit mir teilten.

Da das FuE-Projekt von Thomas Benz (vormals Professor an der NTNU Trondheim, nun an der HfT Stuttgart) initiiert und zuvor geleitet wurde, baut meine Arbeit in großen Teilen auf der von ihm geschaffenen Grundlage auf. Darüber hinaus hat Thomas wichtige Ideen für die Weiterentwicklung des Stoffgesetzes beigetragen, hat potenzielle Verbesserungsmöglichkeiten aufgezeigt und hatte ein offenes Ohr für Diskussionen, wofür ich ihm sehr dankbar bin.

Als Forschende an einer nicht-universitären Einrichtung hat mir die Kooperation mit Professor Ivo Herle von der Technischen Universität (TU) Dresden nicht nur die Möglichkeit gegeben den Doktortitel zu erlangen, sondern mir es auch erlaubt von seinem Wissen und seiner Erfahrung zu

profitieren. Daher möchte ich Professor Herle ganz besonders dafür danken, dass er mich als externe Promotionsstudentin angenommen und mich in diesen Jahren wissenschaftlich begleitet und beraten hat. Er fand Zeit, die letzten Entwicklungen mit mir durchzusprechen und die nächsten Schritte abzustimmen, wann immer ich nach Dresden kam – auch nach sehr kurzfristiger Ankündigung, egal wie eng sein eigener Zeitplan war. Darüber hinaus gilt mein Dank Professor Herle und der BAW, die es mir ermöglichten ein Semester am Geotechnischen Institut der TU Dresden zu verbringen. Dieser Aufenthalt erlaubte mir es nicht nur, mich wieder in alte Studienzeiten zurückversetzt zu fühlen, sondern auch meine Forschung in einem sehr inspirierenden Umfeld mit anderen Doktoranden und in engerem Kontakt zu Professor Herle voranzutreiben. Außer dem regelmäßigen Austausch von Ideen gab mir das Vorbereiten und Halten von Tutorien zur Stoffgesetzmodellierung die Möglichkeit, die Grundlagen meines eigenen Forschungsthemas zu festigen und zu vertiefen. Neben dem rein wissenschaftlichen Aspekt hat es mich sehr gefreut Teil des Instituts gewesen zu sein, wo man auch nicht-fachliche Gedanken bei gemeinsamen Freitagsfrühstücken oder beim Warten auf das Kochen des Teewassers teilen konnte.

Den letzten, aber nicht minder wichtigen Teil meines Danks möchte ich an meine Familie und Freunde richten. Ich danke meinen Eltern, dass sie mich mein Leben lang bedingungslos unterstützt haben. Sie haben mich immer ermutigt meinen Weg zu gehen, ohne mich dabei zu drängen. Neben der rein finanziellen Hilfe während meines Studiums waren sie immer für mich da, haben mir mit Rat und Tat zur Seite gestanden und mir ihre helfenden Hände angeboten – bei jedem Umzug aufs Neue.

Auch wenn diese Promotion meine letzten Jahre dominiert hat: Arbeit ist nicht alles im Leben. Deshalb geht ein ganz besonderer Dank an alle, die mich in der Zeit des intensiven Schreibens abgelenkt haben, allen voran Matthias. Danke, dass du hin und wieder auf kurze Auszeiten bestanden hast, um den Kopf freizubekommen und die Batterien aufzuladen, dass du mich gelegentlich auf den Boden der Tatsachen zurück geholt hast, fürs Zuhören, Verstehen und manchmal auch Ertragen. Sein Name steht natürlich stellvertretend für alle, die für außergewöhliche Momente gesorgt und die mich in harten Zeiten aufgebaut haben. Und auch für diejenigen, die mir Gesellschaft geleistet haben beim alltäglichen körperlichen und geistigen Ausgleich für die Schreibtischarbeit.

Katharina Bergholz

Contents

List of Symbols

If a particular combination of variable and index is not listed in any of the tables, its meaning is derived from the composition of the individual symbols. Occasionally, variables or indices are assigned twice, however, the context will unequivocally insinuate the correct meaning.

Upper-case letters

Symbol	Unit	Meaning
A	$[-]$	Pore pressure coefficient (Skempton)
A_0	$[-]$	Dilatancy surface constant
A_d	$[-]$	Dilatancy surface parameter
B	$[-]$	Skempton parameter
C, V	$[-]$	Cap hardening constants for stress- and strain rate dependency
C_f	$[-]$	Fabric evolution constant in dilatancy related mechanism
C_{fluid}	$[\mathrm{kPa}^{-1}]$	Compressibility of the pore fluid (also: air, soil, water)
D	$[-]$	Dilatancy ratio
E	$[\mathrm{kPa}]$	Young's modulus
E_{oed}^{ref}	$[\mathrm{kPa}]$	Reference oedometer modulus (1D compression) for $\sigma_1 = p_{ref}$
F_f	$[-]$	Fabric evolution constant in dilatancy related mechanism

Symbol	Unit	Meaning
G_0^{ref}	[kPa]	Reference shear modulus for $p = p_{ref}$ and $e \approx 0.821$
$H^{cone,cap}$	$[-,\text{kPa}]$	Hardening modulus of the cone/cap yield surface
$H_{\alpha,m}$	$[-,\text{kPa}]$	Hardening modulus of the kinematic/isotropic hardening mechanism of the cone yield surface [acc. MD97]
$H_{\alpha,p0}$	$[-,\text{kPa}]$	Hardening modulus of the shear/compression hardening mechanism of the closed cone yield surface [acc. TD08]
K	[kPa]	Bulk modulus
K	$[-]$	Constant energy ratio (Rowe)
K_0	$[-]$	Earth pressure coefficient at rest
K_{fluid}	[kPa]	Bulk modulus of the pore fluid (also: air, soil, water)
K_p	[kPa]	Plastic modulus
$M_{c,e}^{b,c,d}$	$[-]$	Inclination of **b**ounding/**c**ritical state/**d**ilatancy surface in **c**ompression/**e**xtension in p-q space (deviatoric stress ratio)
M_{cap}	$[-]$	Steepness parameter of the cap yield surface
M^{el}	[kPa]	Elastic stiffness
N_f	$[-]$	Fabric evolution constant in hardening related mechanism
N_φ	$[-]$	Principal stress ratio
N_Ψ	$[-]$	Principal strain ratio (dilatancy ratio)
R	$[-]$	Elastic limit strain
S_r	$[-]$	Degree of saturation
W	$\left[\frac{\text{kN m}}{\text{m}^3}\right]$	Dissipated energy (per unit volume)

Lower-case letters

Symbol	Unit	Meaning
a	$[-]$	Fabric evolution exponent in hardening related mechanism
b	$[-]$	Fabric evolution exponent w. r. t. minimum void ratio
c	$[-]$	Ratio of limit stress ratio in extension over limit stress ratio in compression
$d^{b,d}$	$[-]$	Scalar distance between actual stress point and its image on the **b**ounding/**d**ilatancy surface
d^b_{ref}	$[-]$	Scalar reference distance between image points on the bounding surface in compression an extension
e	$[-]$	Void ratio
e_{csa}	$[-]$	Critical state void ratio at $p = p_{at}$
e_{cs0}	$[-]$	Critical state void ratio at $p = 0\,\mathrm{kPa}$
f	$[-]$	Yield surface
f_{fab}	$[-]$	Fabric evolution parameter scaling dilatancy
f_p	$[-]$	Fabric evolution parameter in hardening related mechanism
f_{sd}	$[-]$	State function
g	$[-]$	Plastic potential
$g(c,\theta)$	$[-]$	Shape function for model surfaces w. r. t. loading direction
h	$[-]$	Parameter scaling hardening modulus
h_{fab}	$[-]$	Fabric evolution parameter scaling hardening modulus
h_{min}	$[-]$	Fabric evolution parameter w. r. t. minimum void ratio scaling hardening modulus
h_{ss}	$[-]$	Small strain stiffness parameter scaling hardening modulus
$k^{b,d}_{c,e}$	$[-]$	**B**ounding/**d**ilatancy surface parameter for **c**ompression/**e**xtension [acc. MD97]

Symbol	Unit	Meaning
m	$[-]$	Janbu exponent for stress dependency of elastic stiffness
m_b	$[-]$	Bounding surface parameter
m_d	$[-]$	Dilatancy surface parameter
m_{cone}	$[-]$	Opening parameter of the cone yield surface
m_{oed}	$[-]$	Oedometer modulus exponent (stress dependence)
$m_{R,T}$	$[-]$	Small strain stiffness scaling parameter for stress reversals of 180°/90°
m_s	$[-]$	Mode of shear
n_{oed}	$[-]$	Oedometer modulus exponent (void ratio dependence)
p	[kPa]	Isotropic/mean stress
p_0	[kPa]	Pre-consolidation pressure
p_{at}	[kPa]	Atmospheric pressure
p_b	[kPa]	Image stress on the LCC
p_c	[kPa]	Width of the cap yield surface
p_r	[kPa]	Reference pressure of the LCC at $e = 1$
p_{ref}	[kPa]	Reference pressure for stiffness moduli (usually $p_{ref} = p_{at}$)
u	[kPa]	Pore pressure
v	$\left[\frac{\text{m}}{\text{s}}\right]$	Wave velocity

Greek letters

Symbol	Unit	Meaning
α	[°]	Angle of change in loading direction
α, β, γ	$[-]$	Cap hardening exponents for stress- and strain rate dependency
β_R	$[-]$	Intergranular strain exponent in small strain stiffness mechanism
γ	$[-]$	Shear strain

Symbol	Unit	Meaning
γ_{lim}	$[-]$	Limit shear strain for small strain stiffness influence on hardening modulus
Δ	$[-]$	Difference (from one load step to the next)
δ	$[-]$	Distance from the actual state to the LCC
δ	$[-]$	Intergranular strain (scalar)
$\varepsilon_{1,2,3}$	$[-]$	Principal strains
ζ	$[-]$	Stress/strain contour exponent in small strain stiffness mechanism
η	$[-]$	Deviatoric stress ratio
θ	$[-]$	Lode angle
κ	$[-]$	Hardening variable
λ	$[-]$	Inclination of the critical state line in p-e space
λ	$[-]$	Plastic multiplier
μ	$[-]$	Stress ratio at constant volume deformation
ν	$[-]$	Poisson's ratio
ξ	$[-]$	Critical state line exponent
ρ	$[-]$	Relative intergranular strain (related to R)
ρ_c	$[-]$	Inclination of the LCC
$\sigma_{1,2,3}$	[kPa]	Principal stresses
τ	[kPa]	Shear stress
φ	$[\,°\,]$	Friction angle
χ	$[-]$	Intergranular strain exponent in small strain stiffness mechanism
Ψ	$[\,°\,]$	Dilatancy angle
ψ	$[-]$	State parameter [acc. BJ85]
ω	$[-]$	Exponent in the LCC based cap hardening mechanism

Tensors

Symbol	Unit	Meaning
$\boldsymbol{D}^{el,ep}$	[kPa]	**El**astic/**el**asto**p**lastic stiffness matrix
$\boldsymbol{E}$	$[-]$	Matrix of strain constraints
$\boldsymbol{f}$	$[-]$	Fabric evolution tensor
$\boldsymbol{H}^{ep}$	$[\sim]$	Elastoplastic hardening matrix
$\boldsymbol{I}$	$[-]$	Identity tensor
$\boldsymbol{L}$	$[-]$	Loading direction
$\boldsymbol{n}$	$[-]$	Deviatoric loading direction
$\boldsymbol{r}$	$[-]$	Deviatoric stress ratio tensor
$\boldsymbol{S}$	$[-]$	Matrix of stress constraints
$\boldsymbol{s}$	[kPa]	Deviatoric stress tensor
$\mathbf{e}$	$[-]$	Deviatoric strain tensor
$\boldsymbol{\alpha}$	$[-]$	Back stress tensor
$\boldsymbol{\alpha}^{b,c,d}$	$[-]$	Image back stress tensor w. r. t **b**ounding/**c**ritical state/**d**ilatancy surface
$\boldsymbol{\delta}$	$[-]$	Intergranular strain tensor
$\hat{\boldsymbol{\delta}}$	$[-]$	Normalized intergranular strain tensor
$\boldsymbol{\varepsilon}$	[kPa]	Strain tensor
$\boldsymbol{\sigma}$	[kPa]	Stress tensor

Indices

Symbol	Unit	Meaning
0	$[-]$	Initial state
0	$[-]$	Base value
a	$[-]$	Axial
b	$[-]$	Bounding surface
c	$[-]$	Critical state surface
c	$[-]$	Compression
cs	$[-]$	Critical state

Symbol	Unit	Meaning
cv	$[-]$	Constant volume
d	$[-]$	Dilatancy surface
e	$[-]$	Extension
el	$[-]$	Elastic
ep	$[-]$	Elastoplastic
lim	$[-]$	Limit
m	$[-]$	Mobilized
max	$[-]$	Maximum
min	$[-]$	Minimum
PT	$[-]$	Phase transformation
p	$[-]$	Volumetric
p	$[-]$	Primary w.r.t. wave velocity (P-wave = compressional wave)
$peak$	$[-]$	Peak
pl	$[-]$	Plastic
q	$[-]$	Deviatoric
r	$[-]$	Radial
ref	$[-]$	Reference
s	$[-]$	Secondary w.r.t. wave velocity (S-wave = shear wave)
SR	$[-]$	Shear reversal
T	$[-]$	Transpose
tot	$[-]$	Total
v	$[-]$	Volumetric

Abbreviations

Abbreviation	Meaning
BS	Bounding surface
CSL	Critical state line
FE	Finite element

Abbreviation	Meaning
IGS	Intergranular strain
ISO	Isotropic compression test
LCC	Limiting compression curve
OED	Oedometer (1D compression) test
PSO	Particle Swarm Optimisation
SC	Stress/strain contour
SOM	Swept-out memory
TXD	Drained triaxial compression test
TXU	Undrained triaxial compression test

1 Introduction

1.1 General aspects on constitutive modelling

The mechanical analysis of materials, as carried out by various engineering disciplines in terms of numerical simulations (applying for example the finite element method), traditionally follows the basic principles of continuum mechanics. The microscopic structure of a material is disregarded and a body is considered as a continuous mass rather than consisting of discrete particles.[1] For describing the motion of a deformable body due to external loadings, continuum mechanics employ three different types of equations [Alt18]: (i) kinematic equations, which define straining as a function of a body's motion, (ii) balance equations, which correspond to fundamental physical laws describing the effect of outer impacts on physical quantities such as mass, momentum and energy, and (iii) constitutive equations that add individual material specific properties of a body. Together with loading and boundary conditions, kinematic, balance, and constitutive equations fully define a boundary value problem.

While kinematic and balance equations comprise all material independent information, constitutive equations reflect the material dependent behaviour of the continuum. They are a set of mathematical relations describing the link between changes in applied stress and resulting strain, and hence define how materials respond to external excitations. Irrespective of the actual properties of a material (arising from its microstructure), the formulation of constitutive relations for the description of macroscopic phenomena follows similar principles and applies a similar terminology. It has

---

[1]With the increasing computational power, modelling of discrete particles (e. g. discrete element method) progressively becomes an alternative to the conventional continuum based approach.

to be emphasised that constitutive equations are just a simplification of a rather complex physical behaviour, so that the resulting material response will never be exact but always remain an approximation.

General modelling frameworks

Material models can be classified with respect to basic material behaviour in terms of hysteresis and rate dependency of deformation into the following four categories (Fig. 1.1): elasticity, plasticity, visco-elasticity and visco-plasticity [Hau93]. If the material response is independent of the loading rate, it is either elastic in case loading and unloading paths are identical, or the stress-strain curve exhibits hysteresis in loading-unloading cycles in case it is plastic. If, however, the material response is rate-dependent (viscous), hysteresis can be observed in any non-monotonous loading process with a finite loading rate. Nonetheless, only those cases, where hysteresis appears even for hypothetical loading rates of $|\dot{\varepsilon}| = 0$ (static or equilibrium hysteresis), are considered visco-plastic. If there is no static hysteresis, the material response is termed visco-elastic, which concerns mainly materials like rubber or plastics. Based on their fundamentally different behaviour, these four classes offer various constitutive modelling frameworks.

Having spoken in general terms so far, the material playing the leading part in geotechnical engineering (and the present work) is soil. Compared to other materials, with respect to the mathematical description of its mechanical behaviour, soil is one of the most complex materials: it is a multiphase material (grains, water, air), it consists of particles of different sizes and shapes and its mechanical properties vary in space (non-homogeneity) and with loading direction (anisotropy). Consequently, soil mechanical behaviour features a multitude of characteristics, which complicate its mathematical depiction: non-linearity, irreversibility, dilatancy, stress path dependency, rate dependency, to name only a few. In contrast to other civil engineering materials such as steel, the range of behaviour that can be captured with linear elasticity is very small and hence the listed behavioural patterns already need to be taken into account in early loading stages. Thus, transferring this intricate mechanical behaviour into mathematical expressions of an adequate complexity is a challenging task, which has been and still is subject to intense research.

When trying to assign an appropriate constitutive modelling framework to this complex material soil, (linear) elasticity (e. g. Hooke's law) is no suitable approach for describing soil behaviour in conventional stress and

Material model classes for solids
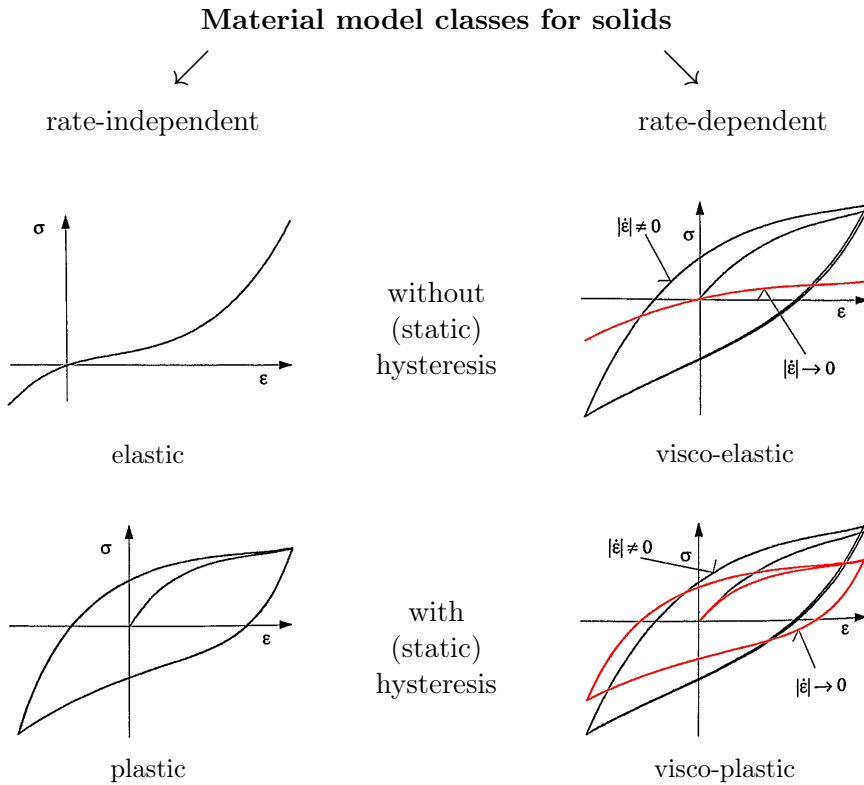
Figure 1.1: Classification of material behaviour according to Haupt [Hau93] (images modified after [Sed00]

strain ranges.[2] In order to capture permanent strains and the load path dependence of deformation resulting from the rearrangement of the grains, plasticity should be the starting point. A soil exhibiting a time-dependent creep under applied loads (or stress relaxation at constant deformation), as for example soft soils or rock salt, might even justify a visco-plastic approach. Assuming, however, a rate-independent behaviour as exhibited by sands, plasticity provides a multitude of subcategories to capture the different shades of irreversible deformation.

In plasticity theory, the elastic-plastic approach is the most well-known and used one. The strain is divided into two additive components: elastic

---

[2]If only monotonous loadings without reversed shearing are considered, a non-linear elastic model as the one by Duncan and Chang [DC70] might actually be an option.

(ε^{el}) and plastic (ε^{pl}) strain. The boundary between stress states causing reversible and irreversible deformations, respectively, is defined by a yield function. The simple case, where the yield stress remains constant after the initial transition from elastic to plastic, is called perfectly plastic behaviour. A popular representative of that type is the linearly elastic - perfectly plastic Mohr Coulomb model. However, soils exhibit strain hardening after yielding, i. e. an increase in irreversible displacement is accompanied by an increasing yield stress.[3] In contrast to perfect plasticity, where the yield function is only dependent on the stress, in so called elastoplasticity the plastic strain additionally controls the evolution of the elastic domain in size (isotropic hardening) and/or location in stress space (kinematic hardening) via a hardening rule. Furthermore, the direction of plastic straining is determined by the plastic potential and its magnitude by the plastic multiplier, which are merged in the so called flow rule.[4]

Since irreversibility also implies that the soil response is dependent on the soil's loading history (path dependence), in conventional stress and strain ranges there is no unique correlation between stress and strain of the form $\boldsymbol{\sigma} = f(\boldsymbol{\varepsilon})$ as applied in elasticity. History dependence can be incorporated into the constitutive equations by choosing an incremental or rate type relation of the form $\dot{\boldsymbol{\sigma}} = f(\boldsymbol{\sigma}, \dot{\boldsymbol{\varepsilon}})$, which is non-linear in $\dot{\boldsymbol{\varepsilon}}$ and where $\boldsymbol{\sigma}$ accounts for the actual (stress dependent) stiffness. [Kol16]

This so called incremental non-linearity is not only applied in elastoplasticity, but also in another material model for describing inelastic behaviour, called hypoplasticity. While elastoplasticity switches between different constitutive equations of the previously quoted form for loading (elastoplastic) and unloading (linearly elastic) with reference to the yield function, hypoplasticity requires only one relation between $\dot{\boldsymbol{\sigma}}$ and $\dot{\boldsymbol{\varepsilon}}$. The stress rate is composed of a stress dependent hypoelastic contribution, which is linear in strain rate, and a non-linear function of stress and strain rate: $\dot{\boldsymbol{\sigma}} = L(\boldsymbol{\sigma})\dot{\boldsymbol{\varepsilon}} + N(\boldsymbol{\sigma})\,|\dot{\boldsymbol{\varepsilon}}|$.[5] This formulation allows for representing irreversible

---

[3]This strengthening effect due to plastic deformation is also called work hardening. The inverse phenomenon is strain (or work) softening – a decrease in strength with increasing plastic strain. In the following these terms are simplified to hardening and softening.

[4]Fundamental equations of elastoplasticity are listed in App. A.1.

[5]Hypoplasticity actually uses the objective stress rate $\overset{\circ}{\boldsymbol{\sigma}}$ (so called co-rotated stress rate by Jaumann) instead of the time derivative of stress $\dot{\boldsymbol{\sigma}}$.

deformations with a single equation, without the need for a yield function prescribing an elastic domain. However, due to the lack of material memory provided by a yield surface, the information on the deformation history needs to be stored differently (e. g. by incorporating the void ratio or a structure tensor into the hypoplastic equation). [Kol91]

Having given a rough overview of general strategies in soil modelling, the elastoplastic approach and its advancement towards bounding surface plasticity will be subject of Chap. 2.

Modelling procedure

Since continuum mechanics is a phenomenological theory, in engineering science constitutive relations are mostly identified by an inductive procedure based on experimental investigations: specific loading cases are studied experimentally, simple observations are transferred to mathematical expressions and these are generalised gradually to constitutive equations. In this process, firstly, material properties are identified experimentally. This is achieved by interrelating external impacts (input) and the observed reaction (output), allowing inferences on the internal state and hence the behaviour of the considered continuum. In a second step the observed behaviour is idealised: essential features are filtered, discarding certain aspects in order to simplify the complex reality and to make it comprehensible and predictable. Subsequently, based on these findings and additional assumptions simple mathematical relations between the phenomenological variables (stress, strain, temperature, . . .) are constructed. They are generalised step-by-step for general loading conditions, ensuring their physical and mathematical consistency. Finally, the material parameters that quantitatively represent the material properties need to be determined experimentally and the validity of the obtained constitutive equations needs to be tested, using experiments that have not yet been used in the process before. [Hau02, Alt18]

The same approach is applied in the constitutive modelling of soil mechanical behaviour: experiments are carried out on soil specimens under well-defined laboratory conditions in order to establish a sound basis with respect to the mechanical behaviour to be captured. Each experiment provides a part of information on the soil behaviour, which will finally give a more or less complete picture that can be translated into constitutive equations. To this end, tests have been designed in a way that a macroscopically homogeneous soil sample is subject to spatially homogeneous states of stress and

strain (and potentially other conditions, e.g. temperature). Consequently, the entire specimen can be idealised as a representative soil element with a single stress and strain tensor, no matter what the sample geometry. Typical, so called, element tests are for example one-dimensional compression tests and triaxial tests (see Fig. 1.2).
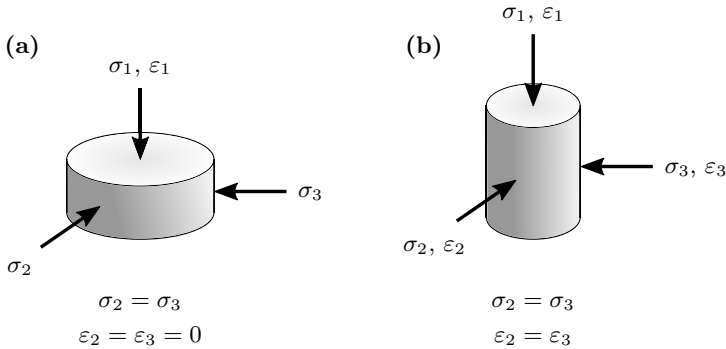
Figure 1.2: Typical element tests and applied stress and strain conditions: (a) 1D-compression (or oedometer) test, (b) triaxial (compression) test

As soon as shear strains localise and a slip plane evolves, the assumption of homogeneity is not valid any longer, so that direct shear tests cannot be considered as element tests and triaxial tests lose their status as element test once failure occurs. Furthermore, non-homogeneity can be caused by sample preparation or testing influences such as end restraint (due to non-lubricated end platens) or membrane effects. Hence, even element tests cannot be expected to accurately reflect "true" soil behaviour. However, element tests provide information on basic soil behavioural patterns that constitutive models aim for reproducing (at least) qualitatively. Vice versa, the numerical simulation of element tests with a certain constitutive model also helps to understand the theory behind the model and to assess its closeness to reality.

In this context, one should bear in mind that constitutive models are only theories approximating reality and the outcome of a model is only as good as the theory it is built on. Observations are abstracted and complemented with assumptions about unknown boundary conditions in an attempt to compass the complex nature of soil, but also to reduce the observed to a comprehensible model. Hence, deviations of the calculated soil response from the experimentally observed one may be due to inaccuracies on the

laboratory scale, but are also very likely to originate from the inevitable gap between theory and reality. Since no model has been developed yet that succeeded in closing this gap, simplifications are not necessarily fatal deficiencies. Houlsby [Hou81] put it aptly with the following statement:

" [...] choosing a theoretical idealisation of a soil, one is not always primarily concerned with accuracy: the best model for solving an engineering problem is not necessarily that which most closely fits the stress-strain curve for the chosen laboratory or field tests. Soil is a very complex material, and any model which achieves a high degree of accuracy is likely also to be complex. A simpler model may have advantages which may outweigh any loss in precision; [...] "

As long as the limitations of a constitutive model arising from approximations are clearly defined and the user is aware of them, when interpreting calculation results, constitutive models provide a valuable framework for understanding and predicting soil mechanical behaviour.

1.2   Motivation and outline of the thesis

Starting point of the present work has been a research project at the German Federal Waterways Engineering and Research Institute (BAW) with the title "Modelling the deformation of sandy soils under cyclic loading induced by lock operation". Unexpected long-term settlements of locks leading to structural damage gave rise to the initiation of the project. It was suspected that the numerous loading and unloading cycles on the construction and the surrounding soil body induced by lock operation are responsible for the accumulation of irreversible deformation in the ground. Thus, the objective was to find or develop a soil model that would be able to predict life-time settlements in order to avoid damage and to design more economically.

This case is just one example in infrastructural design that puts high demands on the constitutive model to be applied in numerical analyses: complex installation processes and the repetitive character of live loads pose considerable challenges. Nevertheless, despite the current omnipresence of cyclic loadings in geotechnical research, an intermediate step in constitutive modelling should be to correctly capture fundamental behavioural patterns

of soil behaviour, such as hardening, dilatancy or state dependence[6], before preceding to more complicated issues. The simulation of element tests and the reproduction of geotechnically relevant stress paths of low and higher complexity represent a proven mean in this process of identifying essential features and advancing constitutive models.

Furthermore, although constitutive modelling is primarily concerned with the analytical requirements of the geotechnical problem, the demands of engineering practice should not be neglected. If application in geotechnical design is desired, material models should not only describe the soil behaviour adequately, but also need to be comprehensible and well-documented to avoid black box usage and encourage confidence. Moreover, a model needs to employ a manageable amount of parameters that can be understood and determined with a reasonable experimental expense (conventional laboratory testing). Last but not least, the availability to the potential user also has a strong influence on the spreading of a model.

Along these lines a set of specific requirements has been worked out as a guideline for the development process. First of all, elastoplasticity has been chosen as an appropriate constitutive framework, offering the additional advantage of a high degree of awareness. Elementary characteristics of soil behaviour that need to be captured include for example shear related phenomena such as hardening/softening, contraction/dilation and attainment of critical state (constant volume shear strength). In addition, capturing barotropy and pycnotropy – the soil's state dependence with respect to strength, stiffness and dilatancy – enables unified modelling. Hence, with only one set of material parameters, the mechanical behaviour of a wide range of initial soil states can be simulated. Moreover, when it comes to stress paths of unconventional orientation, to load reversals or composed stress paths with changes in loading direction, additional features of soil behaviour become important. There is kinematic hardening to allow for stress/strain accumulation, an increased stiffness at small strains or a capped yield surface for plastic straining in constant stress ratio loading, to name only a few.

In light of these demands in an earlier stage of the research project, Benz [Ben03] identified bounding surface plasticity to provide a sound basis for

---

[6]The soil state is not only defined by the current stress level, but also by the soil's density in terms of the void ratio. Other factors describing the soil's state are for example the geometrical arrangement of the grains (soil fabric) or temperature.

the defined needs. In the present work, the development process from the
"original" bounding surface model by Manzari and Dafalias [MD97] towards
the extended version is documented, its performance is demonstrated and
its potentials and limitations are highlighted.

The content of this thesis can hence be outlined as follows:

- **Chap. 2** is concerned with a literature review on bounding surface
  plasticity as well as small strain stiffness and dilatancy – two aspects
  that will be subject to constitutive advancements, described in Chap.
  3.
  The evolution from the more general constitutive concept of elasto-
  plasticity to a multi-surface approach, such as bounding surface plasti-
  city, and the associated benefits for the intended purpose are illustra-
  ted. The "original" bounding surface model by Manzari and Dafalias
  [MD97] and the two different branches of enhancement by Papadi-
  mitriou and Bouckovalas [PB02] and Taiebat and Dafalias [TD08]
  are presented. Furthermore, light is cast on the two soil mechanical
  phenomena small strain stiffness and dilatancy: micromechanical ob-
  servations as well as classical and alternative modelling approaches
  are discussed.

- The extended version of the bounding surface model is portrayed in
  Chap. 3. Its capabilities with respect to fundamental soil behaviou-
  ral patterns, resulting from the underlying bounding surface concept,
  are presented. Moreover, newly developed model features and their
  merits are described. Finally, the limitations of the bounding surface
  model are elaborated, distinguishing between intrinsic insufficiencies
  of the concept, remaining shortcomings of the enhanced model and
  newly introduced deficiencies.

- As mentioned above, the simulation of element tests and the repro-
  duction of simple stress paths are very useful means for the develop-
  ment of constitutive models. Assuming that both material and the
  stress-strain distribution of the soil specimen are homogeneous in
  element tests (see Sec. 1.1), the calculation of one representative soil
  element suffices for obtaining the soil response. Constitutive drivers
  are a valuable tool for this purpose. The structure of the Octave im-
  plementation used for the simulations of the present work is explained
  at the beginning of **Chap. 4**.
  The second half of the chapter is dedicated to the calibration proce-

dure of the extended bounding surface model. A calibration routine is introduced, which determines bounding surface specific parameters on the basis of a user input that is more oriented towards known soil model constants or experimental outcome.

- For validation purposes the performance of the material model is tested in **Chap. 5** by running numerical simulations of a different kind: element tests (drained and undrained triaxial compression as well as isotropic and oedometric compression), non-standard triaxial tests with different loading directions and more general stress paths (non-monotonous, small strain range, combined stress paths). For the evaluation of the unconventional triaxial loadings, response envelops are used. Deviations between numerical and laboratory test results are discussed on a constitutive and an experimental level.

- **Chap. 6** recapitulates the model with its benefits and limitations and concludes in view of the initial motivation and objectives. Perspectives for further development are pointed out.

1.3   Basic assumptions and terminology

This section introduces fundamental assumptions the present work builds on, as well as definitions, notations and conventions applied in the following chapters.

- The mechanical sign convention is adopted: compressive stresses and strains are negative, tensile stresses and strains are positive.

- Soil mechanical constitutive models are generally formulated in effective stresses. Hence, all stress quantities are considered effective and the usual prime is omitted for the sake of convenience – unless stated differently. The same applies to the effective friction angle (referring to full saturation).

- Tensors are denoted by either bold lower-case Latin or Greek letters (vector / first-order tensor) or bold upper-case Latin or Greek letters (matrix / second-order tensor). Scalars (zero-order tensor) are denoted by normal Latin or Greek letters.

- There are several product operations for relating tensors of different orders, using different notations. Let a and b be two scalars, $\boldsymbol{x}$ and $\boldsymbol{y}$ two column vectors of the same dimension and $\boldsymbol{V}$ and $\boldsymbol{W}$ two square matrices of equal dimensions:

    product $a \cdot b = ab = c,\, a \cdot \boldsymbol{x} = a\boldsymbol{x} = \boldsymbol{y}$

    dot / inner / scalar product $\boldsymbol{x} \cdot \boldsymbol{y} = \boldsymbol{x}^T \boldsymbol{y} = z$

    dyadic / outer / tensor product $\boldsymbol{x} \otimes \boldsymbol{y} = \boldsymbol{x}\boldsymbol{y}^T = \boldsymbol{Z}$

    matrix product[7] $\boldsymbol{V}\boldsymbol{W} = \boldsymbol{Z}$

    double dot / double inner product $\boldsymbol{V} : \boldsymbol{W} = \mathrm{tr}(\boldsymbol{V}\boldsymbol{W}) = c$

    NB: The symbol for a product relating scalars or a scalar and a tensor of higher order is sometimes omitted for convenience or purposefully put in order to highlight the structure of an equation.

- According to continuum mechanics the stress state of a point in three-dimensional stress space is defined by the (Cauchy) stress tensor, a second-order tensor consisting of nine components σ_{ij}, given by a 3×3 matrix:

$$\boldsymbol{\sigma} = \sigma_{ij} = \begin{bmatrix} \sigma_{11} & \sigma_{12} & \sigma_{13} \\ \sigma_{21} & \sigma_{22} & \sigma_{23} \\ \sigma_{31} & \sigma_{32} & \sigma_{33} \end{bmatrix} \quad \text{with} \quad \sigma_{12} = \sigma_{21},\, \sigma_{13} = \sigma_{31},\, \sigma_{23} = \sigma_{32}$$

    Since $\boldsymbol{\sigma}$ is a symmetric tensor with only six distinct elements, its order can be reduced by Voigt notation. The tensor is simplified to a six-dimensional vector of the form:

$$\boldsymbol{\sigma} = (\sigma_{11}, \sigma_{22}, \sigma_{33}, \sigma_{23}, \sigma_{13}, \sigma_{12})$$

    This notation has the advantage that conventional operations for vectors can be used instead of specific tensor operations. Hence, the above mentioned double dot product can be replaced by the scalar product, if, for example, two stress tensors are multiplied.

    In this thesis the Voigt notation is used for reducing the second-order

---

[7]The matrix product is only defined, if the number of rows of $\boldsymbol{V}$ equals the number of columns of $\boldsymbol{W}$. Dot product and dyadic product can be considered special cases of the matrix product.

stress and strain tensors to vectors and also to simplify the fourth-order stiffness tensor to a 6×6 matrix.

If the stress state is presented in terms of principal stresses, then the stress tensor simplifies to:

$$\boldsymbol{\sigma} = (\sigma_1, \sigma_2, \sigma_3, 0, 0, 0)$$

- Loading conditions in terms of principal stresses and strains for conventional laboratory tests are defined as follows (see also Fig. 1.2):

  oedometric compression $\quad \sigma_2 = \sigma_3, \quad \varepsilon_2 = \varepsilon_3 = 0$

  isotropic compression $\quad \sigma_1 = \sigma_2 = \sigma_3, \quad \varepsilon_2 = \varepsilon_3$

  triaxial compression $\quad \sigma_1 > \sigma_2 = \sigma_3$
  $\qquad$ with $\sigma_a = \sigma_1$ and $\sigma_r = \sigma_2 = \sigma_3$,
  $\qquad \varepsilon_2 = \varepsilon_3$

  triaxial extension $\quad \sigma_1 = \sigma_2 > \sigma_3$
  $\qquad$ with $\sigma_a = \sigma_3$ and $\sigma_r = \sigma_1 = \sigma_2$,
  $\qquad \varepsilon_1 = \varepsilon_2$

- Invariants serve for expressing a tensor independent from the orientation of the chosen coordinate system. In soil mechanics the Roscoe stress invariants (derived from principal stresses) are widely-used and also employed for the formulation of the present material model:

  mean stress $\quad p = \frac{1}{3} \operatorname{tr} \boldsymbol{\sigma} = \frac{1}{3}(\sigma_1 + \sigma_2 + \sigma_3)$

  deviatoric stress $\quad q = \sqrt{\frac{3}{2} \boldsymbol{s} \cdot \boldsymbol{s}}$

  $\qquad$ with $\boldsymbol{s} = \boldsymbol{\sigma} - p\boldsymbol{I}$ and $\boldsymbol{I} = \begin{bmatrix} 1 & 0 & 0 \\ 0 & 1 & 0 \\ 0 & 0 & 1 \end{bmatrix}$

  $\qquad$ so that $q = \frac{1}{\sqrt{2}} \sqrt{(\sigma_1 - \sigma_2)^2 + (\sigma_2 - \sigma_3)^2 + (\sigma_3 - \sigma_1)^2}$

  which for triaxial compression $(\sigma_2 = \sigma_3)$ reduce to
  $\qquad p = \frac{1}{3}(\sigma_1 + 2\sigma_3) \quad$ and $\quad q = \sigma_1 - \sigma_3$

- In analogy to stress, the strain tensor $\boldsymbol{\varepsilon}$ can be decomposed into a volumetric and a deviatoric component:

    volumetric strain $\varepsilon_p = \varepsilon_v = \operatorname{tr}\boldsymbol{\varepsilon} = \varepsilon_1 + \varepsilon_2 + \varepsilon_3$

    deviatoric strain $\varepsilon_q = \sqrt{\tfrac{2}{3}\mathbf{e}\cdot\mathbf{e}}$ with $\mathbf{e} = \boldsymbol{\varepsilon} - \tfrac{1}{3}\varepsilon_p\boldsymbol{I}$

    so that $\varepsilon_q = \tfrac{\sqrt{2}}{3}\sqrt{(\varepsilon_1 - \varepsilon_2)^2 + (\varepsilon_2 - \varepsilon_3)^2 + (\varepsilon_3 - \varepsilon_1)^2}$

    which for triaxial compression $(\varepsilon_2 = \varepsilon_3)$ reduce to

    $\varepsilon_p = \varepsilon_1 + 2\varepsilon_3$ and $\varepsilon_q = \tfrac{2}{3}(\varepsilon_1 - \varepsilon_3)$

The deviatoric strain component may be converted into shear strain: $\gamma_s = \tfrac{3}{2}\varepsilon_q = \varepsilon_1 - \varepsilon_3$

2 Literature review

The soil model presented in this work is based on widely acknowledged concepts and principles of soil mechanics. The most obvious kinship relation exists to the family of bounding surface plasticity models, a descendent of elastoplasticity. In order to get a sound understanding of the model functionalities, it is indispensable to obtain an insight into the underlying theory. Therefore, the aim of this chapter is to create a notion of bounding surface plasticity and the interrelated concepts such as critical state soil mechanics and state dependence. Describing the path from conventional elastoplasticity to the new concept of a bounding surface in the first subchapter aims at the reader's comprehension of the previous models' deficiencies (which motivated the development) and the benefits for soil modelling arising therefrom.

Having its roots in the first model generation by Dafalias and Popov [DP75] and Krieg [Kri75], respectively, comprising two surface models with a bounding and a yield surface, the bounding surface family had several evolutionary paths since then, followed by different research groups. The direct predecessor of the bounding surface model in this work is the version by Manzari and Dafalias [MD97]. There had also been other developments by Papadimitriou and Bouckovalas [PB02] as well as Taiebat and Dafalias [TD08] having introduced further ideas into the bounding surface concept, which are of importance for the actual model. Consequently, these three model versions are presented in depth in the following subchapter.

Besides the model basics, it is useful to open the view to further topics since the extended version of the original bounding surface model contains new features, which are aimed at ameliorating the model performance and require supplemental theoretical background for a better comprehension. Thus, there are two more sections on the fundamentals of small strain stiffness and dilatancy since these are important characteristics that underwent

modification in the development of the model extension, treated in detail
in Sect. 3.2.

2.1 From elastoplasticity to bounding surface plasticity

As mentioned in the introductory section, there has not only been one parent model to all follow-ups that build the relatively large family of bounding surface models. In the mid-seventies two groups, namely around the researchers Dafalias/Popov and Krieg, laid the foundations for bounding surface plasticity. Motivated by the necessity of describing the material behaviour in the plastic range as close to (experimental) reality as possible, also for more complex loading paths (as in cyclic loading), they created this new class of constitutive models.

Set up in an elastoplastic modelling framework, the development towards bounding surface plasticity permitted to overcome certain deficiencies of the conventional theory of elastoplasticity. At that stage, most elastoplastic models were based on an isotropically hardening yield surface, expanding equally in all directions when activated. It allows for plastic flow as soon as the stress state reaches the yield surface, but causes perfectly elastic and hence fully recoverable strains at unloading, where the stress state remains inside its bounds (see Fig. 2.1 a). Consequently, pre-failure yielding at a larger scale could be treated accurately, but the irreversibility of smaller strains and the stress-strain hysteresis, which are typically observed in experiments, could not be captured on stress paths inside the yield surface.

Improvements have been made by developing kinematic hardening mecha-
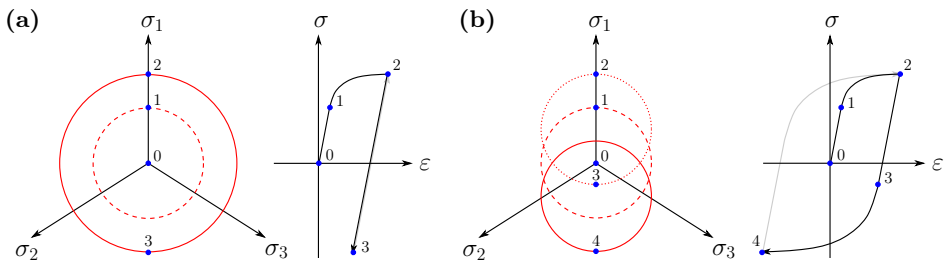
Figure 2.1: Hardening mechanisms and their impact on yield surface and stress-strain evolution: (a) Isotropic vs. (b) kinematic

nisms [e. g. Zie59], which enable accordingly equipped models to reproduce the so called Bauschinger effect: yielding after a stress reversal occurs at a lower tensile stress than previously observed in compression, which can be considered as a directional dependence of the yield stress after plastic deformation. This advancement allowed for reproducing the hysteresis loop appearing in reversed loadings, depicted in Fig. 2.1 b. However, little effort has been put into the specification of the plastic modulus by defining an appropriate non-linear hardening law, which, for example, ensures different plastic moduli before and after shear reversal. This implies a constitutive basis that does not satisfy the modelling requirements in cyclic loading to the full extent.

In order to overcome the problem of pure elasticity within the yield surface, another approach appeared: the introduction of multiple load or yield surfaces. It assumes a kinematically (and isotropically) hardening yield surface, enclosed by a boundary surface. Stress states inside the yield surface are elastic, those on the yield surface with the stress increment vector pointing outside cause elastoplastic behaviour. The novelty is that the domain delimited by the boundary surface is not elastic and plastic flow occurs once the yield condition of the yield surface is satisfied. Instead, the boundary surface serves to define the hardening mechanism of the yield surface, which is a function of the relative configuration of the two surfaces. This is in line with the awareness that the major reason for cyclic phenomena is the change in plastic modulus during the evolution of plastic deformation.

Following this concept, Mróz [Mró67] for example defined a field of harde-
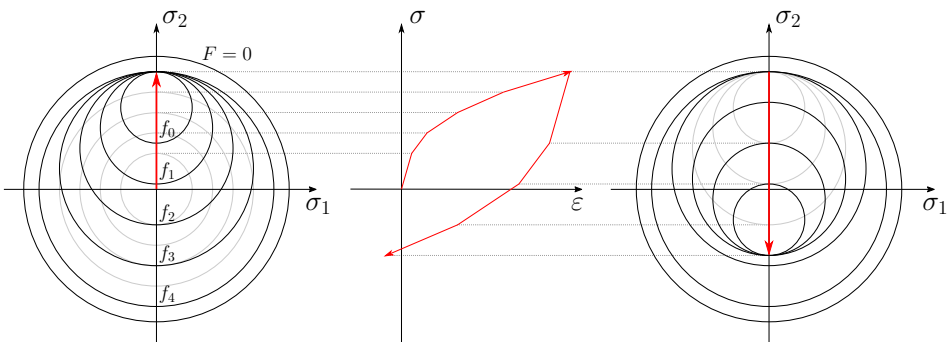
Figure 2.2: Bounding surface (F), yield surface (f_0) and nesting surfaces (f_i) according to Mróz [Mró67] and Mróz et al. [MNZ78]
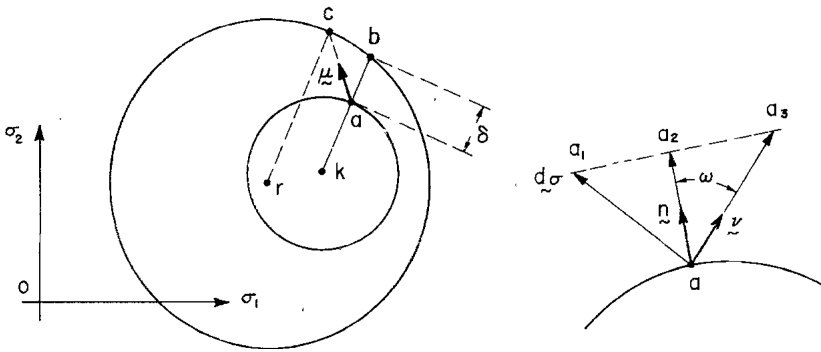
Figure 2.3: Loading/yield surface and enclosing bounding surface and illustration of their motions according to Dafalias and Popov [DP75]

ning moduli through the creation of several nesting surfaces as depicted in Fig. 2.2. A specific constant workhardening modulus is attributed to each of the nested surfaces, resulting in a correspondingly decreasing stiffness. Later, the hardening moduli of the surfaces became a function of their respective distance to an outer bounding surface by Mróz et al. [MNZ78]. This conceptual idea was taken from Dafalias and Popov [DP75] and Krieg [Kri75]. They, however, limited their approach to two surfaces: the elastic region is represented by the interior of the yield surface and the so called bounding surface is some kind of plastic limit in stress space, always enclosing the yield surface. Independently, Dafalias/Popov and Krieg proposed to directly relate the changes in the plastic modulus to the notion of considering the stiffness to be a function of the distance δ between the actual point and a certain limit in stress space located on the bounding surface (see Fig. 2.3). In the course of deformation, the distance changes continuously, namely decreasing when the yield surface approaches the bounding surface, and the plastic modulus does accordingly, tending to a minimum value (or zero) when $\delta = 0$. The distance δ between the current stress state on the yield surface and the corresponding point on the bounding surface is based on an appropriate definition of the latter. There were several proposals for so called mapping rules, but a widely-used strategy is to locate the image point by finding the intersection of the normal to the yield surface (loading vector) with the bounding surface [e. g. MD97, PB02, TD08].

Within the following decade numerous developments enriched the basic formulation by Dafalias and Popov, applying the concept of a bounding surface to different materials such as metals [Daf81], soil [MNZ79, DH80, Bar84]

and concrete [YDH85]. Even though names given to the bounding surface vary throughout the models (limiting surface, failure surface, memory surface . . .), the idea of a distance dependent plastic modulus remained the same. Since the focus of this chapter is not to give an overview of the historical evolution of bounding surface plasticity but rather to describe the functionalities of the reference model for this work, the chronological advancements will not be summarised here. Instead, the following subchapter gives a detailed presentation on the model by Manzari and Dafalias [MD97], laying the foundation of a good understanding of the constitutive ingredients and their impact on the model behaviour as prerequisite for the explanation of the developed model extensions.

2.1.1 Bounding surface model according to Manzari and Dafalias (1997)

Being based on the concept of a bounding or two-surface plasticity formulation according to the ideas of Dafalias and Popov [DP75] and Krieg [Kri75], the model according to Manzari and Dafalias [MD97] extends the fundamental idea of a distance dependent plastic modulus by the concept of state dependence. This feature was motivated by the fact that previous plasticity models (including the bounding surface type) merely considered the impact of stress level on the soil behaviour. They were incapable of capturing the influence of variations in void ratio on the soil response. Consequently, changes in density during the deformation process and their resulting influence on the mechanical properties of the deforming soil body could not be taken into account. Furthermore, especially sands had to be treated as different materials when a wide range of densities was to be considered in soil mechanical calculations. The novelty in the bounding surface model by Manzari and Dafalias was to set up the constitutive relations in a critical state soil mechanics (CSSM) framework (Roscoe et al. [RSW58], Schofield and Wroth [SW68]). This constitutive concept, which is an underlying theory rather than a model, creates the link between the soil density, namely the void ratio, and the applied stress.

The CSSM concept states that granular materials, if continuously sheared, will finally reach a well-defined critical state. This critical state features a steady increase in distortional strain without any further changes in stress or density. For a particular soil, all critical states are joined in a unique line in stress and stress - void ratio space, respectively, the so called critical state line (CSL). According to Schofield and Wroth [SW68] it is defined by the

following two equations, using the stress invariants of triaxial stress space (p,q) and the void ratio e:

$$q_{cs} = M^c \cdot p \tag{2.1}$$

$$e_{cs} = e_{csa} - \lambda \cdot \ln\left(\frac{p}{p_{at}}\right) \tag{2.2}$$

The parameters M^c, λ and e_{csa} are soil constants determining the magnitude of deviatoric stress and the void ratio attained at critical state as functions of the mean effective stress.

The location of a state with respect to the CSL in stress-void ratio space is the crucial element that constitutes the desired state dependence. The soil behaviour differs depending on the distance of the current void ratio e from its "image" e_{cs} on the CSL at the same mean effective stress. If the actual void ratio is located above the CSL in stress-void ratio space, a soil specimen shows behaviour typical for normally compressed (or lightly overconsolidated) soils – contractant and hardening. If it is located below, after an initial contraction it behaves dilatively and softens like heavily overconsolidated soils. This distance, which obviously plays a key role in CSSM, is quantified by

$$\psi = e - e_{cs} \tag{2.3}$$

and was introduced by Been and Jefferies [BJ85] as so called state parameter (see Fig. 2.4 a). In each calculation step it is updated according to the actual size of mean stress p and void ratio e[1]. By incorporating the state parameter ψ into the bounding surface model formulation the state dependence[2] finds its way into bounding surface plasticity.

An alternative to representing current state data (p and e) by means of an "equivalent" void ratio e_{cs} (attained under the same pressure at critical state), would be the equivalent consolidation pressure p_e proposed earlier by Hvorslev [Hvo37]. As shown in Fig. 2.4 b, the equivalent consolidation pressure is the effective mean stress, which would result in the same void ratio in isotropic normal consolidation. Instead of using a difference $(e - e_{cs})$, the

---

[1]The void ratio e depends on the evolving volumetric strain; its rate is derived from $\dot{e} = (1 + e_0)\,\dot{\varepsilon}_v$. Consequently, e is a state parameter itself.

[2]In the context of the state parameter according to Been and Jefferies [BJ85] the definition of "state" is limited to the stress level and the void ratio. There are other factors characterising the soil's state, such as soil fabric (arrangement of the particles) and temperature, which are neglected here.
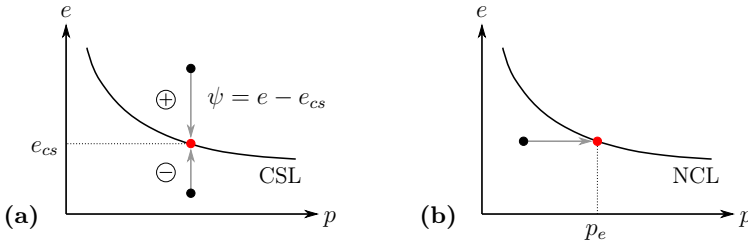
Figure 2.4: Representing current state information by (a) state parameter ψ [BJ85] and (b) equivalent consolidation pressure p_e [Hvo37]

relation between reference state and current state is made by normalisation of p and q with p_e (p/p_e, q/p_e).

In the model by Manzari and Dafalias state dependence is realised by making the model surfaces direct functions of the state parameter ψ. This is done by linking the latter to a stress ratio M that defines the inclination of the respective model surface in triaxial stress space. In case of the bounding surface the expression for the bounding stress ratio for compression (c) and extension (e), respectively, is

$$M_{c,e}^b = M_{c,e}^c + k_{c,e}^b \cdot \langle -\psi \rangle \quad \text{with} \quad M_{c,e}^c = \frac{6 \sin \varphi_{cs}}{3 \mp \sin \varphi_{cs}} \tag{2.4}$$

Hence, the peak (or bounding) stress ratio for a particular state is derived from a linear relationship defined by the critical state stress ratio M^c and the evolving state parameter ψ, scaled by a constant k^b. The Macauley brackets return $\langle -\psi \rangle = -\psi$ if $-\psi > 0$ and $\langle -\psi \rangle = 0$ if $-\psi \leq 0$. Consequently, the initial bounding stress ratio M^b is larger than M^c for dense soils ($\psi < 0$) and it never falls below the critical state stress ratio M^c, so that $M_{c,e}^b = M_{c,e}^c$ in case of loose states ($\psi > 0$). Applied to a standard triaxial compression loading case on dense soil, the stress ratio $\eta = \frac{q}{p}$ starts increasing from zero towards the peak state and simultaneously M^b evolves with progressing state parameter. As long as $\eta < M_c^b$ so that $M_c^b - \eta > 0$, the yield surface hardens. With decreasing distance, the plastic modulus also decreases, causing the soil to lose stiffness. At peak ($\eta = M_c^b$) the stress state momentarily crosses the bounding surface so that the distance $M_c^b - \eta$ becomes negative and consequently the soil starts softening: the stress ratio decreases. Strictly speaking, this evolution violates the original premise that the bounding surface bounds all stress states, but it is a pragmatic way to incorporate softening behaviour. With further straining, the

state parameter approaches zero and it follows from Eq. (2.4) that, when $\psi = 0$, the bounding surface automatically falls onto the critical state surface in stress space, so that the stress state will finally reach critical state, converging from outside the bounding surface. The exact mechanisms of hardening and softening are explained later.
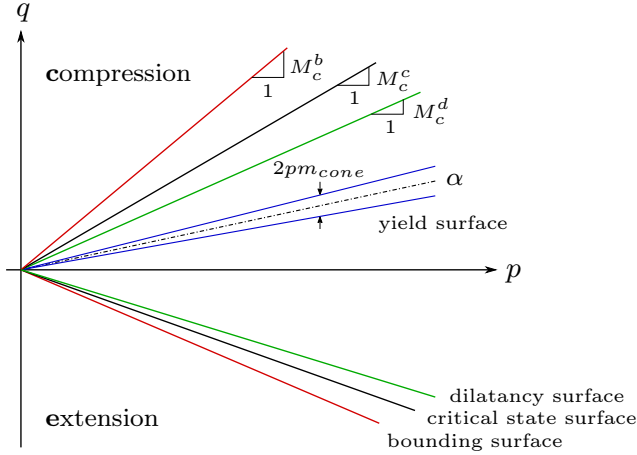
Figure 2.5: Model surfaces in triaxial stress space

Another aspect of CSSM is that not only hardening or softening, but also the soil's volumetric response is linked to the state's position relative to the CSL. In order to allow for the modelling of contractant and dilative soil behaviour, Manzari and Dafalias [MD97] extended the original two-surface model by the volumetric correspondent to the bounding surface, the so called dilatancy surface (see Fig. 2.5), characterised by the state dependent dilatancy ratio:

$$M_{c,e}^d = M_{c,e}^c + k_{c,e}^d \cdot \psi \tag{2.5}$$

In analogy to the bounding surface, the distance from the current stress state to the image stress on the dilatancy surface, $M_{c,e}^d - \eta$, determines the sign of volumetric deformation: as long as $\eta < M_c^d$ the soil response is contractive, once the dilatancy surface is exceeded and $M_{c,e}^d - \eta < 0$ the volume expands. In this sense, the dilatancy surface represents the phase transformation line, described by Ishihara et al. [ITY75], which marks the transition point in stress space from contractant to dilative states. According to their mathematical formulations bounding and dilatancy surface move in opposite directions. Using the example of dense soil in a triaxial compression

test, in contrast to the bounding surface the initial dilatancy stress ratio is less than the critical state stress ratio and approaches M^c when $\psi \to 0$. Making the volumetric response to be a function of the difference $M_{c,e}^d - \eta$, Manzari and Dafalias [MD97] proposed the following relationship for the dilatancy ratio D referring to Rowe's stress-dilatancy theory [Row62] and a suggestion by Nova and Wood [NW79]:

$$D = \sqrt{\frac{2}{3}} A \left(M_{c,e}^d - \eta \right) \tag{2.6}$$

where A is a positive constant and the factor $\sqrt{2/3}$ is only introduced for convenience with respect to a later multiaxial generalisation. Depending on the sign of the distance, D is positive for contraction and takes negative values for dilation. One restriction has to be made on D for the rather hypothetical case of neutral loading of initially dense soil: zero dilatancy is prescribed in case $\eta > M_c^d$ and $\psi > 0$ simultaneously. A detailed explanation for the necessity of this exception is given in Manzari and Dafalias [MD97].

Similar to the dilatancy ratio, the plastic modulus is calculated on the basis of the difference $M_{c,e}^b - \eta$. In order to understand the underlying theory, it is worth taking one step back towards the fundamentals of hardening plasticity. According to the flow rule, it is the plastic multiplier λ that scales the direction of plastic deformations, quantified by the gradient of the plastic potential $\frac{\partial g}{\partial \sigma}$. Based on the consistency condition, the plastic multiplier can be derived in the following form (see App. A.1 for the complete derivation):

$$\lambda = \frac{\frac{\partial f}{\partial \sigma} D^{el} \dot{\varepsilon}}{\frac{\partial f}{\partial \sigma} D^{el} \frac{\partial g}{\partial \sigma} + K_p} \quad \text{with} \quad K_p = -\frac{\partial f}{\partial \kappa} H \frac{\partial g}{\partial \sigma} \tag{2.7}$$

K_p being the plastic modulus. The derivation of this constitutive relation is generally applicable in any elastoplastic framework. What makes this equation distinctive for a particular model is the expression chosen for the hardening modulus H in conjunction with the plastic potential g and the yield surface f. In case of the Manzari/Dafalias model the latter is expressed by the following formulation (in triaxial stress space):

$$f = \eta - \alpha \pm m_{cone} = 0 \tag{2.8}$$

all variables being stress ratio quantities. α marks the centreline of the conical yield surface (Fig. 2.5), representing the back stress that controls

the rotation of the cone around its apex at the origin and consequently being the internal variable responsible for kinematic hardening. The opening of the cone is quantified by the radius m_{cone}, which is chosen to be variable as well, allowing the yield surface to harden isotropically. The $\pm$ stands for the lower and upper limit of the yielding cone, attained when the stress state lies on the respective boundary of the yield surface.

Departing from the formula for the conical yield surface, the derivatives with respect to stress and hardening variables, $\frac{\partial f}{\partial \sigma}$ and $\frac{\partial f}{\partial \kappa}$, can be found.

The gradient of the plastic potential, which is an essential part of the flow rule defining the plastic strain rate direction, is expressed in deviatoric and volumetric components as follows:

$$\frac{\partial g}{\partial q} = \pm 1 \quad \text{and} \quad \frac{\partial g}{\partial p} = D \tag{2.9}$$

Depending on the location of the stress point with respect to the centreline of the yield surface, the sign of the deviatoric part of the plastic potential varies: if $\eta - \alpha > 0$ the derivative is positive, if $\eta - \alpha < 0$ the derivative is negative.

Since the Manzari/Dafalias model comprises two hardening mechanisms – the kinematic (deviatoric) one with respect to α and the isotropic (volumetric) one with respect to m_{cone} – the plastic modulus decomposes into:

$$K_p = -\frac{\partial f}{\partial \alpha} H_\alpha \frac{\partial g}{\partial q} - \frac{\partial f}{\partial m_{cone}} H_m \frac{\partial g}{\partial p} \tag{2.10}$$

Still missing for completion of the plastic modulus are the hardening moduli with respect to their hardening variables, H_α and H_m. Translating the slightly different formulation of Manzari and Dafalias into the present structure, they are defined as

$$H_\alpha = \sqrt{\frac{2}{3}} h \left(M_{c,e}^b - \eta \right) \quad \text{and} \quad H_m = c_m \left(1 + e_0 \right) \tag{2.11}$$

The parameters h and c_m are positive quantities, which are made state dependent functions in the Manzari/Dafalias model as well. A generalised expression for h is given in the multiaxial stress space section. The factor $\sqrt{2/3}$ in H_α is included for convenience with regard to the transformation to general stress conditions.

As claimed earlier, this shows that the hardening modulus related to the back stress α is the point in the constitutive network where the difference

$M_{c,e}^{b} - \eta$ (the distance between current stress state and its image on the bounding surface) determines the size of the plastic modulus and hence the amount of plastic straining.

Multiaxial generalisation

Having introduced all constitutive elements in a triaxial stress environment, it is advantageous to transfer the equations into multiaxial stress space in order to be able to act in a general stress context. Therefore, the given expressions have to be reformulated using directional quantities. The stress invariants p and q are replaced by tensor based quantities, which are deduced from the stress tensor[3] $\boldsymbol{\sigma}$, yielding the hydrostatic stress p and the shear stress tensor $\boldsymbol{s}$ according to

$$p = \frac{1}{3}\operatorname{tr}\boldsymbol{\sigma} \quad \text{and} \quad \boldsymbol{s} = \boldsymbol{\sigma} - p\boldsymbol{I} \tag{2.12}$$

where tr and $\boldsymbol{I}$ denote the trace of a tensor and the identity tensor, respectively. In addition, a deviatoric stress ratio tensor $\boldsymbol{r} = \boldsymbol{s}/p$ is introduced, the multiaxial equivalent of η.

For a better understanding it is useful to create a link between the triaxial expression and its multiaxial counterpart, which is the basis of the applied generalisation. For any deviatoric stress tensor $\boldsymbol{t}$ the following relation holds true:

$$\frac{3}{2}\boldsymbol{t} \cdot \boldsymbol{t} = (t_1 - t_3)^2 \tag{2.13}$$

This is valid, for example, for the deviatoric stress components and equally for the deviatoric stress ratio quantities:

$$\frac{3}{2}\boldsymbol{s} \cdot \boldsymbol{s} = (s_1 - s_3)^2 = (\sigma_1 - \sigma_3)^2 = q^2 \quad , \quad \frac{3}{2}\boldsymbol{r} \cdot \boldsymbol{r} = \eta^2 \quad , \quad \frac{3}{2}\boldsymbol{\alpha} \cdot \boldsymbol{\alpha} = \alpha^2 \tag{2.14}$$

In analogy, the strain tensor $\boldsymbol{\varepsilon}$ is decomposed into a deviatoric and a volumetric part

$$\boldsymbol{\varepsilon} = \mathbf{e} + \frac{1}{3}\varepsilon_p\boldsymbol{I} \tag{2.15}$$

---

[3]All stress and strain tensors are written in Voigt notation. Thus, tensor operations reduce to conventional vector operations. Voigt notation is also applied to the stiffness tensor. See also Sec. 1.3.

with $\varepsilon_p = \mathrm{tr}\,\boldsymbol{\varepsilon}$ and the triaxial and multiaxial deviatoric components are related via

$$\frac{3}{2}\mathbf{e}\cdot\mathbf{e} = (\mathrm{e}_1 - \mathrm{e}_3)^2 = (\varepsilon_1 - \varepsilon_3)^2 = \left(\frac{3}{2}\varepsilon_q\right)^2 \quad \rightarrow \quad \frac{2}{3}\mathbf{e}\cdot\mathbf{e} = \varepsilon_q^2 \qquad (2.16)$$

Based on the foregoing derivations the elastic and plastic constitutive relations can be formulated as follows in the next section. Starting with the generalised expression for the elastic strain rate, it can be written

$$\dot{\boldsymbol{\varepsilon}}^{\boldsymbol{el}} = \dot{\mathbf{e}}^{\mathbf{el}} + \frac{1}{3}\dot{\varepsilon}_p^{el}\boldsymbol{I} = \frac{\dot{\boldsymbol{s}}}{2G} + \frac{\dot{p}}{3K}\boldsymbol{I} \qquad (2.17)$$

with G and K being the elastic shear and bulk moduli, respectively, depending on the mean stress related to the atmospheric pressure p_{at} according to the Ohde or Janbu power law [Ohd39, Jan63][4]:

$$G = G_0\left(\frac{p}{p_{at}}\right)^m \quad \text{and} \quad K = K_0\left(\frac{p}{p_{at}}\right)^m \qquad (2.18)$$

The multiaxial formulation of the yield surface according to Manzari and Dafalias [MD97] is expressed as

$$f = \sqrt{(\boldsymbol{s} - p\boldsymbol{\alpha})\cdot(\boldsymbol{s} - p\boldsymbol{\alpha})} - \sqrt{\frac{2}{3}}m_{cone}\,p = 0 \qquad (2.19)$$

which can be transferred into a similar equation that is based on the deviatoric stress ratios $\boldsymbol{r}$ and $\boldsymbol{\alpha}$, so that the link to its triaxial counterpart η is more straightforward:

$$f = \sqrt{(\boldsymbol{r} - \boldsymbol{\alpha})\cdot(\boldsymbol{r} - \boldsymbol{\alpha})} - \sqrt{\frac{2}{3}}m_{cone} = 0 \qquad (2.20)$$

Represented in the $\boldsymbol{r}$-space as in Fig. 2.6, the wedge of the yield surface in triaxial space geometrically describes a cone with its apex at the origin of the axes. Its cross section on the Π-plane, which is perpendicular to the diagonal of the $\boldsymbol{r}$-space, depicts a circle.

The other model surfaces are also conical, but are generally non-circular in the Π-plane. Depending on the actual loading direction $\boldsymbol{L} = \frac{\partial f}{\partial \boldsymbol{\sigma}}$ (normal

---

[4]Due to the hypoelastic form of the stiffness evolution, closed shear stress cycles produce small irreversible strains. That means, thermodynamic considerations are abandoned, since entropy is not conserved. Consequently, there is no zone of true elastic behaviour.
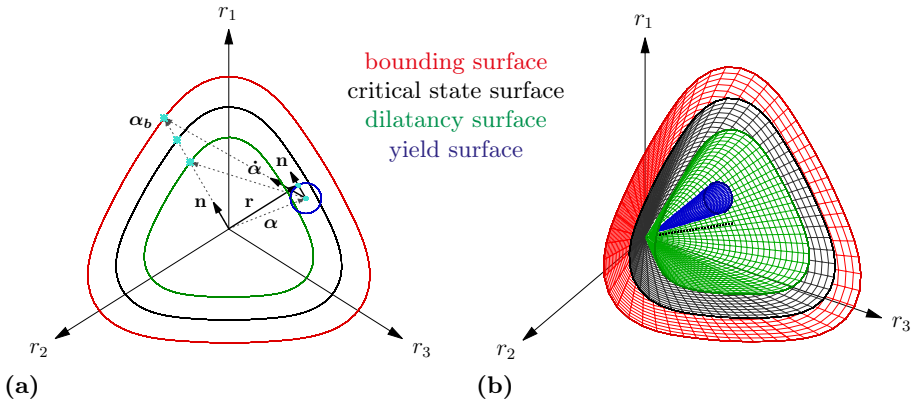
Figure 2.6: Model surfaces in multiaxial stress space (r space): (a) 2D and (b) 3D representation

to the yield surface), the deviatoric stress ratios $M^{b,c,d}$ vary, so that they differ for triaxial compression and extension and take intermediate values in non-triaxial loading cases. For multiaxial stress generalisation the so called Lode angle θ serves as an auxiliary parameter and is calculated on the basis of the deviatoric loading direction $\boldsymbol{n}$ $(= \frac{\partial f}{\partial \boldsymbol{s}})$, which is defined as

$$\boldsymbol{n} = \frac{\boldsymbol{r} - \boldsymbol{\alpha}}{\sqrt{(\boldsymbol{r} - \boldsymbol{\alpha}) \cdot (\boldsymbol{r} - \boldsymbol{\alpha})}} \tag{2.21}$$

Based on its definition as (deviatoric) unit vector, notice that tr $\boldsymbol{n} = 0$ and $\boldsymbol{n} \cdot \boldsymbol{n} = 1$.

For the Lode angle, which is a function of the second and third deviatoric stress invariants, follows

$$\cos 3\theta = \frac{3\sqrt{3}}{2} \left(\frac{\overline{J}_3}{\overline{J}_2} \right)^3 \quad \text{with} \quad \overline{J}_3 = \left(\frac{1}{3} \operatorname{tr} \left(\boldsymbol{n}^3 \right) \right)^{\frac{1}{3}}, \quad \overline{J}_2 = \left(\frac{1}{2} \operatorname{tr} \left(\boldsymbol{n}^2 \right) \right)^{\frac{1}{2}} \tag{2.22}$$

$$\cos 3\theta = \sqrt{6} \cdot \operatorname{tr} \left(\boldsymbol{n}^3 \right) \tag{2.23}$$

In order to adapt the model surfaces to the loading direction, the deviatoric stress ratios in compression of dilatancy, critical state and bounding surface are multiplied by a shape factor $g(c,\theta)$, which is a continuous function of the Lode angle θ and the ratio $c^{b,c,d} = M_e^{b,c,d}/M_c^{b,c,d}$, according to

$$M_\theta^{b,c,d} = g \left(c^{b,c,d}, \theta \right) \cdot M_c^{b,c,d} \tag{2.24}$$

The interpolation rule applied in the Manzari/Dafalias model is the one proposed by Argyris et al. [AFS$^+$74]:

$$g\left(c,\theta\right) = \frac{2c}{(1+c) - (1-c)\cos 3\theta} \tag{2.25}$$

From this formulation follows that, independent of c, in triaxial compression ($\theta = 0°$) $g(c,0°) = 1$ and in triaxial extension ($\theta = 60°$) $g(c,60°) = c$, resulting in a triangular shape with rounded corners. The constant c controls the roundness of this triangle; in case of $c = 1$ the failure surface becomes a circle in the Π-plane.

Finally, in multiaxial stress space the model surfaces are defined in terms of the stress ratio valued tensors

$$\boldsymbol{\alpha}^{b,c,d} = \sqrt{\frac{2}{3}} \cdot M_\theta^{b,c,d} \cdot \boldsymbol{n} \tag{2.26}$$

resulting in three non-circular cones (if $c^{b,c,d} \neq 1$), centred at the hydrostatic axis (Fig. 2.6). The alteration of the bounding and dilatancy surface is shown in Fig. 2.7, plotting the sizes of the two contours in the Π-plane as a function of the evolving state parameter ψ. The connecting lines clarify the linear evolution law expressed by Eqs. (2.4) and (2.5) with the proportionality constants k_b and k_d. From the graphical representation one can conclude that on the dense side ($\psi_0 < 0$), the dilatancy surface always lies inside the critical state surface, the bounding surface encloses both and towards critical state ($\psi = 0$) the two variable surfaces fall onto the static critical state surface. This enables the stress state to cross both surfaces successively and to exhibit dilative as well as softening behaviour after having contracted and hardened first. If on the other hand $\psi_0 > 0$ due to a loose initial soil state, the bounding surface has a constant shape with the size of the critical state surface (due to the Macauley brackets in Eq. (2.4)) and the dilatancy surface remains outside of both throughout the complete shear loading until critical state is reached. Consequently, a loose soil state can never cross the dilatancy surface and hence neither exhibit dilation nor softening[5].

Having described the transformation of the general constitutive elements into multiaxial stress space, the generalised expressions for evolution laws and flow rule are given in the following:

---

[5]There is an exception to this statement, if the initial state is loose, but very close to $\psi = 0$. For more details see Fig. C.5 in App. C.
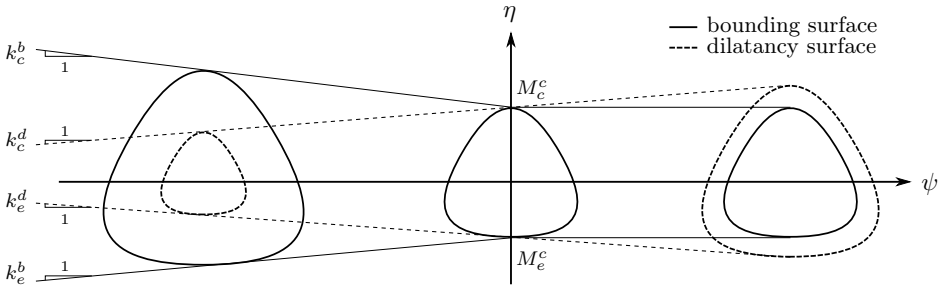
Figure 2.7: Extent of the model surfaces as function of the state parameter ψ

Plastic potential:

$$\frac{\partial g}{\partial \boldsymbol{s}} = \frac{\partial f}{\partial \boldsymbol{s}} = \boldsymbol{n} \qquad \frac{\partial g}{\partial p} = D \tag{2.27}$$

Flow rule:

$$\dot{\boldsymbol{\varepsilon}}^{\boldsymbol{pl}} = \dot{\mathbf{e}}^{\mathbf{pl}} + \frac{1}{3}\dot{\varepsilon}_p^{pl}\boldsymbol{I} = \lambda\left(\frac{\partial g}{\partial \boldsymbol{s}} + \frac{1}{3}\frac{\partial g}{\partial p}\boldsymbol{I}\right) = \lambda\left(\boldsymbol{n} + \frac{1}{3}D\boldsymbol{I}\right) \tag{2.28}$$

Hardening moduli:

$$H_\alpha = h\left(\boldsymbol{\alpha^b} - \boldsymbol{\alpha}\right) \cdot \boldsymbol{n} \qquad H_m = c_m\left(1 + e_0\right) \tag{2.29}$$

Hardening rules:

$$\dot{\boldsymbol{\alpha}} = H_\alpha \cdot \dot{\mathbf{e}}^{\mathbf{pl}} = \lambda \cdot H_\alpha \cdot \frac{\partial g}{\partial \boldsymbol{s}} = \lambda \cdot h \cdot \left(\boldsymbol{\alpha^b} - \boldsymbol{\alpha}\right) \tag{2.30}$$

$$\dot{m} = H_m \cdot \dot{\varepsilon}_p^{pl} = \lambda \cdot H_m \cdot \frac{\partial g}{\partial p} = \lambda \cdot c_m \cdot \left(1 + e_0\right) D \tag{2.31}$$

The parameter h in the deviatoric hardening modulus relates the actual scalar distance d^b to the bounding surface "diameter" d_{ref}^b according to Eq. (2.33) and consequently adds a non-linear dependence on the distance measure to the hardening mechanism:

$$h = h_0 \cdot h_b = h_0 \frac{\left|d^b\right|}{d_{ref}^b - \left|d^b\right|} \tag{2.32}$$

$$\text{with} \quad d^b = \left(\boldsymbol{\alpha^b} - \boldsymbol{\alpha}\right) \cdot \boldsymbol{n}$$

$$\text{and} \quad d_{ref}^b = \sqrt{\frac{2}{3}}\left(M_\theta^b + M_{\theta+\pi}^b\right) \approx \sqrt{\frac{2}{3}}\left(M_c^b + M_e^b\right) \tag{2.33}$$

In analogy to the hardening modulus, the dilatancy coefficient can be generalised by using the multiaxial distance measure from the actual stress state to the dilatancy surface projected onto the loading direction instead of the difference of triaxial stress ratios:

$$D = A_d \left(\boldsymbol{\alpha^d} - \boldsymbol{\alpha} \right) \cdot \boldsymbol{n} = A_d \cdot d^d \tag{2.34}$$

The two distance quantities $d^{b,d} = \left(\boldsymbol{\alpha^{b,d}} - \boldsymbol{\alpha} \right) \cdot \boldsymbol{n}$ are the multiaxial counterparts of $M_{c,e}^{b,d} - \eta$, automatically ensuring the correct surface stress ratio $M_\theta^{b,d}$ according to the current Lode angle and delivering the appropriate sign depending on the loading direction. As long as the stress state is located inside the corresponding limit surface, $\left(\boldsymbol{\alpha^{b,d}} - \boldsymbol{\alpha} \right)$ and the loading direction $\boldsymbol{n}$ always point into the same direction due to the Lode angle dependent definition of $\boldsymbol{\alpha^{b,d}}$. Thus $d^{b,d} > 0$ and consequently $H_\alpha > 0$ and $D > 0$, so that the response will be hardening and contraction, respectively. In case the stress state has crossed the limit surface ($\boldsymbol{\alpha^{b,d}} - \boldsymbol{\alpha}$ points inwards), the signs of H_α and D depend on the orientation of $\boldsymbol{n}$: If $\boldsymbol{n}$ points outwards, $d^{b,d} < 0$ and hence the soil softens and dilates, respectively. If $\boldsymbol{n}$ points inwards in a reverse loading case, $d^{b,d} > 0$, so that hardening/contraction occurs.

The moment the stress state reaches the respective surface, $\boldsymbol{\alpha^{b,d}} = \boldsymbol{\alpha}$ and the distance measure $d^{b,d} = 0$, so that hardening modulus and dilatancy ratio take zero values as well. Consequently, $\dot{\boldsymbol{\alpha}} = \boldsymbol{0}$ momentarily, so that $\boldsymbol{\alpha}$ remains constant, having attained its peak value before softening is initiated. Analogously, $\dot{\varepsilon}_p^{pl} = 0$, which corresponds to the phase transformation state, the transition between contraction and dilation.

2.2 Further development of the original model

Since the publication of the bounding surface model by Manzari and Dafalias [MD97], there have been numerous advancements on the original model mostly by researchers gathered around Dafalias in the subsequent years. To give a rough overview, there have been extensions, for example, by Li and Dafalias: the exchange of the expression for the CSL [LDW99], the modification of the state dependent dilatancy formulation [LD00] and the introduction of a fabric tensor in order to account for inherent fabric anisotropy [DPL04]. Dafalias and Manzari [DM04] improved their basic model by adding a mechanism on the dilatancy equations for fabric evolution in reversed loading. A very similar option was incorporated in the hardening

law of the model version by Papadimitriou and Bouckovalas [PB02]. In cooperation with Dafalias, Taiebat renamed the bounding surface type of models using the term SANISAND (simple anisotropic sand plasticity) and extended the original model by a new yield surface expression that allows for plastic strains in constant stress ratio loading [TD08].

In the following two sections the advancements on the Manzari/Dafalias model by Papadimitriou and Bouckovalas [PB02] and by Taiebat and Dafalias [TD08] are examined. These two examples have been chosen since their contributions inspired the development of the present extended model version to a great extent and are hence an important reference with respect to the explanations following in Chap. 3.

2.2.1   Papadimitriou and Bouckovalas (2002)

The most significant developments presented by Papadimitriou and Bouckovalas [PB02] concern the introduction of a non-linear hysteretic formulation for the elastic strain rate and a fabric evolution mechanism with continuous shear reversals. Both features were considered necessary in order to make the model applicable to small and large strain cycles, referring to the former modification, and on the other hand allow for a realistic simulation of accumulating strains during cyclic shearing. In the following, these two main changes with respect to the original model are explained in more detail.

As already indicated, the proposals were mainly motivated by the perception that the soil behaviour in cyclic shearing was not modelled satisfactorily in all respects. The basic Manzari/Dafalias model addresses cyclic behaviour mostly via kinematic hardening, which ensures the degradation of stiffness with progressive plastic deformation at a certain strain level and the recovery of elastic stiffness at load reversal. The proper reproduction of the stress-strain hysteresis at (very) small strains, however, cannot be captured. Depending on the size of the elastic domain in stress space, which can be roughly translated into a certain strain range, merely elastic deformations occur, ruled only by the stress dependent elastic stiffness formulation given in Eqs. (2.17) and (2.18). This implies a very stiff and even stiffening soil response with further loading inside the elastic range, which does not correspond to the stress-strain hysteresis typically observed in reversed loading conditions. In order to overcome this deficiency, Papadimitriou and Bouckovalas [PB02] incorporated a small strain stiffness degradation mechanism into the elastic stiffness formulation. It is based on the idea that some kind of threshold strain γ_1 exists, up to which plastic strain accumula-

tion is minor and the shear stiffness degrades from an initially high value to a certain minimum [e. g. Vuc94]. Beyond this threshold strain any further decrease in the overall shear stiffness is ascribed to the evolution of plastic strains.

Papadimitriou and Bouckovalas [PB02] extended the elastic shear modulus expression by a void ratio dependence according to Hardin [Har78] and a degrading factor, the latter being responsible for the decrease of the tangential modulus with progressive loading:

$$G = \frac{G_{max}}{T} \quad \text{with} \quad G_{max} = \frac{G_0}{0.3 + 0.7e^2} \sqrt{\frac{p}{p_{at}}} \tag{2.35}$$

The parameter T scales the elastic shear modulus, attaining 1 at the onset of shearing and continuously increasing in order to degrade the elastic stiffness, and is defined as

$$T = 1 + \kappa \left(\frac{1}{a_1} - 1 \right) \left(\frac{\chi_r}{\eta_{eq}} \right)^{\kappa-1} \leq 1 + \kappa \left(\frac{1}{a_1} - 1 \right) \tag{2.36}$$

κ and a_1 are positive parameters: κ being larger than 1 (e. g. $\kappa = 2$) and controlling the non-linearity of the degradation, and a_1, a value less than 1, increasing the intensity of the defined degradation the closer a_1 comes to 0. In addition, the auxiliary parameter χ_r is used as a scalar quantity to estimate the distance from the actual stress ratio to a reference state:

$$\chi_r = \sqrt{\frac{1}{2} \left(\boldsymbol{r} - \boldsymbol{r^{ref}} \right) \cdot \left(\boldsymbol{r} - \boldsymbol{r^{ref}} \right)} \tag{2.37}$$

This reference state concerns the stress ratio at the last shear reversal ($\boldsymbol{r^{ref}} = \boldsymbol{r^{SR}}$) or, in case of primary loading, the stress ratio at consolidation state ($\boldsymbol{r^{ref}} = \boldsymbol{r^0}$). Setting this stress ratio difference in relation to a defined threshold value η_{eq} in Eq. (2.36) allows interpolating the elastic shear modulus between its maximum value G_{max} and its minimum value $G_{min} = \frac{G_{max}}{1+\kappa\left(\frac{1}{a_1}-1\right)}$. Any further stiffness reduction at larger stresses and strains – once $\frac{\chi_r}{\eta_{eq}} > 1$ and the stress state violates the yield surface – is due to the evolution of plastic strains, which quickly dominate the elastic deformation rate at constant stiffness G_{min}.

The mentioned threshold value corresponds to the threshold strain γ_1 quoted earlier. Since this degradation mechanism is operating in stress space, γ_1 has to be translated into a stress measure according to

$$\eta_{eq} = \begin{cases} \eta_1 & \text{first shearing} \\ 2\eta_1 & \text{after SR} \end{cases} \quad \text{with} \quad \eta_1 = a_1 \left(\frac{G^{SR}_{max}}{p_{SR}} \right) \gamma_1 \tag{2.38}$$

using the maximum elastic shear modulus and the mean stress at the last shear reversal (or at consolidation) as reference state. Compared to primary loading, after a shear reversal the transformed parameter η_1 has to be doubled in accordance with the second Masing rule [Mas26]. This leads to the enlargement of the shape of the un- and reloading curves with respect to the initial loading curves by a factor of two.

One aspect, which requires clarification, is the correct understanding of the reversal in loading direction. In the case of Papadimitriou and Bouckovalas [PB02], it is specified as shear reversal, expressed in terms of deviatoric strains. Similarly as for χ_r, a scalar distance quantity χ_e is defined as a function of deviatoric strain at the actual state with respect to the one at the last shear reversal:

$$\chi_e = \sqrt{\frac{1}{2}\left(\mathbf{e} - \mathbf{e^{ref}}\right) \cdot \left(\mathbf{e} - \mathbf{e^{ref}}\right)} \qquad (2.39)$$

A shear reversal is identified, when $d\chi_e$, the variation of χ_e from one load step to the next, changes sign. Consequently, it is not to be mixed with a load reversal, which is defined as the transition from loading $(\lambda > 0)$ to unloading $(\lambda < 0)$ or neutral loading $(\lambda = 0)$. Shear and load reversal can coincide but do not necessarily do, as for example in case of a shear reversal within the yield surface.

Besides the formation of plastic strains as soon as hardening of the yield surface is initiated, this small strain stiffness degradation mechanism enables the model to diminish the overall stiffness of the soil even at small strains within the elastic domain. It should be noted that the resulting strains are not truly elastic since not fully recoverable. This is due to the non-conservative elastic shear stiffness formulation, which is stress and void ratio dependent, similar to Eq. (2.18) in the Manzari/Dafalias model. That is why Papadimitriou and Bouckovalas [PB02] propose calling it a "paraelastic" region according to Hueckel and Nova [HN79]. The clear advantage of both (stress and strain dependent) stiffness reduction mechanisms working in parallel is, that it is possible to model the typical stress-strain hysteresis of small and large strain cycles with the same set of material parameters. Papadimitriou and Bouckovalas [PB02] claim that the numerical difficulties in boundary value problems resulting from this physical inaccuracy are acceptable.

The second major modification introduced by Papadimitriou and Bouckovalas [PB02] concerns the accumulation of strains in repeated loading and

unloading cycles with respect to the fabric evolution during shearing, which mainly comprises reorientation of the contact normals of the grains. In their approach, these fabric effects are captured by a factor that scales the plastic modulus K_p, or more precisely, the hardening modulus H_α controlling the kinematic hardening process. This is realised by extending the hardening parameter h by the factor h_f:

$$h = h_0 h_b h_f \qquad (2.40)$$

Two observations noted by Ladd et al. [LFI$^+$77] led to the definition of this factor: repeated drained shearing cycles of small amplitude result in a progressively stiffening unloading-reloading response. On the other hand, if the strain cycles' amplitude increases, the unloading becomes significantly more compliant. More specifically, Ishihara et al. [ITY75] stated that the latter case occurs only if dilation has been initiated before shear reversal. Consequently, they identified the phase transformation line (or the dilatancy surface) as the limit in stress space between gradually stiffening and more compliant unloading.

Since fabric evolution is basically a directional property, Papadimitriou and Bouckovalas [PB02] established a fabric tensor $\boldsymbol{F}$ [referring to DM99], tracing the restructuration process of the soil during shearing, although it does not directly represent the particle contact orientation. $\boldsymbol{F}$ decomposes into a deviatoric part $\boldsymbol{f}$ and a volumetric part $1/3 \operatorname{tr}(\boldsymbol{F}) \boldsymbol{I} = 1/3 f_p \boldsymbol{I}$. The evolution rules for the two contributions are given with

$$\dot{f}_p = -N \cdot \dot{\varepsilon}_p^{pl} \quad \text{and} \quad \dot{\boldsymbol{f}} = -N \cdot \left\langle \dot{\varepsilon}_p^{pl} \right\rangle \cdot (C\boldsymbol{n} + \boldsymbol{f}) \qquad (2.41)$$

N and C being positive model constants. These definitions underline that f_p traces the complete history of plastic volumetric strain evolution and, due to the Macauley brackets, $\boldsymbol{f}$ changes only if dilation occurs ($\dot{\varepsilon}_p^{pl} > 0$), being a tensor with the same (or opposed) orientation as the deviatoric loading direction $\boldsymbol{n}$ and reaching a maximum length of C. Finally, the two contributions are set in proportion to each other in order to obtain a representative scalar for fabric evolution:

$$h_f = \frac{1 + \langle f_p \rangle^2}{1 + \langle \boldsymbol{f} \cdot \boldsymbol{n} \rangle} \qquad (2.42)$$

In this configuration both numerator and denominator take values larger than 1 only. In the beginning of a shearing path only the numerator increases due to positive volumetric deformations (contraction), leading to a rise

of h_f and hence a gradually stiffening response. The denominator, however, evolves only if $\boldsymbol{f}$ and $\boldsymbol{n}$ point in the same direction ($\boldsymbol{f} \cdot \boldsymbol{n} > 0$). That is why the denominator does not change yet at the initiation of dilation, since $\boldsymbol{f}$ starts growing in the opposite direction of $\boldsymbol{n}$, at most until $\boldsymbol{f} = -C\boldsymbol{n}$, so that $\dot{\boldsymbol{f}} = \boldsymbol{0}$. Once a shear reversal occurs, accompanied by a reversal of $\dot{\boldsymbol{n}}$, the two vectors are equally oriented and hence the denominator becomes active, resulting in a sudden reduction of the parameter h_f and consequently a more compliant unloading.

As an additional remark, Dafalias and Manzari [DM04] developed a similar mechanism for taking account of fabric effects during cyclic shearing. They established the same fabric tensor, but in contrast to Papadimitriou and Bouckovalas [PB02] they used only the deviatoric part and applied it to the dilatancy factor D instead of the plastic modulus K_p by making A_d in Eq. (2.34) a function of $\dot{\boldsymbol{f}}$:

$$A_d = A_0 \left(1 + \langle \boldsymbol{f} \cdot \boldsymbol{n} \rangle \right) \qquad (2.43)$$

Thus, at shear reversal after a dilative phase, A_d increases instantaneously in analogy to the denominator in Eq. (2.42). Consequently, D jumps to a higher value and enhances the contractancy of a drained unloading path or the pore pressure development in an undrained unloading case, respectively. This analytical modification affecting the plastic volumetric behaviour instead of the plastic stiffness is justified by the experimental observation [e.g. Kon78, NT82] that the distribution of the contact-normal orientation of the particles severely changes during dilation. Upon reversal of the shearing direction, the previously preferred orientation of the contact planes remains, the bias towards dilation turns into a bias towards contraction and consequently enhances the contractive effect [Kon78]. Since Dafalias' and Manzari's focus was mainly laid on the assessment of liquefaction phenomena, the stiffening (or stabilising) tendency at stress ratios within the dilatancy surface plays a minor role and is hence not considered in this approach.

2.2.2   Taiebat and Dafalias (2008)

In the present subchapter the model by Taiebat and Dafalias [TD08] is described, which partly integrated the modifications of previous research groups but also added a new feature with the introduction of a closed yield surface. The original bounding surface model by Manzari and Dafalias [MD97] is based on the presumption that merely changes in stress ratio

cause the shearing and rolling of sand grains, which induce plastic shear
and volumetric strains. In contrast, an increase in stress at a constant stress
ratio is assumed to cause elastic strain only (as long as crushing of grains
does not take place, soil density is rather high and stresses do not exceed
the medium range). The constitutive element responsible for reproducing
this behaviour is the shape of the yield surface: an open cone with its apex
at the origin. In constant stress ratio loading the stress path remains on
the central axis of the cone without violating the limits of the yield surface,
so that no plastic strains occur – the soil's response is purely elastic. But
once the stress ratio changes and the loading path deviates from the cone's
axis, the edges of the yield surface are reached quickly and plastic straining
commences.

This underlying concept limits the application of the model to sands of cer-
tain states and stress levels. Otherwise it causes too stiff responses, when
loose sands are loaded at constant stress ratio or when very high pressures
are applied in, e. g., isotropic or one-dimensional compression. In order to
eliminate this limitation, Taiebat and Dafalias [TD08] introduced a new
yield surface type: a modified eight-curve equation creating a closed cone
(Fig. 2.8) that rotates around the origin when hardening, addressing rever-
sed loading and evolving anisotropy. In the following the most important
modifications in comparison to the Manzari/Dafalias model are given: the
new yield surface and consequential alterations in the model formulation are
presented. For the sake of brevity, smaller changes in the constitutive fra-
mework are omitted here. All constitutive equations referring to multiaxial
stress space are provided in generalised form directly.

The mentioned yield surface modification is given in the following equation:

$$f = \frac{3}{2}\left(\boldsymbol{s} - p\boldsymbol{\alpha}\right) \cdot \left(\boldsymbol{s} - p\boldsymbol{\alpha}\right) - m_{cone}^2\, p^2 \left[1 - \left(\frac{p}{p_0}\right)^n\right] = 0 \qquad (2.44)$$

For mean stress levels distinctly lower than the pre-consolidation pressure
p_0, the yield surface resembles the open cone of the original model, since
the appended multiplier in brackets in Eq. (2.44) is close to 1 for $p \ll p_0$,
provided that $\boldsymbol{n}$ is sufficiently large. This case concerns loading accompa-
nied by stress ratio changes. If $p = p_0$, which corresponds to constant stress
ratio loading, the stress state marks the tip of the closed cone, where the
deviatoric stress ratio tensor $\boldsymbol{r}$ equals the back stress $\boldsymbol{\alpha}$.

In contrast to the closed yield surface expression in stress space, the for-
mulation of the flow rule is decomposed into two separate contributions:
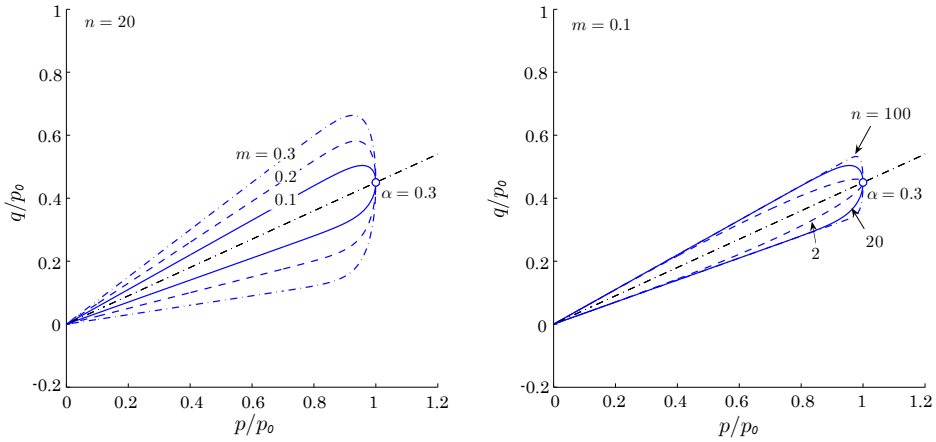
Figure 2.8: Closed conical yield surface according to Taiebat [after Tai09]

plastic strain rates caused by stress ratio changes (1) on one side and those induced by constant stress ratio loading (2) on the other. With the help of an auxiliary function r_{ef}, the transition from one contribution to the other is made mathematically, depending on the loading direction.

Flow rule:

$$\dot{\varepsilon}_p^{pl} = \left[\dot{\varepsilon}_p^{pl}\right]_1 + \left[\dot{\varepsilon}_p^{pl}\right]_2 = \lambda\left(\left[\frac{\partial g}{\partial p}\right]_1 + \left[\frac{\partial g}{\partial p}\right]_2\right) \quad \text{and analogously for } \dot{\mathbf{e}}^{\mathbf{pl}}$$

(2.45)

First contribution:

$$\left[\frac{\partial g}{\partial \boldsymbol{s}}\right]_1 = \sqrt{\frac{2}{3}}r_{ef}\cdot\boldsymbol{n} \qquad \left[\frac{\partial g}{\partial p}\right]_1 = r_{ef}\cdot D \qquad (2.46)$$

Second contribution:

$$\left[\frac{\partial g}{\partial \boldsymbol{s}}\right]_2 = \frac{3}{2}X\exp(-V\cdot r_{ef})\cdot\boldsymbol{r} \qquad \left[\frac{\partial g}{\partial p}\right]_2 = \exp(-V\cdot r_{ef}) \qquad (2.47)$$

$$\text{with} \quad r_{ef} = \sqrt{\frac{2}{3}(\boldsymbol{r}-\boldsymbol{\alpha})\cdot(\boldsymbol{r}-\boldsymbol{\alpha})} \quad \text{and} \quad V \approx 1000 \qquad (2.48)$$

The effect of the transition functions r_{ef} and $\exp(-V\cdot r_{ef})$ in the two plastic strain contributions is described in short with the help of the following conditions:

- constant stress ratio ($\dot{\eta} = 0$):

$$p = p_0, \quad \boldsymbol{r} - \boldsymbol{\alpha} = \boldsymbol{0} \quad \rightarrow \quad r_{ef} = 0, \quad \exp(-V \cdot r_{ef}) = 1 \tag{2.49}$$

- variable stress ratio ($\dot{\eta} \neq 0$):

$$p \ll p_0, \quad \boldsymbol{r} - \boldsymbol{\alpha} \neq \boldsymbol{0} \quad \rightarrow \quad r_{ef} \neq 0, \quad \exp(-V \cdot r_{ef}) \approx 0 \tag{2.50}$$

On the one hand this allows "switching off" the first contribution in constant stress ratio loading and on the other hand almost eliminating the second contribution in case the stress ratio changes under loading. The transition velocity between the two contributions according to the size of stress ratio change depends on the choice of the parameter V.

By means of the plastic potential, the two hardening mechanisms of the cone – rotation and expansion – are also functions of the transition mechanism. Due to the nature of the transition functions, the contributions to the plastic potentials for the respective hardening variable have been simplified in the following way:

$$\dot{\boldsymbol{\alpha}} = H_\alpha \dot{\mathbf{e}}^{\mathbf{pl}} = \lambda H_\alpha \frac{\partial g}{\partial \boldsymbol{s}} = \lambda H_\alpha \left[\frac{\partial g}{\partial \boldsymbol{s}} \right]_1 \tag{2.51}$$

$$\text{with} \quad H_\alpha = \sqrt{\frac{3}{2}} h \left(\boldsymbol{\alpha^b} - \boldsymbol{\alpha} \right) \cdot \boldsymbol{n} \tag{2.52}$$

$$\dot{p}_0 = H_{p0} \dot{\varepsilon}_p^{pl} = \lambda H_{p0} \frac{\partial \boldsymbol{g}}{\partial p} = \lambda H_{p0} \left[\frac{\partial \boldsymbol{g}}{\partial p} \right]_2 \tag{2.53}$$

$$\text{with} \quad H_{p0} = \frac{1+e}{e} \frac{p_0 \cdot K_0}{\left(K_0 \rho_c - \left(\frac{p_0}{p_{at}} \right)^{\frac{1}{3}} \right) (1 - \text{sgn}\,(\delta)\,|\delta|^\omega)} \tag{2.54}$$

Consequently, in case of constant stress ratio loading, $\dot{\boldsymbol{\alpha}} = \boldsymbol{0}$ and the cone hardening does not exhibit any rotation. In analogy to the rotational hardening, the cone does not expand along its centre axis, if the stress ratio rate is sufficiently larger than zero, since $\dot{p}_0 \approx 0$. Only in the very slim transition zone both hardening mechanisms are active.

The corresponding hardening moduli have been modified with reference to the basic model. In case of H_α by adding the factor $\sqrt{3/2}$ for convenience and by extending the factor h. Compared to the original formula for h by Manzari and Dafalias [MD97], which takes only the distance to the bounding surface into account (cited as Eq. (2.32) in Sect. 2.1.1), Taiebat
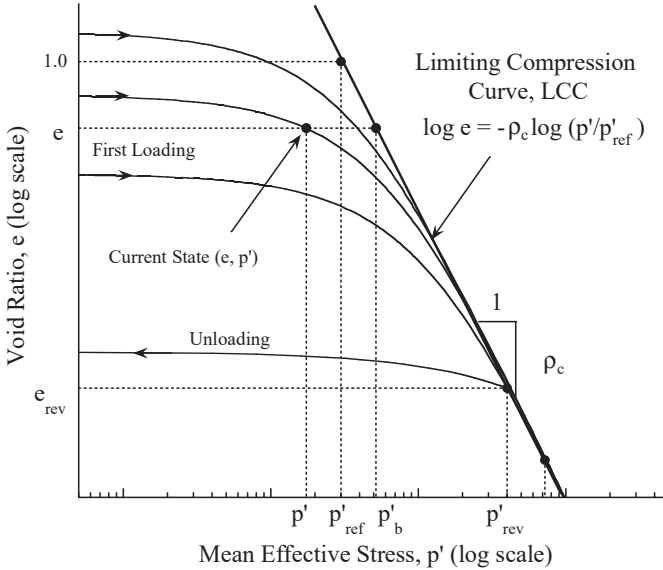
Figure 2.9: Limiting compression curve (LCC) as defined by Pestana and Whittle [PW95]

and Dafalias [TD08] added a void ratio and a mean stress dependence[6] as follows:

$$h = h_0 h_b = h_0 \frac{1}{d_{ref}^b - |d^b|} \left(1 - c_h e\right) \frac{G_0^{ref}}{p_{at}} \left(\frac{p_{at}}{p}\right)^{\frac{1}{2}} \qquad (2.55)$$

The evolution of the hardening variable p_0 via the hardening modulus H_{p_0} is oriented towards a mechanism proposed by Pestana and Whittle [PW95], initially for application in isotropic consolidation and later extended for general constant stress ratio loading cases [PW99]. Their idea was based on the concept of a so called limiting compression curve (LCC), which represents a straight line in $\log p$ - $\log e$ space (Fig. 2.9). While at lower stresses changes in volume are due to elastic compression of the soil fabric and rearrangement of the grains, the principal deformational mechanism at high stress levels is particle crushing [e. g. RdS58, PW95]. In the latter regime, the compression behaviour is independent of the soil's initial density and

---

[6]The mean stress dependence of the factor h_b had already been introduced by Papadimitriou and Bouckovalas [PB02] in a similar form, but was not explicitly quoted in the previous section.

can hence be characterised by the LCC: a locus that is approached asymptotically by all pressure - void ratio curves of soil samples with different initial densities.

The LCC is defined as follows:

$$\log e = -\rho_c \log \frac{p_b}{p_r} \quad \rightarrow \quad -\frac{1}{\rho_c} = \log_e \frac{p_b}{p_r} \quad \rightarrow \quad p_b = p_r \cdot e^{-\frac{1}{\rho_c}} \qquad (2.56)$$

ρ_c and p_r are two reference parameters locating the LCC in $\log p$ - $\log e$ space. The double-logarithmic approach ensures that even at very high stresses the void ratio does not become negative. In order to estimate the plastic volumetric deformation originating from compression up to high pressure levels, Pestana and Whittle [PW95] applied the bounding surface principle of distances to a limit state: the measure δ quantifies the distance between the actual mean pressure p and its image p_b on the LCC, which controls the soil's compressive stiffness (acc. to Eq. (2.54)). Experimental evidence had been given by McDowell et al. [MNH02] for the existence of different LCC if the (constant) stress ratio is different from zero (opposed to isotropic loading): the limiting compression curve moves closer to the origin with an increasing stress ratio and hence the soil response becomes softer. As a result, a modification was incorporated in the original proposition of the distance measure δ, making the image stress p_b a decreasing function of the stress ratio:

$$\delta = 1 - \frac{p}{p_b^*} \quad \text{with} \quad p_b^* = p_b \frac{\boldsymbol{\alpha}^c \cdot \boldsymbol{\alpha}^c}{\boldsymbol{\alpha}^c \cdot \boldsymbol{\alpha}^c + 2\boldsymbol{r} \cdot \boldsymbol{r}} \qquad (2.57)$$

Summing up the effects of the contributing variables in the hardening modulus controlling the evolution of p_0, it can be stated that H_{p_0} rises with increasing density (as a function of the void ratio e), reference bulk modulus K_0 (divided by p_{at}) and pre-consolidation pressure p_0. Furthermore, the quantity δ governs the convergence of the actual state and the LCC: It amplifies H_{p_0} at large distances from the LCC and decreases to 0 (so that it loses its impact on H_{p_0}) when the state approaches the LCC range, with the exponent ω controlling the speed of evolution.

2.3 Small strain stiffness

2.3.1 Observations

In geotechnical engineering, it is commonly accepted that the stress-strain characteristics of soils are highly non-linear. This observation concerns the
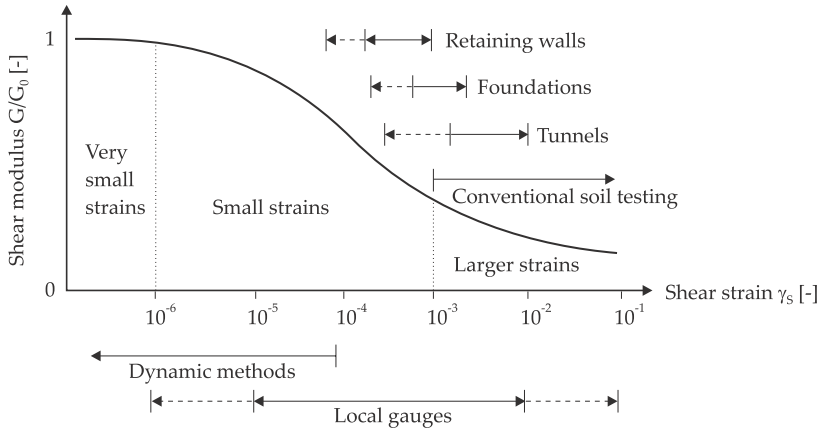
Figure 2.10: Shear stiffness degradation curve with strain ranges for geotechnical applications and laboratory testing [Ben07], based on [AS91, Mai93]

deformational behaviour at large as well as relatively small strains, made for example in the late 1980s by Burland [Bur89], having conducted laboratory tests with local strain measurements on soil samples. Looking at the very small strain range, his experiments revealed a strong decline of shear stiffness in case of the locally measured stress-strain curves, dropping from an initially high tangent shear modulus G_0 to a considerably lower pre-yielding value G. Atkinson and Sällfors [AS91] defined the shear strain limits, in between which this non-linear transition from G_0 to G takes place, with 10^{-6} and 10^{-3}. As can be seen in Fig. 2.10 the stiffness reduction with increasing shear strain is assumed to describe an S-shaped curve on a logarithmic scale.

The impact of the increased stiffness after a stress or strain reversal on the overall stress-strain evolution is rather minor, if loading up to larger strains or close to yielding. In geotechnical applications however, the typical strain levels in the near field of structures like tunnels, foundations and retaining walls lie in the small strain range of 10^{-4} to 10^{-3} [Mai93]. Additionally, in geotechnical problems only selected parts of the soil body experience larger deformations; in most other sections they are rather small. Thus, if the strain path in question is located in the small strain environment, where the change of stiffness with strain is notable, the influence on the permanent deformation can be significant. Consequently, underestimating
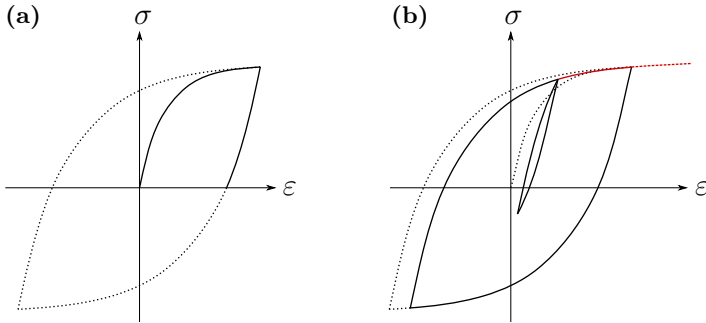
Figure 2.11: (a) Full loading cycle and (b) incomplete loa-
ding/unloading/reloading cycles according to the Masing rules

the stiffness at low strain levels in boundary value problems will lead to an
overprediction of the displacements to be expected.

If the soil is loaded repeatedly at sufficiently large strain amplitudes the
stiffness decay manifests itself in stress-strain loops showing hysteresis (Fig.
2.11 a). The initial loading branch is termed backbone curve, followed by
un- and reloading branches. By connecting the two extreme points of a
hysteresis loop one can determine the secant shear modulus. The area
circumscribed by the hysteresis loop of a full stress-strain loading cycle
(broken line) is the energy dissipated due to internal friction and can be
translated into a damping ratio. Knowing this, it is obvious that secant
shear modulus and damping ratio are strongly dependent on the applied
strain, especially in the small strain range.

Masing [Mas26] has established two rules characterising the non-linear be-
haviour of regular cyclic loadings (constant amplitude) by describing the
geometry of the corresponding stress-strain curves depending on the loa-
ding path. These rules can be summarised as follows:

1. The unloading and reloading curves are shaped equally and are obtai-
   ned by scaling the backbone curve by a factor of 2.

2. After each load reversal the tangent shear moduli are of the same size
   and also correspond to the initial modulus G_0.

If only a stress reversal is considered (continuous line in Fig. 2.11 a), con-
sisting of loading and unloading to the initial stress, the irreversibility of
the deformation due to the non-linear character of the stress-strain beha-
viour becomes apparent by the portion of strain that is not recovered in

unloading. A full loading cycle, however, shows the typical (approximately) closed hysteresis loop (broken line).

The Masing rules, although originally established for brass, have been widely accepted as a basis for modelling the non-linear stress-strain behaviour of cyclically loaded soils. However, linked to the formation of hysteresis loops in cyclic loading is a certain memory for the loading history. It can be observed (Fig. 2.11 b) that depending on the previously experienced stresses, after unloading the stress-strain curve will follow the initial loading curve (backbone curve), when having reached it in reloading. Generally speaking, whenever a stress-strain path intersects a curve from a previous cycle, it will follow this one. These two statements have been formulated, for example, by Pyke [Pyk79] and together with the previously cited two Masing rules, the four rules are also named extended Masing rules. Vucetic [Vuc90] complemented these four rules by a fifth one, accounting for the behaviour of degrading materials such as clay under cyclic loading.

Another aspect of small strain stiffness is that the truly elastic range, where the stress-strain behaviour is (almost) fully recoverable, is actually very small, limited to shear strains of less than 10^{-6} to 10^{-5} for most geotechnical materials [e. g. Har78, HEH87, Vuc94, JSB84]. Thus, in case of consecutive closed stress cycles, even at rather small strains hysteresis can be observed and the stress-strain behaviour is not entirely reversible, so that permanent deformation (or pore pressure, respectively) is accumulated.

2.3.2   Micromechanical considerations

In order to understand the phenomenon of small strain stiffness, the observations described above and the influencing factors, considerations at soil particle level are of avail. A closer look at the soil structure reveals the micromechanical background of soil stiffness: it is the geometrical arrangement of particle contacts and pores (termed fabric) as well as the intergranular forces acting within the soil skeleton and causing inner stability, which represent the soil structure and essentially affect soil behaviour and engineering properties of soil [BS60, HK81]. Within the scope of this section, the application of this approach will not suffice to deduce soil parameters, but it serves to explain experimentally observed soil behaviour.

The global stiffness of a granular material is ascribed to the local interparticle contact properties, in particular the forces acting in between the soil grains, so called contact forces (Fig. 2.12). It is assumed [e. g. Isr11, KJ02]
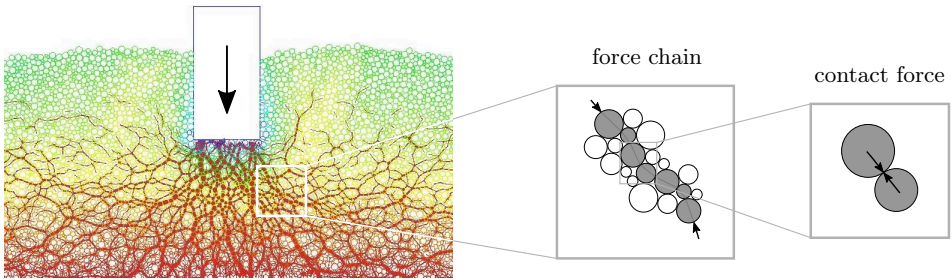
Figure 2.12: From macroscale to microscale: load impact – transfer of force via force chains – contact forces at interparticle contacts (image of DEM simulation by Rafiee [Raf12])

that only the rearrangement of these forces can cause a change in stiffness on a local scale, which affects the global stiffness, as the sum of all local contact stiffnesses, in return. It is the concentrated formation of directional contact chains due to the perturbation of the intergranular forces that is considered to be responsible for a decrease in stiffness. In other words, the interparticle contacts are said to be in a "sticking mode" at the very beginning of loading (see Fig. 2.13). As long as the strain amplitude does not exceed a certain limit, which can be considered as a quasi-elastic very small strain range, this mode is preserved. When the shear strain amplitude increases, more and more particles will start rearranging ("slip"), which causes the local contact stiffnesses to reduce and consequently the global stiffness drops. At strain reversal, the interparticle contacts that were disturbed are set back into "sticking mode" and consequently the maximum stiffness is restored.

Another model concept building upon strain dependent stiffness was proposed by Niemunis and Herle [NH97]. They split the total strain into two components: an intergranular strain, which quantifies the small deformational contribution of the intergranular interface, and the strain originating from the rearrangement of the grains. The concept assumes a quasi-elastic range in strain space with maximum stiffness. Once this domain is exceeded, the intergranular interface starts deforming ("intergranular strain"), which makes the stiffness reduce. Since a certain maximum interface deformation cannot be surpassed, at some stage the rearrangement of the grains dominates the overall strain and controls the stiffness.

In general, the effect of deviatoric loading on the interparticle contacts is
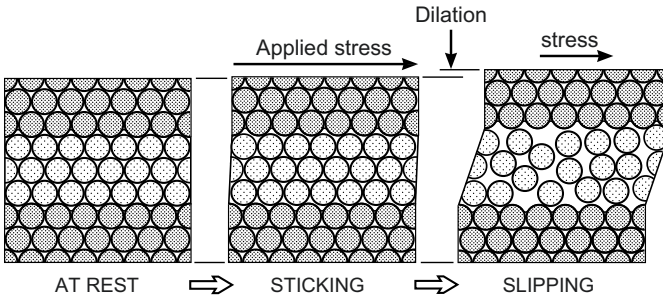
Figure 2.13: Initial configuration of particles – sticking mode at the onset of loading – slipping mode with increasing shear strain, accompanied by dilation (volume expansion), after [Isr11]

significantly stronger than the one of isotropic loading, since the former causes a directional rearrangement of the contact forces whereas the latter only increases their magnitude. This conception has been confirmed by experimental observations [e. g. Jov97, ZJ97, LA05], revealing that, in isotropic compression, un-/reloading stiffnesses are generally considerably higher than those in loading and drop rather slowly with increasing strain. Furthermore, stiffnesses in reloading can hardly be distinguished from those in unloading and there is very little hysteresis. Consequently, it is deviatoric loading that primarily exhibits the characteristics of stiffness evolution at small strains. This partly explains, why in literature, when it comes to small strain stiffness, mostly the deviatoric strain history is considered and isotropic strain is neglected.

Besides the dependence on the strain level, there are more factors influencing the stiffness at small strains, for which it is worth looking closer at the contact points between the grains. Applying the Hertz-Mindlin contact theory [MD53], summarised in Fig. 2.14, to the simplified case of two idealised smooth equal-sized spheres of the same material, the normal contact stiffness K_N at interparticle level can be derived as a function of the elastic material constants (G, ν) and the contact radius a:

$$K_N = \frac{2G}{1-\nu}a \quad \text{with} \quad a = \left(\frac{3F_N R\,(1-\nu)}{8G}\right)^{\frac{1}{3}} \tag{2.58}$$

From Eq. (2.58) can be deduced that the contact surface increases non-linearly with the normal contact force F_N and the sphere radius R. Consequently, with an increase in confining stress the normal contact force grows
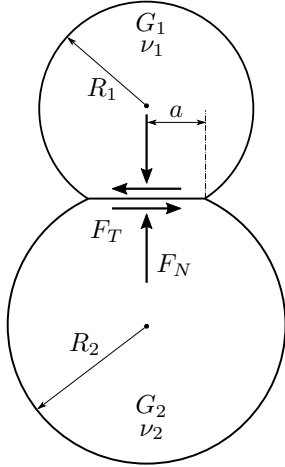
Substitutional radius

$$\frac{1}{R} = \frac{1}{R_1} + \frac{1}{R_2}$$

Substitutional elastic stiffnesses

$$\frac{1}{E^*} = \frac{1}{2}\left(\frac{1-\nu_1^2}{E_1} + \frac{1-\nu_2^2}{E_2}\right)$$

$$\frac{1}{G^*} = \frac{1}{2}\left(\frac{2-\nu_1}{4G_1} + \frac{2-\nu_2}{4G_2}\right)$$

Normal contact stiffness

$$K_N = E^* \cdot a \quad \text{with} \quad a = \left(\frac{3F_N R}{4E^*}\right)^{\frac{1}{3}}$$

Tangential contact stiffness

$$K_T = K_N \frac{G^*}{E^*}\left(1 - \frac{F_T}{\mu \cdot F_N}\right)^{\frac{1}{3}}$$

$$= K_N \frac{2\,(1-\nu)}{2-\nu}\left(1 - \frac{F_T}{\tan\varphi \cdot F_N}\right)^{\frac{1}{3}}$$

Figure 2.14: Hertz-Mindlin contact theory for two spheres [according to MD53]

and therefore the local contact stiffness does accordingly. This observation is reflected in the power laws by Hardin and Richart [HR63] or Janbu [Jan63] (see also Eq. 2.18), defining the initial shear stiffness as a function of the mean stress level.

Parallelly, the impact of void ratio on the soil stiffness can be considered. Depending on the assembly of the grains (which is directly related to the void ratio), packings of different densities result in different contact distributions. The denser the packing, the higher the number of contacts between the particles with reference to a representative unit volume. Although the local contact stiffness drops since the force per contact decreases with augmentation of interparticle contacts, the global stiffness increases due to the elevated number of interparticle contacts.

Referring to the Hertz-Mindlin contact theory once more, it can be stated that the interparticle stiffness might also be increased by enlarging the area at the contact points of the grains. Through an additional cement coating

at the contact point, the contact area is geometrically extended, which represents a bonding effect. The stiffening of the intergranular contacts finally leads to an overall increase in soil stiffness.

Summing up the previous findings derived from micromechanical considerations, the most important factors affecting stiffness, in particular at small strains, are the strain level, the confining stress, the void ratio and interparticle bonding. When it comes to cohesive soils or sands with a significant fines content, there are a few more parameters, which can have a more or less important impact on the small strain stiffness or the reduction curve characteristics (resulting in the damping ratio). Without going further into detail, according to Hardin and Drnevich [HD72b] the degree of saturation, the overconsolidation ratio, grain characteristics and the grain size distribution can be of importance. Vucetic and Dobry [VD91] complemented this list by the plasticity index, concerning cohesive soils only, of course. Due to viscosity, the small strain stiffness of these soils also exhibits a dependence of strain rate as well as inertia effects in dynamic loading. Other time-dependent impacts, which are closely linked to the previously discussed bonding effects, are diagenetic influences that change the soil stiffness by altering the original interparticle structure with time. They are mostly, but not exclusively caused by secondary compression under a constant load (e. g. creep). Besides the already named cementation, ageing as another diagenetic process can play a role in sandy soils.

2.3.3   Very small strain shear modulus G_0

The determination of the shear modulus at very small strains can be carried out by laboratory tests or in-situ testing methods. Since conventional soil testing is technically restricted to strains of more than 0.1% (Fig. 2.10), the measurement of small to very small strains demands special equipment such as local strain transducers or bender elements. The advantage of the former is that it measures locally on the sample, independently from the imperfections of the testing equipment and the sample bedding, which usually impede accurate measurements in the very beginning of a triaxial test. The resolution of the transducer has to be chosen according to the small strain range, of course ($\varepsilon \leq 0.5 \cdot 10^{-5}$, [CDH$^+$97]). Bender elements on the other hand are low voltage piezo-ceramic transducers for measuring wave velocities in triaxial specimens. Due to the high effort for installation and the difficulties in the interpretation of the resulting data, respectively, local strain transducers and bender elements are mainly reserved for research. Al-

ternative lab testing methods are resonant column test, torsional shear test and hollow cylinder apparatus, which allow applying shear stresses through different modes of loading such as rotation or torsional vibration. However, without going further into detail, the laboratory test devices are expensive and hence these methods are much less common in engineering practice.

Field tests on the other hand are solely indirect methods based on geophysical measurements and therefore the geotechnical community has not been familiar with these investigation methods for long. Many of these in-situ tests employ seismic techniques like for example cross and down hole seismic as well as seismic cone and flat dilatometer. In order to conclude on the elastic (or very small strain) stiffness, the propagation velocity of secondary waves needs to be interpreted, assuming a certain density (or deducing it from Poisson's ratio and primary wave velocity).

2.3.4   Constitutive modelling approaches

Having described the soil mechanical background of stiffness in the small strain range and its consequences with respect to the soil response (deformation, strength), it becomes clear that the consideration of small strain stiffness in constitutive modelling is a feature worth taking into account. In soil dynamics, small strain stiffness has already been a well-known phenomenon for decades when the application to static geotechnical problems arose interest. Erroneously, it has long been assumed that loading characteristics such as strain rate and inertia effects are responsible for the different soil responses in static and dynamic problems. It was only in the late 1970s when the awareness was created that it is the strain range that has a decisive impact on the stiffness: the typical strains in soil dynamical applications lie in the small to very small strain range. Hence, measured stiffnesses are distinctly higher than at larger strains and show the discussed S-shaped decay with increasing strain. It was at that time when the first constitutive modelling approaches appeared to capture this behavioural pattern. Benz [Ben07] gives a good overview of the concepts behind the pioneering models, being concerned with the brick model, direct strain-stiffness relations, the multi surface approach and the already mentioned intergranular strain concept, amongst others. In the following, only a very brief summary is presented in order to have a basis to build an understanding for the advancements of the bounding surface model on.

The first models appearing in the end of the 1970s were set up in an elastoplastic modelling framework, consisting of one or more kinematically har-
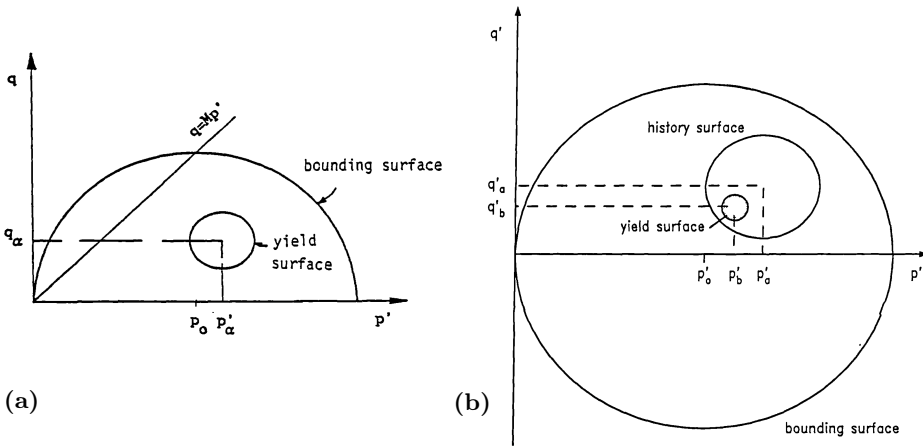
Figure 2.15: Bubble models by (a) Al-Tabbaa [AlT87, AM89] and (b) Stalle-brass [Sta90] for the enhanced modelling of reversed loadings in clays (both graphs taken from [Sta90])

dening yield surfaces, in either stress or strain space [MNZ78, SOC79]. The multi surface aspect allows these models to trace the stress history (mostly via back stress) and the small strain stiffness mechanism is related to the innermost yield surface. About ten years later the bubble models by Al-Tabbaa and Muir Wood [AM89] and Stallebrass [Sta90] were introduced (Fig. 2.15), restricting the multi surface concept to one small bubble shaped kinematic yield surface, responsible for modelling small strain stiffness.

At the same time, a completely different path was taken by a second group of models, making the soil stiffness a direct (non-linear) function of the applied strain. Jardine et al. [JPF$^+$86] established a trigonometric function relating the undrained secant Young's modulus (normalised by the undrained shear strength) to the axial strain. Basically the same principle is pursued by models typically known from soil dynamics, introduced by Ramberg and Osgood [RO43] and Hardin and Drnevich [HD72a]. In their case, the stiffness decay as the ratio of actual shear stiffness G to initial shear modulus G_0 is described by a rational function of shear stress (Ramberg-Osgood) or shear strain (Hardin-Drnevich) as follows:

Ramberg-Osgood:

$$\frac{G}{G_0} = \frac{1}{1 + \alpha \left| \frac{\tau}{\tau_y} \right|^\kappa} \tag{2.59}$$

Hardin-Drnevich:

$$\frac{G}{G_0} = \frac{1}{1 + \left|\frac{\gamma}{\gamma_r}\right|} \tag{2.60}$$

τ_y and γ_r denote some sort of threshold stress and strain, respectively, and α and κ are material constants.

If modelling more complex stress paths including stress reversals, the stress-strain history needs to be tracked in order to attribute the appropriate stiffness, calculated for example by one of the previously named strain dependent models. In this context, it is essential to determine and memorise points of stress reversal in stress or strain space, respectively. One approach has been proposed by Simpson [Sim92] in his brick model. It is based on the image of a man dragging bricks on strings of different lengths behind himself. Depending on the direction of motion, the strings are tensioned or slackened, which symbolises plastic or elastic strains, respectively. Strain history is traced by memorising the bricks' positions and by correlating brick size and string lengths to strain and stiffness the typical stiffness reduction curve can be deduced. Simpson's idea is often reduced to a one-brick model in order to locate and remember load reversal points. Based on the distance from the actual point to the last load reversal (in stress or strain space), the corresponding stiffness can be calculated by applying an adequate stiffness decay relationship. In particular elastoplastic models set up in stress space are well suited to be combined with a stress based stiffness reduction curve. Papadimitriou and Bouckovalas [PB02] followed this strategy and coupled their version of bounding surface plasticity with the Ramberg-Osgood formulation of (elastic) stiffness decay. Further details can be found in Sect. 2.2.1. Alternatively, the combination with a strain based stiffness decay formula, as offered by the Hardin-Drnevich model, was applied by Benz [Ben07] in his small strain adaptation for the Hardening Soil model [SVB99]. It requires tracking the loading history in terms of strain, but the threshold measure can be put in directly as strain and does not necessitate the transfer from strain to stress space as the model by Papadimitriou and Bouckovalas [PB02] does.

2.4   Dilatancy

Compared to other engineering materials, soil exhibits a relatively high porosity, which is characterised by the ratio of the volume of the voids over the total volume. Thus, a disturbing impact on a soil sample, deforming

the outer boundaries of the soil body, will result in a rearrangement of the particles within the structure, which necessarily comes along with a change in the volumetric packing. Imagining the soil in the simplified form of a two-dimensional arrangement of circular particles (as in Fig. 2.16), in a loose configuration, by shearing, the particles of the upper row are pushed horizontally into the gaps below – the overall volume reduces. If, on the contrary, the initial packing is dense, the sideways movement causes the upper particles to ride up over the row below, so that the final volume taken by the structure is larger. This phenomenon of shear induced volume change, which is strongly related to the soil's density, is called dilatancy.
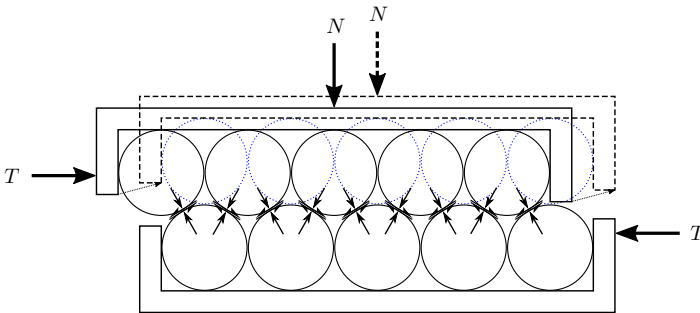
Figure 2.16: Dilation in direct shear of an ideal sphere packing [after BJ04]

As already stated in the previous section, the geometrical arrangement of particle contacts and voids (called fabric) as well as the distribution and size of contact forces between the particles mainly govern the mechanical behaviour of granular material. Consequently, besides density it is also the stress level, the stress history (traced by a particular stress path) as well as the soil's microstructure and its rearrangement through rotation and translation of grains that primarily influence the volumetric strain response of a frictional soil due to shearing.

The development of stress-dilatancy theories relating stress ratio to dilatancy has been largely based on energy considerations (e. g. Rowe [Row62], Roscoe et al. [RST63], and Schofield and Wroth [SW68]). Although it seems self-evident, only few have pursued a micromechanical approach, regarding the internal geometry of fabric. The resulting stress-dilatancy formulation is then mostly transferred into a flow rule in order to be incorporated into an elastoplastic constitutive framework for application in continuum models.

In the following, light is cast on the physical foundations of the ground-

breaking stress-dilatancy relations by Roscoe and Schofield [RS63] as well
as Rowe [Row62], respectively, which are both starting from energy prin-
ciples. Subsequently, deficiencies are identified and potential remedies are
introduced.

Energy considerations reveal that the work input to a soil sample subjected
to certain stresses when undergoing deformation can be expressed as δW,
summing up the products of all contributing stress quantities and corre-
sponding strain increments. Considering the general case of a soil element
being loaded with effective normal stresses $\sigma'_{xx},\sigma'_{yy},\sigma'_{zz}$ and shear stresses
$\tau_{xy},\tau_{yz},\tau_{zx}$, and experiencing normal strain increments $\delta\varepsilon_{xx},\delta\varepsilon_{yy},\delta\varepsilon_{zz}$ and
shear strain increments $\delta\gamma_{xy},\delta\gamma_{yz},\delta\gamma_{zx}$, this work input per unit volume is

$$\delta W = \sigma'_{xx}\delta\varepsilon_{xx} + \sigma'_{yy}\delta\varepsilon_{yy} + \sigma'_{zz}\delta\varepsilon_{zz} + \tau_{xy}\delta\gamma_{xy} + \tau_{yz}\delta\gamma_{yz} + \tau_{zx}\delta\gamma_{zx} \quad (2.61)$$

Projected into principal stress space, the previous equation becomes

$$\delta W = \sigma'_1\delta\varepsilon_1 + \sigma'_2\delta\varepsilon_2 + \sigma'_3\delta\varepsilon_3 \qquad (2.62)$$

Restricting these considerations to triaxial loading cases, the expression for
the work input can be split into an increment of volumetric work δW_v and
an increment of distortional work δW_d, associated to changes in volume and
shape, respectively. This results in a modified version of Eq. (2.62)

$$\delta W = \delta W_v + \delta W_d = p'\delta\varepsilon_p + q\delta\varepsilon_q \qquad (2.63)$$

Part of this work input is stored in elastic deformation of the soil body. But
the major part is dissipated in intergranular friction as the grains roll and
slide on each other. According to Taylor's work hypothesis [Tay48], it can be
assumed that the elastic portion can be neglected and hence the entire work
input is dissipated in frictional resistance. Therefore, the energy available
for dissipation concerns the plastic deformational contributions only:

$$\delta E = p'\delta\varepsilon_p^{pl} + q\delta\varepsilon_q^{pl} \qquad (2.64)$$

In addition, this frictional dissipation can be quantified by

$$\delta E = \mu \cdot p' \cdot \delta\varepsilon_q^{pl} \qquad (2.65)$$

in analogy to a normal load applied to a surface with a particular frictional
coefficient μ, resulting in a tangential frictional force acting in the direction
of the surface. In the original Cam Clay model by Roscoe and Schofield
[RS63], it is assumed that the dissipated energy is constant throughout the

whole deformation process and hence corresponds to the dissipated energy at critical state. Equating Eqs. (2.64) and (2.65) and rearranging them gives

$$p'\delta\varepsilon_p^{pl} + q\delta\varepsilon_q^{pl} = \mu \cdot p' \cdot \delta\varepsilon_q^{pl} \quad \rightarrow \quad \frac{\delta\varepsilon_p^{pl}}{\delta\varepsilon_q^{pl}} + \frac{q}{p'} = \mu \qquad (2.66)$$

Substitution of stress ratio $\eta = \frac{q}{p'}$ and dilatancy ratio $D = \frac{\delta\varepsilon_p^{pl}}{\delta\varepsilon_q^{pl}}$ delivers $D + \eta = \mu$ and finally leads to the simple original Cam Clay stress-dilatancy relationship of the form:

$$D = \mu - \eta \qquad (2.67)$$

The dilatancy ratio D indicates the amount of volumetric deformation with progressive shearing and the stress ratio η is a measure for the currently mobilised shear resistance. The role of μ can be understood when considering the event of constant volume shearing ($D = 0$): the soil distorts without volumetric deformational contribution at critical state and also at phase transition (the moment when volume contraction turns into dilation). In these two cases the stress ratio takes a particular value μ, which is mostly fixed to the critical state stress ratio M^c.

An alternative stress-dilatancy relationship has been proposed by Rowe [Row62]. His approach is based on the hypothesis that the work input by driving stresses related to the work taken out by driven stresses is constant and minimal in any strain increment. In the particular case of triaxial compression, the driving stress corresponds to the axial stress σ_1 and the driven stress to the radial stress σ_3, with the associated strain increments ε_1 and ε_3, respectively, so that the constant energy ratio K can be expressed by

$$K = -\frac{\sigma_1 \delta\varepsilon_1}{2\sigma_3 \delta\varepsilon_3} \qquad (2.68)$$

Through geometrical considerations on particle packings and the application of the principle of least work (concerning the energy dissipated for relocation of the particles until peak), Rowe [Row62] derived another expression for this constant K. It relates K to a friction angle $\overline{\varphi}$ and is independent from the mode of shear. After some reformulation and utilising trigonometric relationships one can write:

$$K = \tan^2\left(\frac{\pi}{4} + \frac{\overline{\varphi}}{2}\right) = \frac{1 + \sin\overline{\varphi}}{1 - \sin\overline{\varphi}} \qquad (2.69)$$

According to Rowe [Row72] the so called equivalent friction angle $\overline{\varphi}$ can take different (but constant) values in order to take account of other deformational mechanisms than sliding of particles, such as particle rolling and rearrangement of particles. It varies between the interparticle friction angle φ_μ (in the pre-peak regime of dense sand) and the friction angle at constant volume φ_{cv} (in the post-peak regime of dense sand and for loose sand) and hence depends on the initial stress level and void ratio. For convenience it is often assumed $\overline{\varphi} = \varphi_{cv}$.

By applying the relation between a particular stress ratio (in terms of triaxial stress variables) and the corresponding friction angle – $\mu = \frac{6\sin\varphi}{3-\sin\varphi}$ (or $\sin\varphi = \frac{3\mu}{6+\mu}$), referring to triaxial compression – Eq. (2.69) can be transformed into

$$K = \frac{3 + 2\mu}{3 - \mu} \tag{2.70}$$

Rewriting Eq. (2.68) in terms of the stress invariants p and q (or stress ratio η) and the corresponding strain increments $\delta\varepsilon_p$ and $\delta\varepsilon_q$, and equating it with the above relation, the following expression for the dilatancy ratio in triaxial compression can be deduced:

$$D = \frac{\delta\varepsilon_p}{\delta\varepsilon_q} = \frac{9\,(\mu - \eta)}{9 + 3\mu - 2\mu\eta} \tag{2.71}$$

By comparing the stress-dilatancy relation originating from Rowe's theory with the one according to Roscoe and Schofield [RS63] (Eq. (2.67)), clear similarities can be found.

Having considered triaxial compression only so far, the equations characterising the stress-dilatancy relation can be generalised for plane strain and axisymmetric conditions following a proposition by Tsegaye et al. [TNB13]. The energy ratio incorporates the stress ratio $N_\varphi = \frac{\sigma_1}{\sigma_3} = \frac{1+\sin\varphi_m}{1-\sin\varphi_m}$ as a function of the currently mobilised shear resistance, the dilatancy ratio $N_\Psi = -\frac{\delta\varepsilon_3}{\delta\varepsilon_1}$ and the shear mode coefficient m_s ($m_s = 1$ for plane strain, $m_s = 2$ for triaxial compression and $m_s = 0.5$ for triaxial extension) in the following way:

$$K = -\frac{\sigma_1\delta\varepsilon_1}{m_s\sigma_3\delta\varepsilon_3} = \frac{N_\varphi}{m_s N_\Psi} \tag{2.72}$$

Note that the so called dilatancy ratio N_Ψ as the quotient of the two principal (plastic) strain rates differs from the dilatancy ratio D specified earlier, indicating the rate of volumetric deformation with progressive shearing. Alternatively, the dilatancy can be quantified by the dilatancy angle, which is

formulated for the different shear modes according to

$$\sin \Psi = \frac{m_s N_\Psi - 1}{m_s N_\Psi + 1} \tag{2.73}$$

Consequently, in case of triaxial compression the angle of dilation can be calculated by

$$\sin \Psi = \frac{2N_\Psi - 1}{2N_\Psi + 1} = \frac{3D}{D - 6} \tag{2.74}$$

using the ratio of principal and volumetric/deviatoric strain rates, respectively.

Combining Eqs. (2.72) and (2.73), incorporating Rowe's energy ratio (Eq. (2.69)) and considering critical state by substituting $\overline{\varphi}$ for the critical state friction angle φ_{cs}, from the generalised form of the dilatancy angle follows

$$\sin \Psi = \frac{\sin \varphi_m - \sin \varphi_{cs}}{1 - \sin \varphi_m \sin \varphi_{cs}} \tag{2.75}$$

In contrast to the general formula, this expression implies that the dilatancy angle is shear mode independent if based on Rowe's assumptions. Furthermore, Eq. (2.75) shows that the dilatancy angle is zero, corresponding to constant volume shearing, if the mobilised friction angle takes the critical state value. This confirms the already recognised parallels to the stress-dilatancy relationship derived from Taylor's work hypothesis.

Both approaches imply that constant volume shearing occurs at the mobilisation level of critical state only, hence phase transition from contractant to dilative behaviour also takes place at critical state stress ratio and consequently is unique for every soil as critical state is. This is an implication that is not in accordance with experimental evidence [e. g. BJ04] (see Fig. 2.17).

Similarly, experiments revealed that the equivalent friction angle defined by Rowe [Row72] is not a constant depending on the initial soil state only, but also varies during the deformation process due to changes in the internal structure. In addition, the initially mentioned dependence of the dilatancy angle on the current void ratio is not captured by Rowe's stress-dilatancy equation (Eq. (2.75)). In order to respect these observations Wan and Guo [WG99] extended the original stress-dilatancy formulation by an additional state parameter: the soil's density. This was realised by replacing the equivalent friction angle with the constant volume friction angle, scaled by a
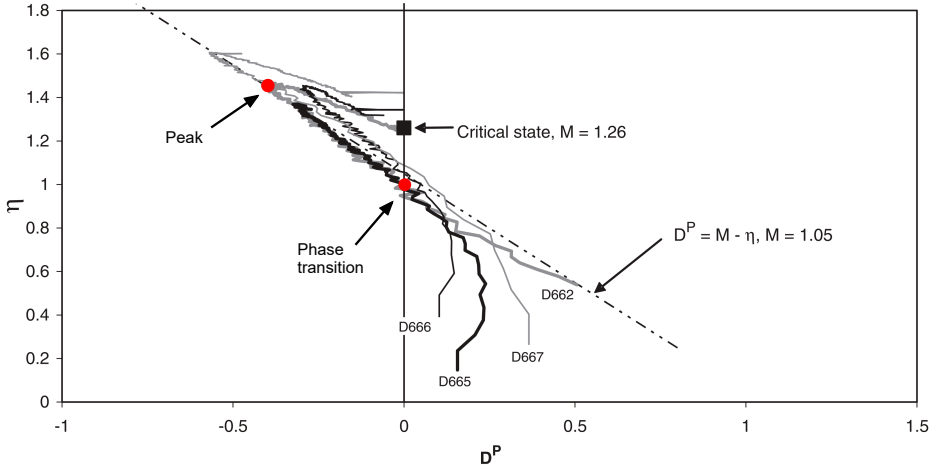
Figure 2.17: Dilatancy in direct shear of an ideal sphere packing [modified from BJ04]

function of the actual void ratio e in relation to the critical state void ratio e_{cs}:

$$\sin \Psi = \frac{\sin \varphi_m - \left(\frac{e}{e_{cs}}\right)^{\alpha} \sin \varphi_{cs}}{1 - \left(\frac{e}{e_{cs}}\right)^{\alpha} \sin \varphi_m \sin \varphi_{cs}} \tag{2.76}$$

As the critical state void ratio e_{cs} depends on the mean stress p, for instance according to Eq. (2.2), this extension does not only account for the soil's current density but also for the stress level, besides the already existing stress dependence via $\sin \varphi_m$. Consequently, the complete deformation process can be described, capturing the volumetric behaviour under a shearing path as a function of stress and void ratio. Instead of a single energy line according to Rowe's original stress-dilatancy rule, this modified relationship leads to a family of dissipation curves. It can also be deduced from Eq. (2.76) that the event of constant volume shearing does not only occur at critical state, where $\sin \varphi_m = \sin \varphi_{cs}$ and $\left(\frac{e}{e_{cs}}\right)^{\alpha} = 1$. The condition $\sin \Psi = 0$ is also fulfilled for a mobilised friction angle of $\sin \varphi_m = \left(\frac{e}{e_{cs}}\right)^{\alpha} \cdot \sin \varphi_{cs}$ with $\left(\frac{e}{e_{cs}}\right)^{\alpha} < 1$, which corresponds to the phase transition point of a dense soil. Therefore, phase transition and critical state do not coincide any longer as they do in the original Rowe stress-dilatancy relation.

Besides this approach on the macroscopic scale, as one research team among very few [e. g. Mat74, GB90], Wan and Guo [WG04] made a proposal on how to improve the dilatancy formulation by explicitly incorporating microstructural considerations. However, it is not a merely micromechanical approach they developed, but rather the attempt to transfer their microstructural concept onto a macroscopic level, coupling it with an elastoplastic modelling framework.

Experimental investigations have indicated that dilatancy is not only dependent on density, stress level and stress history, but also on the variation in particle arrangement (i. e. fabric) and the directional distribution of interparticle contacts. As shown by experiments from Oda [Oda72] in Fig. 2.18, a densely packed soil sample, for example, that exhibits dilative behaviour if loaded perpendicularly to its bedding plane ($\theta = 0°$), tends to a volumetric deformational behaviour of loose soil, if the angle between loading direction and bedding plane decreases ($\theta \to 90°$). This observed influence of the angle of bedding plane, the rotation of the principal stress directions [WA86] or the sample preparation method [ZI97] on the volume change characteristics of a tested soil specimen are a strong lead for the importance of fabric.

Motivated by these observations, several researchers [e. g. Sat82, Oda82, Tob89, WG04] proposed a fabric tensor $\boldsymbol{F}$ that traces microstructural changes (arrangement of contact normals, orientation of long particle axes, shape
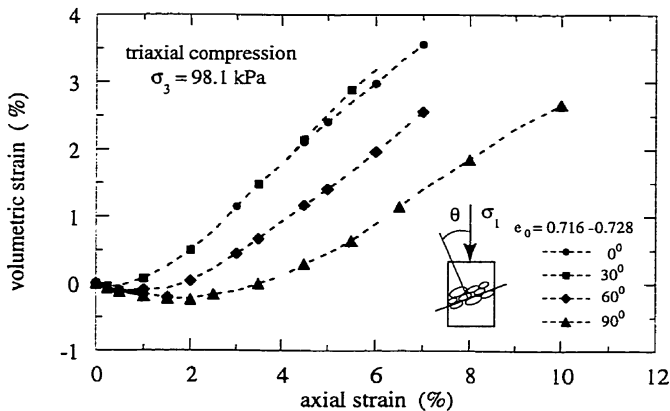

Figure 2.18: Volumetric strain in triaxial compression as function of sample orientation according to Guo [Guo00], based on data provided by Oda [Oda72]
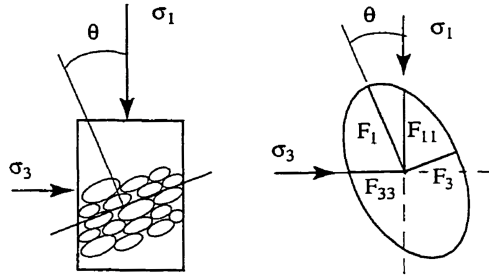
Figure 2.19: Fabric tensor components [Guo00]

of voids) within the soil body in a simplified manner and is hence a mean
to express the soil's anisotropy. The fabric tensor established by Wan and
Guo [WG04] describes the geometrical arrangement of grains via a distri-
bution density function of the orientation of interparticle contact normals.
As shown in Fig. 2.19, the components F_1 and F_3 of the fabric tensor re-
present the principal directions of fabric orientation and they enclose an
angle θ with the principal stress directions σ_1 and σ_3. If the microstructure
is stronger in a particular direction and hence anisotropic, the fabric ratio
$\Omega = \frac{F_1}{F_3}$ is different from 1 ($F_1 > F_3$ if dominant in major principal stress
direction and vice versa).

Oda et al. [OKN80, ONK85] proved experimentally that during a deforma-
tion process of a granular material specimen, the change in orientation of
the grains is primarily linked to the applied stress rather than the plastic
strain. In order to resist the external forces, the contact normals (and hence
the principal direction of fabric) realign in the direction of the major prin-
cipal stress. These experimental observations gave rise to the assumption
that the incremental fabric tensor is coaxial with the incremental stress ten-
sor. Consequently, Guo [Guo00] defined the evolution of $\boldsymbol{F}$ in the direction
of the deviatoric stress ratio change $\dot{\eta}$, scaled with a constant. At critical
state, the deviatoric stress ratio η approaches a constant value and hence
the fabric tensor rate $\dot{\boldsymbol{F}}$ will equally tend to zero, corresponding to a steady
microstructural configuration.

Without going too much into detail, the fabric tensor is finally converted
into a scalar measure in order to transform the local micro-level variable
into a global variable on the macroscopic stress-strain level. In the form of
a fabric factor it extends the previous reformulation of Rowe's equivalent

friction angle used in Eq. (2.69):

$$\sin \overline{\varphi} = \frac{X \frac{F_{33}}{F_{11}} + \gamma^{*pl}}{a + \gamma^{*pl}} \left(\frac{e}{e_{cs}} \right)^{\alpha} \sin \varphi_{cs} \qquad (2.77)$$

X, a and α are material constants. The fabric information is incorporated via the two fabric tensor components F_{11} and F_{33} in the principal stress directions σ_1 and σ_3 (see Fig. 2.19) and indirectly via the variable γ^{*pl}. It represents the plastic shear strain factored with the fabric tensor according to $\gamma^{*pl} = \varepsilon_1 F_{11} - \varepsilon_3 F_{33}$.

In contrast to Rowe's stress dilatancy law, this formulation does not define a unique link between stress ratio and dilatancy rate by a single energy dissipation line but creates a whole family of curves, which correspond to different densities, stresses and – with the embedded microstructure – also fabric states. Equation (2.77) reflects experimental evidence that at small shear strains dilatancy is mainly controlled by the fabric tensor. When shear strains become larger, the importance of fabric vanishes (fabric factor tends to 1) and when approaching critical state, Eq. (2.77) reduces to the original stress-dilatancy relationship by Rowe without stress, void ratio or fabric dependency.

The presented fabric based stress-dilatancy formulation by Wan and Guo [WG04] is one example for the consideration of microstructure referring to dilatancy within the context of elastoplasticity. Of course, describing granular materials at the grain to grain level, namely within the scope of discrete element analyses, seems attractive in the light of correctly simulating real soil behaviour. But with the presently available computational force it is unrealistic to follow this approach when striving for solving boundary value problems. The challenge is to relate the evolution of fabric on the microscale to the macroscopic constitutive framework of continuum mechanical models.

Wan and Guo [WG04] have presented one method to elegantly incorporate microstructure into an elastoplastic model by introducing a tensor that allows for capturing inherent and induced anisotropy. There have been other researchers following similar strategies, e. g. Papadimitriou and Bouckovalas [PB02], Li and Dafalias [LD04] or Triantafyllidis [Tri16]. The latter, for example, sums up formation history (genesis or sample preparation method) and changes in the contact force chains induced by the previous loading history with the term "historiotropy". A second order deviatoric tensor is used in order to describe the internal structure, an evolution law traces its

variation and by simply forming the tensor's norm it is converted into a scalar historiotropic state variable.

The reliability of such a constitutive element depends mainly on the choice of its initial value (inherent anisotropy) and the evolution law that controls the development of the tensor throughout the deformation process (induced anisotropy). In particular the former issue, the initiation of the fabric tensor, is what impedes the successful application of fabric tensors in constitutive modelling at present. The scientific foundation is too scarce and the experimental capabilities not yet technically mature for making good estimates for the initial fabric.

The development towards the integration of micromechanical approaches on the macroscopic scale is desirable and greatly appreciated. Research that aims at investigating the highly complex processes inside the soil fabric is a key element to improving our abilities in modelling soil behaviour. However, this type of research is not subject of the present work. Hence, the application of sophisticated constitutive elements, which add to the complexity of the model without being fully understood, might be worthwhile reconsidering in the context of the current state of the art. In view of the applicability of the model, it is questionable, whether an increase in the intricacy of the constitutive equations and in the effort for determining the soil's initial configuration is expedient under these circumstances. It might be more reasonable to dispense with fabric tensors for now, as long as micromechanical research still investigates the fundamentals, and work with more simply structured models instead. Of course, the user has to be aware that certain phenomena of soil behaviour are not or only deficiently captured by a simpler model. This decision for the present model should by no means discourage further efforts in developing the concept of fabric tensors towards a useful and manageable constitutive element.

3 The extended bounding surface model

The aim of constitutive modelling is to describe the soil behaviour through a constitutive law that finds the optimal compromise between reality and approximation. Seen from an output-driven perspective, this optimisation process is the central aspect of constitutive modelling that focusses on the engineering application of a model. The crucial question is: Which behavioural patterns are required to be reproduced by the model and which peculiarities can be neglected in order to obtain a result with acceptable deviations from the actual soil behaviour?

For application purposes, the important point about a particular model is not necessarily a long list of features, but mainly the knowledge about its limitations. Being aware of the soil properties that cannot be depicted by the model, of patterns that cannot intrinsically be derived from a calculation with a special constitutive law, is vital when it comes to choosing a model for running soil mechanical computations.

In order to meet this requirement, a key element of this work has to be a detailed description of the present model. The starting point is an explanation of the very basic features of soil behaviour that can be reproduced and that are ascribed to the constitutive framework. Referring to the bounding surface concept, this information can be taken from the following subchapter. In the subsequent section, the explications lead up to more sophisticated phenomena and the way the basic model and its extensions are capable of capturing them. The last section is dedicated to the examination of the model limitations, analysing the behavioural patterns that cannot be reproduced and giving an insight into the responsible model deficiencies and missing constitutive elements.

Creating a sound basis for a responsible application of the numerical model, Chap. 3 also prepares the ground for the subsequent chapter concerned with the calibration process of the model parameters.

3.1   Fundamental capabilities of the bounding surface concept

Belonging to the rather advanced models in elastoplasticity, the bounding surface model family is capable of reproducing most of the fundamental properties of soil behaviour. In the following, an overview is given on the very basic features and in the subsequent sections more detailed information on the respective model specific constitutive elements for their realisation is presented.

Based on the bounding surface model according to Manzari and Dafalias [MD97], the proposed extended model basically captures the same elementary behavioural patterns of soil mechanics as the original. These underlying concepts are summarised in a set of hypotheses as follows (adopted from Gajo and Wood [GW99]):

1. Within a small region of stress, the soil's behaviour can be approximated as being elastic.

2. Attaining critical state under continuous shearing, the soil develops large deformations without further changes in stress or density.

3. The shear strength, which is mostly governed by some kind of frictional relationship in case of sand, largely depends on the mean stress level and the soil's density.

4. During monotonic shearing the shear stiffness decreases steadily.

5. As the soil is sheared, it exhibits a volume change in the form of compression or expansion, which is dependent on the soil's state, represented principally by the mobilised friction (or stress ratio) and the density (void ratio). This volumetric deformational behaviour is termed contractancy or dilatancy, respectively.

6. The phenomenon, that soil characteristics as the peak angle of friction and the volumetric deformational behaviour depend on the density and mean stress level of the soil, is termed pycnotropy and barotropy, respectively.

7. During monotonic (oedometric or isotropic) compression the soil stiffness increases steadily.

8. After shear reversal the soil exhibits an increased stiffness.

Below, these basic features, that both original and extended model have in common, are presented separately and supported by exemplary simulations of standard laboratory tests.

3.1.1 Elastic region

An important feature of soil behaviour, which can be observed in laboratory tests as well as engineering applications, is the occurrence of irreversible deformations. However, up to a certain extent of loading the deformation is (approximately) recovered once the load is removed – all strains are reversible (elastic). Laboratory investigations have revealed that this range, which can be considered truly elastic, is actually very small and is defined via a limit strain of approximately 10^{-6} to 10^{-5} (see 2.3 for more information). A fundamental ingredient of elastoplasticity is the translation of this elastic limit strain into a geometrical limit in stress space by the introduction of a yield surface, bounding the elastic domain. If in loading the stress state violates the yield surface, the deformational regime becomes elastoplastic and strains are consequently not fully reversible anymore. Accordingly, the yield surface is responsible for the constitutive decomposition of strains into an elastic and a plastic portion according to:

$$\varepsilon = \varepsilon^{el} + \varepsilon^{pl} \tag{3.1}$$

As bounding surface models are set up in an elastoplastic environment, most of them incorporate a yield surface. In case of the original as well as the present extended version the yield surface has the shape of an open cone with its vertex at the origin. Once the elastic domain is violated, the material hardens kinematically, the yield surface changes its location according to the hardening law and consequently plastic strains add to the elastic deformation so that the overall (elastoplastic) response becomes softer (see also Fig. 3.11).

3.1.2 Critical state

The bounding surface models are based on the so called critical state concept according to Roscoe et al. [RSW58], which was introduced in Sect. 2.1.1. The corresponding constitutive element is the so called critical state line
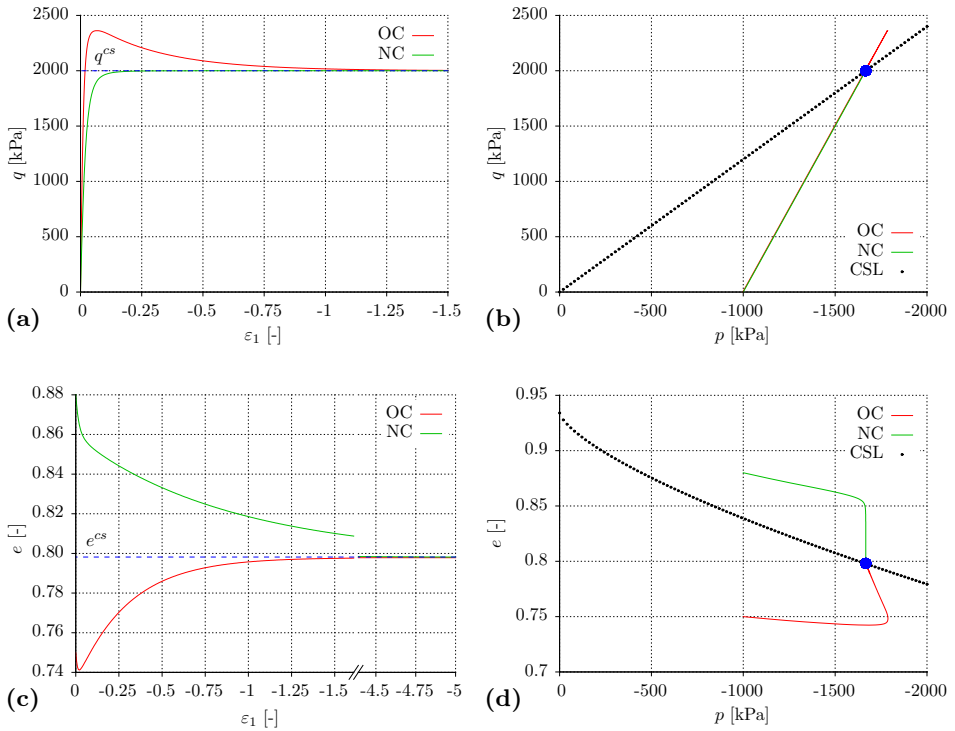
Figure 3.1: Critical state concept in bounding surface plasticity for normally consolidated (NC) and overconsolidated (OC) soil

(CSL), an asymptote defined in both stress and stress-void ratio space via the Eqs. (2.1) and (2.2). Depending on the location of the initial state with respect to the CSL in stress-void ratio space (Fig. 3.1 d), a soil specimen exhibits a distinct hardening and deformation behaviour when sheared: If the state is located above the CSL, the soil sample behaves like loose or normally compressed (or lightly overconsolidated) soil; the typical response of dense or heavily overconsolidated soils can be observed, if the state lies below the CSL. In terms of volumetric strain evolution, subfigures c and d reveal that the former group shows a purely contractant behaviour, whereas the latter one dilates (expands) after an initial contractant phase. Shifting the focus to stress space, in the p-q plot in subfigure b the CSL is represented by a linear function with an inclination of M^c. In case of loose soil, loading is associated with plastic hardening and an increase of the stress ratio $\eta = q/p'$ until the critical stress ratio $\eta = M^c$ is reached. If the initial soil state is dense, the stress ratio increases until a peak state $\eta > M^c$ is reached and

under further loading the soil experiences plastic softening and a decrease of stress ratio, finally attaining the critical stress ratio $\eta = M^c$. The resulting deviatoric stress evolution with increasing axial deformation is presented in Fig. 3.1 c.

Common to both CSL representations is that the locus of critical states is uniquely defined for each material and no matter what the initial state, a soil sample that has been sheared infinitely will finally reach a point on the CSL (blue dots in Fig. 3.1 b and d). Thus, the CSL serves as some sort of attractor – a final state that is asymptotically approached and that can hence be used as a reference state in the constitutive formulations.

The bounding and dilatancy surfaces in stress space, which are responsible for the determination of the peak stress and the dilatancy of a sheared soil, are made functions of the critical state surface: $M^{d,b} = f(M^c)$. By means of appropriate evolution rules, under continuous shearing both surfaces move towards the critical state surface, so that $M^{d,b} \rightarrow M^c$, allowing for the soil to finally converge to its ultimate condition at critical state. In order to ensure that the critical state is reached in both stress and stress-void ratio space, the mentioned evolution rule of bounding and dilatancy surface is dependent not only on the stress but also on the soil's density. This missing link is created by the introduction of the so called state parameter ψ by Been and Jefferies [BJ85], defining the actual state's vertical distance from the CSL in stress-void ratio space ($\psi = e - e^{cs}$). It is at the same time the key to state dependence and barotropy/pycnotropy, discussed in Sect. 3.1.6.

3.1.3 Shear strength

If continuously sheared under triaxial loading conditions, the soil will reach a peak value of shear stress that cannot be exceeded, termed the shear strength of a soil. As previously mentioned, depending on the initial state of the soil sample (density, stress level), it shows a purely hardening or also a subsequent softening behaviour. In case of an initially loose state ($\psi_0 > 0$), the shear strength corresponds to the critical state shear stress: the soil approaches its maximum shear stress at critical state (Fig. 3.2 a) and consequently exhibits hardening only. Regarded in the bounding surface framework the stress state remains entirely inside (or under) the bounding surface ($d^b > 0$) while the state parameter evolves towards zero until all limit surfaces finally fall onto the critical state surface at critical state. If on the contrary the soil is in an initially dense state ($\psi_0 < 0$), after having
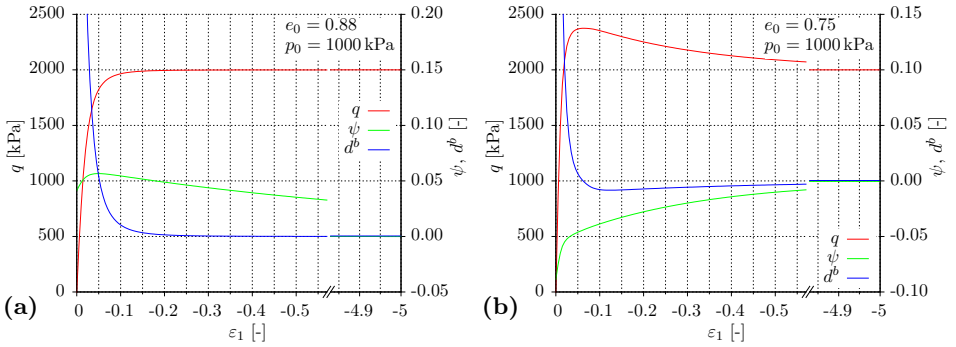
Figure 3.2: Evolution of deviatoric stress q, state parameter ψ and distance measure d^b for (a) loose and (b) dense soil in drained triaxial loading

reached the peak strength the shear stress drops from its peak value down to its ultimate value at critical state. Presented in Fig. 3.2 a this initiation of softening is triggered by the stress state crossing the bounding surface, turning the distance measure d^b into a negative value. Consequently, the hardening modulus drops below zero and causes the typical softening behaviour of dense soils. The declining stress state stays outside the bounding surface, which is shrinking to the size of the critical state surface due to the steadily decreasing state parameter. Thus, the distance d^b remains negative
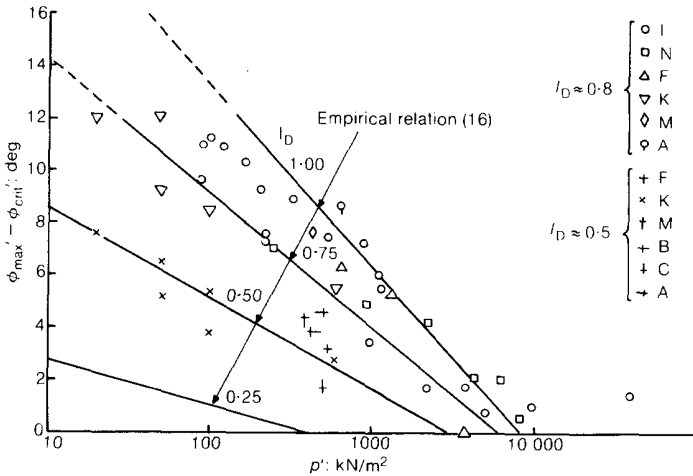
Figure 3.3: Difference of friction angles φ^{peak} and φ^{cs} over mean stress at failure for different sands at two different relative densities [Bol86]

and reapproaches zero towards critical state.

As observed by Bolton [Bol86], for example, the resulting strength envelope connecting the failure points in stress space is not a unique locus as the critical state line, but depends on the soil's initial density. In Fig. 3.3 Bolton compiled strength data of several sands for two different relative densities ($I_D = 0.5, 0.8$): the difference of friction angles at peak and critical state, $\varphi^{peak} - \varphi^{cs}$, is plotted over the mean stress at failure, indicating that at low stresses the peak friction angle is at its maximum, decreasing down to the critical state angle towards higher stresses. Additionally, the maximum value of the peak friction angle and the stress, where the critical state angle is attained, depend on the initial density.
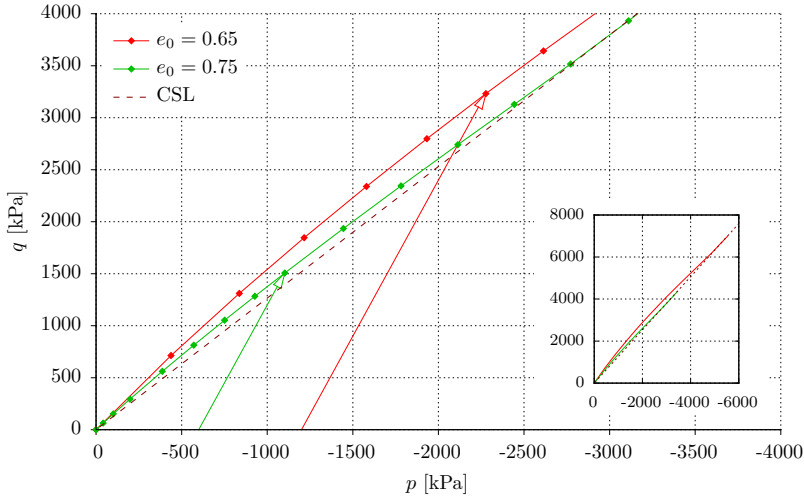
Figure 3.4: Failure envelopes for two different initial void ratios ($e_0 = 0.65, 0.75$), with exemplary stress paths

In order to demonstrate that the state dependent formulation of the bounding surface is capable of capturing Bolton's experimental observations, Fig. 3.4 presents corresponding simulations on Toyoura sand of two different initial void ratios. The resulting curved envelopes with their maximum slopes in the vicinity of the origin, joining the critical state line, reflect the observed evolution of the shear strength with mean stress. The existence of two curves – one envelope for each initial void ratio – confirms the state dependent location of the bounding surface.

3.1.4   Shear stiffness (monotonic)

When a soil sample is continuously sheared towards its maximum strength, shear strains evolve. In triaxial loading, it can be observed that this stress-strain relationship describes a non-linear curve, exhibiting an accelerating amount of strains with increasing (shear) stress. Consequently, the shear stiffness drops, the closer the stress state comes to failure.

In the bounding surface context, this behaviour is modelled via the distance between actual stress state and bounding surface d^b. Once the yield surface hardens, this measure controls the plastic hardening modulus, which in turn determines the shear stiffness for the evolution of plastic strains: with a vanishing distance d^b the hardening modulus decreases and so does the shear stiffness. The example of a triaxial compression test on loose sand in Fig. 3.5 a shows how the hardening modulus decreases to (almost) zero, when the shear stress approaches its critical value, leading to an increasingly soft soil response. Furthermore, the small inset in Fig. 3.5 b indicates the evolution of the hardening modulus in case of an initially dense soil: H drops below zero at peak, reaches its minimum and then slowly reapproaches zero, with the negative value indicating softening behaviour.
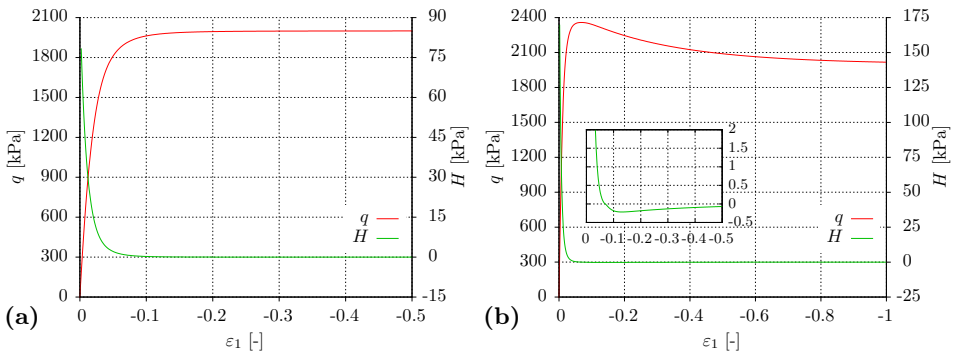
Figure 3.5: Evolution of deviatorice stress q and hardening modulus H in drained triaxial loading for (a) loose and (b) dense soil

3.1.5   Contractancy and dilatancy

One important characteristic of soil behaviour is the evolution of plastic volumetric strains as a shearing process is going on. It has been observed that a loose soil sample under triaxial loading exhibits volume contraction. But the higher the density of the soil, the stronger the tendency to show

volume expansion after an initially contractant phase. This phenomenon is known as contractancy and dilatancy, respectively.

In the context of critical state soil mechanics, the volumetric response depends on the location of the state related to the CSL in stress - void ratio space. In bounding surface plasticity, this dependence is translated into stress space via the state parameter ψ, which governs the extent of the dilatancy surface. As described in detail in Sect. 2.1.1, the distance of the actual stress state to the dilatancy surface determines sign and magnitude of the soil's volumetric response: if located solely under (inside) the dilatancy surface, the soil contracts (Fig. 3.6 a). If the initial state of the soil is a denser one, the stress state will cross the dilatancy surface due to further shear loading and the soil expands, with an increasing rate of deformation the larger the distance of the stress state to the surface. This mechanism is visualised in Fig. 3.6: when the distance measure d^d changes sign (the moment the stress state crosses the dilatancy surface), the initially positive dilatancy factor $D = \frac{\dot{\varepsilon}_p^{pl}}{\dot{\varepsilon}_q^{pl}}$ passes zero, the ε_1-ε_v curve of a drained triaxial test reaches its minimum and consequently volume contraction changes to volume expansion. This point is often called phase transition point [according to ITY75], marking the transition between contractant and dilatant volumetric behaviour.

The described behaviour equally applies to undrained triaxial tests, the difference being that elastic and plastic volumetric deformations compensate one another, so that the overall volume remains constant. In case of undrained behaviour, the tendency for contractancy or dilatancy transla-
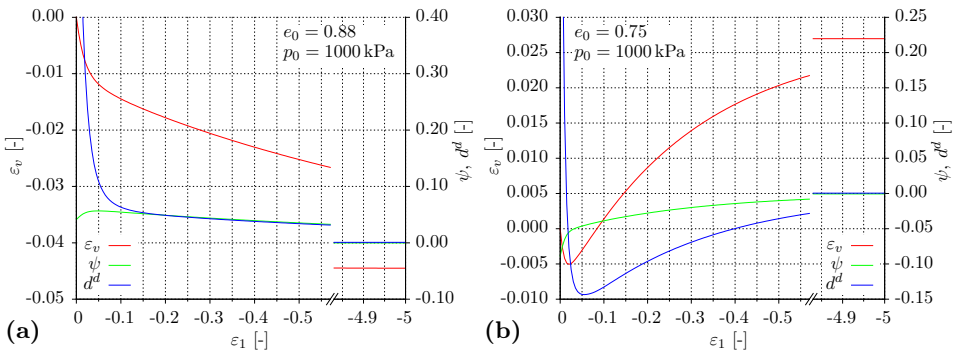
Figure 3.6: Evolution of volumetric strain ε_v, state parameter ψ and distance measure d^d for (a) loose and (b) dense soil in drained triaxial loading

tes into the evolution of excess pore water pressure due to the prevented drainage condition. Consequently, a loose sand specimen will develop positive pore water pressures so that the mean effective stress decreases and the stress path in p-q space strives towards the origin more quickly. In contrast, dense sand will, after a short initial contractant phase, exhibit the development of negative pore water pressures that increase the mean effective stress and therefore stabilise the soil body. In analogy to drained conditions, the moment, when the mean effective stress is minimal (pore water pressure rate changes sign and stress path changes direction from left to right), corresponds to the phase transition (Fig. 3.7).
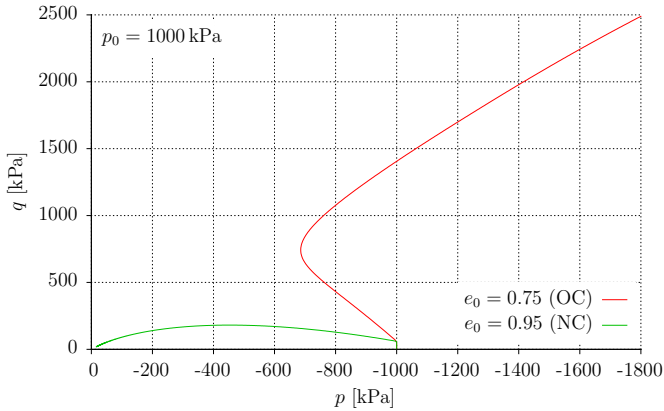
Figure 3.7: Stress paths for loose (NC) and dense (OC) soil in undrained triaxial loading

3.1.6 Barotropy and pycnotropy

The soil behaviour is influenced by the state of the soil, above all the stress level and the soil's density: depending on the magnitude of stress and the actual void ratio soil properties as the stiffness, the shear strength or the evolution of volumetric strains change. These effects are termed barotropy and pycnotropy, respectively [Kol88]. In short, the phenomenon of barotropy concerns the influence of stress level on the soil behaviour. It implies that for a given initial void ratio, the peak friction angle decreases as the stress level increases (see Fig. 3.8 c). Simultaneously, Fig. 3.8 e shows that as the initial mean pressure increases, the soil becomes more contractant – the dilatancy angle decreases. In contrast, pycnotropy describes the impact of density on the soil response. For a given stress level the friction angle
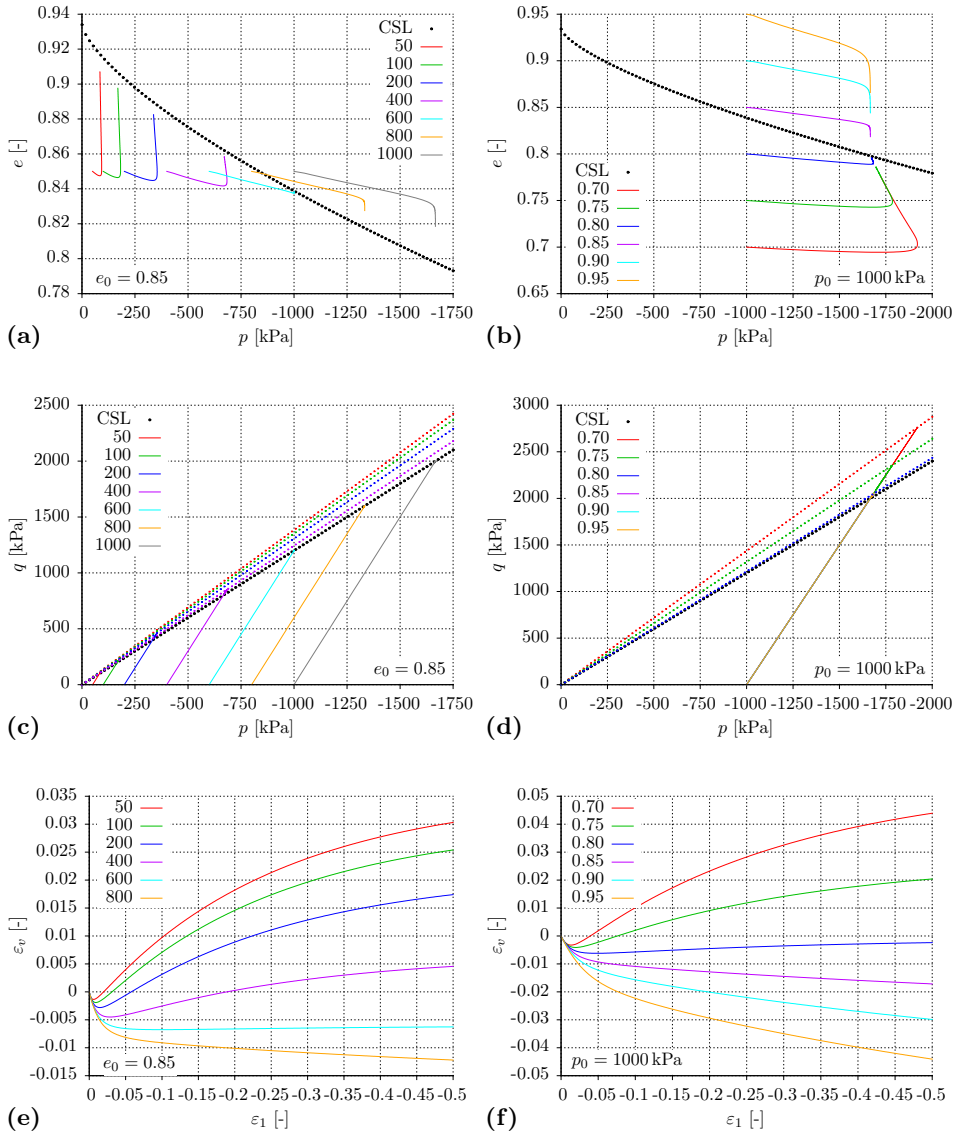
Figure 3.8: Effects of barotropy (a,c,e: variation of p_0) and pycnotropy (b,d,f: variation of e_0) in a series of triaxial compression tests, simulated with bounding surface plasticity

increases with a decrease in void ratio (Fig. 3.8 d) and so does the dilatancy angle: the denser the soil the more dilatant the volumetric response (Fig. 3.8 f).

The consideration of barotropy and pycnotropy within the scope of bounding surface plasticity is possible thanks to the incorporation of the state parameter ψ into the model formulation. With $\psi = f(e,p)$ and making the model surfaces a function of the state parameter, stiffness, strength and volumetric behaviour are governed by the distance of the actual point in stress space to the corresponding state dependent surface and are thereby dependent of stress level and density. Consequently, the model is capable of producing plots of drained triaxial tests as shown in Figs. 3.8 a to f, being qualitatively in accordance with experimental observations [e.g. dBee66, BJ85, KW90].

3.1.7   Compressive stiffness

In contrast to shear, the stiffness in compressive loading behaves differently. As can be observed in isotropic compression or oedometric loading, stiffness increases with increasing stress level, hence the axial deformation decelerates.

The basic bounding surface model contains a cone type yield surface only. Due to the opening of the cone, there is no limitation for the evolution of stress paths along a constant deviatoric stress ratio (η) as for example in isotropic compression or (approximately) in oedometric loading. A cap yield surface, that would delimit the elastic region and that has been introduced into the extended model, is not existent in the basic version. Consequently, when being subjected to, for example, isotropic compressive loading, the stress state remains within the open cone yield surface. Hence, all deformations are purely elastic and no hardening mechanism comes into play. It follows that the stress dependence of the stiffness is merely attributed to the elastic stiffness formulation, which involves the mean stress level p via the shear modulus G and the bulk modulus K according to Eq. (2.18). This formulation ensures that the elastic stiffness increases with the corresponding stress level. But due to the lack of plastic strain contribution, the overall deformational response of the basic model in η-constant loading over a sufficiently large stress range is too stiff. In addition, the appearing stress-strain hysteresis in consecutive loading cycles is limited to the effect of the slight variation of (para-)elastic stiffness with mean stress (Eq. (2.18)).
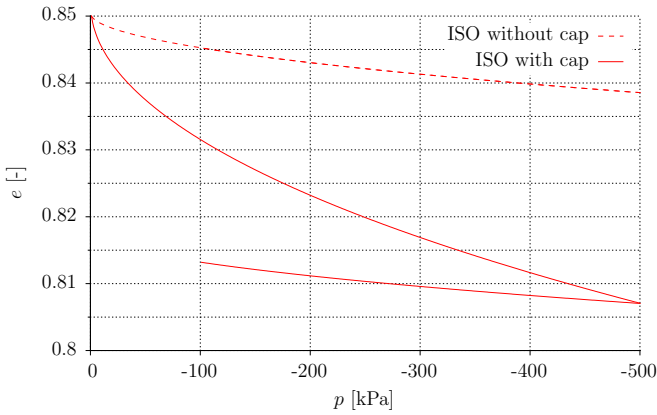
Figure 3.9: Isotropic compression test (loading and unloading) simulated with the capless original bounding surface model (broken line) and with a capped bounding surface model (continuous line)

Figure 3.9, presenting the stress-strain evolution of a loading-unloading cycle of an isotropic compression test, confirms the previous statements: the compressive stiffness increases with stress level so that the strain rate diminishes with increasing stress. Compared to the simulation of an isotropic compression test with a cap model (continuous line) the basic bounding surface model (broken line) shows rather small deformations due to the purely elastic behaviour. Of course, one could argue that by simply adjusting the elastic parameters, the capless model is able to deliver the same amount of deformations at the end of loading. This, however, would likewise affect the soil response in shear loading and consequently impair the overall model performance. Therefore, the decisive benefit of the cap is the creation of plastic strains, resulting in a clear difference of stiffness and hence two distinctly different stress-strain curves in (primary) loading and unloading.

3.1.8   Shear stiffness in reversed loading

Laboratory tests including reversed loading show that when loading continues in an opposite direction, the deformational response becomes distinctly stiffer. Being set up in an elastoplastic framework with a kinematically hardening yield surface, the model ensures that after a stress reversal the stress state crosses the elastic domain before the yield surface starts hardening again in the new loading direction. Consequently, the soil regains its initial elastic stiffness.
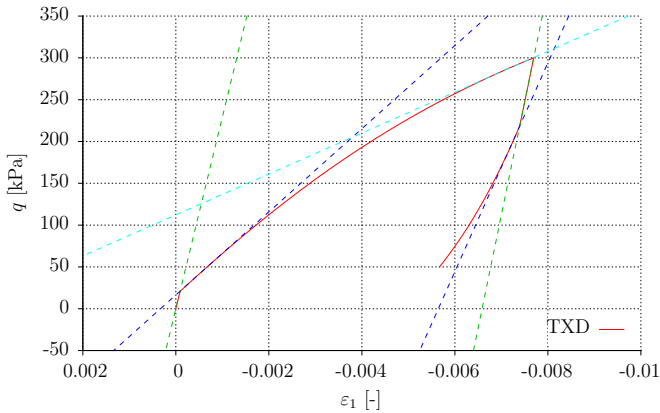
Figure 3.10: Loading-unloading cycle of a drained triaxial compression test

Assuming a triaxial compression test in the first stage of loading, the stress state gradually approaches the bounding surface in compression. With unloading (180° stress reversal) the reference surface for the distance measure d^b (and also d^d) changes from the compression to the extension side of the surface. Accordingly, the distance jumps to a higher value with load reversal before it starts dropping again with further (un)loading. This elevated distance translates into a higher hardening modulus and hence, once the stress state leaves the elastic domain, elastoplastic (un)loading will continue with an increased stiffness (compared to the plastic stiffness at the end of the initial loading).

The described behaviour can be understood by looking at Fig. 3.10, which shows a loading-unloading cycle of a drained triaxial compression test. The approximations of the two initial (elastic) branches of loading and unloading (broken green lines) exhibit roughly the same strong inclination, which originates from the formulation of the stress dependent elastic stiffness. The respective second branches in the elastoplastic regime (broken blue lines) vary evidently. The loading curve is inclined more intensively than the unloading curve already in the earlier part of loading and losing stiffness steadily until stress reversal (light blue), whereupon stiffness recovers and thus proves a stiffer response in unloading.

3.1.9   Additional features

Besides the previous eight patterns that were considered to represent fundamental soil behaviour, there are a few more features that can be named

typical for soil material and that can be captured by the bounding surface model family. In this section, they are discussed in short and the capability of the basic model for reproducing them is attested by exemplary simulations.

Dilatancy in cyclic shearing

One supplemental characteristic soil exhibits can be observed in reversed loading: whenever the loading direction is inversed, the soil volume contracts, irrespective of the actual state relative to the critical state line in stress and stress‑void ratio space. This is realised merely by the bounding surface principle. Similarly as explained in Sect. 3.1.8, with unloading (180° stress reversal) the reference surface for the distance measure d^d changes from the compression to the extension side of the dilatancy surface. Consequently, even if the stress state is previously located outside the dilatancy surface in compression and therefore causes volume expansion, the stress reversal activates the extension side of the dilatancy surface for the calculation of the distance d^d. From this follows that the stress state instantly lies inside the dilatancy surface again and hence the volumetric response shows contraction.

The foregoing statement has to be qualified. In the first instance, the explanation is valid for all plastic strains originating from the bounding surface concept. Regarding the initial part of the stress path after stress reversal, the stress state is located inside the yield surface and hence the deforma-
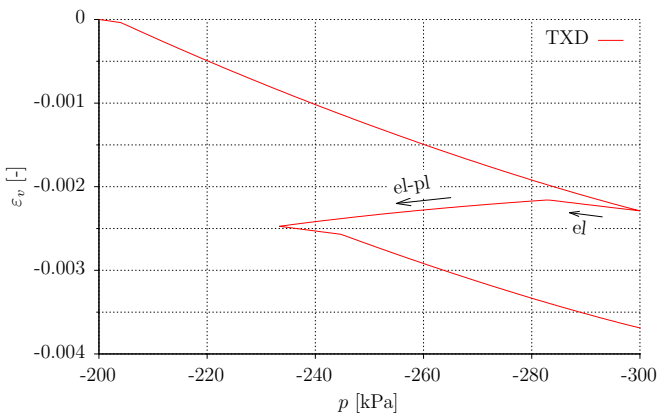
Figure 3.11: Volumetric deformations in a loading-unloading-reloading cycle of a drained triaxial compression test (TXD)

tion is purely elastic. Depending on its direction, which in return depends on the sign of the mean effective stress rate according to Eq. (2.17), the elastic deformation is either contractant or dilatant. Concretely speaking, if the absolute value of p decreases comparably to unloading after drained triaxial compression, the mean effective stress increment is positive, hence the elastic volumetric strain increment is positive as well, corresponding to a volume expansion (see Fig. 3.11). This is in contradiction to the soil mechanical observation. Once the stress state violates the yield surface and the latter begins to harden, contractant plastic strains contribute to the deformation as explained above, which, in the described case, will be oriented in the opposite direction. As long as the elastic part dominates the elastoplastic response, the resulting volumetric deformation remains dilative. But as soon as the plastic strain has grown sufficiently, it overrules the elastic deformation and the elastoplastic response becomes contractant – until the stress state crosses the dilatancy surface anew.

Due to this intrinsic feature of the bounding surface model, particularly in consecutive small stress-strain cycles it is able to accumulate compressive strains. This, however, involves the risk of an undesired overshoot in accumulation, which might not be in accordance with experimental observations. This phenomenon is called ratcheting and will be discussed within the scope of model extensions and limitations.

Cyclic behaviour at very small strains

Looking further at reversed loading, the observation has been made, that in very small strain cycles the deformational behaviour is quasi-elastic [CDH$^+$96, Kuw99, HT00]. This means, if repeated loading/unloading cycles are applied to a drained soil specimen, causing sufficiently small strains, no permanent deformation will accumulate. Within the bounding surface concept, this is realised by the finitely slim conical yield surface. As long as the stress state remains inside the yield surface the response will be purely elastic and hence fully reversible. Consequently, the diameter m_{cone} of the yield surface is the controlling parameter for adapting the basic model to the strain range wherein any monotonic or cyclic loading can be considered to cause elastic deformations only. Thus, the high elastic stiffness is valid only for stress states within the yield surface; for any stress state located outside this elastic domain, the comparably low elastoplastic stiffness applies. In the original model, there is neither a smooth transition in between these stiffnesses nor a strain dependence, which increases the

elastoplastic shear stiffness at (very) small strains for states outside the elastic domain.

Dependence of the failure criterion on the intermediate principal stress

For the implementation of the bounding surface concept a multiaxial model formulation has been chosen, which means that all constitutive relations are expressed in multiaxial stress space. Thanks to this stress generalisation the application of the model is not restricted to triaxial loading conditions but allows for general stress states. In particular, in this way the effect of the intermediate principal stress σ_2, which is neglected in triaxial considerations, can be incorporated.

The stress measures from triaxial space are transferred to multiaxial stress space, so that based on the stress tensor $\boldsymbol{\sigma}$ the scalar invariants p and q as well as the stress ratio η translate into the isotropic stress p, the deviatoric shear stress tensor $\boldsymbol{s}$ and the deviatoric stress ratio tensor $\boldsymbol{r}$, as explained in Sect. 2.1.1. Bounding, critical state and dilatancy lines become conical surfaces, which are generally non-circular in the Π-plane. This means, that depending on the type of loading with respect to the proportion of principal stresses $(\sigma_1,\sigma_2,\sigma_3)$, the deviatoric stress ratios $M^{b,c,d}$ vary. Consequently, they differ for triaxial compression and extension and take intermediate values in non-triaxial loading cases.

According to Eq. (2.22), the loading direction is quantified by the Lode angle θ, which takes account of all three principal stress directions, including the intermediate principal stress. Following Eqs. (2.24) and (2.25), the Lode angle dependence is transferred onto the deviatoric stress ratios $M^{b,c,d}$ by the shape factor $g(c,\theta)$. In triaxial compression ($\theta = 0$), $g(c,0)$ simplifies to 1, thus $M_\theta^{b,c,d} = M_c^{b,c,d}$. In triaxial extension ($\theta = \pi/3$), $g(c,\pi/3) = c^{b,c,d}$ and consequently $M_\theta^{b,c,d} = c^{b,c,d} \cdot M_c^{b,c,d} = M_e^{b,c,d}$. For any non-triaxial case ($0 < \theta < \pi/3$) $g(c,\theta)$ is interpolated. At last, multiplication with the deviatoric loading direction $\boldsymbol{n}$ according to Eq. (2.26) converts the adapted deviatoric stress ratios $M_\theta^{b,c,d}$ into multiaxial surface formulations $\boldsymbol{\alpha}^{b,c,d}$.

From the foregoing derivation follows that the failure criterion, expressed by $\boldsymbol{\alpha}^b$, considers the influence of all three principal stresses and hence does not neglect the effect of the intermediate principal stress on the friction angle under non-triaxial loading conditions.

Loading anisotropy

In the context of bounding surface plasticity, the term anisotropy has to be considered in different respects. Inherent and evolving fabric anisotropy is directly linked to the soil's structure, concerning the initial arrangement of grains and its evolution during shear, with regard to the impact of these factors on the directional properties of the soil body. This is a wide field that has been attended to by many researchers in the attempt of finding an appropriate and efficient way to model fabric anisotropy [e. g. Oda82, NT82, ONK85, DM99, Guo00].

Besides, so called loading anisotropy concerns the fact that the soil's mechanical properties are directionally dependent on the applied effective stress. This refers especially to the soil's strength, stiffness and volumetric behaviour that do not depend on the magnitude of stress only, but also on its direction. Within the bounding surface framework, this is intrinsically included due to the model formulation in multiaxial stress space. According to the definition of the loading direction $\boldsymbol{L} = \frac{\partial f}{\partial \boldsymbol{\sigma}}$ and the assignment of its deviatoric component $\boldsymbol{n}$ – a unit deviatoric stress ratio tensor – in most relevant constitutive equations, the applied stress direction is incorporated profoundly into the calculation of the mechanical response. To pick up on the section concerning the σ_2-dependence of the failure criterion, besides the Lode angle the deviatoric loading direction is required in order to locate the actual image points on the model surfaces. This allows for the determination of the distance to the actual stress state as measure for volumetric behaviour, stiffness and strength, respectively.

The expressions of the model surfaces on their own would not be sufficient for loading anisotropy. It has to be considered in conjunction with the kinematic hardening of the yield surface. This causes the hardening yield surface to rotate and move away from its centred position instead of only expanding isotropically. The elastic region translates through stress space and after change of loading direction, the stress state quickly enters the elastoplastic regime again. According to the bounding surface principle, the image stress on the corresponding reference surface is relocated, resulting in a new distance measure and causing a distinctly different mechanical response than in loading.

Non-associativity of plastic strains

Simplifying the mechanical behaviour of soils, in the past it has often been assumed that the plastic strain increment vector is in the direction of the normal to the yield surface at the current stress state, which corresponds to the hypothesis of normality. Differently said, the plastic deformations (flow) are associated with the yield criterion, so that the material exhibits associated flow. Normality or associated flow has been confirmed experimentally on metals but most soils do not obey this postulate, especially sands. It overestimates the plastic volumetric response by predicting a too strong tendency of volume expansion: the soil dilates too much. Consequently, the application of a non-associated flow rule is required, where yield surface and plastic potential do not coincide.

The basic version of the bounding surface model follows this insight. The expressions for the conical yield surface f and the corresponding plastic potential g differ:

$$\frac{\partial f}{\partial \boldsymbol{\sigma}} = \frac{\partial f}{\partial \boldsymbol{s}} + \frac{1}{3}\frac{\partial f}{\partial p}\boldsymbol{I} = \boldsymbol{n} - \frac{1}{3}\left(\boldsymbol{\alpha}\cdot\boldsymbol{n} + \sqrt{\frac{2}{3}}m_{cone}\right)\boldsymbol{I} = \boldsymbol{n} - \frac{1}{3}\left(\boldsymbol{n}\cdot\boldsymbol{r}\right)\boldsymbol{I} \quad (3.2)$$

$$\frac{\partial g}{\partial \boldsymbol{\sigma}} = \frac{\partial g}{\partial \boldsymbol{s}} + \frac{1}{3}\frac{\partial g}{\partial p}\boldsymbol{I} = \frac{\partial f}{\partial \boldsymbol{s}} + \frac{1}{3}\frac{\partial g}{\partial p}\boldsymbol{I} = \boldsymbol{n} + \frac{1}{3}D\boldsymbol{I} \quad \text{with} \quad D = f\left(d^d\right) \quad (3.3)$$

$$\dot{\boldsymbol{\varepsilon}}^{\boldsymbol{pl}} = \dot{\mathbf{e}}^{\mathbf{pl}} + \dot{\varepsilon}_{\boldsymbol{p}}^{\boldsymbol{pl}} = \dot{\mathbf{e}}^{\mathbf{pl}} + \frac{1}{3}\dot{\varepsilon}_p^{pl}\boldsymbol{I} = \lambda\frac{\partial g}{\partial \boldsymbol{\sigma}} \quad (3.4)$$

Since the dilatancy coefficient $D \neq -\boldsymbol{n}\cdot\boldsymbol{r}$, the equations indicate that the flow rule is associated in the deviatoric stress ratio space but non-associated in volumetric stress space. Depending on the sign of D, which is a function of the distance of the actual stress state to the dilatancy surface d^d, the volumetric part of the plastic strain takes positive or negative values, respectively. Knowing that $D = \frac{\dot{\varepsilon}_p^{pl}}{\dot{\mathbf{e}}^{\mathbf{pl}}}$, the corresponding deformational response becomes contractive or dilative. Considering triaxial compression, for example, the vectors $\boldsymbol{n}$ and $\boldsymbol{r}$ are aligned and hence their dot product results in a positive value. Finally, applying an associated flow rule would cause the volumetric contribution to become negative and would render the soil response merely dilative, which is not in agreement with experimental observations. Thus, the bounding surface model is based on a non-associated flow rule with a sound dilatancy formulation.

3.2 New features of the extended bounding surface model

The previous chapter cast light on the basic functionalities and constitutive capabilities of the bounding surface concept. Besides the discussed fundamental soil properties, there is a number of further behavioural patterns that might be important to be captured by a constitutive model of engineering practice. Some of them can already be reproduced by the original version of the model tracing back to Manzari and Dafalias [MD97]. But there were still a couple of missing features that gave reason to refine the model.

In the present chapter the model extensions, which were incorporated into the standard model within the scope of this work, are introduced. The deficiencies of the basic model are pointed out and justification for the necessity of extending the original model formulation and simultaneously increasing its complexity is given. A detailed description of the constitutive ingredients used for the realisation of the respective soil behaviour is the centrepiece of each of the following subchapters. Comparative calculations of the original and extended model complete the presentation of the new features.

3.2.1 Minor modifications

Compared to the original bounding surface model by Manzari and Dafalias [MD97], a few modifications have been incorporated in the extended model version with minor importance for the overall performance of the model. These adjustments are given shortly in the following, beginning with the elastic stiffness parameters. Similar to the basic model and the presented modified versions, mean stress dependence is incorporated via a power law, proposed in similar forms by Ohde [Ohd39], Janbu [Jan63] or Hardin and Richart [HR63]. In contrast to Eq. (2.18), additional void ratio dependence is included in the shear stiffness with the most frequently applied relationship for sands by Hardin and Black [HB66]:

$$G^{ref} = G_0^{ref} \cdot \frac{(2.17 - e)^2}{1 + e} \quad \rightarrow \quad G = G^{ref} \cdot \left(\frac{p}{p_{ref}} \right)^m \qquad (3.5)$$

Based on results from Hardin and Richart [HR63] the value 2.17 in Eq. (3.5) is valid for round grains (and confining stresses larger than $100\,\text{kPa}$).

In case of angular grains 2.97 is a better fit, which proved to be a good choice for clays as well [HB68].

The other elastic stiffness moduli – Young's modulus E and bulk modulus K – are deduced from the shear modulus G by means of the Poisson's ratio ν:

$$E = 2G\,(1 + \nu) \quad \text{and} \quad K = G\frac{2\,(1 + \nu)}{3\,(1 - 2\nu)} \tag{3.6}$$

For defining the critical state line in stress-void ratio space, the original formula (Eq. (2.2)) has been replaced by a proposal of Li and Wang [LW98], which uses an exponential dependency instead of a logarithmic relation:

$$e_{cs} = e_{cs0} - \lambda \left(\frac{p}{p_{at}} \right)^{\xi} \tag{3.7}$$

The previously used equation, which defines a linear curve in e-$\log p$ space, is appropriate only for clays or for a rather limited stress range in case of sands. Supported by experimental data [e.g. VI96], the proposed relationship is much closer to the locus of critical states of sands over a wide range of stresses [LDW99]. It has therefore been incorporated into the extended material model instead.

It should be noted that both logarithmic and exponential formulations of the critical state line in e-p space deliver negative critical void ratios at very high stresses, which is impossible. However, within a reasonable stress range[1] the chosen expression (Eq. 3.7) approximates the locus of the critical state very well. An alternative formulation, respecting a convergence to $e_{cs} = 0$ at infinitely high stresses, is offered by the relation used in hypoplasticity [Gud96] (see also Eq. (3.23)).

Concerning the bounding surface formulation the main amendments will be presented in the subsequent sections. One alteration relates to the bounding surface expression, an idea borrowed from Li and Dafalias [LD00], who exchanged the originally linear correlation with the state parameter by a non-linear one:

$$M^b = \exp(m_b \cdot \langle -\psi \rangle) \cdot M^c \tag{3.8}$$

---

[1]With increasing stresses the soil particles start crushing and hence the grain size distribution changes. Since basic soil mechanical properties such as critical states are dependent on the available range of packing densities, the grading changes will alter the critical state conditions [MM08] (see also Sect. 3.3.1). Consequently, it is anyway questionable, whether very high stresses need to be considered when defining the CSL for a particular soil, referring to the soil's initial grain size distribution.

From this relationship follows that for an initially dense soil ($\psi < 0$), the inclination of the bounding surface in p-q space drops exponentially with the state parameter from a value larger than M^c until finally reaching the critical state line ($\psi = 0$, $M^b = M^c$). Starting from a loose state ($\psi > 0$) results in a constant M^b of magnitude M^c due to the Macauley brackets. Compared to the original expression by Li and Dafalias [LD00] not using the Macauley brackets, this formulation causes a stiffer response in case of loose sands (due to the larger distance between bounding surface and moving stress state), which was observed to be closer to real soil behaviour.

The formulation for the hardening mechanism of the cone yield surface has been adopted from Taiebat and Dafalias [TD08] with a few minor modifications in the factor h, which captured the soil behaviour more satisfactorily. Consequently, the hardening modulus H_α takes the form of Eq. (2.52) and h is composed of a constant h_0 and three contributing functions: a void ratio dependency, a mean stress dependency and a function of the distance to the bounding surface. The previously used stress relation of Eq. (2.55) has been preserved; however, the impact of density and the reference to peak state have been altered. An extensive simulative study has shown that the influence of the initial void ratio on the stress-strain behaviour was too weak. Thus, the linear function has been replaced by a non-linear relation, allowing for a stronger gradient between two different void ratios and hence resulting in a more pronounced difference in stress-strain behaviour with respect to the initial state. Furthermore, the investigation revealed that the decrease in stiffness when approaching the bounding surface during loading was initiated too early, resulting in a very stretched out appearance of the peak in stress-strain space, which was not in accordance with experimental data. In order to remedy this problem, the distance dependent function in Eq. (2.55) has been replaced by the Manzari and Dafalias [MD97] formulation (Eq. (2.32)), extended by an additional exponent, fixed to 0.5.

Summing up all modifications, the new expression for h in Eq. (2.32) is as follows[2]:

---

[2]The void ratio dependent component is an exponential function with Euler's number as base and the void ratio in the exponent. The factor 3 in the exponent has performed well in various testing cases so that the constant value was kept instead of making it an additional material parameter. The same applies for the exponent in the stress dependent subfunction. If required, they can be adjusted in order to obtain a better fit with respect to the hardening behaviour for different initial states. See Sect. 4.2.2 for more information.

$$h = h_0 \cdot h_b = h_0 \cdot \left(\frac{\left| d^b \right|}{d^b_{ref} - \left| d^b \right|} \right)^{\frac{1}{2}} \cdot \exp\left(3(1-e) \right) \cdot \left(\frac{p_{at}}{p} \right)^{\frac{1}{2}} \qquad (3.9)$$

For the definition of the model surfaces in multiaxial stress space, the shape function $g(c,\theta)$ according to Argyris et al. [AFS$^+$74], cited as Eq. (2.25) in Sect. 2.1.1, has been used in the first model by Manzari and Dafalias [MD97]. In addition to the major alterations given in Sect. 2.2.1, Papadimitriou and Bouckovalas [PB02] had modified this shape function slightly to the following expression in order to improve the strength predictions for non-triaxial loading conditions:

$$g\left(c,\theta \right) = \frac{2c}{\frac{1+c}{2} - \frac{1-c}{2}\cos 3\theta} - \left(\frac{1+c}{2} + \frac{1-c}{2}\cos 3\theta \right) \qquad (3.10)$$

A third proposition was made by Krenk [Kre00]: starting from a cubic polynomial of the principal deviatoric stress components, his formulation describes a convex shape smoothly varying from triangular to circular as function of c and θ. The original formulation by Krenk [Kre00] has been reformulated in terms of the Lode angle by LeBlanc et al. [LHI08], resulting in a shape function $g(c,\theta)$ that is defined as:

$$g(c,\theta) = \frac{\cos\gamma}{\cos\left(\frac{1}{3}\arccos\left(\cos 3\gamma \cdot \cos 3\theta \right) \right)} \quad \text{with} \quad \gamma = \frac{\pi}{3} + \arctan\left(\frac{1-2c}{\sqrt{3}} \right)$$
$$(3.11)$$

Comparing all three approaches for different values of c as shown in Fig. 3.12 b reveals that the expressions give almost identical results for $c \approx 0.8 \ldots 1.0$. However, they increasingly deviate from each other for lower values, which corresponds to friction angles in extension considerably lower than in compression. All formulations meet in stress points of triaxial compression and extension, but give different solutions for non-triaxial loading conditions.

In Fig. 3.12 a the established failure criteria according to Mohr-Coulomb and Lade/Matsuoka-Nakai (LMN) are depicted for comparison, the latter being a formulation by Bardet [Bar90] unifying the mathematical expressions of Lade and Duncan [LD75] and Matsuoka and Nakai [MN74]. There is experimental evidence [e. g. KS68, PB69, SM69, LD73, YI79, YIV98] that the LMN criterion is a suitable choice for capturing the three-dimensional strength of sand. In contrast to Mohr-Coulomb, the LMN criterion accounts for the influence of the intermediate stress σ_2 on the soil strength. This way,
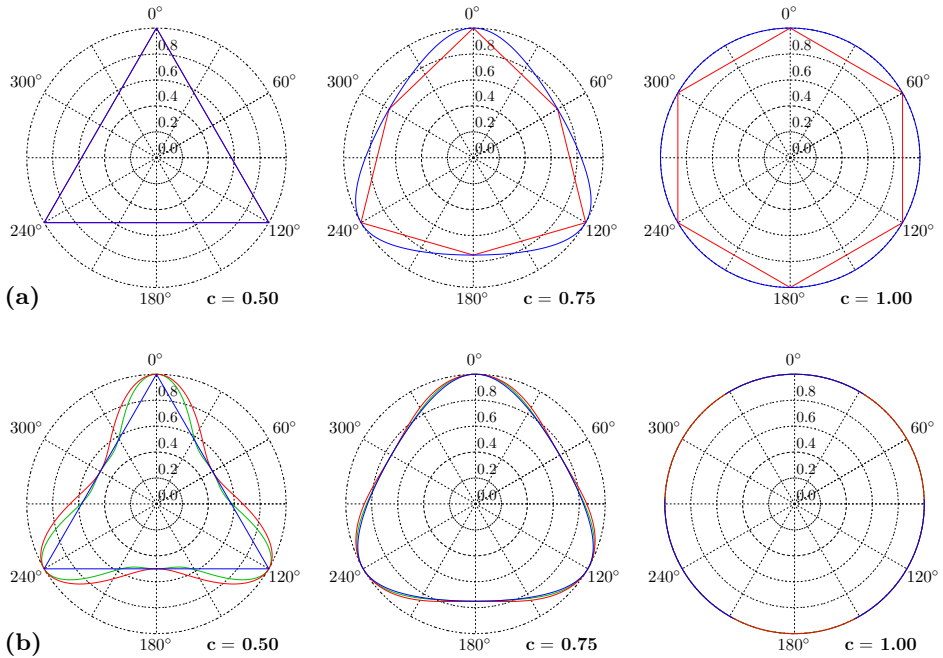
Figure 3.12: Shape functions $g(c,\theta)$ for varying c according to (a) Mohr-Coulomb ——, Lade/Matsuoka-Nakai (LMN) [Bar90] —— and (b) Argyris et al. [AFS$^+$74] ——, Papadimitriou and Bouckovalas [PB02] ——, Krenk [Kre00] ——

particularly under non-triaxial loading conditions, such as plane strain deformation cases, bearing capacity reserves neglected by Mohr-Coulomb can be exploited applying the LMN criterion.

In Fig. 3.13 failure points experimentally obtained under general stress conditions are given in terms of M_θ^b (varying with Lode angle θ) for three different sands [KS68, PB69, LD73]. The shape function by Krenk [Kre00] is geometrically very close to the LMN criterion and has hence been used (with an appropriate choice for c) to approximate the experimental data in Fig. 3.13. Since the mathematical expression according to Eq. (3.11) offers a continuous formulation over the full range of Lode angles, Krenk's proposal has been incorporated into the present version of bounding surface plasticity.
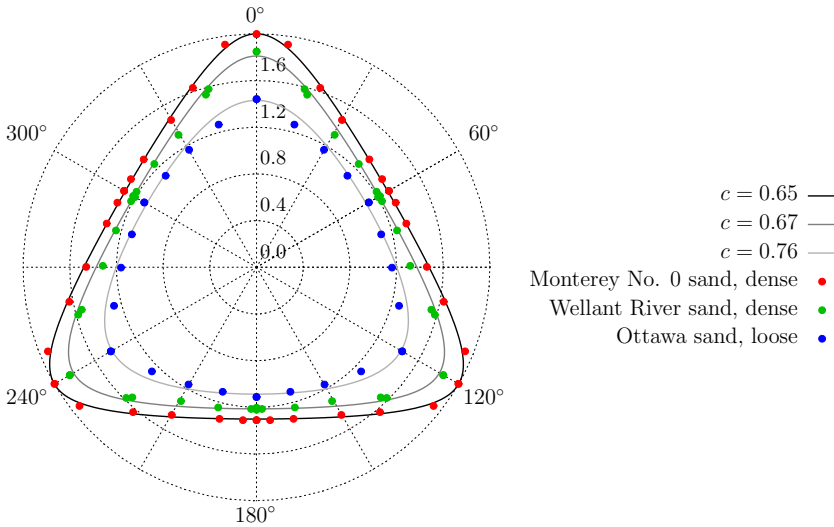
Figure 3.13: Experimental failure points M_θ^b of different sands (● , loose Ottawa sand [KS68], dense Wellant River sand [PB69], dense Monterey No. 0 sand [LD73]) and suitable Krenk failure surfaces (—) using different c

3.2.2 Dilatancy formulation

In the application of the basic bounding surface model it has been observed that the reproduction of drained and undrained triaxial test data causes problems, especially concerning the volumetric behaviour of sands. Simulating the volumetric response in drained triaxial tests on the three different sands introduced in Chap. 4, the range of properly depicted densities is rather narrow: loose states exhibit too little contraction, dense states do not react sufficiently dilative. Besides, in undrained triaxial tests the initial contractive phase of dense sands often shows a too high pore pressure development and consequently results in a too flat effective stress path (see also Sec. 5.1.2). This observation is often attributed to an overestimation of the contractant behaviour at small stress ratios, e.g. by Søreide [Sør03], Wehnert [Weh06], and Scharinger [Sch07].

Identifying the reason for this issue is not a trivial task to solve since the volumetric behaviour of a soil is influenced by different parts of the network of constitutive equations. In order to understand the scope of possible solutions, it is helpful to give a glance at the contributing elements of volumetric

strain, here in simplified triaxial stress space notation:

$$\dot{\varepsilon}_v = \dot{\varepsilon}_v^{el} + \dot{\varepsilon}_v^{pl} = \frac{\dot{p}}{K} + \lambda D = \frac{\dot{p}}{\frac{2}{3}\frac{1+\nu}{1-2\nu}G} + \frac{\dot{\eta}}{h\left(M^b - \eta\right)} \cdot A_d \left(M^d - \eta\right) \quad (3.12)$$

Due to the summation of elastic and plastic fractions there are two distinctly different directions of impact. On one side all parameters linked to the elastic bulk stiffness can be considered, on the other side the plastic contributions via hardening mechanism and dilatancy formulation play an important role. In this context it has to be taken into account that in drained soil behaviour the elastic deformations only matter in the very beginning of a loading path since they are dominated by plastic deformations afterwards, assuming elastoplastic behaviour. On the contrary, in undrained loading elastic and plastic strains are equally important since $\dot{\varepsilon}_v = \dot{\varepsilon}_v^{el} + \dot{\varepsilon}_v^{pl} = 0$.

The implications of changes in the constitutive equations are rather difficult to assess since the effects of stiffness and dilatancy are interrelated so that an uncoupled consideration is hardly possible. All eligible stiffness related modifications – elastic and plastic – are treated elsewhere. In the present section, the stress-dilatancy relationship of the basic bounding surface model and potentially expedient reformulations are analysed. In order to get access to the dilatancy mechanism, the underlying constitutive structure has to be clarified. Tsegaye [Tse14] has made a proposal for a general expression of the stress-dilatancy relationship based on Taylor's work hypothesis, which is a valuable starting point for further development of new dilatancy approaches. In the following, his essential idea is explained and a new formulation is derived.

The stress-dilatancy relation based on Taylor's work hypothesis and advanced by Roscoe and Schofield [RS63] to the Cam Clay dilatancy was derived in Sect. 2.4 and given in Eq. (2.67) as

$$D = \mu - \eta \quad (3.13)$$

This expression can be evaluated for the parameter μ at the point of constant volume deformation, where $D = 0$ (assuming that the elastic strain rates are sufficiently small), which actually corresponds to two distinct states: the phase transformation state and the critical state. In case of the latter, the result is obvious and yields $\mu = \eta_{cs} = \frac{6\sin\varphi_{cs}}{3\pm\sin\varphi_{cs}}$ – the stress ratio at critical state (for triaxial extension and compression, respectively). Concerning dense soils at phase transformation, when contraction turns into dilation, the soil body also deforms at constant volume momentarily. However, according to experimental observations [e. g. by BJ04], this transition

takes place at friction angles lower than the critical state friction angle, as shown in Fig. 2.17. Additionally, referring to triaxial stress space, indications are given that, in contrast to the critical state line, there is no intrinsic phase transformation line, hence the stress ratio μ is not a material constant. It is a parameter that depends on the critical state friction angle and state variables such as void ratio and effective confining pressure. This state dependence can be expressed by a state function $f_{sd} = f(e,p,\dots)$ as a scaling factor of the critical state friction angle according to the actual state. Incorporating it into μ yields a state modified critical state stress ratio

$$\overline{\mu} = \frac{6 f_{sd} \sin \varphi_{cs}}{3 \pm f_{sd} \sin \varphi_{cs}} \tag{3.14}$$

The requirement for the newly introduced state function is, that, when approaching critical state, it gives $f_{sd} = 1$, so that $\overline{\mu} = \eta_{cs}$. Instead of making it a function of different state variables, the state parameter ψ of Been and Jefferies [BJ85], which was introduced in Sect. 2.1.1, can be used directly, so that $f_{sd} = f(\psi)$.

Applying this general principle to bounding surface plasticity, the state dependent critical state stress ratio $\overline{\mu}$ translates into the dilatancy parameter M^d, which quantifies the opening of the dilatancy surface as a function of the state. Consequently, the stress-dilatancy relationship of Eq. (3.13) can be modified to

$$D = \overline{\mu} - \eta = M^d - \eta = \frac{6 f_{sd} \sin \varphi_{cs}}{3 \pm f_{sd} \sin \varphi_{cs}} - \frac{6 \sin \varphi_m}{3 \pm \sin \varphi_m} \tag{3.15}$$

which, in its general form, strongly resembles the bounding surface dilatancy expression (Eq. (2.6)). Whereas the presented basic bounding surface models use stress-dilatancy relations with a linearised or an exponential modification of the critical state stress ratio,

$$D = \sqrt{\frac{2}{3}} A_d \left(M^d - \eta \right) \quad \text{with} \tag{3.16}$$

$$\text{Manzari and Dafalias [MD97]:} \quad M^d = M^c + k_d \cdot \psi \tag{3.17}$$
$$\text{Li and Dafalias [LD00]:} \quad M^d = M^c \cdot \exp(m_d \cdot \psi) \tag{3.18}$$

the new proposal for the dilatancy parameter

$$M^d = \frac{6 f_{sd} \sin \varphi_{cs}}{3 \pm f_{sd} \sin \varphi_{cs}} \tag{3.19}$$

incorporates the state dependence in the form of an adaptable state function as direct modification of (the sine of) the critical state angle instead. The difference in the resulting dilatancy ratio is rather minor, but the derivation of the underlying theory is more straightforward and hence more consistent with regard to adaptations. Furthermore, the basic implementation contains an additional parameter A_d as a (constant) prefactor for scaling the dilatancy ratio. This offers the opportunity for incorporating further dependences on state variables or other influencing parameters into the stress-dilatancy relationship.

In literature, there are several approaches for possible state functions fulfilling the mentioned requirements. A selection, which will be analysed hereafter, is the following:

$$\text{Li and Dafalias [LD00]:} \quad f_{sd}^{LD} = \exp(m_{LD} \cdot \psi) \tag{3.20}$$

$$\text{Wan and Guo [WG98]:} \quad f_{sd}^{WG} = \left(1 + \frac{\psi}{e_{cs}}\right)^{\beta_{WG}} = \left(\frac{e}{e_{cs}}\right)^{\beta_{WG}} \tag{3.21}$$

$$\text{Gudehus [Gud96], Bauer [Bau96]:} \quad f_{sd}^{GB} = \left(1 + \frac{\psi}{e_c - e_d}\right)^{\beta_{GB}}$$

$$= \left(\frac{e - e_d}{e_c - e_d}\right)^{\beta_{GB}} \tag{3.22}$$

where e_{cs} is the mean effective stress dependent critical state void ratio according to Eq. (3.7) and e_c and e_d are the critical state and minimum void ratio, respectively, according to a common dependence after Gudehus [Gud96]:

$$e_x = e_{x0} \cdot \exp\left(-\left(\frac{3p}{h_s}\right)^n\right) \qquad x = c,d \qquad e_{x0}, h_s, n \ldots \text{material constants} \tag{3.23}$$

Consequently, the Gudehus - Bauer formula also includes a dilatancy limit for maximum densification since $f_{sd} = M^d = 0$ for $e = e_d$. The three expressions for state functions are unified by the fact that they deliver a dilatancy parameter M^d larger than 1 as the soil is in a loose state ($\psi > 0$) and a value less than one if the soil is dense ($\psi < 0$). Finally, when the state converges critical state ($\psi \to 0$), on the contractive side f_{sd} decreases to unity and on the dilative side it increases to unity. Figure 3.14 presents

the general run of the three state functions with evolving state parameter. The curves are based on the simulations of a drained triaxial test on loose and dense sand, respectively, shown in Fig. 3.1 in Sect. 3.1.2, using an exemplary choice of parameters for the back-calculation of $f_{sd}{}^3$. As can be seen, the overall trend is very similar and it is mostly the inclination of the curves that can be influenced by modification of the parameters.

In order to understand the potential for improvement of the present dilatancy formulation, it is useful to look at Fig. 3.15. It shows the curves for dilatancy parameter M^d resulting from two different state functions and additionally the evolution of the deviatoric stress ratio η. The filled areas illustrate the difference between a M^d-graph (exemplary for the Li and Dafalias state function) and the η-curve as measure for dilatancy. The initially mentioned issue of finding an appropriate set of dilatancy parameters for a wide range of void ratios is difficult to rectify, if only the inclination of
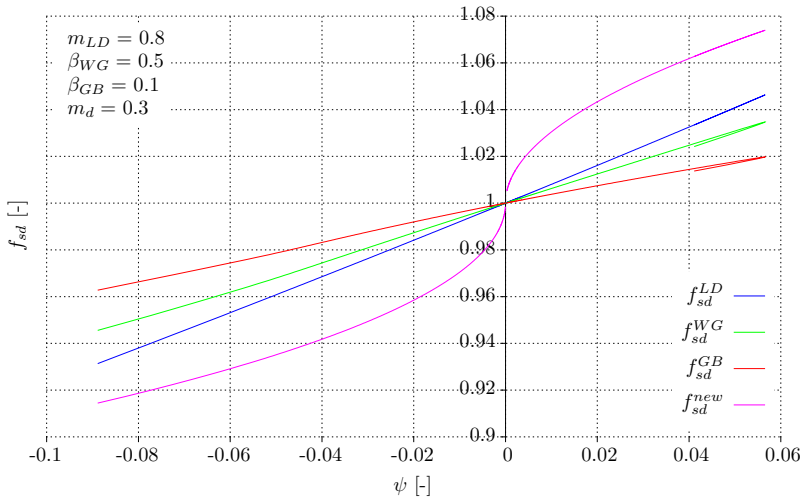
Figure 3.14: Back-calculation of the state functions f_{sd} according to Eqs. (3.20) to (3.22) and (3.24)

---

[3]For the back-calculation of the state function f_{sd}^{GB} in the example in Fig. 3.14, e_c has been replaced by e_{cs} in order to be consistent with the computation of the state parameter ψ. Consequently, only e_d follows the dependence by Gudehus (Eq. (3.23)). Furthermore, elastic strains are neglected in the back-calculation, since it is based on total strains. Hence potential initial effects caused by the dominating elastic deformational contribution are not visible in this representation of the state function.
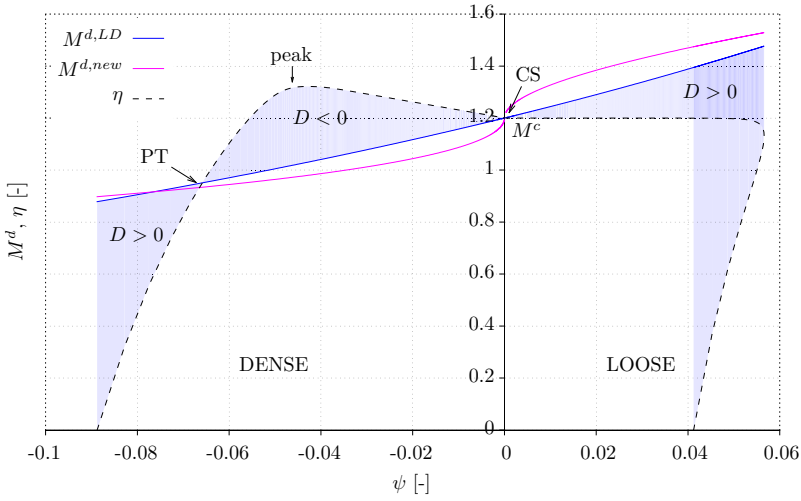
Figure 3.15: Evolution of the deviatoric stress ratios η and M^d with ψ according to the state functions in Eqs. (3.20) and (3.24)

the M^d-line can be altered. This might increase the contractancy for loose states but by experience the simultaneous increase in dilatancy is not sufficiently intense. A new proposal for a state function resembles the expression given by Li et al. [LDW99]:

$$f_{sd}^{new} = \exp\left(m_d \cdot \operatorname{sgn}\psi \cdot \sqrt{|\psi|} \right) \tag{3.24}$$

Compared to the other state functions introduced, this formulation assumes a stronger non-linearity by taking the square root of ψ. Alternatively, replacing the square root by a variable exponent as in Li et al. [LDW99] increases the flexibility in the shape of the state function, but adds one more parameter to determine. The new mathematical expression allows for more contractant and more dilatant volumetric responses. This effect is illustrated by comparative simulations for different initial states in Fig. 3.16. The respective parameters have been chosen so that the resulting initial contractancy on the dense side is the same for both state functions. The evolution of M^d and η for both state functions in analogy to the schematic diagram in Fig. 3.15 is shown in subfigure a. The corresponding axial and volumetric strains are depicted in subfigure b, indicating that the new formulation allows for stronger dilatancy and contractancy, resulting in a slightly stronger spreading of the ε_1-ε_v curves.
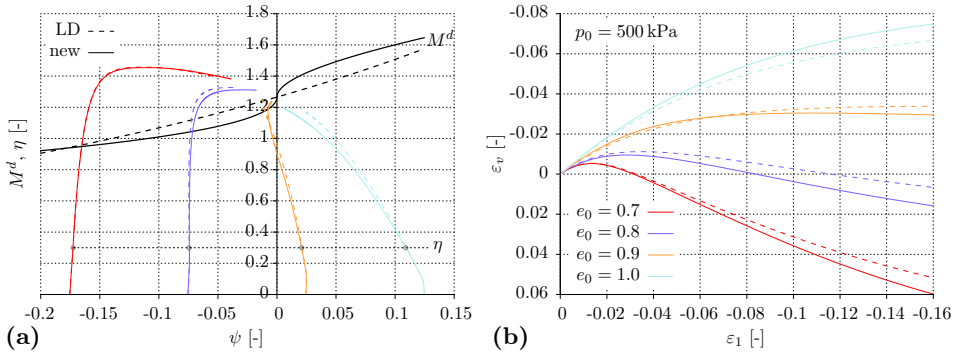
Figure 3.16: Triaxial compression tests ($p_0 = 500\,\text{kPa}$) of different initial void ratios e_0 applying two different state functions (f_{sd}^{new} ——, f_{sd}^{LD} ·····): (a) evolution of M^d (black) and η (coloured lines) with ψ, (b) strain evolution ε_1-ε_v

The feature of a compaction limit included in the Gudehus-Bauer dependence, preventing the soil from undercutting a defined minimum void ratio in contractant shearing, is not incorporated in the newly proposed dilatancy formulation. It is accounted for by an additional factor in the hardening law instead (see 3.2.5), which basically has a similar effect on the soil response.

The introduction of a state function also offers a straightforward opportunity to incorporate further dependences on other state variables or material parameters into the stress-dilatancy relationship. In addition to that, looking at Eq. (3.16), an alternative way for controlling the dilatancy ratio in a similar fashion as above is to make the scaling Li and Dafalias constant A_d function of the state. In contrast to the previous mechanism, this would change the dilatancy ratio by simply scaling the distance measure instead of modifying the distance itself through manipulation of the dilatancy surface according to the state. This offers a simple mean to remedy the mentioned problem of too high contractancy at low mobilisation levels: making the prefactor A_d a stress dependent parameter can serve for downscaling the initial contractancy. Following the proposal of Søreide [Sør03] a possible expression for A_d could be:

$$A_d = A_0 \left(\frac{\eta}{M^b} \right)^{\mu} \tag{3.25}$$

With this approach, the dilatancy ratio is scaled by a value interpolated between 0, at the start of a triaxial test when $\eta = 0$, and A_0, at the peak

and critical state when $\eta = M^b(= M^c)$. For a non-linear influence the exponent μ can be chosen to be a constant larger than 0: the higher μ the more long-ranging the downscaling effect on the dilatancy ratio. The exponent could even be made a function of other state variables.

Attention has to be drawn to the fact that the described contractancy issue concerns the beginning of stress paths only so that one has to be careful with overestimating potential initial effects. They might be due to deficiencies in the experimental set-up or a disregarded influence of the soil structure caused by the previous loading history, which is either unknown or cannot be taken into account by the present type of soil model. Thus, the proposed expression for the dilatancy parameter A_d is a rather inelegant way to get a grip on unappealing side effects in order to improve the congruence of experimental and simulated data. Admittedly, it does not solve the underlying problem of a lack of fabric tensor (or something related) in order to capture the structural redistributions. Models exist that include fabric tensors as mentioned in Sect. 2.4, but a still not fully solved question is the appropriate initiation of such a tensor (due to the lack of micromechanical foundation). This concern, however, is decisive for the final result and the reasonableness of a constitutive ingredient increasing the model's complexity in such an extent.

The multiaxial counterpart of the triaxial formulation of the new dilatancy approach follows the scheme introduced in Sect. 2.1.1. Hence, Eq. (2.34) becomes

$$D = A_d \left(\boldsymbol{\alpha^d} - \boldsymbol{r} \right) \cdot \boldsymbol{n} \quad \text{with} \quad \boldsymbol{\alpha^d} = \sqrt{\frac{2}{3}} \cdot g(\theta,c) \cdot M^d \cdot \boldsymbol{n} \qquad (3.26)$$

Using the actual deviatoric stress ratio tensor $\boldsymbol{r}$ instead of the back stress tensor $\boldsymbol{\alpha}$ is not a necessity but seems more straightforward. $\boldsymbol{r}$ is usually used in bounding surface models that apply a vanished elastic region (e. g. Wang et al. [WDS90], Andrianopoulos et al. [APB05]). Because of the likeness of both tensors due to the generally very small elastic domain in case of granular materials (also with regard to the incorporated small strain stiffness treated in one of the following sections), they are basically interchangeable without major impact on the result.

3.2.3   Cap yield surface

In contrast to the original bounding surface model according to Manzari and Dafalias [MD97], as described in Sect. 2.1.1, the present version con-

sists of not only one yield surface in the shape of a cone but also of a second surface limiting the elastic region in the compression domain: a cap surface. The intention is straightforward and can be found in the deficiency of the original model to correctly reproduce for example isotropic or one-dimensional (oedometer) compression tests. Generally speaking, it is the family of stress paths that does not include any changes in the deviatoric stress ratio η throughout the loading process. This type of stress path is also called proportional stress path and is characterised by constant ratios of the principal stresses ($\sigma_1 : \sigma_2 : \sigma_3 = $ const.) according to Goldscheider [Gol76]. Consequently, in case of an open cone, the stress path evolves merely within the elastic region, not causing any hardening with respect to the conical yield surface in terms of deviatoric back stress. Hence, no plastic strains are induced – the soil body reacts purely elastically.

This simulated behaviour is not in accordance with experimental observations. In geotechnical applications, there are two cases where permanent deformations of non-negligible extent occur in constant stress ratio loading. On the one hand, very loose sands exhibit plastic volumetric strains when being loaded at medium stress levels. On the other hand, if sand (independent of its density) is loaded up to very high pressures, grain crushing is initiated and accompanied by volumetric (and deviatoric) deformations. These loading cases might occur near the base of high earth dams, in deep mine shafts or tunnels (up to 7 MPa) and reach up to 350 MPa under the tips of deep-driven pile foundations, e. g. for offshore constructions [YBL96]. In order to ensure the development of irreversible strains even in loading at constant stress ratios an additional constitutive ingredient is required: a complementing yield surface that caps the elastic domain and hence causes plastic strains to emerge if the yield condition is violated.

There are different strategies that were followed in previous modelling attempts. The most common approach is to define a second yield surface, often called cap, as done for example in the double hardening model by Vermeer [Ver78] or in the bounding surface model by Wang et al. [WDS90]. This results in two independent yield surfaces with separate parameters defining their shapes, and rules for controlling their evolution. As long as only one surface is activated by a loading event, the hardening mechanisms work completely independently. This is a decisive advantage, because it allows the two sets of surface parameters to be calibrated independently from one another, i. e. with triaxial test data in case of the cone and for example with the results of an isotropic compression test in case of the cap. The
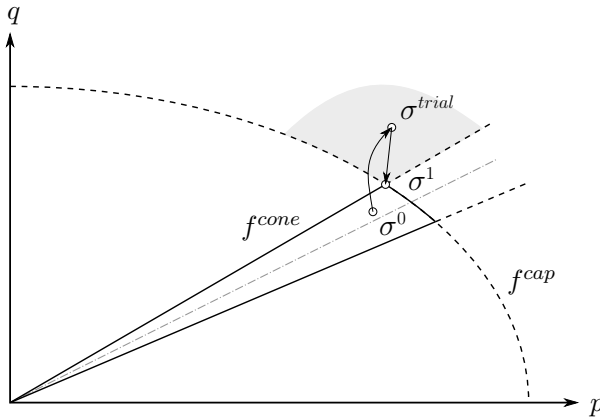
Figure 3.17: Corner region at the intersection of cone and cap yield surface

challenge is to handle loading cases, where the elastic trial stress ends up
in the exterior corner enclosed by the two surfaces (see Fig. 3.17). There
are numerical schemes for dealing with this corner problem, for example
developed by de Borst [dBor87], which is based on Koiter's rule [Koi53] and
will be presented in detail in Chap. 4.

As the "two yield surface approach" necessitates a higher complexity of
implementation, a second strategy is to replace the open cone by a single
yield surface with a closed formulation without discontinuities. Taiebat and
Dafalias [TD08] included a modified eight-curve equation into their version
of bounding surface model (see Sect. 2.2.2), which basically resembles the
open cone, but is closed in the p-direction (Fig. 2.8). The mathematical
formulation of this kind of surface is more intricate, so that the provision of
potentially required higher order derivatives in case of implicit integration
schemes may cause difficulties. Nevertheless, the numerical treatment of
corner problems is omitted.

Another restriction of a closed surface is the interrelation of hardening me-
chanisms in shear and compression that is difficult to control. There is no
clear attribution of loading type to a corresponding yield surface, so that for
example the "compression part" of the surface often hardens although the
soil is predominantly stressed in shear. In case of the SANISAND model by
Taiebat and Dafalias [TD08], this issue is encountered by making the plas-
tic potential dependent on the type of loading ($\eta = $ const. or $\eta \neq $ const.)
and hence reduce the hardening of the uninvolved part of the surface to a
minimum.

As the aim of this model is to meet the requirements of engineering practice, the two parted yield surface was chosen. The advantage of calibrating the yield surfaces independently with two corresponding types of laboratory tests is considered to be more straightforward and easier to handle and comprehend by a geotechnical engineer in routine design. The detailed calibration procedure will be discussed in Sect. 4.2. The incorporated cap surface is depicted in p-q space and multiaxial stress space in Fig. 3.18. In the following its mathematical formulation as well as the associated hardening law are explained.

(a)   **(b)**
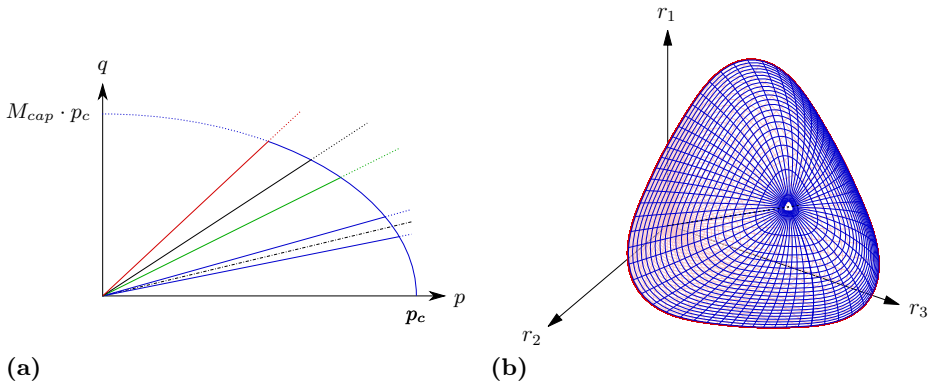
Figure 3.18: Model surfaces including the cap yield surface: (a) in p-q space and (b) in multiaxial stress space ($\boldsymbol{r}$ space)

The equation for describing the cap in triaxial stress space is

$$f^{cap} = \frac{q^2}{M_{cap}^2} + p^2 - p_c^2 = 0 \tag{3.27}$$

and in multiaxial stress space the following expression can be used alternatively:

$$f^{cap} = \frac{3}{2}\frac{\boldsymbol{s} \cdot \boldsymbol{s}}{M_{cap}^2} + p^2 - p_c^2 = 0 \tag{3.28}$$

This formulation corresponds to the cap yield surface also used by the so called hardening soil model according to Schanz et al. [SVB99] and geometrically describes an ellipse centred at the origin. Reformulating Eq. (3.27) in its canonical form

$$\frac{q^2}{M_{cap}^2 \cdot p_c^2} + \frac{p^2}{p_c^2} = 1 \tag{3.29}$$

allows to directly extract the major and minor semiaxes of the surface (see also Fig. 3.18 a): the intersection with the p-axis is specified by p_c, an internal variable that traces the isotropic pre-consolidation pressure[4]. $M_{cap} \cdot p_c$ determines the intersection of the surface with the q-axis and consequently the cap parameter M_{cap} controls the ellipse's steepness.

The variation of p_c is the constitutive ingredient that reflects the hardening process of the cap yield surface. By defining an isotropic pre-consolidation stress larger than the initial isotropic stress, an overconsolidated state can be simulated. In contrast to the kinematically hardening cone, the cap surface hardens isotropically, p_c defining its size. Therefore, with respect to compressive stress paths (or generally $\eta = \text{const.}$), unloading from a certain stress level will always result in purely elastic strains. The same applies to a reloading branch up to the previous maximum load: since the cap surface can only expand isotropically (no translation or rotation in stress space) and does not include any softening mechanism that would allow for the contraction of the surface, the loading from a stress state inside the elastic domain up to its border does not create any plastic deformation.

The cap surface is associative, which means, that the corresponding plastic potential equals the cap surface definition, $g^{cap} = f^{cap}$, and consequently, the vector of plastic strains is unidirectional with the normal to the yield surface.

The parameter M_{cap} is chosen to be a function of several state parameters allowing the yield surface and plastic potential to adapt to the current state. The motivation for this mechanism is the aim of simulating oedometer tests correctly by producing a stress path with an inclination according to the predefined K_0-value. The underlying concept is based on a one-dimensional compression test with confined lateral strains ($\dot{\varepsilon}_2 = \dot{\varepsilon}_3 = 0$), where the violation of the cap by a stress increment $\dot{\sigma}_1$ causes an elastoplastic strain increment $\dot{\varepsilon}_1$, accompanied by the hardening of the surface through a corresponding increase in pre-consolidation pressure. The stress state inside the oedometer cell can be described by the applied vertical load and the radial stress arising from the lateral confinement, which is assumed to be linked

---

[4]In isotropic compression p_c reflects the largest mean stress the soil has experienced in its loading history. If, however, the cap hardens due to non-isotropic loading, the actual mean stress p is less than the updated p_c of the cap, quantifying the cap's new geometrical extent. In this case p_c should rather be considered an "equivalent isotropic pre-consolidation stress".

to the vertical stress component by the lateral earth pressure coefficient at rest ($\sigma_3 = K_0\sigma_1$). The latter correlation ensures the appropriate inclination of the simulated stress path. In addition, the incremental loading process is characterised by the two stress dependent stiffness quantities E (elastic Young's modulus) and E_{oed} (elastoplastic oedometer stiffness) as well as the Poisson's ratio ν. In analogy to the triaxial stiffness quantities the stress dependence of the oedometric modulus E_{oed} follows a power law[5], but the mean stress is replaced by the axial stress. As proposed by Janbu [Jan63], the so called modulus number, which scales the stress dependency, is not a constant but represents the soil's stress-strain history. Thus, an additional void ratio dependence is included, but the rational function used in shear related stiffness moduli (e.g. Eq. (3.5)) is exchanged by an exponential term in order to increase the non-linearity of stiffness with respect to the soil's density. This is supported by experimental findings, summarised for example by Janbu [Jan63] or Hornig [Hor11]. The resulting expression for the oedometric stiffness is:

$$E_{oed} = E_{oed}^{ref} \cdot \left(\frac{e}{e+1}\right)^{-n_{oed}} \cdot \left(\frac{\sigma_1'}{p^{ref}}\right)^{m_{oed}} \tag{3.30}$$

The evaluation of an elastoplastic load step from the actual stress state results in the following expression for the modified cap parameter[6]:

$$M_{cap} = \frac{3}{\sqrt{2}}\sqrt{\frac{(E - E_{oed} \cdot (1 + 2K_0) \cdot (1 - 2\nu)) \cdot (1 - K_0)}{(E - E_{oed} \cdot (1 - K_0) \cdot (1 + \nu)) \cdot (1 + 2K_0)}} \tag{3.31}$$

A rather small user input for K_0 leads to large M_{cap}-values, inducing a steep cap. If on the contrary, the choice for K_0 is comparably large, the resulting M_{cap}-value will be smaller, so that the cap is flatter and more pointed around the p-axis.

---

[5]One-dimensional compression (with lateral confinement) has been first investigated with the oedometer test apparatus developed by von Terzaghi [vTer25]. In his consolidation theory [vTer25, vTer43, vTPM96] he related the ratio of void ratio change Δe and applied stress increment $\Delta \ln \sigma_1$ in primary consolidation to the compression index C_c. Alternatively, the observed soil stiffness $\frac{\Delta\sigma_1}{\Delta\varepsilon_1}$ can be quantified by the oedometer modulus E_{oed}, which can be reformulated in terms of Terzaghi's compression index as $E_{oed} = \frac{1+e_0}{C_c}\sigma_1$, resulting in a linear function of the axial stress. Ohde [Ohd39] (and later Janbu [Jan63]), however, proposed a power law of the form $E_{oed} \propto \sigma_1^w$, which is applied here.

[6]The complete derivation of this formula can be found in App. A.5.

Based on the plastic deformations, the change in the hardening variable p_c is derived via the hardening rule associated to the cap surface:

$$\dot{p}_c = \lambda \cdot H^{cap} \cdot \left[\frac{\partial g^{cap}}{\partial p}\right]_{cap} = \lambda \cdot H^{cap} \cdot \left[\frac{\partial f^{cap}}{\partial p}\right]_{cap} = \lambda \cdot H^{cap} \cdot 2p \quad (3.32)$$

The formula for the hardening modulus H^{cap} established for the present model accounts for the interaction of both yield surfaces and the resulting corner problem already mentioned in the context of numerical integration. It was stated before, that loading cases involving only one yield surface are rather easy to handle. But as soon as the stress increment activates both surfaces, plastic strains are contributed by each. Consider a triaxial compression test starting from an isotropic stress state equal to the pre-consolidation pressure p_c (i. e. normally consolidated). Provided that the first load step is large enough to surpass the elastic limit of the slim cone, it will already cause the violation of both, cap and cone. Consequently, the resulting irreversible deformation will be composed of two contributions and hence the overall reaction will be rather soft – softer than experimental observations for sand might justify. That means, that in contrast to the model concept, there are indications that shear loading including a variation in deviatoric stress ratio ($\eta \neq$ const.) obviously causes only the cone to harden and leaves the cap surface more or less unchanged. More precisely, as opposed to the cone, the cap does not produce any deformation when hardening as a consequence of violation. A conceivable remedy to solve this problem is to adjust the hardening rule of the cap depending on the type of loading in terms of deviatoric stress ratio rate:

$$H^{cap} = H_0^{cap} \cdot h\left(\dot{\eta}\right) \quad (3.33)$$

If $\dot{\eta} = 0$, the cap hardening modulus is calculated according to the "normal" state dependent relationship to be defined in the following as H_0^{cap}. If on the contrary $\dot{\eta} \neq 0$, the hardening modulus (and hence the plastic stiffness attributed to the cap) is artificially increased to a very high value, so that the cap surface delivers basically no plastic strains. This could be realised by some sort of step function, which would however introduce numerically disagreeable discontinuities. An alternative approach is an exponential function of the form $f(\dot{\eta}) = \exp(-V\dot{\eta})$, with V being an arbitrary large number (e. g. 1000), so that $f(\dot{\eta}) = 1$ in case of constant stress ratio loading ($\dot{\eta} = 0$) and $f(\dot{\eta}) \approx 0$ in shear loading ($\dot{\eta} \neq 0$). One possible expression fulfilling these requirements is

$$h\left(\dot{\eta}\right) = C^{\alpha} \quad \text{with} \quad \alpha = 1 - \exp(-V\left|\dot{\eta}\right|) \quad (3.34)$$

The advantage of this formulation lies in the fact that the extreme value of the final factor scaling the hardening modulus does not tend to infinity in case of $\dot{\eta} \neq 0$, but takes values between zero and a defined large number C (numerical default parameter).

Following the proposed strategy, the results for isotropic compression and general constant stress ratio paths will meet the expectations, but oedometer tests cause problems. These tests follow so called proportional strain paths, featuring constant rates of the principal values $\varepsilon_1 : \varepsilon_2 : \varepsilon_3$ (oedometric loading: $1 : 0 : 0$). According to Goldscheider [Gol76], when starting from a stress-free state, proportional strain paths lead to proportional stress paths, and hence also require the activation of the cap. However, the resulting stress paths do not describe a perfectly straight line in numerical simulations, but rather a curve that evolves towards the desired inclination ($\dot{\eta} \approx 0$)[7]. The consequence is that even small deviations from $\dot{\eta} = 0$ will cause the cap's hardening modulus to be increased considerably and hence there will be hardly any deformation contributed from the cap. If, in addition, the perturbations are small enough that the stress path does not violate the slim cone yield surface, the overall strain response will be almost elastic and therefore too stiff.

In order to overcome this issue, Eq. (3.34) is extended by introducing a second factor similar to α:

$$h\left(\dot{\eta}, \dot{\varepsilon}_p, \dot{\varepsilon}_q\right) = C^{\alpha \cdot \beta} \quad \text{with} \quad \beta = 1 - \exp(-V \left| \Delta \frac{\dot{\varepsilon}_p}{\dot{\varepsilon}_q + a} \right|) \qquad (3.35)$$

The new factor contains the change of the ratio $\dot{\varepsilon}_p / \dot{\varepsilon}_q$ from one loading step to the next. The parameter a is just an auxiliary quantity of very small size (e.g. 10^{-10}) in order to prevent infinity in case of $\dot{\varepsilon}_q = 0$. In all kinds of constant stress ratio paths as well as in drained triaxial loading, the ratio itself takes values different from 0, but only in the latter case there is a variation of this ratio throughout the loading process, so that $\beta = 1$. From this follows, that for any proportional strain path test (such as an oedometer test) $h\left(\dot{\eta}, \dot{\varepsilon}_p, \dot{\varepsilon}_q\right) = C^{1 \cdot 0} = 1$ and consequently, the cap will

---

[7]This is mainly due to inaccuracies in the M_{cap} calculation (originating from error tolerances), which assumes the same value for M_{cap} when referring to the initial and the final state of the calculation step, respectively (see App. A.5). The error vanishes if the step size tends to zero, but under usual conditions and without expensive numerical stabilisation measures the error cannot be avoided.

contribute to the irreversible deformations as for the other constant stress ratio types of loading.

One last aspect has to be considered in this context. If one considers an undrained triaxial test ($\dot{\varepsilon}_p = 0$), so far h will give the same (low) cap stiffness as in an oedometer test, since $\Delta \frac{\dot{\varepsilon}_p}{\dot{\varepsilon}_q + a} = 0$ in both cases. Consequently, along with the activated cone the model reacts too softly. To remedy this issue, a third factor completes the formulation of Eq. (3.35):

$$h\left(\dot{\eta}, \dot{\varepsilon}_p, \dot{\varepsilon}_q\right) = C^{\alpha \cdot (\beta + \gamma)} \quad \text{with} \quad \gamma = \exp(-V\left|\dot{\varepsilon}_p\right|) \qquad (3.36)$$

Introducing the rate of volumetric strains (elastic and plastic!), which is zero only in the mentioned undrained triaxial loading case, makes sure that $h\left(\dot{\eta}, \dot{\varepsilon}_p, \dot{\varepsilon}_q\right) = C^{1 \cdot (0+1)} = C$ and consequently the cap will be sufficiently stiff.

Having explained the working principle of the function $h\left(\dot{\eta}, \dot{\varepsilon}_p, \dot{\varepsilon}_q\right)$, Table 3.1 gives an overview of the values it takes depending on the type of loading.

One could have considered limiting the factor h to a dependency of the stress ratio rate and making it less sensitive to perturbations (for example by choosing a lower value for V). This would however imply that for load steps of very small stress ratio rates, e. g. in triaxial loading if the step size is chosen to be very small, the cap delivers deformations. The additional consideration of strain rates allows for a more precise control of the cap contribution according to the loading type.

Having ensured that only constant stress ratio loadings (including oedometer tests) will cause the cap to produce non-negligible plastic strains, the missing link for completing the cap hardening modulus formulation is the definition of the factor H_0^{cap} representing the physical basis of the cap stiffness. One possibility is to apply the relationship having been used by

Table 3.1: Cap mechanism for different loading cases

	$\dot{\eta}$	α	$\Delta \frac{\dot{\varepsilon}_p}{\dot{\varepsilon}_q + a}$	β	$\dot{\varepsilon}_p$	γ	$h\left(\dot{\eta}, \dot{\varepsilon}_p, \dot{\varepsilon}_q\right)$
ISO	$= 0$	0	$= 0$	0	$\neq 0$	0	$C^{0 \cdot (0+0)} = 1$
η-const.	$= 0$	0	$\neq 0^*$	1	$\neq 0$	0	$C^{0 \cdot (1+0)} = 1$
OED	$\neq 0^*$	1	$= 0$	0	$\neq 0$	0	$C^{1 \cdot (0+0)} = 1$
TXD	$\neq 0$	1	$\neq 0$	1	$\neq 0$	0	$C^{1 \cdot (1+0)} = C$
TXU	$\neq 0$	1	$= 0$	0	$= 0$	1	$C^{1 \cdot (0+1)} = C$

* takes values close to zero

Taiebat and Dafalias [TD08] in their version of bounding surface plasticity, which is based on the concept of the limiting compression curve (LCC) by Pestana and Whittle [PW99] and described in detail in Sect. 2.2.2 (Eq. (2.54)). Since the elastic moduli are defined slightly differently in the present model (see Sect. 3.2.1) compared to the SANISAND formulation by Taiebat and Dafalias [TD08], their equation for H_0^{cap} has been altered as follows:

$$H_0^{cap} = \frac{1}{\frac{e}{p(1+e)}\rho_c - \frac{1}{K}} \cdot \frac{1}{1 - \text{sgn}(\delta)\,|\delta|^\omega} \quad \text{with} \quad \delta = 1 - \frac{p}{p_r \cdot e^{-\frac{1}{\rho_c}} \cdot \frac{\boldsymbol{\alpha^c \cdot \alpha^c}}{\boldsymbol{\alpha^c \cdot \alpha^c} + 2\boldsymbol{r \cdot r}}}$$

$$(3.37)$$

The bulk modulus K is derived from the shear modulus G according to Eqs. (3.5) and (3.6), hence it is a function of the actual state with respect to stress and density. In the original formula (Eq. (2.54)), p was substituted by p_0, the current pre-consolidation pressure, which was due to the peculiar shape function of the yield surface of the SANISAND model. Since there is no necessity any longer, the actual mean pressure p returned in Eq. (3.37).

Similarly as in case of the cone hardening modulus H^{cone}, Eq. (3.37) can be split into three influences: a void ratio and mean stress dependence as well as a factor, that reflects the distance of the actual state to the LCC and the impact of the size of the (constant) stress ratio on the cap stiffness. From this expression it can be deduced that, if the cap is activated, the soil response becomes stiffer with decreasing void ratio or with an increase in mean pressure. Besides, the stronger the inclination of a constant stress ratio path in p-q space and hence the larger the deviatoric stress component, the smaller the cap hardening modulus. Consequently, an oedometer test will effect more deformations than an isotropic compression test, which is in accordance with experimental observations.

Looking closely at a simulated oedometer stress path using the above hardening modulus, one can observe that the stress path is actually not a perfect straight line and hence the deviatoric stress ratio is not constant. Consequently, the cone yield surface is activated as well and contributes to the overall deformation, albeit marginally. In addition, the stress path's mean inclination roughly reflects the provided K_0-value, but does not reproduce it very well. In order to remedy these deficiencies the hardening rule needs to be aligned with the assumptions underlying the derivation of M_{cap}, so

that an alternative hardening modulus H_0^{cap} is obtained as[8]:

$$H_0^{cap} = \frac{\sqrt{\left(\frac{1-K_0}{M_{cap}}\right)^2 + \left(\frac{1+2K_0}{3}\right)^2} \cdot E_{oed} \cdot E}{E - (1+2K_0)(1-2\nu) \cdot E_{oed}} \qquad (3.38)$$

In contrast to the previous hardening modulus expression following the LCC concept, the advantage of this formulation is the correct capture of an oedometric stress path with a constant inclination of η_{K_0}, which is a function of the user-defined K_0:

$$\eta_{K_0} = 3\frac{1-K_0}{1+2K_0} \qquad (3.39)$$

Along these lines, running a triaxial test with a predefined stress path inclination of η_{K_0} by controlling σ_1 and σ_3 accordingly, will automatically result in zero lateral strains and hence $\varepsilon_v = \varepsilon_1$, reflecting oedometric loading conditions.

For the further development of the model, the proper simulation of oedometric loading conditions in terms of stress path inclination and strain evolution was preferred. With the definition of the well-established elastoplastic oedometric stiffness E_{oed} [e. g. Ohd39, Jan63, SVB99] and a smooth stress path calculation the cap can be easily calibrated. In addition, the qualitatively and quantitatively satisfactory reproduction of the oedometric soil response seems more important to the author than isotropic loading conditions, since the former stress state is more relevant in the geotechnical context. Aside from that, the experimental foundation the LCC concept is based upon is rather weak. It is hence worth challenging the more complex LCC hardening mechanism, if the simpler alternative has not proven to be severely deficient. Furthermore, the stress-strain evolution at very high compressive stresses, where the M_{cap}-mechanism is most likely to deviate noticeably from real soil behaviour, is secondary for most geotechnical applications.

The newly introduced cap and the mechanisms for controlling its impact on the overall deformation allow for modelling not only the typical triaxial loading situations, where shear dominates the loading process, but also enables

---

[8]The complete derivation of this formula can be found in App. A.5.

the bounding surface model to produce plastic strains with respect to prevailing compression. Whenever a soil element's history beneath the surface level is considered, it is likely to be anisotropically consolidated – it concerns mostly K_0-consolidation, since lateral deformations can be considered as being constrained. Thus, in geotechnical problems where consolidation cases are concerned or where stresses are assumed to act isotropically on the soil body and loading reaches a certain level of stress, so that the occurrence of plastic deformations is to be taken into account, the cap extension is a valuable constitutive ingredient enriching the bounding surface concept.

3.2.4   Small strain stiffness mechanism

In advanced elastoplastic material models the non-linearity of soil stiffness is a characteristic respected within the model formulation. In the first place, it is the transition from elastic to plastic behaviour, defined via the yield surface in stress space and its associated hardening rules, which produce non-linear stress-strain relations. In case of bounding surface plasticity, it is the distance of the actual stress state to the bounding surface that controls the stiffness degradation with continuous shear loading as function of the soil state (stress, void ratio). In addition to that, it is the aspect of increase in initial stiffness with increasing pressure level or density, which is taken into account by a corresponding stress and void ratio dependent calculation of the elastic stiffness parameters, e.g. according to Janbu [Jan63] and Hardin and Black [HB66], respectively. But besides pressure and density, it is also the level of strain that has an influence on the stiffness of the soil after a shear reversal. As stated in Sect. 2.3, the observed quasi elastic shear stiffness at very small strains (for example straight after a load reversal) and the steady stiffness decay at small strains down to a certain minimum, is an important feature of soil behaviour, which is worth considering in many geotechnical applications.

In the basic bounding surface model introduced earlier, the elevated elastic stiffness determines the stress-strain evolution as long as the stress state is within the bounds of the yield surface. As soon as the latter is violated, the rather large plastic portion of deformation is added, causing an abrupt reduction in stiffness and hence a quite sharp bend in the stress-strain curve. The only handle for shifting the point of stiffness change and hence influencing the transition from very stiff to lower stiffness ranges is the size of the elastic domain in stress space.

Papadimitriou and Bouckovalas [PB02] incorporated a strain dependent

stiffness reduction mechanism into the elastic range: the elastic shear modulus decreases with increasing shear strain (delimited by a minimum value), so that the passage is smoother once plastic strains occur (see Sect. 2.2.1 for details). This version of small strain stiffness degradation has the disadvantage of not being thermodynamically consistent. The elastic domain has to be considered "paraelastic", as termed by Hueckel and Nova [HN79], since no fully reversible strains can be produced.

A different strategy, which avoids the issue of non-conservativism, is to transfer the stiffness decline to the plastic range. In order to create a smooth degradation, the hardening modulus has to take very high values at the initiation of plasticity and decrease to the "normal" bounding surface controlled level with increasing shear strain. Consequently, straight after violating the elastic domain and becoming elastoplastic, the plastic contribution is negligibly small and hence the stress-strain behaviour still very stiff, almost elastic. With evolving shear strain towards a certain limit, the artificial magnification factor decreases to one, so that the original bounding surface (BS) hardening mechanism takes over (Fig. 3.19 a). The modified hardening modulus for the cone, which was denoted H_α in Eq. (2.29), can be expressed in general terms as:

$$H^{cone} = H_0^{cone} \cdot h_{ss} \qquad (3.40)$$

Based on this concept, it is understood, that the elastic domain will most likely be a very slim cone (with a small value for m_{cone}), since the rather
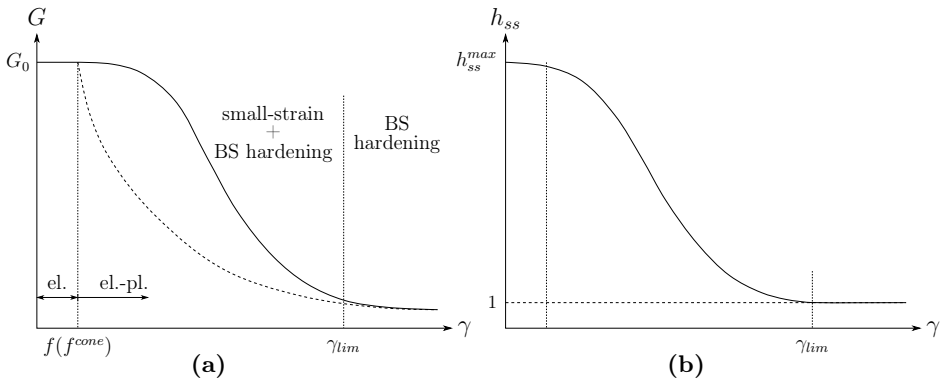

Figure 3.19: Degradation of (a) the secant shear modulus G and (b) the small strain stiffness factor h_{ss} with (——) and without ($\cdots$) small strain hardening option (BS = bounding surface)

stiff zone of small strain hardening (making the transition between fully elastic and the elastoplastic bounding surface hardening region) extends the strain range of stiffer soil response. One could even think of shrinking the yielding cone to a line and making the elastic domain to vanish completely. The formulation for h_{ss} (or H^{cone} in general) would need to be adapted, of course, by including the distance between the actual state and the last shear reversal, in order to make the hardening modulus tend to infinity (or a rather large value) straight after a load reversal as to result in a quasi-elastic stiffness. This strategy has been discussed by Andrianopoulos et al. [APB05] and later pursued by Dafalias and Taiebat [DT16] in their newest bounding surface model version SANISAND-Z. The vanished elastic region necessitates the modification of the model formulation with respect to back stress and projection rules, but is said to simplify the constitutive framework and facilitate the numerical integration procedure. In addition, there is experimental evidence that the truly elastic domain and hence the region of fully reversible deformations is indeed very small, especially for granular soils. Despite these recent developments, in the present bounding surface model the elastic region delimited by the yield surface is maintained in order to preserve a clearly defined range of elasticity, easing the treatment of load reversals and cyclic loading.

In the attempt to provide a sound proposition for the hardening modulus, an appropriate formulation for the small strain stiffness factor h_{ss} has to be found, describing a degradation curve as sketched in Fig. 3.19 b. It needs to take account of the shear strain evolution and also recognise load reversals as indicator for resetting the factor to its initially high value and subsequently restarting the degradation process.

There are several possibilities for achieving this goal. In constitutive modelling, there have been two basically different approaches to trace loading history: either there are the mostly kinematically hardening elastoplastic models, which track loading in stress space with some sort of memory surface(s), e. g. Al-Tabbaa and Muir Wood [AM89], Puzrin and Burland [PB98], and Papadimitriou and Bouckovalas [PB02]. Or the loading history can be memorised in terms of strain as was done for example by Simpson [Sim92] in his brick concept (which has been closely implemented into an elastoplastic constitutive framework by Länsivaara [Län99]) or the small strain overlay for the Hardening Soil model by Benz [Ben07]. Both strategies have their justification: since stiffness degradation is a strain dependent phenomenon it seems evident to remain in strain space. Alternatively, the

Masing rules, which are considered to describe important features of cyclic soil behaviour, are formulated with reference to stress quantities (see Sect. 2.3). In the following, two different approaches are presented – one being set up in a stress, the other in a strain environment – to explain the merits and drawbacks of both strategies.

Stress contours

Inspired by an existing small strain stiffness mechanism used by Schädlich [Sch12] in his multilaminate model, for the present bounding surface model extension a similar kind of memory surface in stress space has been introduced, which will be called stress contour in the following. Since it is mainly the deviatoric component of loading that affects the rearrangement of particle contacts and hence causes the typical stiffness degradation at small strains to appear in a more pronounced way than in compressive loading, the simplifying assumption is made that only deviatoric stress quantities need to be considered in the mathematical formulation. The quantity to be traced is the deviatoric stress ratio change with respect to the last shear reversal:

$$\Delta\eta^{SR} = \sqrt{\frac{3}{2}\left(\boldsymbol{r} - \boldsymbol{r^{SR}}\right)\cdot\left(\boldsymbol{r} - \boldsymbol{r^{SR}}\right)} \qquad (3.41)$$

The stress tracking contours are represented by circles, which expand and shrink in η-direction and are defined by their centre coordinates and the coordinates of their fixed end. The latter point corresponds to the last shear reversal, the moving point on the opposite side of the contour represents the current deviatoric stress ratio state and consequently, the centre can be located and stored in the memory as auxiliary point. Crucial for tracing stress history is the identification of reversals in loading direction. They may be found by continuously checking whether the increment in deviatoric strain (with respect to the last shear reversal) from one step to the next changes its sign:

$$\Delta\varepsilon_q^{SR} = \sqrt{\frac{2}{3}\left(\mathbf{e} - \mathbf{e^{SR}}\right)\cdot\left(\mathbf{e} - \mathbf{e^{SR}}\right)} = \chi_e \quad \text{and} \quad \dot{\chi}_e = \chi_e^i - \chi_e^{i-1} \qquad (3.42)$$

This definition corresponds to the procedure proposed by Papadimitriou and Bouckovalas [PB02] and detects a change in loading direction whenever the deviatoric part of the strain tensor indicates a reversal. It implies that changes in loading direction where the strain rate tensors of two successive load steps include an angle larger than 90° might not be detected if it is the
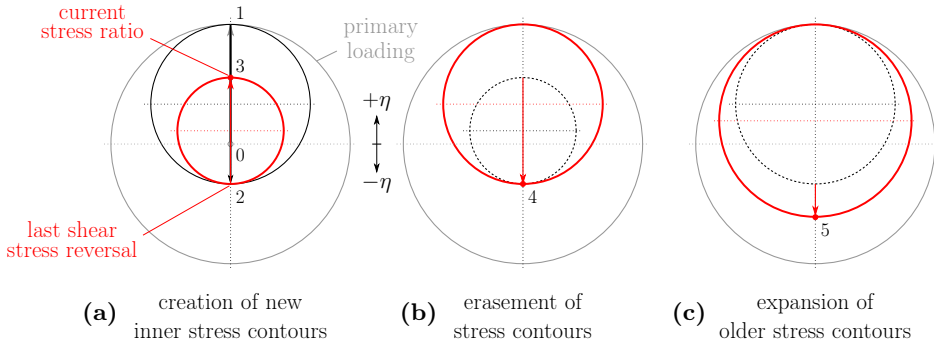
Figure 3.20: Evolution of stress contours with shear loading including shear reversals

volumetric strain component that is mainly reversed. Consequently, it is more correct to speak of shear reversals and one should bear in mind that it is the reversal of deviatoric strain increment that marks a change in loading direction. In addition, one cannot conclude on the intensity of reversal – whether the direction changes by 180° or less.

An alternative approach, which follows the basic idea of the hypoplastic intergranular strain (to be explained in detail later), might be not to restrict the change in loading direction to the deviatoric strain component. In this case the total strain tensor is used and it is checked whether the directions of strain increments from one step to the next enclose an angle larger than 90°:

$$\dot{\varepsilon}^i \cdot \dot{\varepsilon}^{i-1} < 0 \tag{3.43}$$

Thus, not only full 180°-reversals, but even turns of 90° and more would be considered as triggers for resetting the small strain stiffness to its initial value. This way it was also possible to detect a load reversal where the deviatoric strain component keeps following its direction, whereas the volumetric strain increment changes sign, resulting in a change of straining direction of at least 90°. In the present model, the first approach is implemented to remain consistent by only taking deviatoric stress and strain quantities into account.

In the contour concept, the actual state is traced by the active stress contour (bold red line in Fig. 3.20). In primary loading, a particular case, loading starts with one sphere being centred at zero (0), expanding equally to both sides (centre point remains fixed). As soon as a shear reversal is detected

(1), a new sphere is created, becoming the new active contour that is fixed to the updated reversal point and starts expanding in the opposite direction. The two final coordinates of the previous deactivated contour are shifted one level down in the memory stack. At the next load reversal (2), the same procedure recurs (see Fig. 3.20 a): the previous contour becomes inactive, is stored at the top position of the memory vector and a newly created sphere traces the current stress evolution (3). Now imagine that the innermost contour expands until it reaches the closest inactive sphere belonging to the previous strain cycle. In this case, the actual circle is erased from the active stress history and the most recent contour from the memory stack is reactivated (4, Fig. 3.20 b), being reloaded into the active contour vector and continuing to expand (5, Fig. 3.20 c). This way a previous stress path can be intersected and resumed, which may also apply to the primary loading path.

The radius of the current stress contour, which can be easily derived from its coordinates, reflects the actual shear stress and is the key for making the link to the plastic stiffness. As described earlier, there is a certain shear strain limit γ_{lim} that separates the zone of influence of the small strain stiffness degradation factor h_{ss} from the region that is controlled merely by H_0^{cone} (since $h_{ss} = 1$), originating from the bounding surface hardening rule. By relating the current stress ratio with reference to the last shear reversal $\Delta\eta^{SR}$ to the stress ratio limit η_{lim}, which is a function of the shear strain limit γ_{lim}, the small strain factor h_{ss} is interpolated between 1 and a maximum value m_R (indicated as h_{ss}^{max} in Fig. 3.19 b):

$$h_{ss} = 1 + (m_R - 1)\left(1 - \min\left(\frac{\Delta\eta^{SR}}{\eta_{lim}},1\right)\right)^{\zeta} \tag{3.44}$$

The exponent ζ, which can be chosen to be a default value, controls the curvature of the stiffness degradation function. If the change in loading direction was detected with the help of Eq. (3.43) in the form of a concrete angle, the parameter m_R could be defined as a function of that angle as there are experimental indications for a corresponding dependence (see following section "Intergranular strain concept"). The user defined shear strain limit γ_{lim} needs to be translated into a limiting stress ratio η_{lim}. This can be done by expressing the limit stress ratio by the ratio of deviatoric and mean stress increment with reference to the last shear reversal, approximating the former as product of the elastic shear modulus at shear reversal and the user
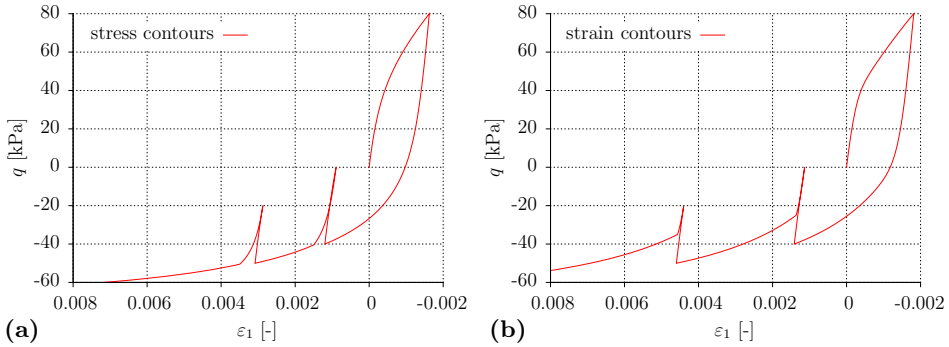
Figure 3.21: Comparison of soil response to stress controlled shear cycles (triaxial loading between different deviatoric stress ratios) modelled with (a) stress and (b) strain contours respectively

defined limit shear strain:

$$\eta_{lim} \approx \frac{\Delta q_{SR}}{\Delta p_{SR}} \approx G_{SR}\frac{\gamma_{lim}}{p_{SR}} \tag{3.45}$$

By following the stress contour approach, the extended Masing rules, as quoted in Sect. 2.3, are fulfilled. The special case of primary loading, where the backbone curve is followed and the hysteretic loop is only half as steep as in any un- or reloading curve, is accounted for by the related particular way of expansion: In primary loading the actual deviatoric stress ratio increment increases the radius of the sphere; in un- and reloading, however, the same deviatoric stress ratio increment increases the diameter. As a consequence, a contour's radius as measure for $\Delta\eta^{SR}$ will approach the limiting value twice as fast in case of primary loading and hence the stiffness decreases more quickly, resulting in a flatter stress-strain curve.

In addition, the Masing rule extension, demanding the continuation of intersected previous cycles, is met due to the mechanism of erasement of previous stress contours as well as resumption and expansion of older spheres. Since the Masing rules define the response of soil to certain loading patterns in stress-strain space and the hardening modulus is formulated with a stress dependency, the clear resumption of reactivated loading curves can be modelled without problems. This is shown in an exemplary simulation in Fig. 3.21 a.

The approximation of the limiting stress ratio with respect to the shear strain limit for small strain stiffness according to Eq. (3.45) is an auxiliary mean, which allows remaining in stress space and hence sticking to the

basic model concept of surfaces in stress space defining soil behaviour. An alternative could be to transfer the memory surface concept into a strain environment, i. e. working with strain contours instead of stress spheres. This implies that the stress measures need to be exchanged by strain variables. Since it has been stated that the formulation can be reduced to the shear relevant components, the deviatoric strain will be used instead of the deviatoric stress ratio. Consequently, a translation of the defined shear strain limit γ_{lim} is no longer required and the ratio $\frac{\Delta\eta^{SR}}{\eta_{lim}}$ in Eq. (3.44) is replaced by $\frac{\Delta\gamma^{SR}}{\gamma_{lim}} = \frac{\frac{3}{2}\Delta\varepsilon_q^{SR}}{\gamma_{lim}}$, so that h_{ss} becomes an interpolation function for scaling the hardening modulus subject to the evolving deviatoric strain. Compared to the stress related solution, such a basic modification in the small strain concept will result in a curve as shown in Fig. 3.21 b, where the resumption of the initial unloading branch is not neatly reproduced anymore. This is due to the stress path dependence of deformation, so that the plastic strain in unloading will not necessarily be the same as in reloading. Consequently, in rather small un-/reloading cycles the fourth Masing rule might be fulfilled, but as soon as cycles become larger, the original loading curve (or the backbone curve in case of primary loading) will not be continued perfectly. The necessity of capturing this feature and hence the merits of making a transfer from one space to the other, is discussed at the end of this chapter.

As described above, the coordinates of the stress (or strain) contours need to be stored in a vector as some sort of state variable. The size of this memory vector theoretically limits the number of stress cycles that can be modelled, provided that subsequent spheres are all nested. In the current implementation the vector consists of 20 elements. However, considering a cyclic test oscillating between two levels of deviatoric stress, the expanding stress ratio contours are erased straight at the next shear reversal and a new one is created, so that the memory vector will never reach its maximum extent and cycling could continue infinitely. Same applies for loading cycles between two constant strain levels in case of strain contours, of course.

Intergranular strain concept

Based on the idea of a strain dependent stiffness degradation mechanism, the intergranular strain concept has been adopted in the present model as an alternative overlay model to the previously presented strain contours. It dates back to Niemunis and Herle [NH97], who incorporated it into the constitutive framework of Hypoplasticity in order to remedy the strong ratcheting effect (excessive accumulation of deformation or pore pressure,

respectively). The underlying theory is based on the assumption that strain is composed of the initial microdeformations of an intergranular interface layer up to a certain maximum and the subsequent slip of the particle contact by rearrangement (i. e. sliding) of the grains. The first contribution is called intergranular strain and denoted by δ. With the onset of deformation (strain increment $\dot{\varepsilon} = D = -1$ in Fig. 3.22 b) it evolves until it reaches its limit $\delta = -R$ and remains distorted while deformation continues as sliding of the grains. At the reversal of the strain increment the intergranular layer deforms in the other direction, passing its neutral state (Fig. 3.22 d) until it reaches its opposite extremum $\delta = R$. As experimental observations indicate that the extent of the elastic domain is stress independent [e. g. Lo 95], Niemunis and Herle [NH97] propose the choice of a constant value for R. The evolution of the intergranular strain δ with deformation is determined according to:

$$\dot{\delta} = \begin{cases} \left(1 - \frac{|\delta|}{R}\right)\dot{\varepsilon} & \text{for } \delta \cdot \dot{\varepsilon} > 0 \\ \dot{\varepsilon} & \text{for } \delta \cdot \dot{\varepsilon} \leq 0 \end{cases} \tag{3.46}$$

This simplified expression for the one-dimensional case has been adapted for multiaxial strain space and slightly modified in order to eliminate a small geometric inaccuracy of the original formulation:

$$\dot{\boldsymbol{\delta}} = \begin{cases} \dot{\boldsymbol{\varepsilon}} - \rho^{\beta_R}\left(\hat{\boldsymbol{\delta}}\hat{\boldsymbol{\delta}} \cdot \dot{\boldsymbol{\varepsilon}} + x\right) & \text{for } \boldsymbol{\delta} \cdot \dot{\boldsymbol{\varepsilon}} > 0 \\ \dot{\boldsymbol{\varepsilon}} & \text{for } \boldsymbol{\delta} \cdot \dot{\boldsymbol{\varepsilon}} \leq 0 \end{cases} \quad \text{with} \quad \rho = \frac{|\boldsymbol{\delta}|}{R}, \quad \hat{\boldsymbol{\delta}} = \frac{\boldsymbol{\delta}}{|\boldsymbol{\delta}|}$$

$$\tag{3.47}$$

The exponent β_R controls the non-linearity of the intergranular strain evolution and had been set to 1 in the simpler version (Eq. (3.46)). The hat operator denotes the norm of the corresponding tensor. Aiming for "pulling" the intergranular strain vector towards the strain rate direction, as long as the intergranular strain and the strain rate enclose an obtuse angle, the intergranular strain increment is coaxial with the strain increment. As
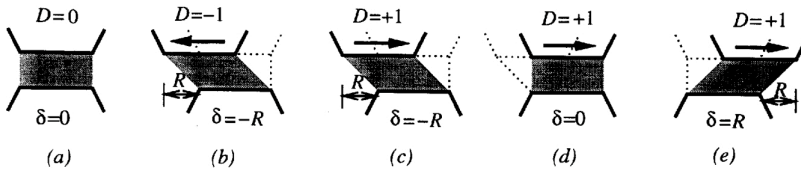
Figure 3.22: One-dimensional consideration of the intergranular strain concept [NH97]
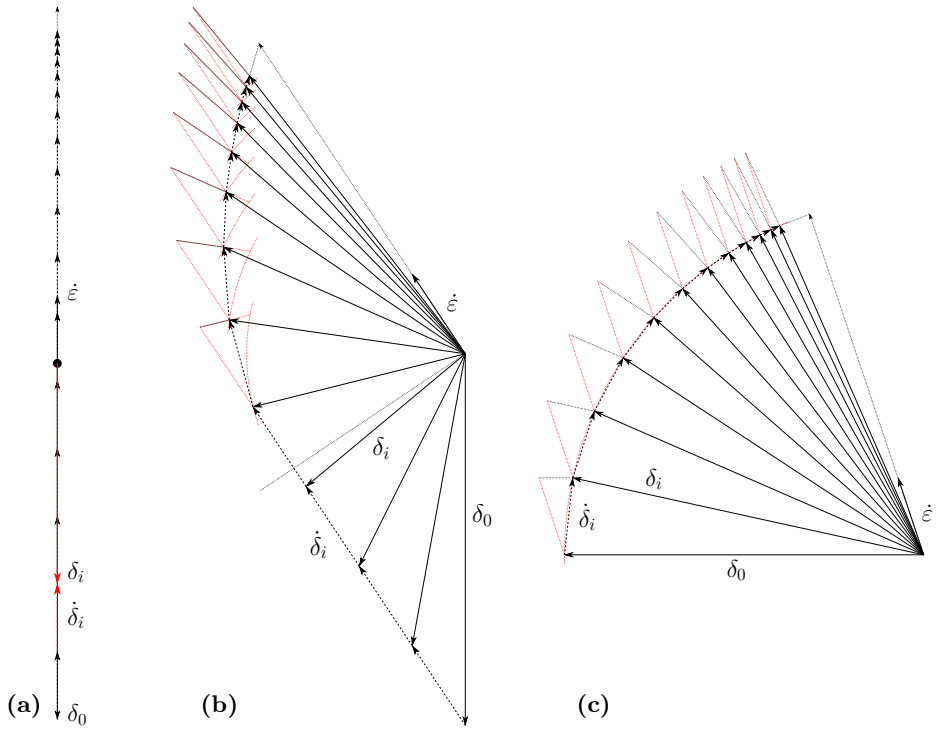
Figure 3.23: Intergranular strain evolution after a change in loading direction of different sizes: (a) $\alpha = 180°$: $\boldsymbol{\delta} \cdot \dot{\boldsymbol{\varepsilon}} < 0$, (b) $90° < \alpha < 180°$: $\boldsymbol{\delta} \cdot \dot{\boldsymbol{\varepsilon}} = 0$, (c) $\alpha < 90°$: $\boldsymbol{\delta} \cdot \dot{\boldsymbol{\varepsilon}} > 0$ ($\rho_0 = 1$)

soon as this angle α falls below 90°, the intergranular strain increment turns stronger towards the strain rate direction. With a decreasing step size (due to the factor ρ^{β_R}) the intergranular strain finally becomes unidirectional with the strain rate and reaches its maximum length $|R|$ (see Fig. 3.23 b). In the special event of a full reversal, i. e. the one-dimensional case of Eq. (3.46), the intergranular strain vector is first progressively shrunk to zero and restarts growing in the strain rate direction at decreasing "speed" until having attained its opposite extremum $-R$ (Fig. 3.23 a). The reader's attention is called to one further particular case: if the intergranular strain and strain rate vectors are initially at an acute angle and the former is already of length R, then Eq. (3.47) ensures pure rotation of the intergranular strain vector towards the strain rate direction without any changes in its length (Fig. 3.23 c). This is realised by the modification x with respect to the original formulation by Niemunis and Herle [NH97]:

Figure 3.24: Interpolation of stiffness with respect to direction ($\alpha = \sphericalangle\, \delta, \dot{\varepsilon}$) and magnitude ($\rho = \frac{|\delta|}{R}$) of intergranular strain [Tse14]

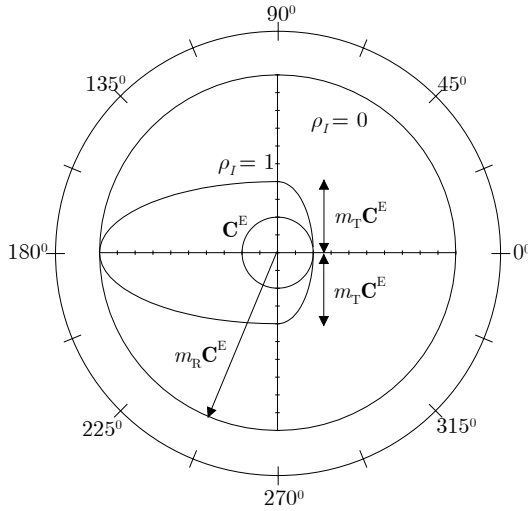$$x = \left(|\boldsymbol{\delta}| - \sqrt{|\boldsymbol{\delta}|^2 - |\dot{\boldsymbol{\varepsilon}}|^2 \left(1 - \left(\hat{\boldsymbol{\delta}}^T \cdot \hat{\dot{\boldsymbol{\varepsilon}}} \right)^2 \right)} \right) \cdot \hat{\boldsymbol{\delta}} \qquad (3.48)$$

The derivation of this geometrical adjustment can be found in App. A.6.

Having provided the evolution law of the intergranular strain, the strain dependent formulation for the hardening factor h_{ss} in analogy to the strain contours can be set up:

$$h_{ss} = \left\{ \begin{array}{ll} (\rho^\chi \cdot m_T + (1 - \rho^\chi) \cdot m_R) + \rho^\chi \cdot (1 - m_T) \cdot \hat{\boldsymbol{\delta}}^T \cdot \dot{\boldsymbol{\varepsilon}} & \text{for } \boldsymbol{\delta} \cdot \dot{\boldsymbol{\varepsilon}} > 0 \\ (\rho^\chi \cdot m_T + (1 - \rho^\chi) \cdot m_R) + \rho^\chi \cdot (m_T - m_R) \cdot \hat{\boldsymbol{\delta}}^T \cdot \dot{\boldsymbol{\varepsilon}} & \text{for } \boldsymbol{\delta} \cdot \dot{\boldsymbol{\varepsilon}} \leq 0 \end{array} \right.$$
$$(3.49)$$

Equation (3.49) is based upon a proposal for an intergranular strain overlay for elastoplastic models by Tsegaye et al. [TYB13]. The stiffness is interpolated between m_T and m_R, the stiffness factors for a change of loading direction of 90° and 180°, respectively, with χ controlling the non-linearity of interpolation. However, it is the angle α between the current directions of intergranular strain and the strain rate that determines the stiffness: the factor $\hat{\boldsymbol{\delta}}^T \cdot \dot{\boldsymbol{\varepsilon}}$ in Eq. (3.49) equals the cosine of their enclosed angle. In addition, the amount of intergranular strain with respect to its allowed

maximum R has an impact on the hardening factor. The combined effect of direction and magnitude of the intergranular strain on the hardening factor h_{ss} is visualised in Fig. 3.24: the highest stiffness occurs either when intergranular strain and strain rate are opposed ($\alpha = 180°$) or if the interparticle interface is not deformed at all ($\delta = \rho^\chi = 0$). The lowest stiffness is attained once the intergranular strain has fully converged with the strain rate's direction ($\alpha = 0°$) and reached its maximum length ($\rho^\chi = 1$). Any other combination of angle α and relative length ρ is interpolated between the extremal curves. Consequently, this small strain stiffness strategy takes account of the evolution of an assumed interparticle interface layer in both orientation and magnitude, and hence follows an approach with a stronger physical background.

On the basis of the established rule for determining the small strain magnification factor h_{ss} as a function of the size and orientation of the intergranular strain, the resulting stiffness evolution with strain can be summarised as depicted in Fig. 3.25. After a full stress reversal, the soil response will be elastic due to the stress state location within the yield surface. As soon as the behaviour becomes elastoplastic, the bounding surface based plastic stiffness will be scaled by h_{ss}, which takes its maximum value in case of a 180° turn (upper curve in Fig. 3.25). The corresponding plastic strains are very small, so that the initial elastoplastic stiffness remains almost at the elastic level. If on the contrary the change in loading direction is considerably smaller, for example only 90°, the initial plastic stiffness will be scaled with a smaller h_{ss} value and hence the plastic stiffness drops from a lower level (middle curve in Fig. 3.25). In the second case, most of the time there is a purely elastic part of deformation, where the elastic stiffness determines the initial strains, provided that the 90° change in strain direction corresponds to a deflection of the stress path back inward the yield surface.

According to Hypoplasticity with the intergranular strain extension, the initial zone of (nearly) constant high stiffness is considered to be quasi-elastic and is quantified by a maximum deformation R, taking values of approximately 10^{-5}. Applying the intergranular strain concept as an overlay model to bounding surface plasticity, the purely elastic domain is solely determined by the yield surface expression in stress space and R has no direct influence on the stress strain curve in this strain range. But simultaneously, R is also the parameter that delimits the evolution of the intergranular strain. Roughly at this stage, where intergranular strain and strain rate are finally unidirectional and $\frac{|\delta|}{R} = 1$, the stiffness has degraded to a level, where it
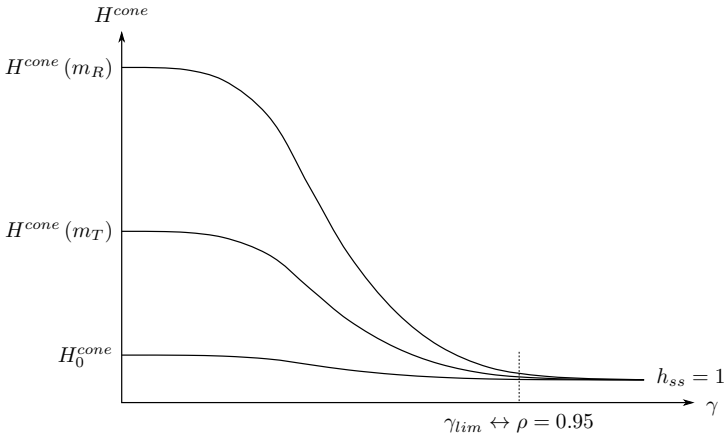
Figure 3.25: Evolution of the hardening modulus H^{cone} depending on the change in loading direction, exemplary for a full reversal (m_R), a 90°-reversal (m_T) and without any change (H_0^{cone})

regains its low value typical for normal monotonic loading. Niemunis and Herle [NH97] call it the "swept-out memory" (SOM) point and define it as the strain, where the additional stiffness has decayed out by more than 90 %. The corresponding SOM-strain, estimated to amount to about 10^{-3}, is synonymous with the limit shear strain γ_{lim} having been used in the context of stress/strain contours. In the present elastoplastic model environment it marks the deformation where $h_{ss} \to 1$, specifically, where h_{ss} has decayed from its initial value by 95 %[9]. Thus, the plastic stiffness is almost solely determined by the bounding surface concept related plastic modulus $(H^{cone} \approx H_0^{cone})$. Depending on the choice of R, the resulting limit shear strain γ_{lim} is controlled by the two exponents χ and β_R. Consequently, the parameter R shapes the run of the stiffness degradation curve (together with χ and β_R), but cannot be directly linked to a particular point in strain space. In contrast to the original hypoplastic context, it can only be roughly correlated with the initiation of the stiffness reduction.

A last remark should be given on the Masing rules. Since the basic principle, the dependence on strain instead of stress, is the same for both mechanisms, the intergranular strain overlay for the bounding surface model produces similar stress-strain curves as the strain contours do – in principle

---

[9]The slightly higher decay compared to Niemunis and Herle [NH97] has been chosen in order to bring the definition of the limit strain γ_{lim} closer to the contour concept.
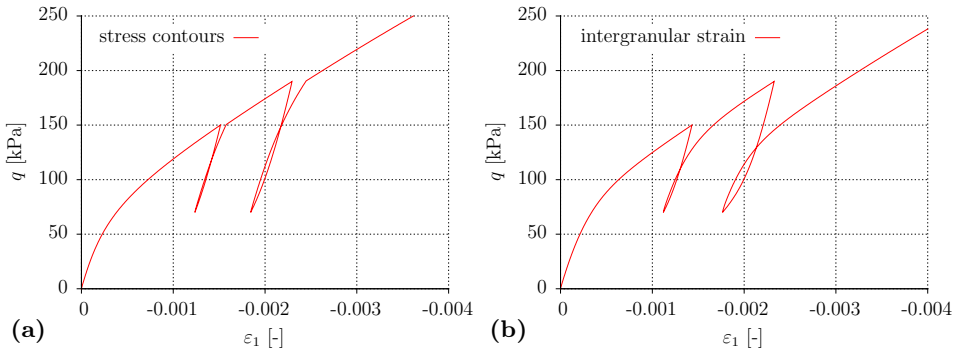
Figure 3.26: Comparison of stress-strain cycles calculated with (a) the stress contour overlay model and (b) the intergranular strain overlay model

the Masing rules are fulfilled. The same way the primary contour expands and contracts twice as fast as any other contour, the intergranular strain starts evolving from zero to R in virgin loading, but has to pass from R to $-R$ (or vice versa) any time after (speaking in simplified terms of a 180°-turn). The resulting effect is basically the same: the stiffness in un- and reloading becomes considerably higher by increasing the quasi-elastic range.

However, the same shortcomings apply to both models, too. After having inserted un- and reloading cycles, the backbone curve is only resumed at particular strain ranges: the comparison with the previously introduced stress based contour model in Fig. 3.26 shows that the second un- and reloading cycle is not closed in case of the intergranular strain overlay model. This is due to the degradation characteristic determined by the evolution of intergranular strain and hence by the associated constant parameters R, χ and β_R. Consequently, the stress has no (direct) influence on the shape of the hysteresis loops and the previously left point in stress-strain space is not necessarily met again.

Comparison of the small strain mechanisms

As stated in the introductory section of this chapter, it is a logical consequence of the nature of small strain stiffness to formulate an appropriate hardening mechanism as a function of strain. Although there are certain benefits in stress based concepts like stress contours (full compliance with extended Masing rules), two strain related approaches – the strain contours and the intergranular strain overlay – have been presented and implemented additionally. Since all relevant quantities of the strain based concepts

are traced in strain space, cumbersome (and error-prone) transformations between stress and strain space as required in the stress contour model ($\gamma_{lim} \leftrightarrow \eta_{lim}$ in Eq. (3.45)) are omitted.

The detection of changes in loading direction of different angles (larger than 90°) is based on the straining direction and their consideration by a corresponding adjustment of initial small strain stiffness is included in the intergranular strain overlay. With the given propositions for modifications in the stress/strain contours' stiffness and reversal formulations, a similar direction dependence could be integrated in the contour models. After a reversal, both approaches exhibit quasi-elastic strains (due to the paraelastic domain) before stiffness degradation via the reduction of the initially superelevated hardening modulus starts.

Whether it is a necessity to meet the (extended) Masing rules by all means, referring to the resumption of old loading branches with respect to stress, is an open question. The experimental foundation for Masing's postulation is rather weak and hence its fulfilment maybe not an unconditional requirement. Depending on the importance the user might put into the reproduction of perfect Masing cycles, strain based concepts can be an alternative worth considering or not. In boundary value problems the simulative results of both approaches will most likely deviate to a certain extent, depending on the chosen parameters and the loading scheme in question (stress / strain / void ratio range, number of cycles).

Seen from a use-oriented point of view, the stress/strain contours are a beneficial strategy for modelling small strain stiffness. Due to their geometrical character and close relationship to memory surfaces, this concept is straightforward and hence easy to grasp. But while the stress/strain contours remain a rather artificial constitutive mean, the intergranular strain has a more physical background with a stronger micromechanical basis. Nevertheless, its formulation with the rather intricate evolution of the intergranular strain vector is of higher complexity and hence requires the determination of a larger amount of material constants. Regarding for example the parameter m_T, it is legitimate to trade off the effort of constitutively distinguishing 90° and 180° turns (and the experimental determination of m_T) against the relevance of its final effect on the simulated response.

Both approaches have been implemented and tested. Their calibration and performance are described and compared in Sect. 4.2.

3.2.5   Cyclic loading mechanism

The decisive advantage of kinematically hardening constitutive models, as any of the bounding surface type, is the potential for modelling load reversals and hence appropriately simulating cyclic loading. The key feature of the bounding surface concept is the allowance for different stiffnesses in loading and unloading: depending on the loading direction, the reference surface, which serves for the determination of the distance based hardening modulus, is redefined. After a shear loading path with decreasing stiffness and a subsequent reversal, the new hardening properties in unloading are calculated with respect to the bounding surface in extension, so that the resulting stiffness is higher than prior to reversal before redescending. Referring to the previous section, it has been discovered, that the stiffness after a load reversal needs to be increased even more than the original bounding surface formulation provides due to the phenomenon of small strain stiffness. This issue and its consideration on a constitutive level is treated in Sect. 3.2.4 and will not be regarded here.

If the loading scheme is not only composed of a single reversal but of several un- and reloading cycles, the same rule applies. Assuming a drained triaxial loading pattern that is located under the dilatancy surface (phase transition line, PTL) in stress space, the contractant volumetric response of consecutive cycles hardly changes. The distance measure to the bounding surface for calculating the stiffness after each complete cycle remains (ap-
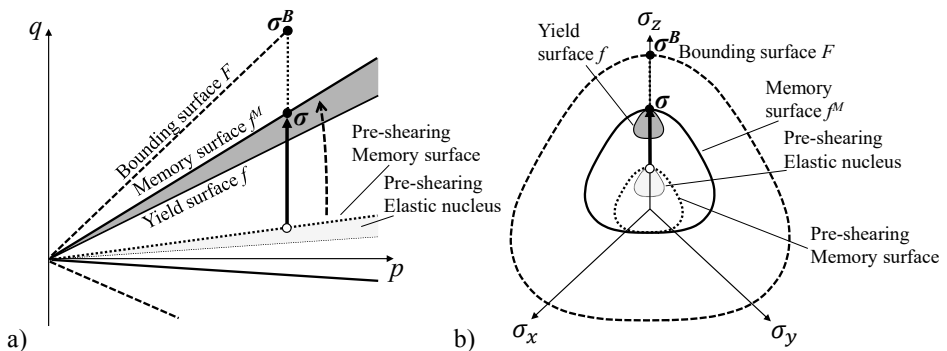

Figure 3.27: Memory surface concept by Corti [Cor16]: surface expansion in case of volumetric contraction, in (a) p-q space and (b) multiaxial stress space [from CDM$^+$16]

proximately) the same. Consequently, except for the rather small influence of void ratio, the prospect of evolution in the hardening process is limited. This is not in accordance with experimental observations, which exhibit a clear trend of densification with increasing number of cycles until no further deformation is accumulated ("shake down"). Speaking in micromechanical terms, it is the evolution of the soil structure, namely the rearrangement of grains and interparticle contacts, that causes the observed continuously stiffening un-/reloading behaviour. The problem produced by many constitutive models not accounting for this effect is called ratcheting: a missing deceleration mechanism in strain accumulation and hence a far too soft soil response in cyclic loading.

Consequently, it is worth incorporating a functionality that accounts for an enhanced densification and pore pressure development respectively with an increasing number of cycles (or a different suitable reference measure). There have been several approaches in literature to meet these requirements: Papadimitriou and Bouckovalas [PB02] established a hardening modulus scaling mechanism that is based on the evolving plastic volumetric strains and has been described in Sect. 2.2.1. A very similar idea was proposed by Dafalias and Manzari [DM04]: instead of addressing the hardening modulus they adjust the dilatancy parameter A_d according to the irreversible portion of incremental volumetric deformation. Picking up the idea of a factor scaling the hardening modulus, Corti [Cor16] developed a memory surface based concept: if the soil experiences contractive volumetric strains, the memory surface expands, resulting in a progressive increase of the hardening modulus and hence a stiffening effect (Fig. 3.27). Dilation, on the other hand, leads to a contraction of the memory surface and a decreasing hardening modulus, accompanied by a reduction in plastic soil stiffness. Although this approach uses a geometrical mean in stress space for tracing the fabric evolution, it basically is the plastic volumetric deformation that governs the cyclic mechanism.

For the present model extension, the mathematical algorithm of the accumulation mechanism as the common basis of the formulations by Papadimitriou and Bouckovalas [PB02] and Dafalias and Manzari [DM04] will be used. However, a different measure will serve as a reference for quantifying the accumulation trend: the amount of dissipated energy.

Dissipated energy

The idea of relating material behaviour to hysteresis energy is dating back to the beginning of the 20th century, originating from the context of fatigue life prediction in the field of material science [e. g. Bai11, Han47]. Besides, in their fundamental essay on the precursor model of bounding surface plasticity, Dafalias and Popov [DP75] proposed that the plastic modulus should be a function of the amount of plastic work $W^{pl} = \int \sigma \, \mathrm{d}\varepsilon^{pl}$ accumulated during the preceding plastic deformation. Soil related laboratory investigations revealed that the micromechanical restructuration of the structure due to repeated loading – the rearrangement of the grains and their interparticle contacts – involves a certain amount of energy. This observation served Nemat-Nasser and Shokooh [NS79] as starting point for their energy theory: it requires an increment of dissipated energy dW to change the void ratio of drained soil or the pore pressure of undrained soil. They established a differential equation that relates the energy dissipated into the soil in cyclic shearing to the densification of sand and the increase in pore water pressure, respectively. This energy loss is represented by the area of the hysteretic stress-strain loop (Fig. 3.28). In contrast to the previously mentioned plastic volumetric strain evolution, the accumulated dissipated energy (with respect to several un-/reloadings) considers both the amplitude of shear strain and the number of cycles and combines the impact of stress and strain on the cyclic response.

In recent publications by Lenart [Len09] and Taborda et al. [TPZ16] in the context of dynamic finite element analysis, dissipated energy has been used
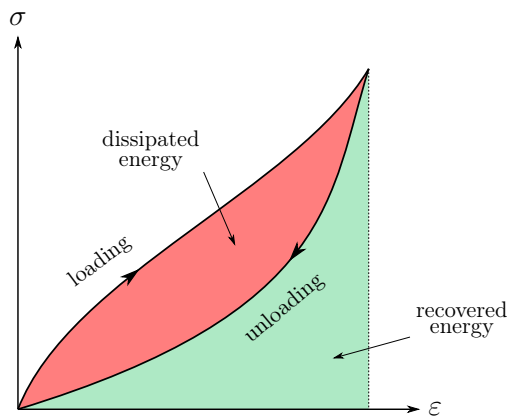
Figure 3.28: Hysteresis loop enclosing dissipated energy

as a means to quantify cyclic soil behaviour. They assess the accumulated dissipated energy based on the stress strain curves by analysing each half-cycle (since the stress strain loops are seldom perfectly closed), concluding the dissipated energy of loadings and recovered energy of reloadings (Fig. 3.29 b) and tracing the resulting accumulated energy over successive cycles. Similarly, in the present model extension the dissipated energy is calculated from hysteresis loops by numerically integrating the area under the stress-strain curve from one load step to the next by the following relation (see also Fig. 3.29 a):

$$W = \sum_{i=0}^{n} \mathrm{d}W_i \quad \text{with} \quad \mathrm{d}W_i = \left(\frac{\sigma^{i-1} + \sigma^i}{2} - \sigma_{SR} \right) \cdot \left(\varepsilon^i - \varepsilon^{i-1} \right) \qquad (3.50)$$

The quantity σ_{SR} denotes the stress at the last shear reversal introducing a loading branch in case it exceeds the level of the previously stored value (Fig. 3.29 c). It needs to be tracked in order to relate the dissipated energy increment to the proper stress and hence energy level.
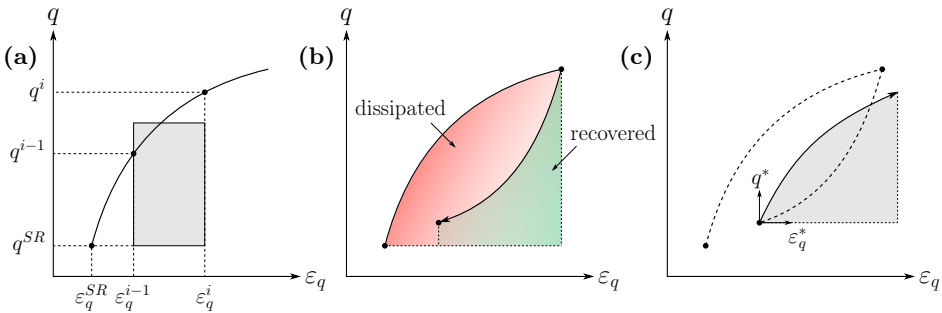
Figure 3.29: Calculation of dissipated energy: (a) numerical integration, (b) dissipated and recovered energy, (c) redefinition of reference point at shear reversal

Depending on the observed cyclic phenomenon, the dissipated energy per cycle decreases or increases. Consequently, in case of a shakedown, the resulting accumulated dissipated energy grows sublinearly and stabilises after a finite number of cycles, indicating a stiffening soil response and being linked to drained cycling below the phase transition line (PTL). On the contrary, a superlinear increase in hysteresis energy indicates an incremental collapse, where the soil body steadily loses its stability and finally

fails, occurring if cycling takes place above the PTL. These correlations
can now be translated into appropriate rules within the constitutive frame-
work, reflecting both the evolution of plastic stiffness and dilatancy with
accumulation of dissipated energy. While Papadimitriou and Bouckovalas
[PB02] proposed to let the hardening mechanism take account of cyclic ef-
fects exclusively, Dafalias and Manzari [DM04] transferred the dilatancy
related stronger compliance to the flow rule. The present model merges
these two approaches: it adopts the denominator of Eq. (2.42) for tracing
the complete history of energy dissipation and equally applies it to the har-
dening law as an additional factor h_{fab} (in analogy to the small strain plastic
stiffness correction h_{ss}). This way the stiffening effect with increasing dis-
sipated energy is incorporated. Furthermore, the increased compliance in
unloading after a shear reversal over the PTL ($D < 0$) is regarded as an
amplified contractive tendency, following the idea of Dafalias and Manzari
[DM04].

Thus, there is the variable f_p fulfilling the first task by simply summing up
all increments of dissipated energy and a vector $\boldsymbol{f}$ that evolves only once
the PTL has been crossed up to a certain limit C_f:

$$\dot{f}_p = N_f \cdot \mathrm{d}W_i \quad \text{and} \quad \dot{\boldsymbol{f}} = \begin{cases} -F_f \cdot |\mathrm{d}W_i| \cdot (C_f \boldsymbol{n} + \boldsymbol{f}) & \text{for } D < 0 \\ 0 & \text{for } D \geq 0 \end{cases} \quad (3.51)$$

The scaling parameter h_{fab} for the modification of the hardening modulus
is deduced from the first contribution:

$$h_{fab} = 1 + \langle f_p \rangle^a \tag{3.52}$$

and the flow rule extension f_{fab} is found by combining the second contri-
bution and Eq. (2.43):

$$A_d = A_0 \cdot f_{fab} \quad \text{with} \quad f_{fab} = 1 + \langle \boldsymbol{f} \cdot \boldsymbol{n} \rangle \tag{3.53}$$

As long as the stress state remains contractive, only the stiffness related h_{fab}
evolves according to the amount of dissipated energy, steadily increasing the
hardening modulus. When trespassing the dilatancy line, $\boldsymbol{f}$ starts to grow,
albeit in the opposite direction of $\boldsymbol{n}$, so that $\boldsymbol{f} \cdot \boldsymbol{n} < 0$ and hence the dilatancy
related f_{fab} remains inactive due to the Macauley brackets. Finally, if a
shear reversal occurs in the dilative range, $\boldsymbol{n}$ changes sign, $\boldsymbol{f}$ and $\boldsymbol{n}$ become
unidirectional (or enclose an angle of less than 90° for a change in loading
direction of more than 90°) and hence $\boldsymbol{f} \cdot \boldsymbol{n} > 0$. Consequently, f_{fab} becomes
active and suddenly augments the contractive effect. As a result, unloading

becomes more compliant (drained) or excess pore pressures increase more intensively (undrained), respectively. For a better understanding, the latter feature – the impact on an undrained triaxial compression test with stress reversal in the dilative range – is visualised in the simulation in Fig. 3.30, clearly showing the typical more compliant response described by e. g. Ladd et al. [LFI$^+$77].
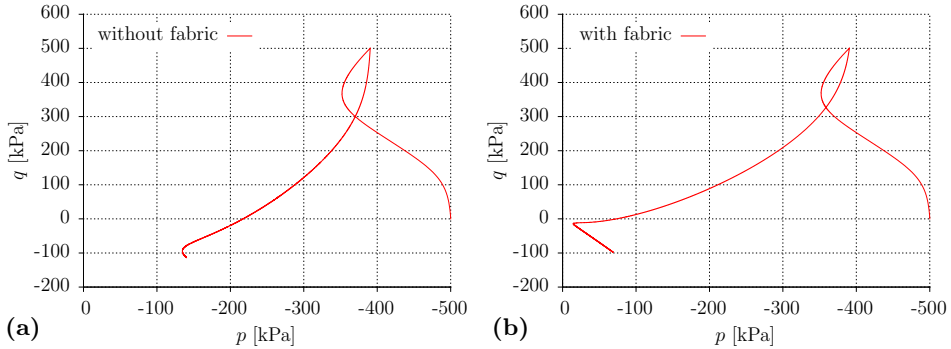
Figure 3.30: Load cycles below the phase transition line (PTL) in case of an undrained triaxial compression test: (a) without and (b) with fabric option

The parameters included in Eqs. (3.51) to (3.53) allow for influencing the separate mechanisms of stiffness and dilatancy evolution: N_f simply scales the dissipated energy accumulated in both contractant and dilatant stress paths, the exponent a accelerates the associated stiffness increase. C_f corresponds to the maximum length ever to be attained by the vector $\boldsymbol{f}$ and hence defines the maximum value of f_{fab} for upscaling A and realising more compliant/contractive unloadings. The factor F_f allows for a better control on the evolution speed of $\boldsymbol{f}$ towards its maximum.

Minimum void ratio

An additional fabric effect has been taken into account in the context of densification with increasing dissipated energy. One has to pay attention to the fact that soil cannot be densified infinitely by cyclic shear but approaches its minimum void ratio asymptotically. Youd [You72] found out that shear induced compaction even exceeds the maximum density obtained by standard vibratory procedures according to the ASTM. Thus, a minimum void ratio mechanism has been incorporated as a last factor scaling the hardening modulus. If the current volumetric state converges the user defined

minimum void ratio, the factor sharply increases the hardening modulus within a few cycles so that no further strain can be accumulated. This is realised by the following formula:

$$h_{min} = 1 + 100 \cdot \left(\frac{e_{cs} - e}{e_{cs} - e_{min}} \right)^{100b} \quad \text{with} \quad e_{min} = e_{min0} - \lambda \left(\frac{p}{p_{at}} \right)^{\xi} \quad (3.54)$$

The exponent controls the intensity of the increase in plastic stiffness, which is set to a rather large number in order to have an impact only if the void ratio is close to its minimum value. b was set to a default value of 2. As postulated by Gudehus [Gud96], the minimum and maximum densities are a function of the stress, similarly as the critical state void ratio. Hence, the minimum void ratio e_{min} is determined with the same stress dependence as used for the critical state line in Eq. (3.7) (in analogy to the relation used by hypoplasticity, see Eq. (3.23)). The reference minimum void ratio e_{min0} to be provided by the user should preferably be the highest density determined by cyclic shear with small amplitudes. If not available, the value determined by usual vibration methods applied in laboratory testing standards is a sufficient approximation.

The effect of implementing this additional mechanism can be understood when comparing the two simulations of the same amount of triaxial compression cycles in Fig. 3.31, clearly indicating a compaction towards the minimum void ratio (b) when applying the relation of Eq. (3.54).

A supplemental remark concerns the role of critical state in the context of shear induced compaction. Starting from a contractant state ($\psi > 0$) the
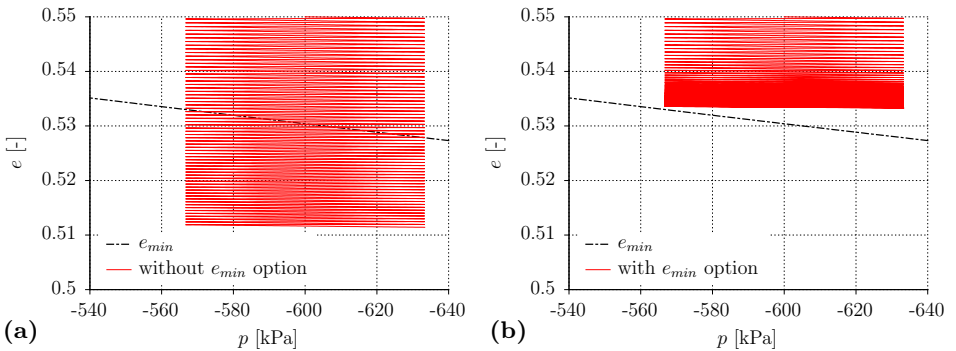

Figure 3.31: Equal number of load cycles of drained triaxial compression: (a) without and (b) with minimum void ratio fabric option

void ratio will steadily approach its critical value with proceeding densification and hence the state parameter ψ will tend towards zero. In contrast to stress-strain space, in stress space the stress state does not approach the critical state line, provided that the shear cycles are defined by a minimum and maximum stress below the critical state line, so that a failure cannot occur. Consequently, due to the continuous compaction the state parameter will change sign and the dilatancy and bounding surface will change position with respect to the critical state surface. Therefore the following cycles will even start exhibiting slight dilation on the compressive triaxial path and finally approach the predefined minimum void ratio.

3.2.6   Summary

The extensions to the bounding surface model by Manzari and Dafalias [MD97] introduced in this chapter result in a parameter set that combines the original material constants with a few new parameters controlling the complementary model features. Besides the adjustment of the dilatancy formulation, the main focus lies on the modification of the hardening moduli governing the evolution of cone and cap yield surface. By introducing additional scaling factors with respect to the loading direction (cap) as well as the small strain stiffness, fabric evolution and minimum void ratio (cone) the plastic stiffness evolution is directed. These different influences are reflected by the following modified hardening moduli:

$$H^{cap} = H_0^{cap} \cdot h\left(\dot{\eta}, \dot{\varepsilon}_p, \dot{\varepsilon}_q\right) \qquad (3.55)$$

with H_0^{cap} according to Eq. (3.38)

$$H^{cone} = H_0^{cone} \cdot h_{ss} \cdot h_{fab} \cdot h_{min} \qquad (3.56)$$

with H_0^{cone} according to Eqs. (2.29) and (3.9)

By setting the h-factors to 1, the different influences on the hardening behaviour of the surfaces are switched off. Thus, the extended bounding surface model is of a modular type: depending on the complexity of modelling requirements, the options can be activated separately by making a sound choice of the attributed parameters. Alternatively, if the geotechnical problem to solve does not necessitate the new features, by turning them all off, the model simplifies to the basic bounding surface implementation comparable to the original version by Manzari and Dafalias [MD97].

Table 3.2: Summary of all parameters of the extended bounding surface model

		parameters	equations
Elasticity		G_0^{ref}, m, ν, m_{cone}	(3.5), (3.6), (2.19)
Critical state line		$\varphi_{cs}^{c,e}$, e_{cs0}, λ, ξ	(3.7)
Kinematic hardening		m_b, h_0	(3.8), (3.9)
Dilatancy		m_d, A_d	(3.16), (3.19), (3.24)
Cap	M_{cap}: LCC:	$E_{oed,0}^{ref}$, m_{oed}, n_{oed}, K_0 ρ_c, p_r, ω V, C	(3.30), (3.31) (3.37) (3.36)
Small strain stiffness	SC: IGS:	γ_{lim}, m_R, ζ R, m_R, χ, β_R, m_T	(3.44), (3.45) (3.47), (3.49)
Fabric evolution		e_{min0}, F_f, C_f, N_f, a	(3.51), (3.52), (3.54)

In Table 3.2 all model parameters of the fully extended version are listed, grouping them by their constitutive sphere of influence. Compared to the parameter list of the predecessor models introduced in Chap. 2, the extended model counts a few more material constants, to be determined by the engineer with good care, preferably on the basis of experimental data. How such a parameter calibration can be conducted, will be explained in detail in Sect. 4.2. By assuming default values or interrelations for the greyed out constants, the amount of parameters to calibrate can be reduced considerably. Proposals for appropriate values are also given in Sect. 4.2.

3.3 Limitations of the bounding surface model

The motivation for developing a new constitutive model or for advancing an existing model is the aim of enriching the present pool of modelling tools by a more powerful one. This can either be in the form of an improved isolated property that can be reproduced more satisfactorily or the merging of several constitutive components to a model with a globally better performance. In order to pave the way for application by a preferably large number of users, most of the time, instructions for use consist of a more or less profound description of the model capabilities. Aspects that are seldom properly illuminated concern the limitations of a model. It is useful to know which expectations a model can fulfil. But it is much more

important to be aware of its imperfections. Which type of soil behaviour cannot be reproduced and why? Which constitutive component is missing or is simplified in its mathematical formulation to an extent that it delivers dissatisfying results? Only on the basis of an all-encompassing knowledge on constitutive models, including their insufficiencies, can an appropriate choice be made for the demands of a problem to solve in order to carry out a sound numerical analysis.

After having introduced the bounding surface concept and its merits in the preceding parts of this work – the features of the original model by Manzari and Dafalias [MD97] as well as the additional properties included by the model extensions presented in the previous chapter – the actual section will give a critical insight into the remaining model deficiencies. In this context, one has to differentiate between shortcomings of various origins. On the one hand, there are disabilities based on the model concept of bounding surfaces or even of elastoplasticity itself, which can hardly be solved with model improvements remaining within the same constitutive framework. They will be termed intrinsic insufficiencies. Compared to the basic model by Manzari and Dafalias [MD97], some of the shortcomings have been rectified by the present extensions, but there still exist a number of issues, which are not yet solved, although there might already have been proposals in literature. Explanations for the intentional preservation of simplicity in the model formulation at the expense of the proximity of calculation results to reality are given. As a third group there are modelling deficiencies that have been introduced by the model extensions themselves. This occurred if the overall effect of the modification can be considered beneficial or the improved feature had a higher priority in the author's eyes than the newly introduced deficiency.

In the following, the three types of insufficiencies will be presented and the effect of the respective issue on the simulated soil behaviour will be described and visualised with the help of exemplary simulations. Finally, a concluding remark will be given, pointing out the most important limitations of the present version of bounding surface plasticity to the user and assessing the severity of the not yet remedied shortcomings with reference to possible fields of application.

3.3.1 Intrinsic insufficiencies of the bounding surface concept

The bounding surface concept is a very powerful constitutive framework allowing for modelling all fundamental features of soil behaviour (dilatancy, irreversibility, barotropy etc.) and a few more advanced properties in addition (reversed loading, stress anisotropy etc. – see Sect. 3.1). Though, there are certain behavioural patterns that are not reproduced properly or stress paths, where simulation and experimental observation do not coincide due to intrinsic constitutive deficiencies. Additionally, in this section shortcomings are listed which concern very specific features of soil behaviour. It shall not be precluded that an implementation of these aspects in the bounding surface environment is possible. Though, in most cases, there are no corresponding constitutive provisions in nowadays conception of bounding surface models and the constitutive framework might not be the first choice for a respective extension, giving it yet another dimension of complexity.

Elastic unloading

One example of intrinsic insufficiencies is the volumetric response of a soil element after shear reversal. This issue has already been shortly discussed in Sect. 3.1 in the context of dilatancy at cyclic shear. Usually, after a loading event, no matter if dilative or contractive, one would expect a purely contractant unloading. Opposed to experimental evidence, the model response after shear reversal always exhibits a small relaxation before the contraction sets in (see Fig. 3.11). This is due to the definition of elastic volumetric strains according to:

$$\dot{\varepsilon}_p^{el} = \frac{\dot{p}}{K} \tag{3.57}$$

From this equation follows that the elastic volumetric strain rate is negative as long as the stress increment is negative, corresponding to contraction and compression, respectively, as for example in triaxial loading. At unloading, the stress increment is reversed, becoming positive and hence the volumetric response will be positive as well, corresponding to volume expansion. This effect dominates the soil behaviour as long as the elastic strain prevails over the plastic deformation. Contraction will only be visible once the plastic contribution is larger than the elastic portion (and before the dilative range is reached again). Based on this intrinsic insufficiency, one

has to be aware of the model response in case the elastic domain is quite large. In comparably small loading cycles under the phase transition line, the relaxation in unloading might dominate the overall deformation trend, so that contractive loading branches are largely compensated by mainly expansive unloading branches. Consequently, the densification of the soil is slowed down considerably and it takes many more cycles to reach a certain compaction state.

This issue could be, however, remedied by simply shrinking the yield surface and hence the elastic domain to (approximately) zero, so that elastic strain portions cannot distort the soil response after a shear reversal.

Ratcheting

One aspect that should be considered an intrinsic insufficiency of the bounding surface concept, is the (numerical) phenomenon of ratcheting – although it is no problem any longer in the extended model thanks to the introduction of the small strain and cyclic loading related hardening mechanisms. Consider consecutive triaxial loading cycles between two stress ratios below the phase transition line (hence loading is purely contractant). At each stress reversal terminating a loading branch, the bounding surface (as reference for the calculation of the plastic stiffness) changes from the compression to the extension side, and vice versa for unloading. Thus, after each stress reversal the distance measure from the current stress state to the reference surface is instantly increased and so is the soil stiffness (see also Sec. 3.1.8). However, this span hardly changes with increasing number of cycles, except for the small influence of the slowly decreasing void ratio on the state parameter, and hence the location of the bounding surface. Consequently, there is too little evolution in the plastic stiffness from one cycle to the next. Compared to the decelerating accumulation exhibited by corresponding experiments, this results in an exaggerated build-up of compressive strains termed ratcheting.

The newly introduced strategies for solving or at least attenuating this intrinsic problem manipulate the hardening rule by modifying the pre-factor h (e. g. Eq. (2.30)). h is, however, just a factor scaling the distance measure $\boldsymbol{\alpha^b} - \boldsymbol{\alpha}$, which is the actual constitutive element responsible for the state dependent plastic stiffness. Thus, it is the projection rule that should be considered deficient when it comes to cyclic loading. An alternative way to remedy the ratcheting issue would consequently be to rethink the definition of the distance measure.

Time-dependent effects

Besides the previous, more profoundly discussed insufficiencies of the bounding surface concept, there are further patterns of soil behaviour that cannot be reproduced with a model of this kind. The reason lies in the basic constitutive structure, which does not accommodate certain features. As a first example, there are numerous effects resulting from time dependence that are not included in the model: stress relaxation, creep, viscosity and (strain) rate dependence in strength and deformation processes. The model lacks a visco-plastic formulation of its constitutive laws in order to reproduce time dependent soil behaviour.

Linked to these time related properties, the effect of ageing can also be named, although the time scale is different and therefore modelling approaches rather use cementation mechanisms than viscosity. It generally is a strength enhancing process caused by the creation of additional or the hardening of existing interparticle bonds due to physico-chemical or microbiological processes or internal stress redistribution. Conversely, damage and destructuration mechanisms can be included to account for the degradation of cemented grain contacts.

Partial saturation

A second major soil property, which cannot be reproduced within the bounding surface modelling environment, is the mechanical behaviour of unsaturated soils. The mathematical formulation of equations does not contain any constitutive element to account for suction resulting from capillary forces due to partial saturation. Soil is only considered as a two phase medium and the supporting effect of additional suction stresses on the grain skeleton (resulting in apparent cohesion and tensile strength) is not regarded. Some sort of state variable would be required, tracing the matric suction pressure as difference between air and water pressure, which finally enters the calculation of the effective stresses, weighted by the degree of saturation. Following Bishop's proposal [Bis59, BB63] the effective stress is calculated according to

$$\sigma' = \sigma - p_{air} + \chi \cdot s \quad \text{with} \quad s = p_{air} - u \tag{3.58}$$

with χ being a function of the degree of saturation S_r. Besides, in the Barcelona Basic Model by Alonso et al. [AGJ90], for instance, an additional yield locus, the so called loading collapse curve, is introduced in stress-suction space (p-s plane) in order to increase the yield surface (p-q plane) in size and hence the soil's strength with increasing suction.

Aside from the stabilising effect of suction, the consideration of soil as a three-phase-medium also contains potential inclusions of gas in the pore fluid. The usual assumption of an incompressible pore fluid simplifies the reality of a fluid stiffness, which actually reduces when gas enters the fluid phase. This can have considerable effects on the soil behaviour in undrained loading cases, where the fluid stiffness has an important influence on the evolution of pore pressures (see also discussion on discrepancies in Sec. 5.1.2).

Grain breakage

Another feature disregarded in the bounding surface model concept is grain breakage. If soil is loaded to high stresses, particles start crushing and consequently the soil mechanical properties change. Research in this field has long been secondary, but it intensified within the last two decades. Muir Wood and Maeda [MM08] stated that in particular critical state conditions are strongly dependent on the available density ranges of packing and hence on the grading of the material. Their finding (resulting from DEM simulations) that grain breakage predominantly reduces the value of e_{cs0} has been confirmed by experimental data from Ghafghazi et al. [GSD14]. Moreover, some interesting ideas arose on how to take account of this phenomenon. Hicher and his group [YHD+16], for example, proposed to adapt the critical state line and the elastic stiffness according to the intensity of grain breakage using a correlation with plastic work.

3.3.2 Remaining shortcomings of the advanced model version

Elastic domain

One issue that is attributed to most bounding surface models of the first generation, as the one by Manzari and Dafalias [MD97], is the extent of the elastic region. The yield surface has the shape of a cone: reduced to a point at the origin and a widening diameter with increasing effective mean pressure. This implies that the circumference and hence the stress range of the elastic domain increases with the stress level. This assumption is corroborated by experimental evidence as for example provided by Wichtmann [Wic05], referring to Fig. 3.32: the amount of elastic straining on different triaxial compression paths starting from an anisotropic stress state along $\eta = 0.75$ increases with mean stress.
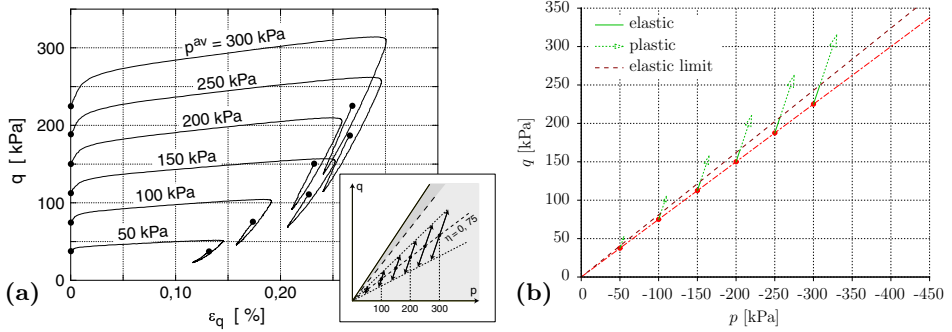
Figure 3.32: (a) Evolution of deviatoric strain in triaxial compression star-
ting from anisotropic stress states along $\eta = 0.75$, (b) identification of the
elastic limit in p-q stress space based on strain evolution of the loading
branch [according to Wic05]

Consequently, whether cyclic loading of the same stress amplitude takes
place at low or high stresses has a great impact on the resulting deformation
(see Fig. 3.33 a): in the first case, the cycles exhibit plastic deformation so
that irreversible strains will accumulate. However, due to the enlargement of
the yield surface, at significantly higher stresses the same cycles may happen
to be located entirely within the yield surface, so that the response will be
fully elastic and no permanent deformation will remain. Those cycles can
basically be oriented in any arbitrary way, but, of course, the effect is most
severe in stress paths with an inclination close to the actual back stress.
Imagine for example a q-constant stress path, cycling between two different
values of effective mean pressure, which might occur during the continuous
build-up and drop in pore water pressure in a fully saturated soil. A typical
case would be a static variation in the phreatic surface, which might be
due to lock operation or tide. At a sufficiently high mean stress level, a
rather low deviatoric stress amplitude and an inappropriate choice for the
cone opening these cycles might not leave the elastic domain.[10] Since it is a
purely isotropic load increment, as long as the charging/discharging process
remains elastic, shear deformations do not occur.

This simulated behaviour partly contradicts experimental observations.

---

[10]Stabilising/destabilising effects due to suction pressure caused by partial saturation
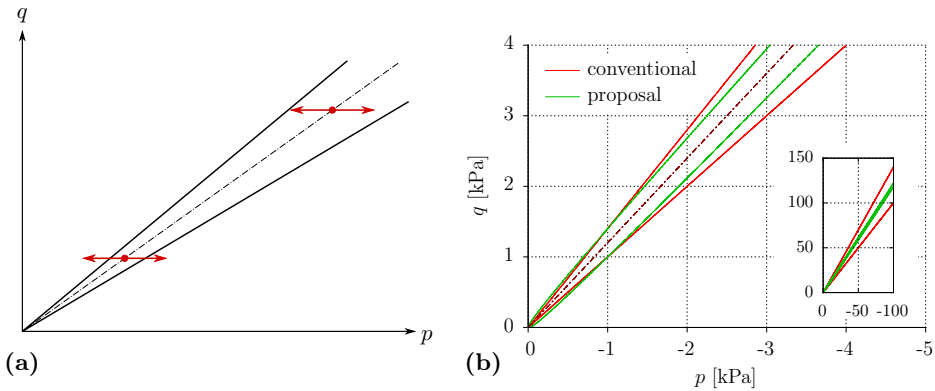possibly occurring during phreatic level movements are not concerned here.

Figure 3.33: (a) Stress path with pore water pressure variation at two different mean (effective) stress levels, (b) comparison of yield surface shapes: conventional cone (—) and slimming cone (—)

Wichtmann [Wic05], for example, carried out cyclic tests with varying inclinations and amplitudes of stress cycles, starting from a non-isotropic stress state (Fig. 3.34 a). For the q-constant cycles ($\alpha_{pq} = 0°$) the diagram in Fig. 3.34 b reveals accumulated deformations in both volumetric and deviatoric direction. This confirms the model behaviour – provided that the cycling violates the yield surface – because the occurrence of deviatoric strains is attributed to a change in back stress, which is linked to the generation of plastic strains. Unfortunately, this trend was not investigated for higher mean stresses at constant stress cycle amplitudes. But based on the general conclusion that deformations are accumulated in volumetric as well as deviatoric direction for the full range of tested amplitudes, it is likely that the size of the yield surface should be limited even at high stress levels in order to ensure the generation of plastic strains.

According to findings by several researchers (e. g. Hardin [Har78], Hicher et al. [HEH87], Vucetic [Vuc94], and Jardine et al. [JSB84]), fully reversible behaviour occurs up to a certain strain threshold, which is quantified by approximately 10^{-6} to 10^{-5}. The question whether this elastic limit strain is stress dependent or not is discussed ambivalently: investigations by Hicher et al. [HEH87] confirm an increase in elastic strain threshold with increasing mean stress, Lo Presti [Lo 95] negates the existence of dependency. However, the definition of an elastic domain in stress space by means of a yield surface can only be an approximation of the more or less constant strain

range. It is reasonable to assume that such a yield surface must take a shape that widens with increasing stress level, so that an opening cone seems to be an appropriate choice for a geometrical representation of the elastic domain in stress space. Though, this shape introduces some difficulties, as the problem of elastic strains at high pressures mentioned above, which is not necessarily in accordance with experimental evidence. The effect of this issue strongly depends on the choice of the opening parameter m_{cone} of the cone, which has an impact on the small strain behaviour in return. This problem is even intensified when considering an isotropic compression path starting from an anisotropic stress state within the elastic domain at very high pressures: an increasingly large stress increment is required to actually create plastic strains.

This issue could be accommodated by substitution of the linearity in the yield surface formulation by a sublinear equation, resulting in a "slimming cone" with a reduced widening (Fig. 3.33 b):

$$f^{cone} = \sqrt{(\boldsymbol{s} - p\boldsymbol{\alpha}) \cdot (\boldsymbol{s} - p\boldsymbol{\alpha})} - \sqrt{\frac{2}{3}} m_{cone} \sqrt{p} \qquad (3.59)$$

Alternatively, the concept of a yield surface could be discarded fully, as proposed within the context of small strain stiffness, and reduce the elastic domain to a line, creating very small but irreversible strains after changes in loading direction merely with the proposed small strain hardening mechanism.
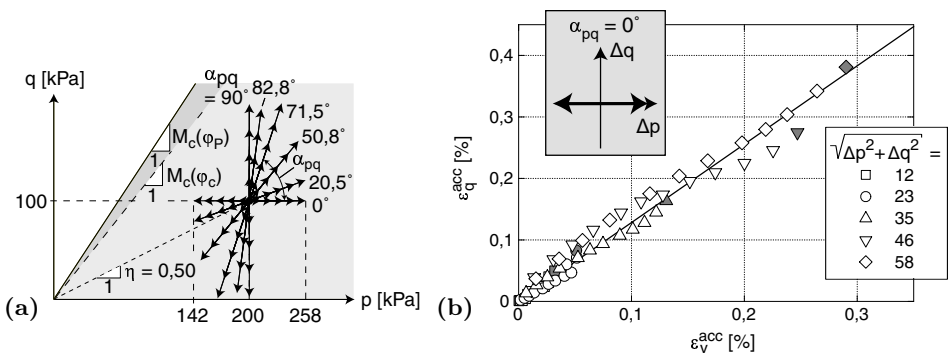

Figure 3.34: (a) Stress cycles of different inclination in p-q space, (b) accumulated volumetric and deviatoric strains for q = const. stress cycles of different initial stress states after 10000 cycles [modified after Wic05]

Inherent fabric anisotropy

Another aspect of insufficiently modelled soil behaviour is anisotropy. As noted in Sect. 3.1, the bounding surface concept is capable of accounting for stress induced anisotropy. Due to the multiaxial model formulation and the rotational kinematic hardening, the simulated soil response is dependent on the loading direction: the hardening parameters change with respect to the direction of applied stresses and hence the plastic stiffness and dilatancy variables control the resulting deformations accordingly. Besides, there is the feature of inherent fabric anisotropy that concerns the directional dependency of soil behaviour on the orientation of the grains and the interparticle contacts. This property is strongly linked to the micromechanics of the soil structure and is not included in the bounding surface on a constitutive level. As indicated in Chap. 2 in the context of small strain stiffness and dilatancy, there have been attempts to introduce fabric tensors representing and tracking the distribution and reorientation of the interparticle contacts (e. g. Oda [Oda72], Wan and Guo [WG04]). The usual procedure is then to transfer this tensorial quantity into a scalar in order to incorporate it into the constitutive equations controlling important behavioural patterns such as dilatancy, stiffness etc. Li and Dafalias [LD02], for instance, transformed the deviatoric fabric tensor $\boldsymbol{F}$ into a scalar fabric anisotropy variable A that enters the definition of a newly established dilatancy state line. As the fabric evolves towards its critical configuration (which is aligned with the deviatoric loading direction), the dilatancy state line converges with the critical state line. A modified state parameter ψ_A quantifies the distance from the new dilatancy state line to the current void ratio and replaces the old state parameter in all other constitutive equations, so that the fabric state affects all important aspects of soil behaviour.

The foundation of the described concept is a properly defined initial fabric state, an appropriate evolution law for the fabric tensor and well-founded correlations to the other constitutive equations. It has already been indicated that this is still a challenge of micromechanical research and a satisfying solution has not yet been found. This is the reason why the author has decided not to incorporate such a mechanism into the present model version. Consequently, the influence of inherent anisotropy on the deformation process cannot be reproduced.

Application to cohesive soils

Although the title of this work clearly states that the presented bounding surface model aims for the application to sands, it should be stated that the model can be equally used for the simulation of clay. However, there are some aspects that confine the application to clays or cohesive soils in general, which will be pointed out in the following.

It is not the bounding surface concept that disqualifies the model for clays – there are actually models based on bounding surface plasticity, which are dedicated for cohesive materials, such as the SANICLAY model family introduced by Dafalias et al. [DMP06] and advanced for bounding surface plasticity by Seidalinov and Taiebat [ST14]. What distinguishes the two types of soils, is mainly their yielding behaviour and the consequent shape of their respective elastic domain. Due to the different character of rounded sand grains compared to flaky clay particles significant irrecoverable deformations within geotechnically relevant stress ranges are produced by different loadings. Sands deform plastically mainly if stress ratio changes occur in shear loadings, resulting from the rearrangement of the grains, whereas plastic strains due to constant stress ratio loadings are minor.[11] Clays on the other hand exhibit substantial irreversible strains particularly when loaded in (isotropic) compression, or generally, along constant stress ratio paths. Experimental observations by Smith et al. [SJH92] deduced from stress probe tests on Bothkennar clay have indicated that the region of reversible straining ("Y_2 surface") is bounded by an approximately circular to elliptical surface. This dissimilar deformational response could be accommodated with corresponding yield surface shapes, which resemble slender cones for sands and look rather bulky for clays. However, the shape of the yield surface is not a criterion for exclusion: the different appearance of the elastic range for clays can also be achieved by a wider opening of the cone, controlled by m_{cone}, in combination with the additional cap and potentially a revision of the hardening rules.

Furthermore, in case of sand the important hardening mechanism is a kinematic one (translating/rotating yield surface) in order to account for stress anisotropy. Clayey soils require isotropic hardening/softening (expanding/shrinking yield surface) in addition for capturing restructuration

---

[11]Compressive stresses (e.g. isotropic, oedometric) play a role in case of very loose sands or at large mean stresses. Hence they cannot generally be neglected, which was the reason for the introduction of the second cap shaped yield surface.

processes in sensitive clays (bond increase/degradation). In most constitutive approaches [e. g. GN93, BS04, TDP10] the size of the yield surface is made a function of the amount of damage to bonding (between particles) during plastic straining, contrasting natural (bonded) with intrinsic (unbonded) material.[12] If this structure loss, however, does not dominate the behaviour of the cohesive soil in question, the extended bounding surface model can still be an appropriate choice.

When shifting the focus from yielding to failure, cohesion as an additional portion of strength, which is assumed to be present at zero normal stress, comes into play. Distinction can be made between true and apparent cohesion, of which the former can be considered a soil property originating from electro-chemical bonds between the clay particles or from cementation processes. Apparent cohesion on the other hand mainly concerns capillary attraction forces due to interstitial water in unsaturated soils (suction), which get lost upon wetting or drying. The proposed bounding surface model does not offer a mean to include cohesion – neither true nor apparent[13] – into the failure criterion. The resulting failure envelopes have a hyperbolic shape, following the critical state line at higher stresses and leaving it for relatively higher strength values at lower stresses, being crooked towards the origin (see Fig. 3.4). The last characteristic accounts for the increased frictional resistance at lower stresses.

When comparing the model outcome for sand to experimental clay data, a very similar behaviour can actually be observed: there is strong indication that, in contrast to the usual assumption of the classical linear Mohr-Coulomb criterion, defined by φ and c, (true) cohesion in its conventional meaning does not exist (e. g. de Mello [dMel77], Atkinson and Farrar [AF85], Baker [Bak04], and Bergholz and Herle [BH17]). The alternative Hvorslev strength relationship [Hvo37] proposes a tripartition: density dependent failure lines spanning between CSL and no-tension line ($q = 3p$ in triaxial compression), the latter ensuring the condition of zero effective radial stress assuming that soil cannot withstand tensile stresses (Fig. 3.35). This representation qualitatively resembles the outcome of the proposed bounding surface model, so that describing the failure state without a co-

---

[12]Based on this, the necessity for isotropic hardening might not be limited to clays, but also come into consideration for cemented sands.

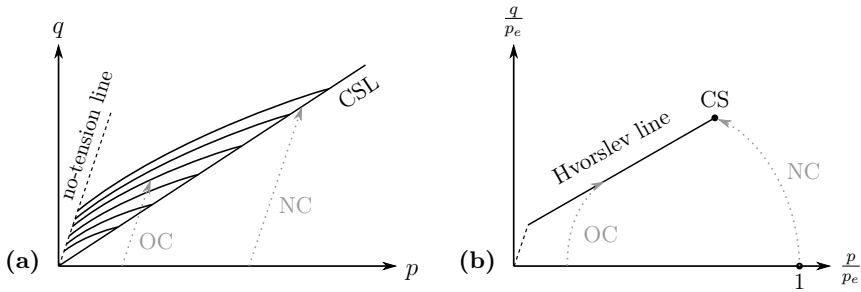[13]See Sect. 3.3.1 for further notes on the inability of capturing apparent cohesion due to partial saturation.

Figure 3.35: Composed failure surface as proposed by Hvorslev [Hvo37]: (a) multiple failure lines in p-q space, reducing to (b) one single Hvorslev failure line spanning between no-tension line and critical state locus (CS) in normalized p/p_e-q/p_e space (see also Sec. 2.1.1)

hesion c is basically possible, although the curvature might not be crooked enough and hence the gain in strength on the overconsolidated side too low. Alternatively, if the "cohesive" effect was not sufficient, one might consider shifting the intersection of the model surfaces along the x-axis to the extension side by the amount $c \cdot \cot \varphi$, or even introducing a non-linear expression for the bounding surface having a similar effect and respecting the no-tension postulation.

To conclude, despite some constitutive elements, which were originally intended for the application of the model to sand – the slim cone, purely kinematic hardening, no cohesion – the extended bounding surface model can also be used for cohesive soils, respecting the constraints given above. Most characteristics of clay can be accommodated satisfactorily by adapting the corresponding model parameters or by minor constitutive changes (e.g. "cohesion shift"). Consequently, depending on the intended use (soil properties, loading path etc.), this model might still capture the behaviour of clay with sufficient accuracy.

3.3.3 Newly introduced deficiencies

Hardening mechanism of the cap yield surface

As described in Sect. 2.2, the modified model has been extended by a second yield surface in the shape of a cap, closing the elastic domain with respect to compressive stress paths. In contrast to the cone, the cap is not a kinematically hardening yield surface that rotates in stress space, but hardens isotropically by remaining centred at the origin and expanding equally

in all directions. Of course, this already enables the model to produce plastic strains in compressive loadings (e. g. isotropic, oedometric), which is a decisive improvement with regard to the previously implemented open cone resulting in purely elastic strains. It also allows for capturing overconsolidated stress states of soil, reflecting its previous loading history. But due to the type of hardening, the cap does not retract in unloading. Consequently, discharging a soil element effects only elastic strain, which equally applies for reloading until the pre-consolidation pressure is exceeded and the primary loading branch is resumed. This means that the initial non-linear stress-strain curve will be followed by an elastic and hence (almost) linear unloading and reloading path – the only non-linearity resulting from the stress dependence of the elastic stiffness.

It can be concluded that in monotonic loadings at constant stress ratio, the cap clearly has its merits since it allows for irreversible strains and hence distinct stiffnesses in (primary) loading and unloading – contrary to the original model version. However, with respect to cyclic compressive loadings, after the initial primary loading the hardened cap has no further effect on the stress-strain evolution: repeated un- and reloadings will remain purely elastic and hence will not accumulate any further plastic deformation (as long as the stress level remains under the pre-consolidation pressure). Consequently, besides the first loading the reproduced cyclic behaviour most likely is too stiff – as stiff as if no cap had been introduced. Thus, opposed to cyclic shear, the model might be considered less suitable for repeated loadings at constant stress ratio.

However, one has to admit that soil accumulates far less plastic strain in cyclic compression than in cyclic shear. Ko and Scott [KS67], for example, found out that, generally, isotropic compression causes non-linear but almost elastic strains, because the stress-strain evolution stabilises after very few cycles. Hence, further cycles will not increase the total irreversible deformation considerably. According to their experimental investigations, laterally constrained one-dimensional compression (oedometer) exhibits a significantly larger amount of plastic strains (Fig. 3.36 a). Cyclic data from Mróz et al. [MNZ79], however, has shown that the material progressively densifies but reaches a steady state already after a few cycles (Fig. 3.36 b). Equally, Muir Wood [Mui90] states that oedometric cycles below the pre-consolidation pressure are essentially elastic and the stress-strain hysteresis is insignificant. Thus, the strain accumulation in cyclic oedometric loading (or constant stress ratio loadings in general) is practically negligible and
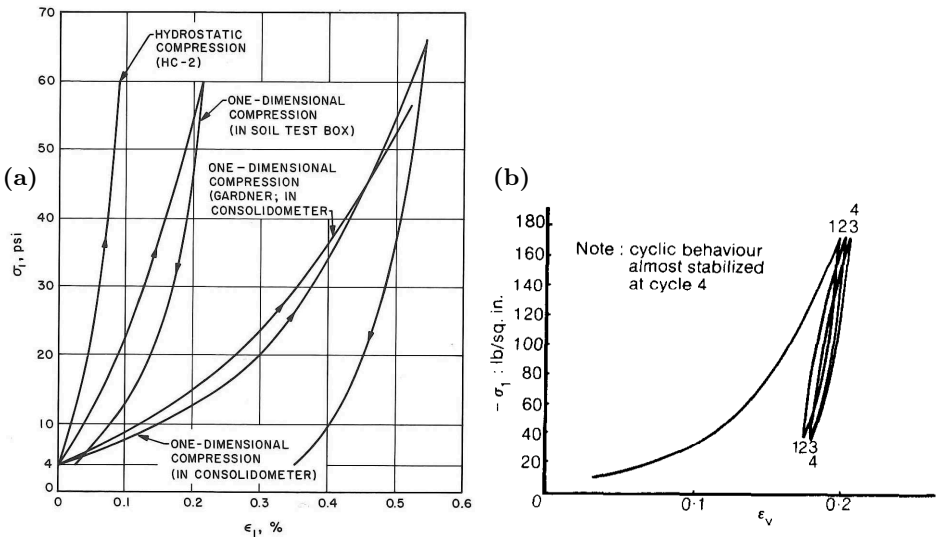
Figure 3.36: (a) Comparison of stress-strain response in isotropic (hydrostatic) and one-dimensional compression [KS67], (b) cyclic one-dimensional compression [MNZ79]

consequently an isotropic hardening mechanism is a reasonable choice for the cap yield surface.

Another more fundamental aspect is less concerned with the numerical background of the cap yield surface, but rather with the stress range of applicability. As stated in Sec. 3.2.3, this constitutive element becomes particularly valuable in case of loose states or very high pressures. At low stress levels, volume changes are attributed to elastic deformation of the soil skeleton and particle rearrangements (sliding, rolling), whereas the occurrence of high stresses is accompanied by crushing of the grains [e. g. RdS58, PW95]. These two deformation mechanisms control the compressibility of a sand, which appears as a more or less pronounced change of stiffness with increasing stress. The sand's susceptibility to grain breakage and hence the location of this transition in stress-strain space depends on various factors: the soil's physical properties (particle size, angularity and uniformity) [LF67], its mineralogical composition [YBL96] as well as the portion of shear stress in anisotropic consolidation [LF67, LY93]. Due to the strong variation, it is not possible to generalise the breakage behaviour, but for most sands this transition between the two mechanisms takes place

roughly between 1 and 10 MPa.

It has to be noted that grain breakage and fragmentation imply a change of the soil's physical properties, particularly its grain size distribution and angularity, which leads to a modification of the soil mechanical properties as well. However, there are no constitutive means included in the model formulation to account for potential changes in stiffness (or strength) due to particle crushing (see also Sec. 3.3.1). Consequently, from the onset of grain breakage the computed soil response is actually based on wrong assumptions. The cap yield surface is hence a sound mean for predicting plastic deformations within typical stress ranges of geotechnical engineering (≤ 1 MPa), but simulation results beyond the point, where grain crushing dominates the deformational behaviour, have to be interpreted with care, particularly if other loadings follow.

The limiting compression curve (LCC) concept, developed by Pestana and Whittle [PW95] and described in Sec. 2.2.2, offers one approach to face this inconsistency. It treats both compression mechanisms (particle rearrangement and breakage) as one and merges all irreversible deformations as plastic strains, evolving as a function of the distance between the current stress and its image on the LCC. Consequently, the soil's state approaches the LCC asymptotically and the location and appearance of the stiffness change is controlled by the corresponding parameters. Thus, the LCC concept does not take particle breakage into account explicitly, but determines irrecoverable deformations in a "smeared" way on the basis of the initial physical and mechanical soil properties.

Nevertheless, one has to be aware that, when continuing loading on a different stress path after oedometric (or isotropic) compression up to the grain crushing regime, based on the altered particle size distribution the shearing characteristics might differ from those of the initial soil configuration. However, after determining the grading of one-dimensionally compressed sands at different loading stages, Nakata et al. [NHH+01] proposed the existence of a critical particle size distribution, towards which the grading curves evolve and for which no further particle crushing occurs. Consequently, the mentioned limitation with respect to altered mechanical properties due to grain crushing seems to have a natural limit.

Superposition of hardening mechanisms

Relating to the new hardening mechanisms, one has to object that although
the different options can be switched on and off, they cannot be activated
and combined arbitrarily without reconsidering the choice of parameters.
This applies mainly to the hardening component of the fabric evolution
mechanism when it comes to cyclic loading: the increased plastic modulus as
a function of the dissipated energy enhances the stiffening of loose soils with
progressive shear cycles. This effect adds to the void ratio and the stress
level dependent plastic stiffness already included in the basic hardening rule
by Manzari and Dafalias [MD97] via the state parameter (Eqs. (2.24), (2.26)
and (2.30) ff.). Since the new fabric hardening option is already active on
the first loading branch of a cyclic loading scheme, which corresponds to a
monotonic loading if considered in isolation, the fabric parameters have to
be chosen sensibly, so that the mechanism does not yet have a noticeable
effect on this initial loading. This is mainly a matter of the modelled stress
and strain range, as will be shown in Sect. 5.3.

Similarly, if the basic model is used for repeated loadings, the enhanced
stiffness after each reversal is respected by the choice of a correspondingly
large elastic domain (parameter m_{cone}). Straight after violating the cone
yield surface for the first time, overall stiffness drops significantly and har-
dening proceeds according to the original formulation. Activating the small
strain stiffness mechanism, the initial plastic modulus drops from a much
higher level so that the strain range of high, quasi-elastic stiffness is exten-
ded into the plastic domain. This stiffening effect adds to the potentially
activated fabric hardening mechanism. The same applies for the third har-
dening option with respect to the minimum void ratio. After all, these
stiffening effects can even be counteracted by the second, dilatancy related
fabric mechanism, causing compliance. Thus, the stress - strain response for
a particular stage in the complex (or cyclic) stress path will differ depending
on the chosen hardening options and their corresponding parameters.

In summary, it has to be taken into consideration that the different harde-
ning mechanisms need to be coupled with care. It is advisable to follow a
certain order of calibration when activating the model extensions. Recom-
mendations are given in Sect. 4.2.

High-cyclic loading

Having already pointed at the cyclic accumulation mechanism, a supplemental comment needs to be made on the range of application it is aimed at. In general, a kinematically hardening elastoplastic model in combination with the concept of bounding surfaces is convenient for reproducing reversed loading: loading with an initially high stiffness, degrading with further straining, and regaining the initial stiffness at each reversal before its reduction recommences. As long as only very few cycles are simulated, the basic version of bounding surface plasticity delivers satisfactory results. But if phenomena such as shakedown, incremental collapse or liquefaction are to be modelled, an additional mechanism is required in order to increase or decrease the accumulation effect with advancing cycles. Examples for possible solutions were presented in Sect. 3.2.5: based on either the accumulated plastic volumetric strain or the dissipated energy, the hardening modulus is scaled up or down steadily. Theoretically, once properly calibrated it could be applied to a large number of cycles. Practically, calculating cycle by cycle implies a comparably high numerical effort, potentially involving the risk of an increasing numerical error [NWP$^+$05]. That is why Niemunis and his group proposed to use so called explicit strategies for high-cyclic loadings ($N > 1000$) in combination with conventional implicit methods [NWT05].[14] This means that the simulation starts with the implicit calculation of a few initial cycles with the underlying constitutive model – in their case the hypoplastic model. Subsequently, a large package of cycles is treated explicitly with a particular constitutive formulation for high-cycle accumulation (**H**igh-**C**ycle **A**ccumulation model). The handling of an amount of ΔN cycles of a given strain amplitude can be compared to the creep deformation due to a time increment Δt in viscoplastic models, N substituting for t. Without calculating the strain of each cycle implicitly, the accumulation rate is determined explicitly on the basis of the initially identified strain amplitude, assuming it being constant for the package of cycles. Afterwards, another implicit control cycle needs to follow in order to recalculate the strain amplitude, which might have changed in the meantime due to compaction or redistribution of stress, serving as a basis for the subsequent package of explicitly determined cycles. The calculation process of this hybrid method is depicted in Fig. 3.37.

---

[14]Time integration methods are not meant here, which are also called "implicit" and "explicit". The two terms refer to the calculation strategies of low-cycle (implicit) and high-cycle (explicit) loadings.
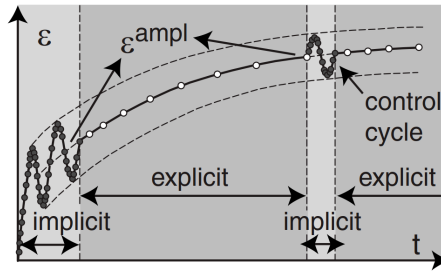
Figure 3.37: Combined implicit-explicit strain calculation with the High-Cycle Accumulation model by Niemunis et al. [NWT05] [taken from WNT09]

Closely related to this strategy, Benz et al. [BSV05] raised the idea of an extrapolation algorithm for load cycles. Based on a proposal by Foerch et al. [FGM$^+$00], the deformation and state variable evolution of a few implicitly calculated initial load cycles are extrapolated by a Taylor series expansion for a certain amount of cycles. The skipped cycles are then followed by a re-equilibrium step similar to the previously mentioned control cycle before the next extrapolation unit succeeds.

Since a high-cycle accumulation mechanism along the lines of the described algorithms is not included in the extended bounding surface model, the application to a very high number of cycles is strenuous and not recommended with regard to numerical accuracy.

4 The numerical model and its calibration procedure

After a thorough description of the new model – an extended version of the family of bounding surface models, including a comprehensive explanation of its features and also a critical analysis of its weaknesses or limitations – in this chapter the model is examined in the light of its practical application. For the purpose of testing, the model has been implemented in two different environments. In order to investigate its performance with respect to fundamental behavioural patterns, as described in Sect. 3.1, it is useful to simulate very basic soil tests and compare the achieved results with experimental data. Is the model capable of reproducing well-known properties qualitatively? And if the simulation generally captures the soil behaviour, is it also in accordance with the experiments quantitatively?

These questions in mind, a rather simple computational programme has been set up based on the constitutive law that is able to calculate soil tests of different kind, to combine single tests to a series and hence realise not only monotonic loadings but also load reversals and cyclic loading schemes (Sect. 4.1). This way the functionalities of the model could be tested excessively, which also helped to detect unexpected deficiencies that had not yet been identified by theoretical considerations. In some cases, after the discovery of insufficiencies the attempt to remedy these problems led to modifications and advancements that can now be considered part of the new model features of the extended version.

Besides the technical aspects, a material model also needs to fulfil the practical requirements of application. It needs to be accessible to the designing engineer with regard to its availability as numerical tool. An implementation into a widely used FEM software is needed, ideally in an open source environment, but at least in the form of a freely available user-defined soil

model that can be linked to the library of a commercial software. The open source concept might also encourage users to take part in the development process by independently adapting the code to their needs and hence advancing the material model for the community. This idea is in line with the call for a freely available constitutive model database issued earlier by the *soilmodels.info* group [GAG+08]. In addition to the aspect of accessibility, for successfully establishing a model in routine design, its numerical robustness in boundary value problems needs to be ensured. This is a point that might also benefit from the idea of open source.

Based on these thoughts, in a next step, the implementation of the constitutive model as a user-defined soil model (UDSM, UMAT) will be completed for application in engineering FEM software such as PLAXIS or Abaqus in order to not being restricted to element tests and extend the investigations to boundary value problems. In this context a calibration routine has been developed that allows replacing bounding surface specific input parameters by more physical or familiar quantities in order to ease the application of the model. This auxiliary tool is presented and discussed in Sect. 4.2. Nevertheless, the results shown in this work were all generated using the element test programme.

Before a constitutive model, as the heart piece of a numerical analysis, can be used for a simulation, its set of parameters needs to be carefully chosen. The mentioned calibration tool is meant to facilitate a first very rough estimation. Its intention is not to spare the user the effort of calibration. Whenever an analysis is to be carried out, a calibration of the involved parameters is an inevitable first – or in this case second – step. Since there is no unique choice for the parameter set for one particular soil, the calibration procedure is an optimisation process with respect to the boundary and loading conditions to be reproduced. In Sect. 4.2 a step by step description is given for the determination of the model parameters on the basis of an exemplary set of experimental data for three different sands. The reader will be given advice on the minimum information that needs to be provided on the soil to be simulated in order to ensure a solid basis for the calibration and further calculations. Distinction is made between the preparatory measures for the application of the original model and which information is required additionally for calibrating the features of the model extension.

4.1 Octave implementation of an element test programme

As mentioned in the introductory section, a rather simply structured testing routine, initially on the basis of the original constitutive model, was implemented using the software GNU Octave, which features a high-level programming language based on the C++ standard library (similar to MATLAB). The intention was to create a tool easing the development process, capable of simulating standard stress paths in order to examine the model's behaviour with respect to usual loading conditions. The most common procedure in constitutive modelling is to test fundamental behavioural patterns (reflected by corresponding stress paths) by running soil test simulations. Assuming that certain standard laboratory tests, triaxial tests in particular, induce fully homogeneous deformations, where each point within the soil sample is loaded equally, they can be considered as element tests (see also Sect. 1.1). Thus, the computer code simulates the loading of only one representative element (one stress point within the sample) under the given test conditions. The resulting deformation can be transferred to an ideal specimen with a uniform stress and strain field, remaining perfectly cylindrical during the whole test. However, especially at large strains these conditions are not necessarily fulfilled due to end restraint, insufficient drainage or membrane effects and a triaxial sample deforms into a barrel shape, for instance. Consequently, the comparison of simulated element tests with experimental data has to be evaluated with care.

For the purpose of element test simulations a non-commercial constitutive driver has been used, developed by Tamagnini in 2012 [Tam12]. Originally intended for teaching purposes within constitutive soil modelling, the constitutive driver is a powerful tool for development, evaluation and parameter identification of material models. The core piece of the driver provides the explicit integration procedure and calculates the stress-strain behaviour according to the incremental elastoplastic constitutive equations defined in the attached material model routines. Correspondingly, the bounding surface concept has been implemented, thoroughly tested and extended gradually during the development process.

In the following the Octave implementation of the constitutive driver and the material model are described in more detail. The former consists of a main routine – the control unit calling the subordinate parts of the programme such as input, initialisation, calculation and postprocessing – and
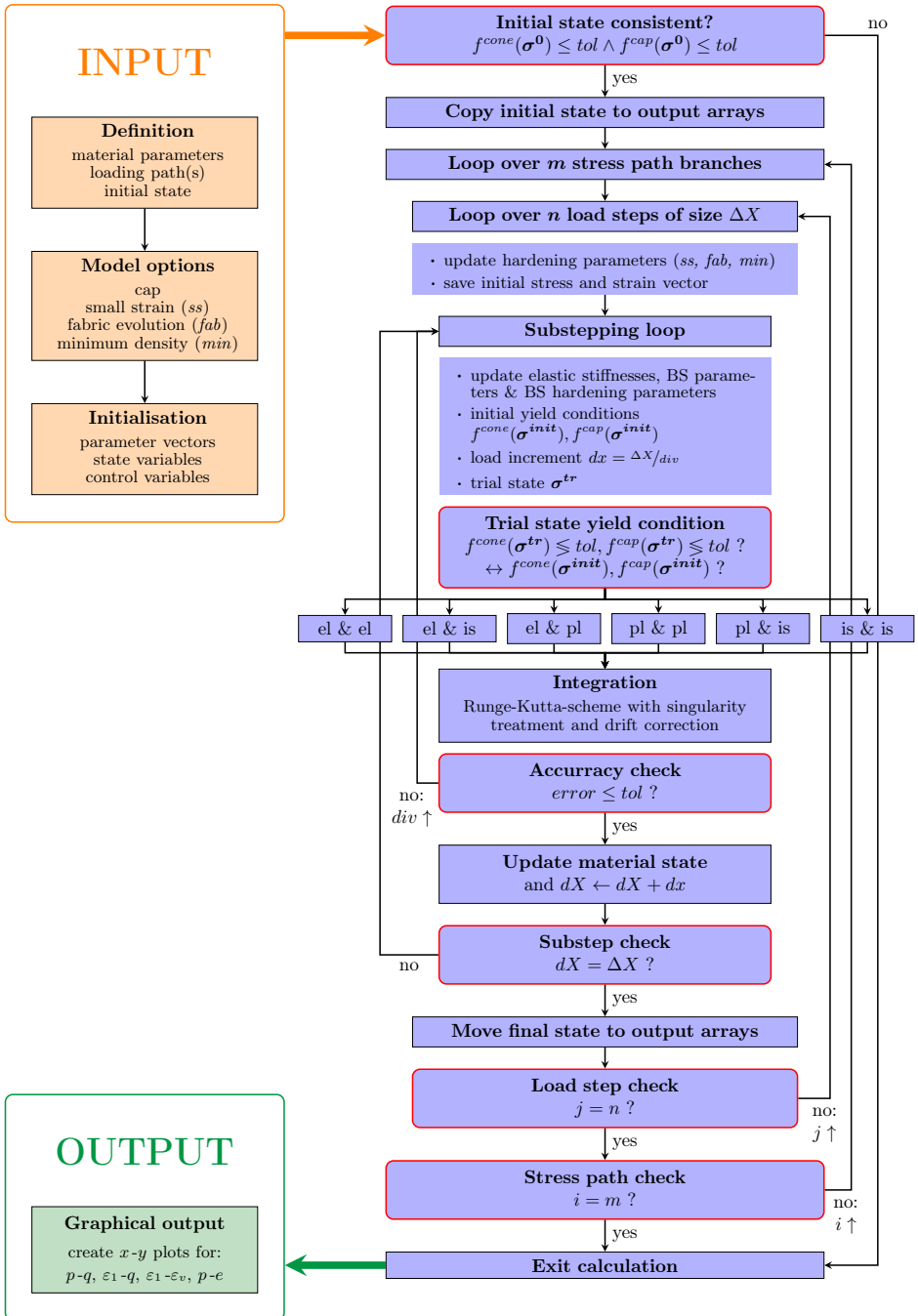
Figure 4.1: Conception of the constitutive driver

the subroutines containing the corresponding data and commands. Figure 4.1 presents the structure of the constitutive driver in a simplified flow chart, including the integration loop and linked subroutines.

In the *input section* the user defines all material model related parameters and numerical constants (e. g. error tolerances, maximal number of substeps) as well as the initial state. In addition, the characteristics of the loading path are specified: type of loading for assigning the proper boundary conditions (e. g. drained and undrained triaxial compression, isotropic compression, oedometric compression, stress paths of arbitrary inclination in p-q space), total load increment (stress or strain, depending on the chosen test control) and number of load steps. If desired, the loading path can consist of several branches as to simulate more complex stress paths or load reversals. Furthermore, certain constitutive features can be selected or deactivated such as small strain stiffness or the cap yield surface.

After the initialisation of the state variables according to the user-defined input, the *integration procedure* as the constitutive driver's heart piece is entered. It is constructed like two nested loops over the user-defined number of stress path branches and load steps. The procedure itself applies a numerical technique proposed by Bardet and Choucair [BC91]: the loading constraints of laboratory experiments with respect to stress and strain are linearised, coupled with the constitutive relations and transferred into a linear system of differential equations:

$$\boldsymbol{S} : \dot{\boldsymbol{\sigma}} + \boldsymbol{E} : \dot{\boldsymbol{\varepsilon}} = \dot{\boldsymbol{V}} \tag{4.1}$$

For this purpose, the symmetric stress and strain tensors are transformed into vectorial notation (Voigt notation). $\boldsymbol{S}$ and $\boldsymbol{E}$ represent the coefficient matrices containing the loading constraints and $\boldsymbol{V}$ defines the resulting loading vector. This system of six linear equations for six unknowns (provided that the stress increment is a function of the strain increment) is finally solved for the strain increment and subsequently the stress increment is found:

$$\begin{cases} (\boldsymbol{S} \cdot \boldsymbol{D}^{ep} + \boldsymbol{E}) \cdot \dot{\boldsymbol{\varepsilon}} = \dot{\boldsymbol{V}} \\ \dot{\boldsymbol{\sigma}} = \boldsymbol{D}^{ep} \cdot \dot{\boldsymbol{\varepsilon}} \end{cases} \tag{4.2}$$

The $\boldsymbol{S}$ and $\boldsymbol{E}$ constraint matrices as well as the loading vector required for the simulated laboratory tests within this work can be found in App. A.4.

For the solution of the system of equations, an explicit adaptive Runge-Kutta integration scheme combined with a substepping algorithm according to Sloan [Slo87] has been implemented by Tamagnini [Tam12]. In this

case, the computed solutions of two Runge-Kutta-schemes of different order (second and third) are compared for estimating the substep size, which would provide a solution with the desired accuracy. In order to improve solution accuracy and to stabilise the calculation process, but also to correct for user-defined step sizes that have been chosen too large for the loading case to be simulated, an additional inner substepping loop was added by the author. It further divides the current step size, if the solution does not comply with the tolerated numerical error.
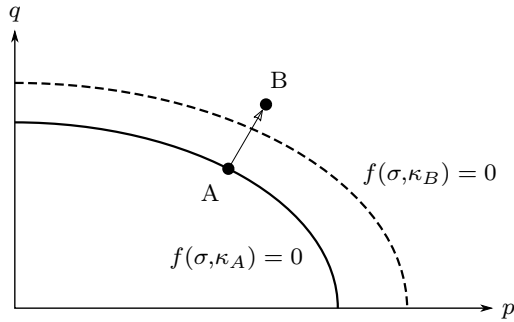

Figure 4.2: Yield surface drift [acc. MAK97]

Besides, in explicit methods the so called yield surface drift is an inevitable phenomenon destabilising the numerical integration process: the predicted stress state at the end of a plastic integration step is not necessarily located on the yield surface updated according to the hardening law (Fig. 4.2). In the present model version a drift correction according to Mattsson et al. [MAK97] at the end of each integration step adds supplementary accuracy. It is based on a study by Potts and Gens [PG85] but extends the drift correction algorithm from strain control to mixed control (stress and strain controlled). This is particularly interesting in the simulation of conventional triaxial tests by means of constitutive drivers where confining stress and vertical strain are often used as control variables (e. g. triaxial compression: $\Delta\sigma_2 = \Delta\sigma_3 = 0$, $\Delta\varepsilon_1 = \Delta\varepsilon$).

Due to the combination of two yield surfaces, cone and cap, the integration process had to be adapted in order to take account of the event that both yield surfaces are activated simultaneously. An internal switch for the type of integration procedure depending on the activation of yield surfaces was required. There are several aspects that need to be considered. First of all, whenever the load increment causes an elastoplastic response, the calcula-

tion loop determines the intersection point with the violated yield surface and the corresponding elastic strain first. In a second step, the plastic contribution of deformation is computed, applying the appropriate integration rules. If the initial position of the stress point lies on the border of the yield surface (or outside but still within the error tolerances (tol_f)), an intersection point does not need to be determined (or does not even exist) and the soil response consists of a plastic strain contribution only. From this follows that there are three combinations of locations of the initial (f^{init}) and the trial stress (f^{trial}) with reference to the respective yield surface that need to be taken into consideration:

- "elastic" = initial and trial state within the yield surface:

$$f^{trial} < tol_f$$

- "intersect" = initial state inside, trial state outside the initial yield surface:

$$-f^{init} > 0 \quad \wedge \quad f^{trial} > tol_f$$

- "plastic" = initial state on the yield surface (or outside within the error tolerance), trial state outside the initial yield surface:

$$\text{(all remaining cases)}$$

Furthermore, depending on the number of activated yield surfaces there are finally six cases to be distinguished when specifying the integration procedure, depicted in Fig. 4.3.
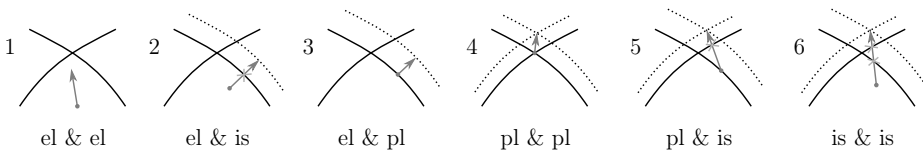
Figure 4.3: Case differentiation for the numerical treatment of the integration procedure

In case 1, no yield surface is crossed, the stress state remains elastic and no plastic contribution occurs. Case 2 corresponds to the usual event of violating one yield surface by intersection, which is solved as described in the previous paragraph. Case 3 is the already mentioned reduced version of case 2, since detecting of the intersection point can be omitted. The second

case can basically be considered as a succession of case 1 and 3. Concerning
the latter two cases, where only one surface is violated (case 2 and 3), it
needs to be noted that each surface hardens isolated from the other: the
hardening of the two surfaces is decoupled.

The fourth case requires a new solution strategy, since the violation of both
surfaces activates the singularity at the corner point where cap and cone
are joining. An integration algorithm for singular yield surfaces according
to de Borst [dBor87] has been implemented, which is based on Koiter's rule
[Koi53], stating that in case of two active yield surfaces the plastic strain
rate composes of both contributions as follows:

$$\dot{\varepsilon} = \lambda_1 \frac{\partial g_1}{\partial \sigma} + \lambda_2 \frac{\partial g_2}{\partial \sigma} \tag{4.3}$$

g_i are the plastic potentials belonging to the two yield functions and λ_i the
respective plastic multipliers. The geometric representation of Koiter's non-
associated flow rule (Eq. (4.3)), valid at a corner point of two intersecting
yield surfaces, is depicted in Fig. 4.4.
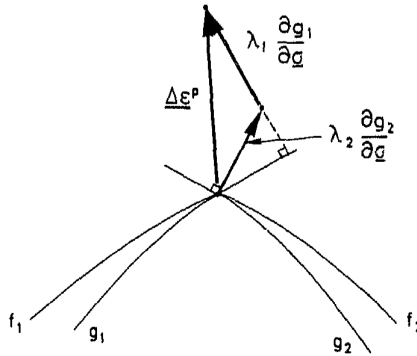
Figure 4.4: Plastic flow at a singular point in the yield surface [dBor87]

Combining this flow rule for singular yield surfaces with basic equations of
elastoplasticity (App. A.1) gives the stress rate:

$$\dot{\boldsymbol{\sigma}} = \boldsymbol{D}^{el} \cdot \left(\dot{\varepsilon} - \lambda_1 \frac{\partial g_1}{\partial \sigma} - \lambda_2 \frac{\partial g_2}{\partial \sigma} \right) \tag{4.4}$$

Applying Eq. (4.4) and satisfying the consistency conditions for the first
as well as the second yield surface ($f_i = 0$), results in a set of equations,
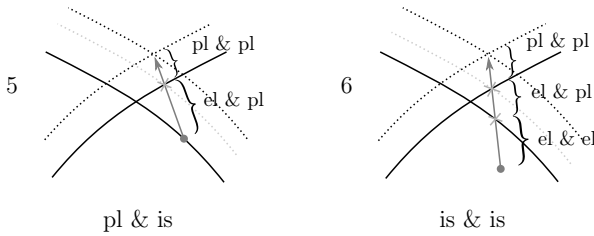
Figure 4.5: Two special cases in the integration procedure

which can be solved for the plastic multipliers λ_1 and λ_2. These finally allow determining the elastoplastic stiffness matrix $\boldsymbol{D^{ep}}$ for yield surfaces with singularities required for the solution of the previously formed system of equations (Eq. (4.2)). The complete derivation of $\boldsymbol{D^{ep}}$ is given in App. A.3.

Returning to Fig. 4.3 after having explained the numerical handling of two active yield surfaces (case 4), the two last cases are particular, since they are divided into substeps of the previous types and treated successively in the calculation process, as depicted in Fig. 4.5. If the initial stress state lies in the elastic domain and is forced to cross both yield surfaces by the applied load increment (case 6), then the intersection points with both are determined first. Based on the distance of the closest yield surface, the elastic deformation is calculated, representing an elastic step according to case 1. Afterwards, the plastic strain contribution of this first violated surface is determined up to the intersection point with the second one, which corresponds to case 3. Finally, the last substep can be compared to case 4, so that the combined effect of both yield surfaces will be taken into account during the hardening process. Again, case 5 is technically a reduction of case 6, starting directly from the border of the closest yield surface with a substep of type 3, without an initial purely elastic step.

Once an iteration step has passed the accuracy check, the material state (stress, strain, state variables) is updated and the next step follows until the substepping procedure is completed for one load step. Before a new load increment is applied, the last updated material state is transferred to the output arrays, required for post-processing the simulated data after the last stress path branch has been computed.

In the last part of the programme, the *output section*, the results that have been stored throughout the calculation process are visualised by means of diagrams tracing the evolution of stress, strain and other state variables

with loading. For this purpose Octave is internally coupled with gnuplot, another GNU software designed for the graphical representation of data. All resulting data is stored in ASCII files and the produced graphs are directed to image files.

To summarise the presented constitutive driver, its features and merits, the decisive advantage of this type of testing tool is its accessibility and straightforward implementation. Since the underlying constitutive driver was programmed in a freeware environment, it is possible to access and modify the code and to extend it to the application of additional material models such as the bounding surface model. The structure of the implementation (main routine as well as subroutines for parameter input and constitutive equations) is clear and hence easy to understand and manipulate. The programme is restricted to element tests on purpose, without additional code for complex simulation cases or further sophisticated options, so that it does not lose its simplicity and remains a basic but efficient constitutive modelling tool. Moreover, the explicit integration algorithm allows for a higher numerical stability if sufficiently small integration steps are chosen, which can be valuable particularly in the development process of a material model.

4.2   Calibration procedure

The intention of establishing the constitutive driver was presented in the previous chapter. One of its most important advantages is its application as a tool for verifying constitutive models by comparing simulated with experimental data qualitatively as done in Chap. 3. In addition, it is a useful auxiliary mean for calibrating material models for their use in FE analyses. Element tests as carried out in laboratory experiments can be simulated with little computational effort, easily reproduced and repeated arbitrarily often with different material parameters and initial states until a satisfying parameter set for the soil in question is found. The constitutive driver can even be coupled with an optimisation routine that undertakes the parameter calibration automatically up to a certain point, as for example realised by Mattsson [Mat99]. A basically similar but simpler version will be introduced in this chapter.

Although a tool for deriving a first rough estimation for an appropriate parameter set is available, it by no means replaces an adequate calibration by the user. That is why the entire subchapter is dedicated to the calibration

procedure of material parameters. Three sands will be introduced in the following section – Toyoura sand, Sacramento River sand and Hostun sand – that were used for manually optimising the parameters for experimental data provided in literature. Subsequently, it will be demonstrated how to actually determine proper values for the material parameters: the required type of laboratory experiments and deduced physical properties, enriched by a recommended order in parameter calibration due to interrelations, as well as indications with respect to sensitivities of certain parameters to divergences. The latter mainly concerns cases where values are intentionally chosen to differ from the best fit of one element test in order to improve the compliance with selected other experiments. This information will be given separately for the original bounding surface parameters and the parameters added by the model extensions.

4.2.1   Sands for calibration

The calibration procedure will be presented using the examples of Toyoura sand, Sacramento River sand and Hostun sand. The reason for this choice is mainly the availability of extensive experimental data in literature so that an all-encompassing calibration of the model is possible, referring to different types of laboratory tests. This is due to the fact that the optimum will necessarily never fit perfectly for all element tests and most likely reproduces the behaviour under certain experimental conditions better than others. Consequently, the challenge consists of identifying a parameter set that will be the best compromise with respect to the simulation of several laboratory experiments with different loading characteristics, under varying testing conditions (drainage, preparation method etc.) and with various initial states. In the following, the most important mechanical quantities of the three sands are listed, grain size distributions are given and further properties such as the grain shape are described.

Toyoura sand

The Japanese standard sand, Toyoura sand, has been used in the often cited triaxial experiments by Ishihara [Ish93] and Verdugo and Ishihara [VI96]. They characterised it as a uniform fine to medium sand with sub-rounded to sub-angular particles. According to analyses by Oda et al. [OKH78], it is composed of 75% quartz, 22% feldspar and 3% magnetite. Toyoura sand's grain size distribution is presented in Fig. 4.6, which allows for a deduction of specific particle properties as listed in Table 4.1. The coeffi-
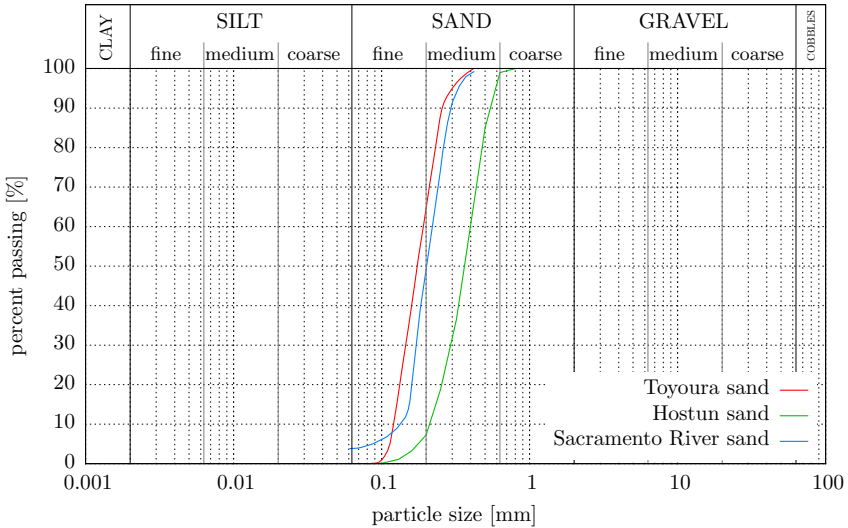
Figure 4.6: Grain size distribution of Toyoura sand, Hostun sand and Sacramento River sand

cient of uniformity C_U and the coefficient of curvature C_C are calculated as follows:

$$C_U = \frac{D_{60}}{D_{10}} \quad \text{and} \quad C_C = \frac{D_{30}^2}{D_{10} \cdot D_{60}} \tag{4.5}$$

Miura and Yamanouchi [MY75], whose research had a stronger focus on the compressive behaviour of sand, reported slightly different values for the physical and geological properties of Toyoura sand. The mineralogical composition is shifted towards quartz (80 %) at the feldspar's cost (17 %) and the supplement of magnetite is replaced by 3 % chert. The uniformity coefficient was quantified by 1.5 and the minimum and maximum void ratios amounted to 0.58 and 0.92.

Table 4.1: Particle related and physical properties of Toyoura sand

D_{50} [mm]	C_U [$-$]	C_C* [$-$]	e_{min} [$-$]	e_{max} [$-$]	ρ $\left[\frac{\text{g}}{\text{cm}^3}\right]$	φ_{cs} [°]
0.17	1.7	0.92	0.60	0.98	2.65	31.5

* All values taken from Ishihara [Ish93], except for C_C, which was deduced from grain size distribution curve.

Sacramento River sand

Sacramento River sand, originating from a river section not far from San Francisco Bay, has been mostly used by Lee and Seed [LS67] in their experimental study on the drained strength characteristics of sands. Looking at the particle size distribution curve in Fig. 4.6, the gradation is very similar to Toyoura sand and can hence be classified as fine to medium, uniform sand. The sand particles can be described as sub-rounded to sub-angular as well. The sand is primarily composed of feldspar and quartz without substantial proportions of mica, calcite or similar supplements that might influence the critical state friction angle or the sand's crushability. However, according to experimental observations [Lee66, Koe70, Bol86], feldspar dominated sands can attain significantly higher critical state angles than quartz sands, which might partially explain the difference in critical state angle between Toyoura and Sacramento River sand. Further physical properties can be found in Table 4.2.

Table 4.2: Particle related and physical properties of Sacramento River sand

$D_{50}{}^*$	$C_U{}^*$	$C_C{}^*$	e_{min}	e_{max}	ρ	φ_{cs}
[mm]	$[-]$	$[-]$	$[-]$	$[-]$	$\left[\frac{\text{g}}{\text{cm}^3}\right]$	$[°]$
0.20	1.66	1.01	0.61	1.03	2.68	33.3

* All values taken from Lee and Seed [LS67], except for particle size related properties, which were deduced from grain size distribution curve.

Hostun RF sand

The third sand used for calibration is a French standard sand called Hostun RF sand, often used for soil modelling similar to the Japanese Toyoura sand. This medium sand with angular grains is extracted in the municipality of Hostun in the Isère valley on the west side of the Vercors mountains. It has been characterised in an extensive experimental study by Flavigny et al. [FDP90], resulting in the grain size distribution given in Fig. 4.6 and the additional physical properties listed in Table 4.3. Hostun sand is mineralogically mainly composed of quartz with a slight fraction of feldspar [LE05].

Table 4.3: Particle related and physical properties of Hostun RF sand

D_{50}	$C_U{}^*$	$C_C{}^*$	e_{min}	e_{max}	ρ	$\varphi_{cs}{}^{**}$
[mm]	$[-]$	$[-]$	$[-]$	$[-]$	$\left[\frac{\text{g}}{\text{cm}^3}\right]$	$[°]$
0.35	1.89	1.03	0.65	1.04	2.65	34

[*] All values taken from Flavigny et al. [FDP90] except for C_U and C_C, which were deduced from grain size distribution curve.
[**] φ_{cs} taken from Schanz and Vermeer [SV96]

4.2.2 Calibration of basic parameters

After having introduced the soils used for the verification of the material model, this section deals with the difficult task of choosing the proper parameters when applying the model for geotechnical simulations. The method for determining an appropriate parameter set is to calibrate the model with the help of experimental data available for the soil to be modelled. Ideally, a parameter reflects a concrete soil mechanical property and can be directly deduced from the run of the corresponding graphical representation of the laboratory results, respecting statistical requirements in view of the amount of identical tests. In other cases, several experiments of the same kind but of different initial conditions regarding the soil state might be needed, since the parameter in question influences a behavioural pattern that changes with stress level or density, such as stiffness or dilatancy. The calibration becomes more intricate, if a material constant cannot be directly linked to one particular experimental result, since several parameters have an impact on the stress-strain path's shape and the influence of one parameter cannot be isolated from others. The probably most undesirable way of determining parameters is pure curve-fitting by trial and error, which is often the case for exponents, controlling the non-linearity of a curve, or purely numerical constants.

The latter two mentioned cases should possibly be treated last, once all parameters with a direct reference have been determined. Optimisation algorithms can ease this last part of the calibration procedure by automatically calculating different scenarios out of which the best fit assigns the optimal parameter choice. This option is examined in the last section. The intention of the present and the successive section is to mainly give a detailed view on the calibration of the parameters that belong to the former group. Starting with a tabular compilation of the basic parameters to be determined, listing the required type and amount of laboratory tests and

making a proposal for a reasonable order of treating the material constants will be the first step. Along these lines, the first part of Table 3.2 is repeated here and completed with the respective information.

Table 4.4: Parameters for the basic features of the extended bounding surface model with corresponding laboratory tests for determination

	parameter	laboratory test
Elasticity	G_0^{ref}	TXD / elastic wave propagation
	m	multiple/cyclic TXD
	ν	TXD / elastic wave propagation
	m_{cone}	(multiple) TXD
Critical state line	$\varphi_{cs}^{c,e}$	TXD (compression and extension)
	e_{cs0}, λ, ξ	multiple TXD/TXU
Dilatancy	m_d, A_d	(multiple) TXD
Kinematic hardening	m_b, h_0	(multiple) TXD

The procedure is demonstrated exemplarily on the basis of experimental data of one of the previously introduced soils. The calibration of the same material constants for the other soils is done analogously, if not stated differently. The calibration of the extended model parameters will be explained in the following section. All resulting parameters are summarised in Table 4.6 at the end of Sect. 4.2.3, accompanied by a common range for each constant.

Elasticity

In order to describe the elastic behaviour of soils, the model requires the input of three parameters: the G_0^{ref} parameter defining the elastic or very small strain shear modulus ($\varepsilon < 10^{-5}$), the exponent m controlling the stress dependency of stiffness and the Poisson's ratio ν for quantifying the transversal expansion with respect to axial compression. The latter is needed for converting the given shear stiffness into elastic moduli for different loading conditions (according to Eq. (3.6)), such as Young's modulus E and bulk modulus K for axially or volumetrically applied stresses, respectively. The additional parameter m_{cone} quantifies the opening of the conical yield surface and hence defines the extent of the elastic domain in stress space.

As explained in Sect. 2.2, there are different possibilities for determining

the elastic shear stiffness. One way is to use wave propagation properties, namely the shear wave velocity v_s identified in field or laboratory tests, in combination with the soil's density, which can be determined by elementary classification tests, and apply the following relationship:

$$G_0 = \rho \cdot v_s^2 \tag{4.6}$$

Alternatively, triaxial compression tests with special instrumentation for registering strains of very small size (local strain transducers with high resolution) can be executed to approximately calculate the shear stiffness at very small strains by evaluating the inclination of the initial stress-strain branch of loading or unloading:

$$G_0 = \frac{\dot{q}}{3\dot{\varepsilon}_q} = \frac{\dot{q}}{2\left(\dot{\varepsilon}_1 - \dot{\varepsilon}_3\right)} \tag{4.7}$$

In order to subtract the stress and density influence from G_0 for concluding on G_0^{ref}, the relation of Eq. (3.5) has to be applied, resulting in:

$$G_0^{ref} = G_0 \cdot \frac{1+e}{(2.17-e)^2} \cdot \left(\frac{p_{ref}}{p}\right)^m \tag{4.8}$$

Similarly, the Poisson's ratio can be deduced from the same laboratory test, evaluating the initial ratio of radial to axial strain (or alternatively in terms of axial and volumetric strain):

$$\nu = -\frac{\dot{\varepsilon}_3}{\dot{\varepsilon}_1} = \frac{1}{2}\left(1 - \frac{\dot{\varepsilon}_v}{\dot{\varepsilon}_1}\right) \tag{4.9}$$

In analogy to the elastic shear modulus, the Poisson's ratio can also be calculated from the shear and compression wave velocities v_s and v_p according to:

$$\nu = \frac{v_p^2 - 2v_s^2}{2\left(v_p^2 - v_s^2\right)} \tag{4.10}$$

It should be noted that distinction has to be made between the latter dynamic Poisson's ratio and the static one. Experiments show that the static Poisson's ratio is mostly greater than the dynamic one [e. g. SK12]. While dynamic tests range within elastic strains, the static Poisson's ratio is usually determined by conventional laboratory tests (e. g. triaxial compression), where it is technically difficult to measure in the elastic or even in the small strain range. Hence, deformations most likely involve irrecoverable portions, which is suspected to cause the difference.

Following the relation between elastic stiffness quantities mentioned above, if the Poisson's ratio is available, the model parameter G_0^{ref} can also be deduced from the bulk stiffness K via Eq. (3.6), which can be determined from small strain isotropic compression data according to:

$$K_0 = \frac{\dot{p}}{\dot{\varepsilon}_v} = \dot{p}\frac{1+e_0}{\dot{e}} \qquad (4.11)$$

Analogously, if triaxial test data is available in terms of axial stress and strain only, the shear stiffness can be calculated via Young's modulus $E_0 = \frac{\dot{\sigma}_1}{\dot{\varepsilon}_1}$ and Poisson's ratio, applying the same correlations as cited above (Eq. (3.6)). This was the case in cyclic triaxial compression tests on Hostun sand with measurements in the small strain range, which have been carried out by Hoque and Tatsuoka [HT00]. Results in terms of axial stress and strain as well as axial and radial strain for an exemplary initial loading path are presented in Fig. 4.7. They were used to calculate E_0 and ν for this particular state with an initial void ratio of 0.72 and to finally conclude on $G_0^{ref} = 69\,\mathrm{MPa}$.
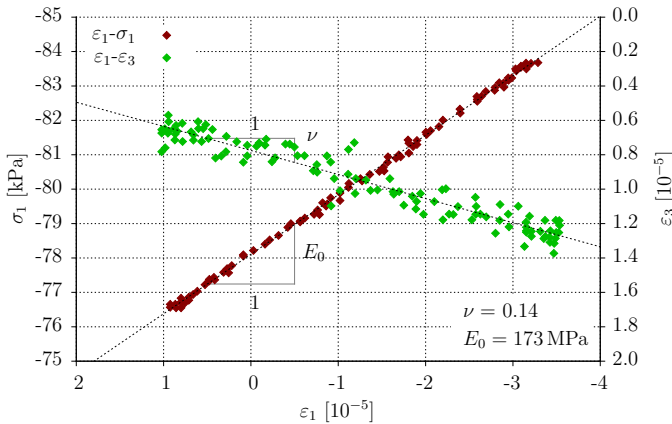
Figure 4.7: Determination of E_0 and ν from experimental data of Hostun sand, provided by Hoque and Tatsuoka [HT00]

The exponent m has to be chosen with respect to the change in stiffness with the corresponding stress level. Thus, in case of the elastic shear modulus, m needs to be fitted to the stiffness evolution with increasing mean stress level. Thus, multiple triaxial tests of different initial states or a cyclic triaxial test to various stress levels are required. For non-cohesive soils, appropriate values have shown to lie between 0.40 and 0.55. Values larger

than 0.5 ranging up to 1.0 seem to better capture the stiffness increase with pressure in case of cohesive soils [Jan63, Ben07]. Using the cyclic triaxial data provided by Hoque and Tatsuoka [HT00], not pictured here, the stress dependence of Hostun sand is well captured by a value of $m = 0.47$.

The size of the elastic domain determined by m_{cone} is closely related to the applied small strain handling strategy. If one of the proposed small strain stiffness mechanisms is active, the elastic zone can be very small ($m_{cone} \leq 0.01$). Otherwise a value of $m_{cone} = 0.06 \ldots 0.07$ [PB02] or $m_{cone} \approx 0.05\, M^c$ [MD97] has shown to ensure a high elastic shear stiffness within a certain stress range after shear reversals.

Critical state line

The position of the locus of all critical states is defined in stress $(p\text{-}q)$ as well as stress-strain $(p\text{-}e)$ space. In case of the former, the critical state friction angle $\varphi_{cs}^{c,e}$ is needed, for compression and extension separately. They are internally transformed into the corresponding critical state stress ratios $M_{c,e}^c$, required as model input:

$$M_c^c = \frac{6 \sin \varphi_{cs}^c}{3 - \sin \varphi_{cs}^c} \quad \text{and} \quad M_e^c = \frac{6 \sin \varphi_{cs}^e}{3 + \sin \varphi_{cs}^e} \tag{4.12}$$

The resulting parameter $c^c = {}^{M_e^c}\!/\!{}_{M_c^c}$ takes values less than 1, so that the critical stress ratio and hence the inclination of the critical state line in $p\text{-}q$ space is larger in compression than in extension, leading to the typical subangular triangle in the Π-plane of principal stress space. In this context, a critical state (or failure) surface of a conical shape with a circular opening similar to Drucker-Prager would imply that the friction angle in extension needs to be considerably larger than the one in compression, which is unlikely for soils.

Theoretically, one triaxial test in compression and one in extension would be sufficient for determining the corresponding critical state friction angles. However, in view of statistical reliability, a few more would be desirable – as shown in the example of Toyoura sand in Fig. 4.8 a. The calibration confirms the critical state friction angle in compression of $\varphi_{cs}^c = 31.5°$, listed in Table 4.1. Since triaxial extension data is scarcely available, which is aggrevated by the requirement for critical stress range data, the friction angle in extension can be assumed to be of the same size. This assumption of approximate equality of the critical state friction angles in triaxial
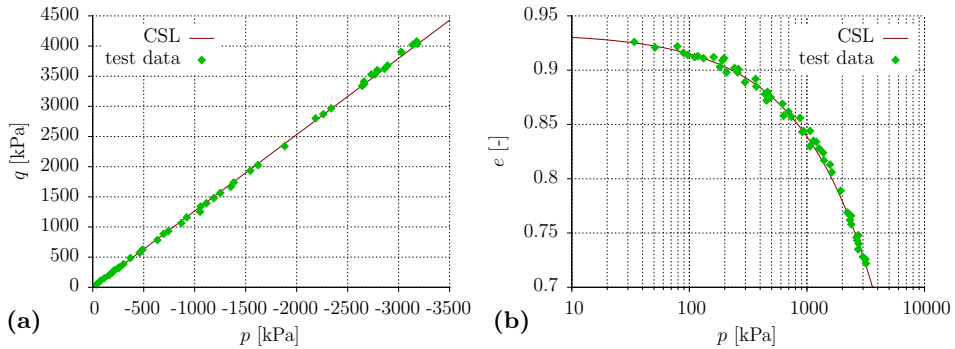
Figure 4.8: Critical state line for Toyoura sand (a) in p-q space and (b) in p-e space, data from Verdugo and Ishihara [VI96]

compression and extension is corroborated by experimental findings [e. g. VCK90, ACT$^+$17].

The ratio c^c deduced from the critical state stress ratios is assumed to be of the same size for the bounding and dilatancy surface related ratios $c^{b,d}$, which enter the shape function for the multiaxial definition of the model surfaces according to Eqs. (2.24) to (2.26). From this follows, that a certain value $c^{b,c,d}$ results in a constant ratio M_e^b/M_c^b, which leads to a peak friction angle that (with growing soil strength) is increasingly larger in extension than in compression. This model behaviour is in accordance with experimental observations [e. g. KS68, PB69, LD73].

The critical state line in p-e space is defined via the critical state void ratio at zero pressure e_{cs0}, the inclination λ and the exponent ξ (Eq. (3.7)). For the latter, 0.7 has shown to be an appropriate choice for several sands [e. g. LW98, TD08], so that Li et al. [LDW99] even proposed using it as a default value. Depending on the stress range of interest, the exponent ξ might, however, serve for adjusting the function's curvature and hence adapting the crookedness of the critical state line. The former two parameters need to be calibrated by evaluating experimental data of several drained and/or undrained triaxial tests driven approximately up to the critical state and fitting the curve to the data points. The calibration of the critical state parameters for Toyoura sand on the basis of the data from Verdugo and Ishihara [VI96] resulted in the best fit parameters $e_{cs0} = 0.934$ and $\lambda = 0.019$ (Fig. 4.8 b).
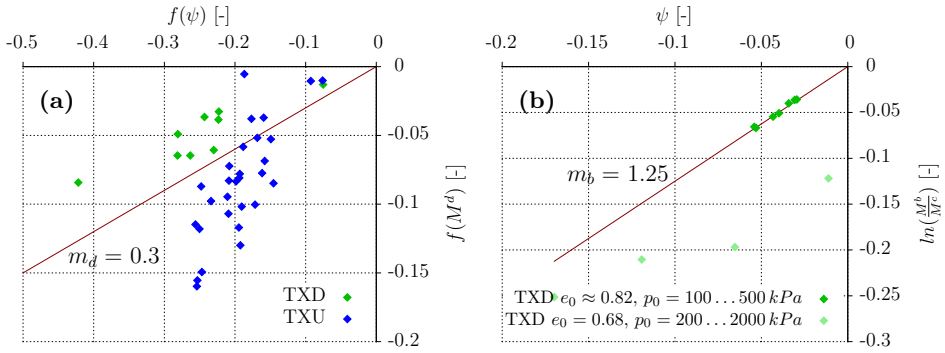
Figure 4.9: Determination of parameters (a) m_d and (b) m_b, data from Verdugo and Ishihara [VI96] and Sun et al. [SHS$^+$07]

Dilatancy

In the bounding surface modelling environment, the volumetric behaviour of soil is strongly influenced by the soil state, expressed by the state parameter ψ. It is interrelated with the dilatancy ratio D through the state dependent formulation of the dilatancy surface's inclination M^d (Eq. (3.16)), which is in turn a function of the critical state stress ratio M^c and the state function f_{sd} according to Eq. (3.19). Depending on the complexity of the chosen mathematical expression for f_{sd}, in addition to the constants A_d and φ_{cs}, one or more parameters need to be determined. In Sect. 3.2.2 the proposal

Figure 4.10: Determination of dilatancy parameter A_d from experimental data of Toyoura sand by Sun et al. [SHS$^+$07]

of Eq. (3.24) is made for the state function, introducing the parameter m_d. According to the model formulation its value is constant for any arbitrary state – such as the state at phase transformation, characterised by the state parameter ψ^{PT} and the corresponding inclination of the dilatancy surface $M^{d,PT}$. Solving Eqs. (3.19) and (3.24) for m_d for this particular state results in:
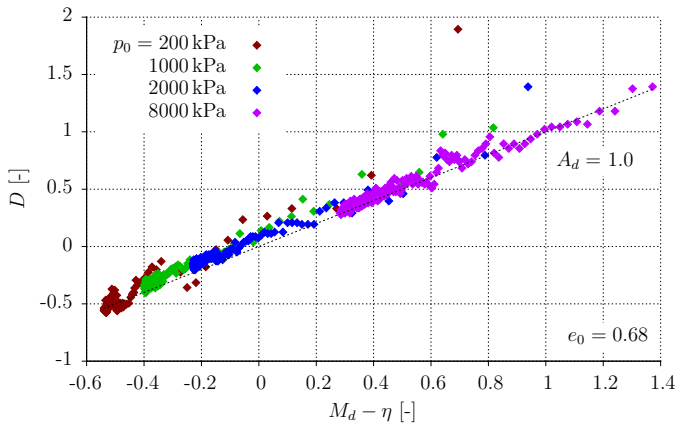
$$m_d = \frac{1}{\text{sgn}\,\psi^{PT} \cdot \sqrt{|\psi^{PT}|}} \cdot \ln \frac{3M^{d,PT}}{(6 + M^{d,PT})\sin\varphi_{cs}} \qquad (4.13)$$

At phase transition the stress state crosses the dilatancy surface and the dilatancy ratio is zero ($D = 0$, no volumetric deformation), which leads to $M^{d,PT} - \eta^{PT} = 0$ or $M^{d,PT} = \eta^{PT} = f(\varphi^{PT})$ (Eq. (3.16)), quantifying the mobilised frictional resistance, when contraction turns into dilation. The corresponding state parameter ψ^{PT} can be found by evaluating the current void ratio and mean stress according to Eqs. (2.2) and (2.3). Based on this correlation, m_d can be calculated for one or several drained triaxial compression tests of different initial states, resulting in a mean value for the desired constant. In case of Toyoura sand $m_d = 0.3$ was found to be an appropriate choice (see Fig. 4.9 a). It should be noted that the graphical representation reveals a divergence of drained and undrained triaxial test results; possible explanations are discussed in Sec. 5.1.2. The choice of $m_d = 0.3$ tries to fit with both drainage conditions. Of course, an increase or decrease of m would improve the undrained or drained simulative response, respectively.

The second dilatancy parameter A_d scales the distance between the current stress point and the dilatancy surface according to Eq. (3.16). Thus, assuming that elastic strains can be neglected and hence the dilatancy ratio D can be approximated by the ratio of total volumetric over the deviatoric strain rate, A_d can be deduced from ε_v-ε_1 (ε_p-ε_q) data of one (or several) triaxial compression test(s):

$$\frac{\dot{\varepsilon}_p}{\dot{\varepsilon}_q} \approx \frac{\dot{\varepsilon}_p^{pl}}{\dot{\varepsilon}_q^{pl}} = D = A_d\left(M^d - \eta\right) \quad \rightarrow \quad A_d = \frac{\dot{\varepsilon}_p}{\dot{\varepsilon}_q} \frac{1}{M^d - \eta} \qquad (4.14)$$

Of course, the parameter M^d is calculated according to Eq. (3.19), applying the previously determined m_d and the corresponding state function. The result of this procedure is shown in Fig. 4.10 and indicates a value of 1.0 for A_d.

An explanatory annotation has to be made here, being however generally valid in the context of parameter choice. Based on the experimental data used

for calibration, the determination of particular values is rarely unambiguous. In some cases, the parameters have been picked purposefully according to the better fit regarding the simulations presented in Chap. 5. However, they remain in a reasonable deviation from the experimentally indicated value – such as A_d, to give an example, which could have been chosen to be in the range of 1.0 ± 0.1. Further remarks are given in the context of model evaluation in Chap. 5.

The impact of changes in the dilatancy parameters on the simulated stress and strain evolution can be inferred from Figs. 4.11 and 4.12, showing results of triaxial compression tests under drained and undrained conditions, respectively. This parametric study gives an idea as to how alterations in these model parameters influence the soil response qualitatively and quantitatively. The dark blue curve corresponds to the reference curve for a triaxial compression test at a confining pressure of $500\,$kPa and an initial
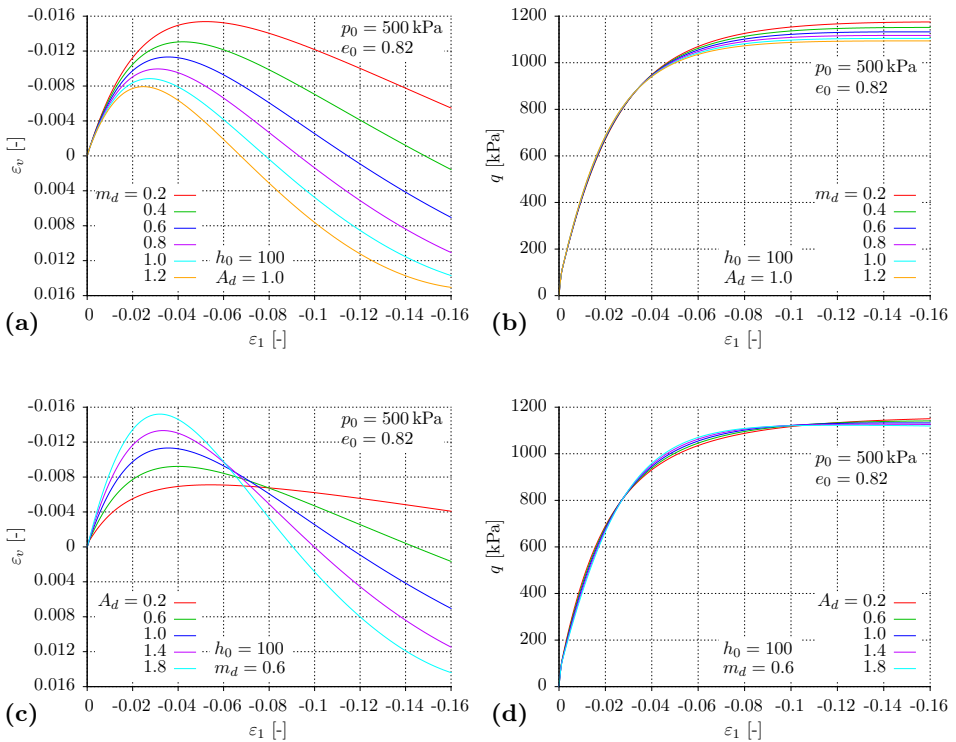
Figure 4.11: Variation of dilatancy parameters m_d and A_d and their impact on drained triaxial compression tests in (a, c) ε_1-ε_v and (b, d) ε_1-q space
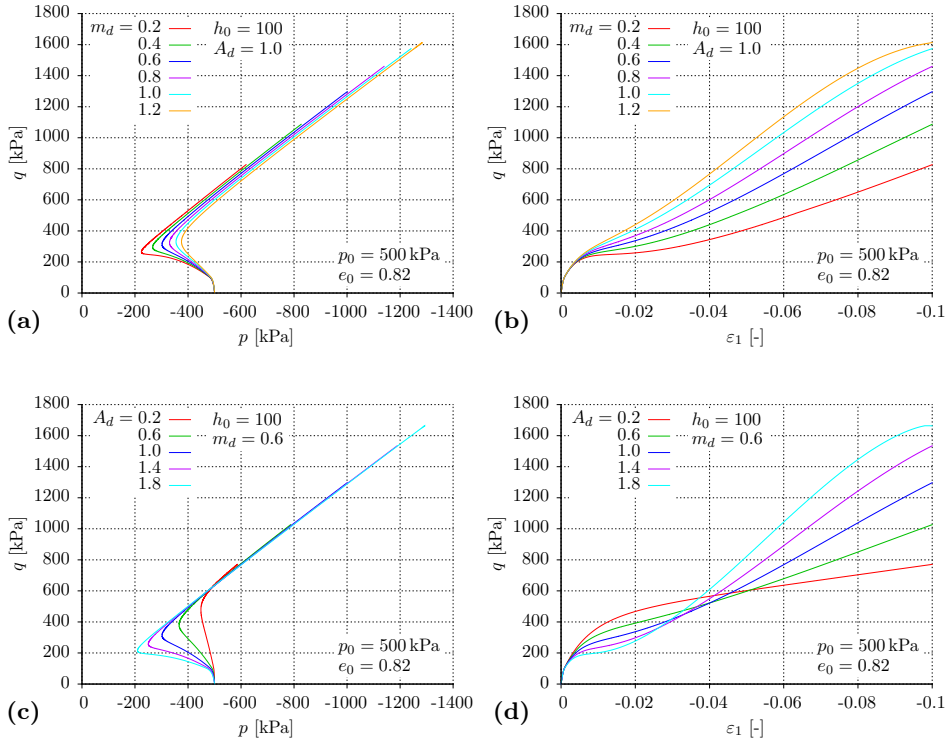
Figure 4.12: Variation of dilatancy parameters m_d and A_d and their impact on undrained triaxial compression tests in (a, c) p-q and (b, d) ε_1-q space

void ratio of 0.82, using the provided standard parameter set for Toyoura sand. Figures 4.11 b and d reveal that the effect on the drained stress-strain evolution in ε_1-q space is minor. On the contrary, in the undrained case (4.12 b and d) the impact is clearly visible.

Kinematic hardening

Similarly as in case of dilatancy the bounding surface parameter m_b, which controls the state dependent variation of the surface's inclination according to Eq. (3.8), can be calculated analytically. Reorganising this equation for m_b results in:

$$m_b = \frac{1}{\langle -\psi \rangle} \cdot \ln\left(\frac{M^b}{M^c}\right) \quad \xrightarrow{peak} \quad m_b = \frac{1}{\psi^{peak}} \cdot \ln\left(\frac{M^{b,peak}}{M^c}\right) \quad (4.15)$$

For any given state characterised by the state parameter ψ and the corresponding position of the bounding surface M^b following the model defini-
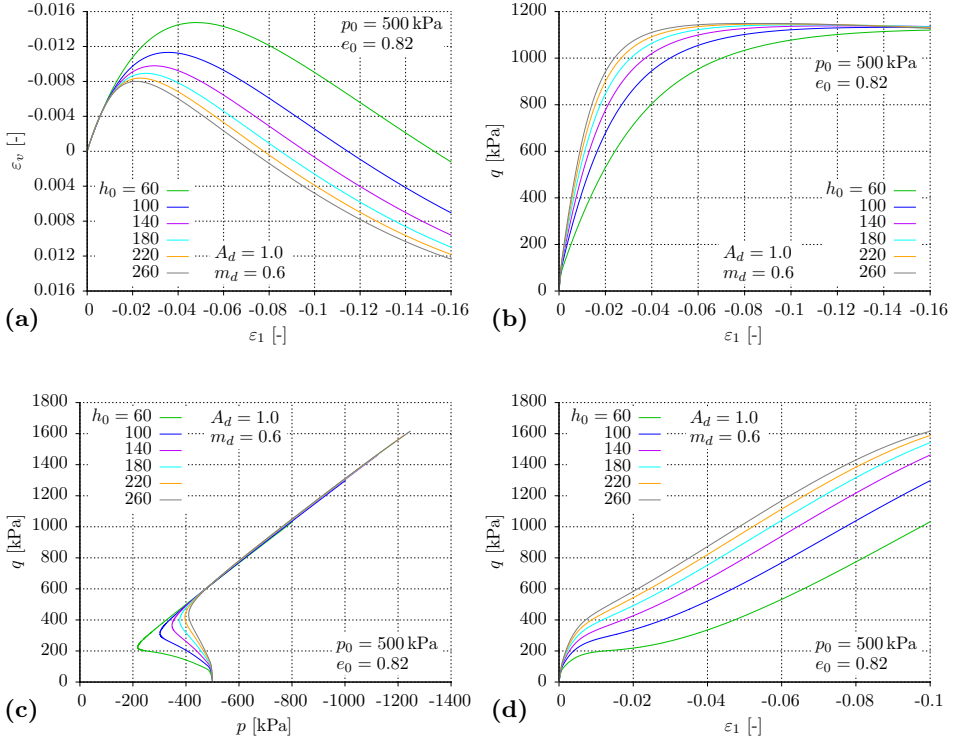
Figure 4.13: Variation of hardening parameter h_0 and its impact on simulated (a, b) drained and (c, d) undrained triaxial compression tests

tion, the parameter m_b attains a constant value. Choosing the peak state of a drained triaxial compression test[1] for calibration, where the stress state lies on the bounding surface ($M^{b,peak} = \eta^{peak} = f(\varphi^{peak})$), besides the initial state (e_0, p_0), it requires the friction angle (or deviatoric stress ratio) at peak φ^{peak} (η^{peak}) and the corresponding volumetric strain ε_v^{peak} (or void ratio e^{peak}) in order to calculate the missing input values for Eq. (4.15). The result of this procedure for Toyoura sand is depicted in Fig. 4.9 b and delivers a value of $m_b = 1.25$.

---

[1]Triaxial compression tests on dense samples are most suitable for this calibration procedure, since they generally exhibit a clearly distinguishable peak in the stress-strain curve at rather early stages of loading. For initial states looser than critical ($\psi > 0$) the bounding surface is identical to the critical state surface (Eq. (3.8)) and will hence only be attained at critical state, which is seldomly reached in laboratory test.

In addition to the bounding surface parameter m_b, there is a hardening variable h, which scales the distance measure $M^b - \eta$ in analogy to the dilatancy mechanism. Despite the introduction of an enhanced formulation for h according to Eq. (3.9), there remains one more constant to be determined: h_0. Unfortunately, there is no direct correlation for assessing h_0 – such as Eq. (4.14) in the dilatancy context – since it influences the hardening behaviour rather globally. Consequently, its calibration reduces to a simple fitting procedure with respect to triaxial compression data (mainly in ε_1-q space).

In analogy to the graphical representations of the influence of the dilatancy parameters in the previous section, Fig. 4.13 imparts the effect of modifications on the hardening parameter h_0 in drained and undrained triaxial compression tests.

Recommendations on the sequence of calibration

Generally, it is advised to commence with the calibration of the elastic parameters, followed by the critical state constants, and to proceed with plasticity related mechanisms, since the latter can not be treated independently from the former (whereas the opposite is possible). When it comes to hardening and dilatancy, it should be noted that a particular strategy is recommended in order to avoid recalibration of certain parameters due to interrelations between different mechanisms. It can be summarised as follows, referring to drained triaxial tests in the first place:

1. m_b
   · controls deviatoric stress at peak state q^{peak}
   · based on dense TXD data

2. m_d
   · controls location of phase transition in ε_1-ε_v curve
   · based on dense TXD data

3. h_0
   · controls steepness of ε_1-q curves
   · based on loose TXD data
   REMARK 1: Simulations need to be based on an assumed A_d (or estimated from experimental data by procedure described above).
   REMARK 2: $f(e)$ and $f(p)$ in h can be adjusted by altering the exponents in order to increase or decrease the spreading of ε_1-q curves w. r. t. void ratio and mean pressure, respectively.

4. A_d
   · controls spreading of ε_1-ε_v curves (intensity of contractancy/dilatancy
   $\rightarrow$ dilatancy angle)
   · based on dense and loose TXD data
   REMARK: A readjustment via h_0 and/or m_d is potentially beneficial.

The essential hint is to start with the hardening parameters, since in drained triaxial tests they influence both ε_1-q and ε_1-ε_v curves, whereas the impact of the dilatancy parameters on the soil response in ε_1-q space is negligible with respect to calibration (see Fig. 4.11). Since the two parameters m_d and m_b can be found directly from experimental data, this concerns mainly h_0 and A_d, which require a more iterative procedure for determination. Thus, the scaling dilatancy factor A_d is the last parameter to be chosen in order to obtain the appropriate spreading of ε_1-ε_v curves for different initial states, translating into the dilatancy angle. Small readjustments of h_0 might be beneficial, though, for improving the strain-strain evolution.

Figure 4.14 gives a simplified overview of the impact of the four cited parameters on the hardening and dilatancy behaviour in stress-strain and strain-strain space in case of drained conditions. It summarizes Figs. 4.11
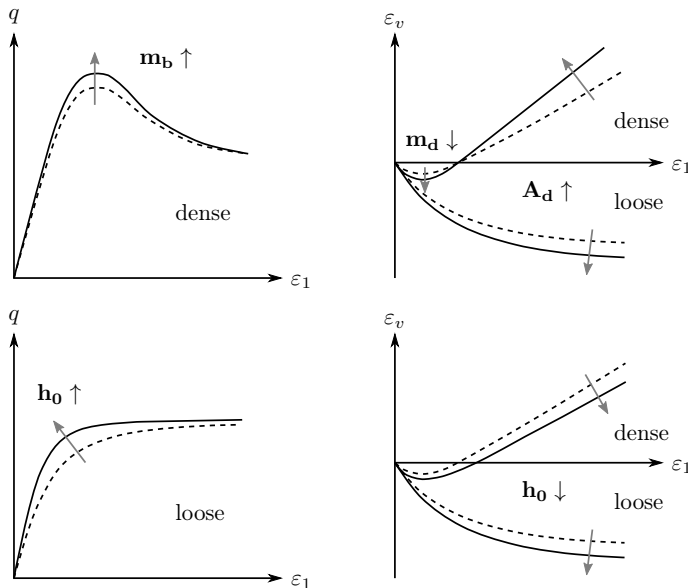

Figure 4.14: Impact of hardening and dilatancy parameters on ε_1-q and ε_1-ε_v curves
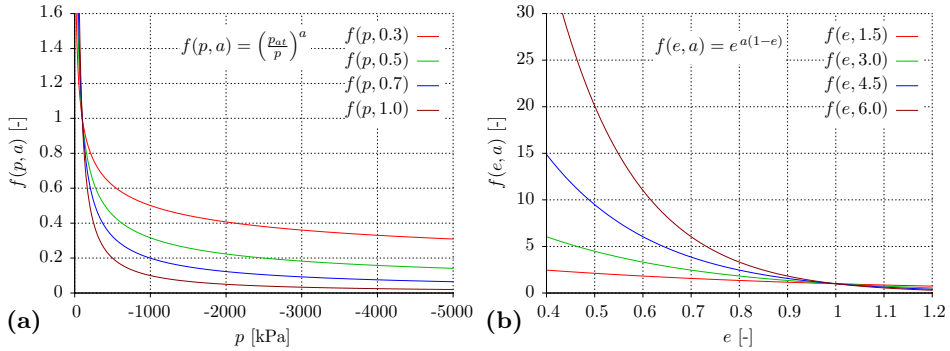
Figure 4.15: Variation of exponents in the hardening subfunctions (a) $f(p)$ and (b) $f(e)$ and their impact on the resulting contribution to the hardening function h

to 4.13 and is supposed to facilitate working off the above calibration list, knowing how to influence the appearance of soil response curves.

Concerning the hardening function h (Eq. (3.9)), containing the constant h_0 as well as a density and a stress dependent subfunction, usually the latter two do not require any calibration since the exponents are fixed. But it might turn out handy to be able to modify them in order to obtain a stronger variation in the resulting soil response with respect to different initial states. Figure 4.15 visualises the impact on the resulting hardening parameter h when adjusting $f(e,a)$ and $f(p,a)$, with a being the setting screw for changes in the respective subfunction. The green lines correspond to the implemented default functions.

In this context, it is particularly valuable to have a set of triaxial test data for a particular initial mean stress p_0 (corresponding to the confining pressure) with (at least two) different initial void ratios e_0 and a second set for a particular initial void ratio e_0 with (at least two) different initial isotropic stresses states p_0, as depicted in Fig. 4.16. This allows to properly calibrate the two hardening mechanisms independently from each other for distinctly different initial states. Disregarding this special case, it is generally useful to base the recommended calibration procedure on such a set of experimental data in order to capture the full range of state dependence of strength and dilatancy.

Most suggestions given above with respect to an efficient calibration procedure refer to drained triaxial test conditions. Of course, the parameter set
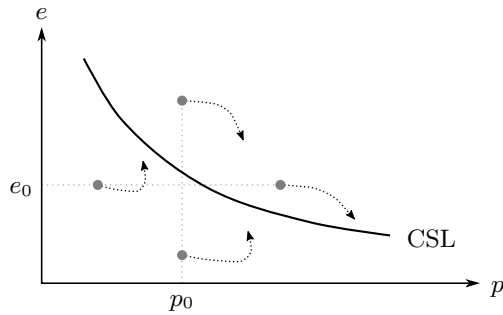
Figure 4.16: Recommended triaxial experimental test data regarding different initial states and their position with reference to the CSL for the determination of the hardening function h

can also be calibrated by means of undrained triaxial test data – the behaviour of the model towards parameter variations has been discussed and depicted for both TXD and TXU. However, as noted earlier, drained tests offer the advantage of a "decoupled" determination of the dilatancy and hardening parameters, since the influence of the former on the stress-strain evolution is marginal. This is not the case for undrained triaxial loading, which makes its calibration more complex.

4.2.3   Calibration of extended model parameters

Having presented the procedure for calibrating the basic model parameters, in this section the determination of all missing variables linked to the extended model features will be demonstrated. Table 4.5 summarises all extensions with their respective constants[2] and the laboratory tests needed for their calculation: the cap and the directly related limiting compression curve, the small strain stiffness option and the fabric evolution mechanism. The following paragraphs are dedicated to these features.

Cap yield surface

Looking at the governing equations of the cap (see Sect. 3.2.3), the parameters to be determined originate from the definition of its surface (Eqs. (3.27), (3.28)) and the associated plastic potential on one side, and the har-

---

[2]Parameters that can often be set to default values and hence do not necessarily require calibration are greyed out.

Table 4.5: Parameters for the additional features of the extended bounding surface model with corresponding laboratory tests for determination

	parameter	laboratory test
Cap	$M_{cap}\begin{cases} E_{oed,0}^{ref}, m_{oed}, n_{oed} \\ K_0 \end{cases}$	multiple 1D compression tests K_0-TXD, instrumented or thin-wall (soft) oedometer test, (in-situ earth pressure measurements)
	V, C	— (numerical parameters)
LCC	ρ_c, p_r, ω	isotropic compression test
Small strain stiffness	SC: γ_{lim}, m_R, ζ IGS: $R, m_R, \beta_R, \chi, m_T$	TXD in small strain range (after SR, optionally after change in loading direction $\alpha = 90°$)
Fabric evolution	N_f, a F_f, C_f e_{min0}, b	cyclic TXD (below PTL) cyclic TXU (above PTL) high-cyclic shear / striking fork test (DIN 18126)

dening rule (Eqs. (3.32) ff.) on the other side. The former concerns mainly the geometry of the cap, namely its steepness M_{cap}. The latter is composed of the mechanism controlling the cap's contribution to deformation depending on the loading and straining direction ($h(\dot{\eta}, \dot{\varepsilon}_p, \dot{\varepsilon}_q)$) as well as the hardening variable H_0^{cap}, combining the influence of stress and density. The identification of the remaining cap related constants is presented in the following; the calibration of the limiting compression curve parameters for the alternative H_0^{cap} formulation (Eq. (3.37)) is treated in a distinct successive section.

The cap steepness M_{cap} is determined analytically in a first step according to the approach described in Sect. 3.2.3: an oedometric load increment induces a certain elastoplastic strain increment, whose direction is dependent on the parameter M_{cap} due to the associated flow rule of the cap ($f(M_{cap}) = g(M_{cap})$), and results in a p-q stress path along the K_0-line. The analytical solution for M_{cap} given in Eq. (3.31) requires the input of the reference stiffness moduli for elasticity (E^{ref} or G^{ref}) and oedometric loading (E_{oed}^{ref}) as well as the Poisson's ratio (ν) and the coefficient of lateral earth pressure at rest (K_0). The elastic stiffness moduli and the Poisson's ratio were discussed in the previous section (4.2.2). The required parameters for the stress and void ratio dependent oedometer stiffness (Eq.
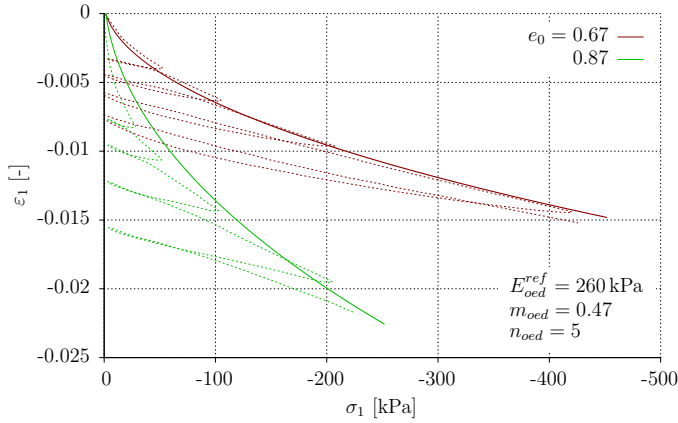
Figure 4.17: Calibration (——) of the oedometer parameters by means of one-dimensional compression test data (- - -) for dense ($e_0 = 0.67$) and loose ($e_0 = 0.87$) Hostun sand [test data from VDZ00]

(3.30)) can be determined from a one-dimensional compression test, fitting the parameters E_{oed}^{ref}, m_{oed} and n_{oed} to the evolution of the σ_1-ε_1 curve. The stress exponent m_{oed} usually corresponds to m, the one used for the other stiffness dependencies (section 4.2.2). The void ratio exponent n_{oed} on the other hand was found to lie between 2.5 and 3.5 for a large variety of different soils and rocks [Hor11]. However, according to a parametric study on the sands treated in this thesis, higher values of 4 to 8 turned out to be more appropriate. Thus, with a choice of $n_{oed} = 5$, $m_{oed} = m = 0.47$ and $E_{oed}^{ref} = 260$ kPa oedometric test data for both dense ($e_0 = 0.67$) and loose ($e_0 = 0.87$) Hostun sand can be reproduced satisfactorily (see Fig. 4.17).

The coefficient of lateral earth pressure at rest K_0, quantifying the ratio of effective horizontal to vertical pressure, is a parameter difficult to assess. Exact in-situ measurements of earth pressure are intricate to realise. Both direct (self boring pressuremeter) and indirect methods (penetration tests such as flat dilatometer or CPT) struggle with the effect of soil disturbance due to insertion of the instrument, which makes the interpretation of resulting data difficult to impossible [Mar85]. Laboratory measurements have proven to be more reliable and can be split into compensating methods (e. g. K_0 triaxial test) and methods with quasi-rigid confinement (e. g. thin-wall/soft oedometer) [KB93]. In non-standard triaxial compression tests under K_0-conditions, the cell pressure is increased simultaneously with the vertical load in a way that no lateral strains occur ($\varepsilon_2 = \varepsilon_3 = 0$). The

soft oedometer developed by Kolymbas and Bauer [KB93] allows for small
lateral deformations upon vertical loading due to the elastic nature of the
thin-walled ring, from which the lateral pressure can be deduced. In both
cases, the resulting ratio σ_3'/σ_1' gives the desired K_0.

Alternatively, the well-known formula by Jáky [Ják44, Ják48], based on the
soil's friction angle, can be used to estimate K_0 (for normally consolidated
soils):

$$K_0^{NC} = \left(1 + \frac{2}{3}\sin\varphi'\right) \cdot \tan^2\left(45° - \frac{\varphi'}{2}\right)$$

$$= \left(1 + \frac{2}{3}\sin\varphi'\right) \cdot \frac{1 - \sin\varphi'}{1 + \sin\varphi'} \approx 1 - \sin\varphi' \qquad (4.16)$$

It is acknowledged that the earth pressure coefficient at rest varies with over-
consolidation ($OCR \uparrow \to K_0 \uparrow$) and density ($D_r \uparrow \to K_0 \downarrow$). Consequently,
K_0 is not a material constant, but for instance a function of the overcon-
solidation ratio, which was proposed by Mayne and Kulhawy [MK82] as a
relation of the form:

$$K_0^{OC} = K_0^{NC} \cdot OCR^{\sin\varphi} \qquad (4.17)$$

Furthermore, it is not obvious, which friction angle is to be used in Jáky's
formula. By experimental investigations, Lee et al. [LPK+13] for example
found out that the often applied peak state friction angle φ^{peak} is likely to
underestimate the K_0-value for a particular initial density.

One could alternatively link the K_0-value to the soil's (initial) relative den-
sity, using the following simple empirical interpolation rule:

$$K_0^{NC} = 0.6 - 0.2 D_r = 0.6 - 0.2 \frac{e_{max} - e_0}{e_{max} - e_{min}} \qquad (4.18)$$

In the present case, the latter option has been applied for determining K_0,
making it range linearly between the generally approved limits 0.6 ($e_0 = e_{max}$) and 0.4 ($e_0 = e_{min}$).

It has to be noted that M_{cap} is not a constant but a variable due to the state
dependent nature of the stiffness moduli and hence needs to be computed
anew in each integration step. Thus, its determination is in fact not part of
the calibration procedure but belongs to the parameter update introducing
each integration step.

Proceeding to the hardening mechanism, the factor $h(\dot{\eta}, \dot{\varepsilon}_p, \dot{\varepsilon}_q)$ contains two
constants that have little soil mechanical background and can be conside-
red as purely numerical parameters: C and V. In conjunction with the

exponential functions they shape the smoothened step functions for the cap
contribution according to loading and strain direction. The choice of rather
large values, e. g. 1000, has shown to work well, in order to ensure a clear
but numerically reasonable shift from $\eta = $ const. to $\eta \neq $ const. behaviour.
Thus, these two parameters can be fixed to default values in order to reduce
the amount of user input.

Aside from the loading part of the hardening mechanism, H_0^{cap} needs to
be calculated. However, its determination does not require any additional
parameters, disregarding those already used for M_{cap}. In this context, the
reader is advised to Sect. 5.1, where the limitation for the choice of the
elastic stiffness parameters (ratio E/E_{oed}) is discussed in detail.

Limiting compression curve

As presented in Sect. 3.2.3, the limiting compression curve (LCC) concept
is an alternative to the incorporated cap hardening mechanism. For pa-
rametrising the limiting compression curve, laboratory tests of η-constant
loading up to high stress ranges are required (10 MPa and more). Ideally,
isotropic compression tests ($\eta = 0$) are recommended to be used, since this
way the otherwise additional effect of a certain constant deviatoric stress
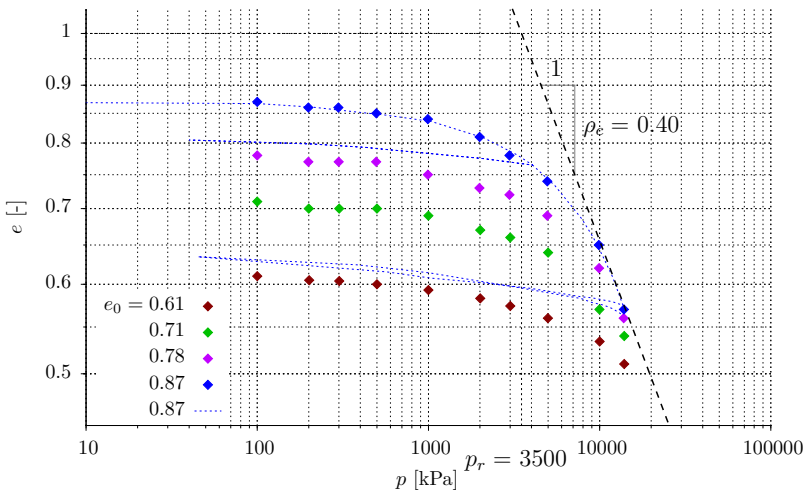
Figure 4.18: Calibration of the LCC parameters for Sacramento River sand
by means of isotropic compression test data ($\blacklozenge$ from [LS67] and $\cdots$ from
[Lad77])

ratio captured by Eq. (2.57) does not affect the LCC.

The LCC is constructed as a straight line in $\log p$ - $\log e$ space (see also Sect. 2.2.2) and is asymptotically approached by the experimental data curves towards higher stresses.[3] The LCC's inclination ρ_c and the reference mean pressure p_r associated to a void ratio of $e = 1$ can be taken from its graphical representation as shown in Fig. 4.18: based on isotropic compression test data by Lee and Seed [LS67] and Lade [Lad77] the LCC parameters for Sacramento River sand were determined to be $p_r = 3500\,\text{kPa}$ and $\rho_c = 0.4$. Once the rough location and inclination of the LCC have been found in terms of p_r and ρ_c, the impact on the simulated soil response in mean stress - void ratio space is rather small (Fig. 4.19 a). In order to adapt the curve's flexion towards the LCC, the third parameter ω can be adjusted; its effect is depicted in Fig. 4.19 b. According to numerical investigations by Taiebat and Dafalias [TD08], a value of 0.2 has shown to satisfactorily approximate experimental data of several sands.
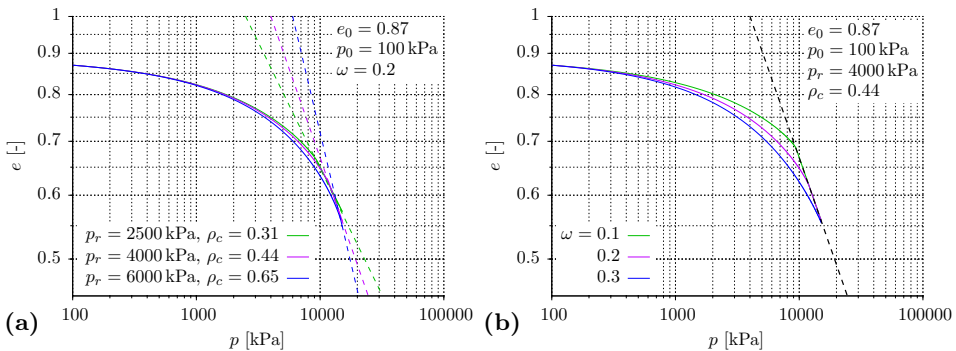
Figure 4.19: Variation of (a) the LCC's location and inclination via p_r and ρ_c and (b) the shape parameter ω and their impact on the resulting deformation in p-e space

Small strain stiffness

As described in detail in Sect. 3.2.4, there are two basically different proposals for modelling the degradation of stiffness at small strains: a stress and a strain based approach. Their common aim is to artificially increase the

---

[3]Due to the double-logarithmic formulation of the LCC, no limit stress is required in order to ensure non-negative void ratios.

hardening modulus by the factor $h_{ss} \geq 1$ in order to suppress the evolution of plastic strains at early loading stages. The parameter shared by both models, which marks the unaffected evolution of plastic strains according to the bounding surface concept, is the threshold shear strain γ_{lim}. This quantity is used for the determination of h_{ss}, which attains its minimum value 1 when the shear strain reaches its limit γ_{lim} (Eqs. (3.44) and (3.45)). It can be assessed by comparing the stiffness evolution along a particular shearing path, starting from a certain (plastic) stress state, with an equivalent one that has been directly preceded by a full shear reversal. The strain, where both stiffness degradation curves join, roughly marks the limit shear strain (or SOM state), as depicted in Fig. 4.20. Since the secant stiffness G does not drop to the "normal" strain stiffness instantly once $h_{ss} = 1$, but gradually degrades, γ_{lim} is only an approximate value. It also corresponds to the limit between small and larger strains and can be quantified by approximately 10^{-3} (see also Fig. 2.10).
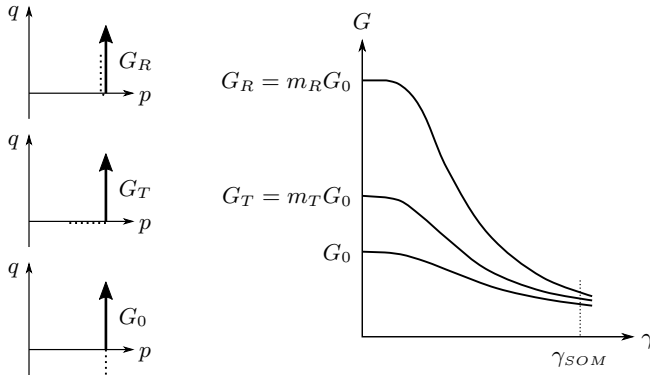
Figure 4.20: Comparison of degradation curves for shear after full reversal, 90° change of loading direction and continued shearing [after Nie02]

Stress/strain contours

As listed in Table 4.5, the stress or strain contour model requires two additional parameters: m_R, the maximum value of h_{ss}, and ζ, the exponent controlling the speed of stiffness decay via $h_{ss} = m_R \rightarrow 1$ and hence the shape of the degradation curve. Both parameters might be set to default values and adapted only if necessary. Magnifying the bounding surface hardening modulus by a factor of 10 to 100 showed to be sufficient in order to inhibit the evolution of plastic strains in the initial small strain range. The
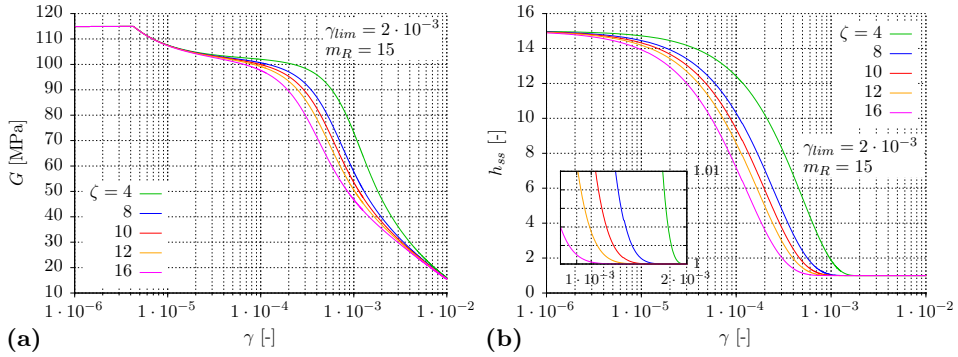
Figure 4.21: Effect of strain contour parameter ζ on (a) stiffness degradation curve and (b) evolution of hardening variable h_{ss}

effect of ζ on the stiffness degradation characteristic can be described as a shift along the strain axis with a slight influence on the curve's steepness. It is visualised by Fig. 4.21 a and can be compared to the combined effect of β_R and χ of the intergranular strain concept (see following section). Figure 4.21 b shows the evolution of h_{ss} with increasing shear strain and the inset plot indicates that the SOM point, predefined by the choice of γ_{lim}, is approached at different rates, depending on the value of ζ. It has to be noted that ζ for stress and strain contours is likely not to be of the same size due to the non-linear stress-strain evolution. As documented in Table 4.6, in case of Toyoura sand the strain contour model takes a value of $\zeta = 10$ for the strain contours; for the stress contours $\zeta = 7$ showed to give comparable results.

One peculiarity of the stiffness degradation curve should be commented. Due to the existence of a (para-)elastic domain, there is an inevitable transition from a very high (elastic) to a continuously decreasing (elastoplastic) stiffness level (discontinuity at $\gamma \approx 4 \cdot 10^{-6}$ in Fig. 4.21 a), which is more or less pronounced depending on the choice of the small strain stiffness parameters. The higher the plastic stiffness in terms of h_{ss} (controlled by m_R) at the onset of elastoplastic straining, the lower the plastic strain contribution and hence the elastic stiffness level is almost preserved, causing a less perceptible transition. However, as long as the elastic domain has a certain size ($m_{cone} \neq 0$), this discontinuity cannot be fully eliminated.

Intergranular strain

Similarly to the contour model, the intergranular strain concept also uses an exponent for controlling the degradation process, here called χ. Its value can be chosen accordingly. By applying a second exponent $\beta_R < 1$ on the ratio of the current intergranular strain $|\delta|$ to its maximum R, the evolution of the intergranular strain towards the strain increment is accelerated or decelerated, which finally also influences the speed of degradation, as will be explained in the following.
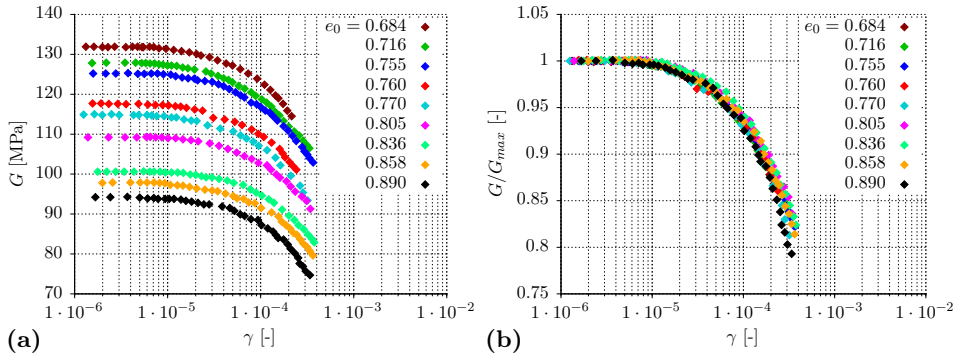
Figure 4.22: Determination of parameter R by evaluating (a) γ-G or (b) γ-G/G_{max} data of Hostun sand [data from Gou15]

The third parameter R, bounding the magnitude of intergranular strain, can be approximately correlated with the elastic limit strain. As cited in Sect. 2.3, for most geotechnical materials the latter amounts to roughly 10^{-6} to 10^{-5}. Based on experimental data from Goudarzy [Gou15], R is set to 10^{-5} for Hostun sand. In Fig. 4.22 it is approximately the point where the horizontal part of the stiffness degradation curve passes over to the distinctly descending branch. Goudarzy's investigations also confirm that, if stiffness degradation curves for different initial soil densities are normalised with respect to the maximum shear stiffness, at least in the small strain range all curves follow the same path (Fig. 4.22 b). Thus, the size of the elastic strain range and hence parameter R is a state independent material property.

The choice of R and the previously described parameters β_R and χ indirectly determine the location of the SOM point (γ_{lim}), where the additional

small strain stiffness becomes less than 5 % of its initial value[4]. Considering a monotonic simple shearing path and accounting for the boundary condition $\rho^\chi\left(\gamma = \gamma_{lim}\right) = 0.95$, a correlation can be established for the ratio of elastic limit to SOM strain and the two parameters β_R and χ. A detailed derivation of this mathematical relation can be found in App. A.7. A graphical solution for Eq. (A.54) is given in Fig. 4.23, which is a rough orientation for facilitating the parameter choice. Knowing the ratio γ_{lim}/R and with an estimate for one of the two exponents, the second one can be assessed easily.

If, for example, R is taken to be $1 \cdot 10^{-5}$ and the additional small strain stiffness is supposed to have decayed by 95 % ($h_{ss} = m_R - 0.95\left(m_R - 1\right)$) at shear strains of $1 \cdot 10^{-3}$, the ratio γ_{lim}/R amounts to 100. With a medium value of $\chi = 5$, following Fig. 4.23, the proper choice for β_R would be 0.04. Generally, one can conclude that the smaller β_R, the larger the ratio γ_{lim}/R and hence the more stretched out the degradation curve. It should be noted that the two used strain limits are only approximate values and should not be expected to be reproduced exactly by the secant stiffness curve. In the elastoplastic constitutive framework, γ_{lim} refers to the 95 %-decay of h_{ss} – this cannot be directly transferred to the degradation of the shear stiffness G due to its definition as secant modulus. In addition, the original meaning of R as elastic limit gets lost, since it mainly bounds the intergranular strain evolution and hence enforces the degression of h_{ss} towards 1.

The determination of these parameters is subject to a fitting procedure, since specific values cannot be deduced directly from experimental small strain data. In order to get a better understanding of the influence of the involved quantities, Fig. 4.24 shows the effect of parameter variation on the shape of the final stiffness degradation curve and the evolution of the hardening factor h_{ss}. In each diagram the red curve, corresponding to the original parameter set, serves as reference. It can be seen that the effect of R and β_R is very similar, shifting the h_{ss} curve and hence the SOM point along the strain axis and causing the stiffness degradation to be more or less distended. The quantity χ can be considered a shape parameter determining the steepness of the curve. Finally, the scaling factor m_R mainly controls the

---

[4]In their original version of the intergranular strain concept, Niemunis and Herle [NH97] define the SOM point at 10 % of the initial additional stiffness. In order to bring the meaning behind the intergranular strain parameters closer to the contour models, the limit is chosen to be nearer to the full decay of small strain stiffness.
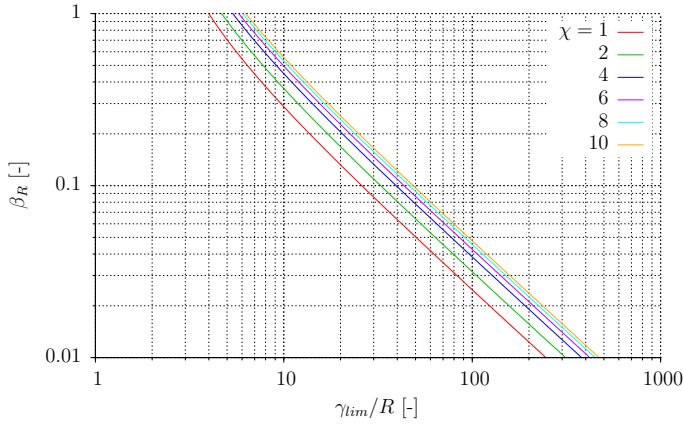
Figure 4.23: Estimation of β_R and χ based on the strain ratio γ_{lim}/R

stiffness evolution at the onset of plastic deformation. As already mentioned in the previous subsection on stress/strain contours, choosing a rather large value for m_R results in a smoother transition from elastic to elastoplastic stiffness – the discontinuity in the stiffness degradation becomes less pronounced (see Fig. 4.24 a). However, there is an upper limit to m_R: if the plastic stiffness remains on an elevated level for too long, the overall stiffness is controlled by the elastic stiffness. The latter increases under small strain shear due to compaction and a raise in mean pressure, which causes the unrealistic bump to appear in the stiffness degradation curve that can be seen in Fig. 4.24 a for $m_R = 100$.

Due to its direction dependent nature, aside from the magnification factor m_R the intergranular strain concept requires one more parameter: m_T. It increases the overall stiffness in case of a 90° change of direction (in contrast to m_R for a full reversal). An interpolated value is used for any directional change 90° $< \alpha <$ 180°. It is the relative size of m_T with respect to m_R that is responsible for a faster decay of the overall stiffness. Since experimental data for 90° shear reversals is hardly available[5], the often applied correlation $m_T = 0.4 \cdot m_R$ [based on NH97] can serve as an estimate. Based on a

---

[5]Experimental data for 90° shear reversals is rare, although it is not too intricate to produce: an isotropic compression path followed by undrained triaxial compression (approximately) results in a 90° change in loading direction, allowing a reasonable estimate for m_T. A p-constant stress path would be even better than undrained triaxial compression, but is a less conventional laboratory test.
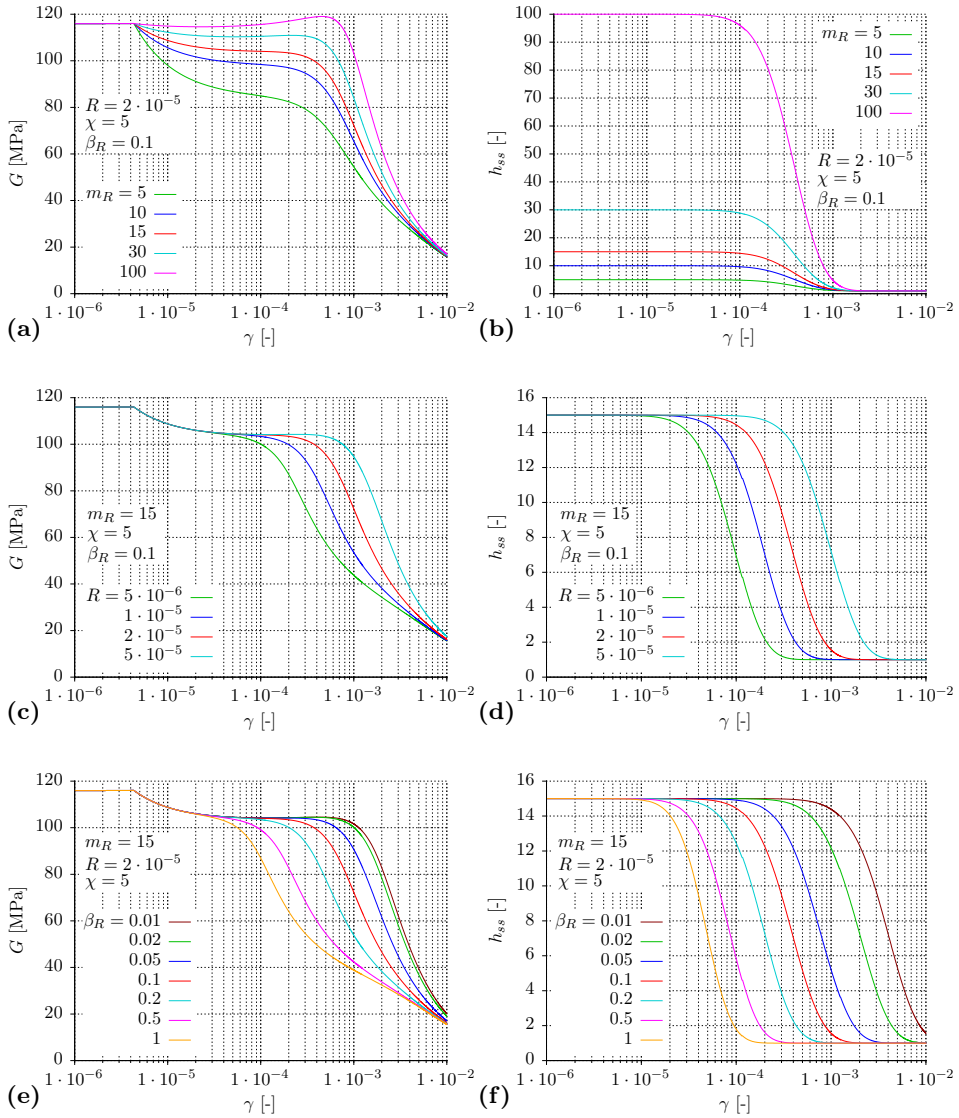
Figure 4.24: Effect of intergranular strain parameters m_R, R, χ and β_R on (a,c,e,g) stiffness degradation curve and (b,d,f,h) evolution of hardening variable h_{ss}

(g)

(h)
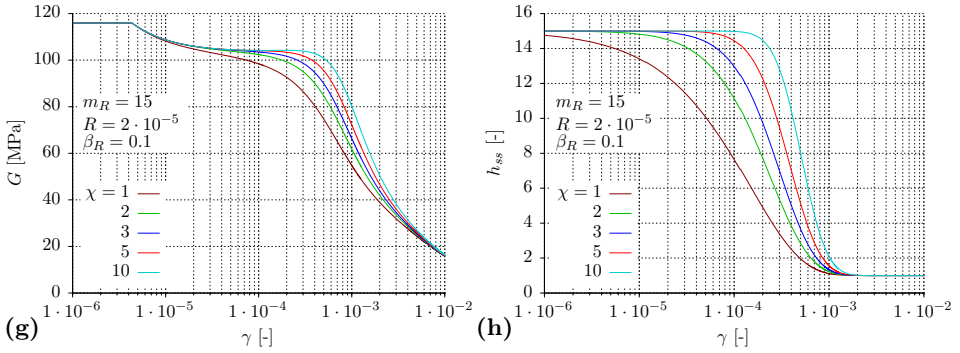
Figure 4.24: (continued) Effect of intergranular strain parameters m_R, R, χ and β_R on (a,c,e,g) stiffness degradation curve and (b,d,f,h) evolution of hardening variable h_{ss}

recent experimental investigation on Toyoura sand, Hong et al. [HKZ$^+$17] recommended a factor of 0.5 instead of 0.4. The general correlation was chosen and implemented in the soil model, so that an additional user input is not required.

Figure 4.25 a presents the calibration result for Toyoura sand with an initial density of $e_0 \approx 0.64$ and different confining pressures. It clearly shows the elastoplastic character of deformation: an initial horizontal branch of constant high shear stiffness, which originates from the elastic domain, is followed by a steady decay of the secant stiffness as plastic strains evolve. The opening of the conical yield surface with increasing stress level can be identified by the growing elastic limit strain with raising confining pressure. The shape of the degradation curve with its discontinuity at the onset of plasticity is not optimal and could be improved by increasing m_R and adjusting β_R and χ accordingly. But the overall stiffness degradation is captured satisfactorily, so that the chosen parameter set was considered appropriate.

For comparison, the simulated stiffness degradation of a triaxial compressive loading path at a confining pressure of $p_0 = 49\,\mathrm{kPa}$ without any small strain stiffness option was added, represented by the broken blue line. The difference is evident and its impact on the resulting stress-strain evolution particularly at small strains is decisive. The simulated G-γ curves for the other two small strain options based on the parameters listed in Table 4.6 are very similar and hence not plotted additionally.

Figure 4.25 b adds an alternative representation of the stiffness degradation

curves, being normalised with their respective initial elastic stiffness G_0. At very small to small strains (in the diagram up to $\approx 1 \ldots 3 \cdot 10^{-5}$), all experimental data points fall onto one curve and hence confirm the trend observed by Goudarzy [Gou15] on Hostun sand (see Fig. 4.22). However, with growing shear strain the stiffness evolution deviates, degrading more quickly at lower confining stresses. Due to the discontinuous transition from elastic to plastic occurring at different strain levels, the model simulations
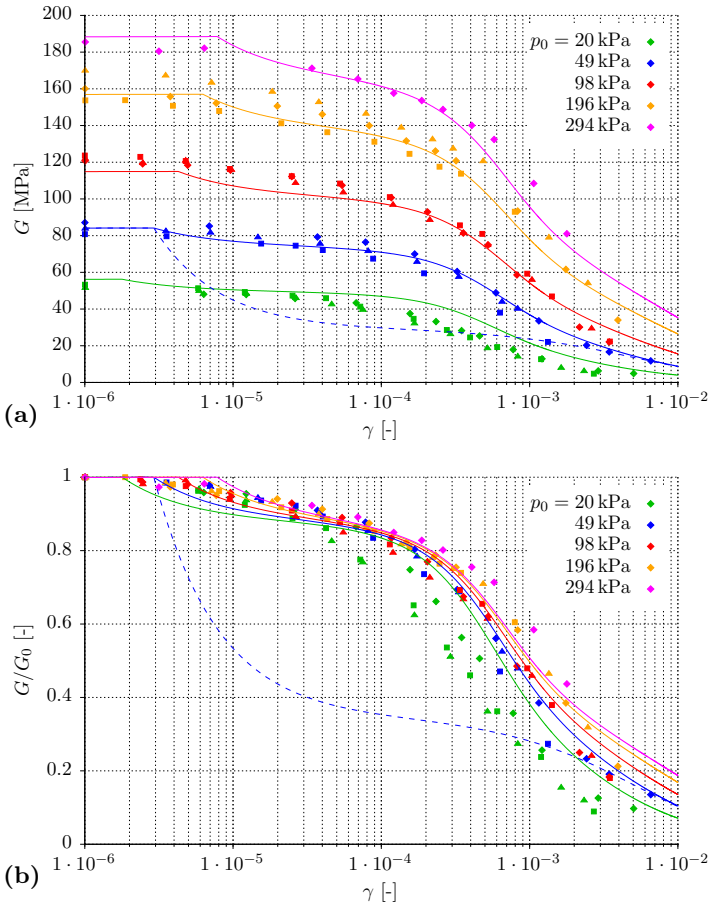
Figure 4.25: Calibration result of the intergranular strain parameters for Toyoura sand with $e_0 \approx 0.64$ and varying p_0: (a) shear stiffness degradation, (b) G_0-normalised shear stiffness degradation (♦ ▲ ■ experimental data by Kokusho [Kok80], — simulations using $R = 2 \cdot 10^{-5}$, $m_R = 15$, $\beta_R = 0.1$, $\chi = 1$, - - - simulation without small strain stiffness option)

do not succeed in reproducing a single curve at very small strains. The subsequent fan-out of the degradation curves is captured by the model, although at lower confining stresses it is initiated too late and not of sufficient intensity (with respect to the chosen intergranular strain parameters).

Fabric evolution

Dissipated energy mechanism

The control of fabric evolution during cyclic loading is realised by the plastic modulus scaling factor h_{fab} and the dilatancy scaling factor f_{fab}. The mathematical expressions in Eqs. (3.51) to (3.53) respect the evolution of dissipated energy with simultaneous consideration of the soil's volumetric tendency and requires the determination of three (or four) constants: N_f (and optionally a), F_f and C_f. For the former, cyclic triaxial test data with smaller stress cycles below the dilatancy surface is needed. Scaling the total dissipated energy, the value of N_f is chosen so that it satisfactorily captures the deformation (or pore water pressure) accumulated after a certain number of cycles, more precisely, the decelerating trend of accumulation. The exponent a can optionally be included in this calibration process by changing it from its default value 2 in order to adjust the acceleration in stiffness increase.

Parameters C_f and F_f come into play, if cycling takes place beyond the dilatancy surface, being responsible for more or less contraction in unloading. Thus, an unloading branch of an undrained triaxial compression test after a shear reversal at stress states above the phase transition line is required for properly choosing this constant (such as in Fig. 3.30). Alternatively, an equivalent response of a drained test can be used, of course. As mentioned earlier, C_f limits the evolution of the directional quantity $\boldsymbol{f}$ and hence bounds the amplifying effect of f_{fab} with respect to contraction to a factor of $f_{fab}^{max} = 1 + C_f$. The additional parameter F_f can be modified for adjusting the evolutional speed.

For facilitating the trial and error based choice of the fabric related parameters, the diagrams in Fig. 4.26 might provide assistance with respect to C_f and F_f. Subfigure a clearly shows that C_f controls the intensity of compaction by the enhanced volumetric contraction after each shear reversal. The effect of F_f (subfigure b) is similar, but much less pronounced. Its impact can be understood when looking at subfigures e and f: if a rather large value is chosen for F_f, vector $\boldsymbol{f}$ develops quickly towards its maximum C_f,
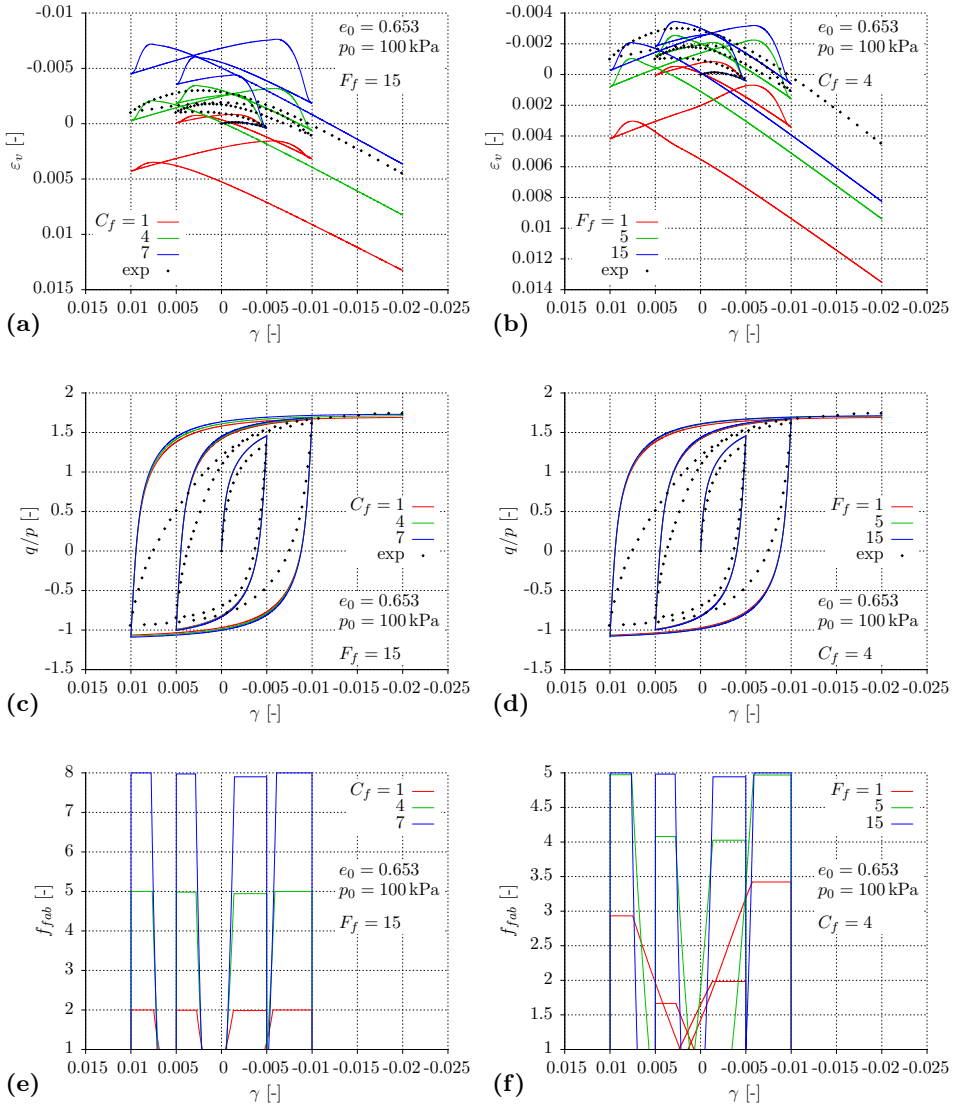
Figure 4.26: Effect of the variation of fabric evolution parameters (a,c,e) C_f and (b,d,f) F_f, respectively, on (a,b) dilatancy, (c,d) stress-strain evolution and (e,f) evolution of dilatancy variable f_{fab} (compared to experimental data by Pradhan et al. [PTS89] for dense Toyoura sand)

since a relatively small amount of dissipated energy needs to be accumulated to reach it. Consequently, in subfigure e, where $F_f = 15$, after each shear reversal f_{fab} (almost) amounts to its maximal value. On the contrary, if F_f is chosen to be less, such as in case of the red and green lines in subfigure f, smaller cycles produce $f_{fab} < 1 + C_f$ and hence the amplification of the contractive effect is weaker, although the same C_f applies.

It may be interesting to note that the deviatoric stress-strain evolution (Figs. 4.26 c and d) hardly changes with parameter variation. This is due to the fact that only dilatancy characteristics are affected by this part of the fabric mechanism, which have little impact on the stress-strain curve (as discussed in Sect. 4.2.2). (Conversely, a modified plastic stiffness would affect both stiffness and dilatancy evolution). In this context it might be worth mentioning that this was partly the reason to transfer the stronger compliance after a shear reversal in dilation from the hardening law [according to PB02] to the flow rule [according to DM04]. The discontinuity emerging from the Macauley brackets in Eq. (3.53) and in the denominator of Eq. (2.42) (flow rule and hardening law, respectively), causes a sudden break – either in the dilatancy evolution only or in both dilatancy and stiffness evolution. Thus, aside from the stronger micromechanical reference, the author favoured the dilatancy related constitutive provision.

Based on the drained cyclic triaxial test data on Toyoura sand by Pradhan et al. [PTS89], which has partly been used as reference in Fig. 4.26, the flow rule related parameters of the fabric evolution mechanism were chosen to be $F_f = 4$ and $C_f = 2$. The resulting simulation gives a satisfactory match with experimental data; it is presented in Sect. 5.3 and potential deficiencies are analysed.

Having determined parameters F_f and C_f on the basis of a few shear reversals including dilation, leaves the user with the choice of N_f (and optionally a). These two parameters control the hardening part of the fabric mechanism, slowing down the overall accumulation trend, which can be considered secondary in case of the very first one or two cycles used in the calibration of the dilatancy related parameters. By increasing N_f, the accumulation decelerates more quickly, with a larger value for a the stiffening effect can be postponed to later cycles. In order to capture this behaviour appropriately, test data with at least ten cycles should be used for calibration. Finding a good combination of N_f and a is a matter of trial and error. For Toyoura sand $N_f = 0.12$ and $a = 3$ have been chosen based on test data by Hinokio et al. [HNH$^+$01]; the result is presented and discussed in Sect. 5.3.

Minimum void ratio

Related to fabric effects in repeated loading, the model offers to take a minimum void ratio into account, suppressing further plastic strains, if the soil approaches a particular minimum density in cyclic shearing. Via Eq. (3.54), the factor h_{min} is computed on the basis of the aforementioned minimum void ratio e_{min}, the initial void ratio e_0 and the current void ratio e. As stated in Sect. 3.2.5, the shear induced e_{min0}, needed for computing the stress dependent e_{min}, mostly undercuts the minimum void ratio defined by standardised tests. But in the absence of respective test data, it can be approximated by the minimum void ratio determined for example by the striking fork test according to DIN 18126 (compaction by striking energy). This alternative is used here, so that the minimum void ratios for the three sands correspond to the e_{min0} given in Tables 4.1 to 4.3.

The stiffness increase in the vicinity of e_{min} can be accelerated by raising the exponent b, but it can alternatively be kept at a default value of 2.

Recommendations on the sequence of calibration

As stated earlier in the context of the basic parameter calibration, it has proven beneficial to stick to a certain sequence in the parameter determination process in order to avoid recalibration. Thus, the author recommends the following strategy:

1. Basic bounding surface parameters
   · preferably based on TXD data
   · adjustment for undrained loading cases via elastic parameters

2. Small strain stiffness parameters
   · based on small strain TXD data
   · potentially back-check basic hardening parameters (need depends on defined zone of influence of small strain stiffness)

3. Fabric evolution mechanism: dilatancy related parameters
   · preferably based on cyclic TXD data
   · if TXU data is used for calibration, make sure that monotonic soil response is captured properly (e. g. reduced stiffness parameters)

4. Fabric evolution mechanism: hardening related parameters
   · based on cyclic TXD or TXU data
   · respect comparability of stress and strain ranges regarding calibrated and to be simulated case

5. Fabric evolution mechanism: minimum void ratio
   · based on cyclic TXD data

6. Cap parameters
   · based on oedometric and/or isotropic test data

Since, obviously, small strain stiffness is particularly important within the small strain range and in undrained loading, it is advisable to base the calibration of the fabric mechanism on a properly adjusted set of small strain stiffness parameters. This is important because the effects of these two mechanisms are likely to overlap and it is possible to distinguish small strain stiffness by appropriate experiments from the other fabric influences, but scarcely vice versa. The two latter points – minimum void ratio and cap surface – are rather independent from the other extensions and should primarily be based on a well balanced basic bounding surface parameter set.

Summary of model parameters

All parameters, the basic ones as well as those of the extended model, are summarised in the following Table 4.6. All simulations evaluated in Chap. 5 use these sets of parameters unless stated otherwise.

4.3   User friendly calibration routine

Throughout the last decades the development in the field of constitutive modelling has progressed considerably, though when comparing the amount of newly established material models with the number of actually used models in geotechnical design there is a severe imbalance. Most academically developed models never leave university ground. Intended to reproduce an increasing variety of soil behavioural patterns, constitutive models become more and more complex – in the mathematical formulation as well as in the amount of required input on the soil in question. Consequently, the accessibility to potential users gets lost: On one side, the model's structure is too intricate or abstract to remain transparent and allow an average engineer understanding the way of functioning and assessing the model's capabilities and limitations for a reasonable usage. And on the other side, the resulting versatility of many new models is due to a rather high number of parameters controlling different aspects of soil behaviour quantitatively. Thus, the user is expected to know the impact of each material parameter and how to make a good estimate referring to the concrete case of application.

Table 4.6: Summary of all parameters of the extended bounding surface model for the three model sands and with typical ranges

		parameter	TOY	SAC	HOS	range
Elasticity		G_0^{ref} [MPa]	82	58	69	$40\ldots150$
		m	0.45	0.5	0.47	$0\ldots1$
		ν	0.15	0.15	0.14	$0\ldots0.5$
		m_{cone}	0.01	0.01	0.01	$>0\ldots0.1$
Critical state line		φ_{cs}^c	31.5°	33.3°	33°	$28\ldots38°$
		φ_{cs}^e	31.5°	33.3°	33°	$25\ldots35°$
		e_{cs0}	0.934	0.92	0.93	$0.8\ldots1.0$
		λ	0.019	0.025	0.022	$0.01\ldots0.05$
		ξ	0.7	0.7	0.7	$0.5\ldots1.0$
Dilatancy		m_d	0.3	0.4	0.4	$0.1\ldots5$
		A_d	1.0	1.1	0.8	$0.1\ldots5$
Kinematic hardening		m_b	1.25	1.4	1.5	$0.1\ldots5$
		h_0	70*	175	90	$1\ldots500$
Cap	(a) M_{cap}	$E_{oed,0}^{ref}$ [MPa]	40	1.2	0.26	$0.01\ldots100$
		m_{oed}	0	0.3	0.47	$0\ldots1$
		n_{oed}	2	4	5	$1\ldots10$
		K_0	according to Eq. (4.18)			$0.4\ldots0.6$
	(b) LCC	p_r [MPa]	14	3.5	1	$1\ldots20$
		ρ_c	0.55	0.4	0.2	$0.1\ldots1$
		ω	0.4	0.35	0.1	$0.1\ldots0.5$
		V, C	1000	1000	1000	$100\ldots10000$
Small strain stiffness	(a) SC	m_R	15	15	15	$1\ldots100$
		γ_{lim}	$2\cdot10^{-3}$			$10^{-4}\ldots10^{-2}$
		ζ	7 | 10**			$1\ldots10$
	(b) IGS	R	$2\cdot10^{-5}$			$10^{-6}\ldots10^{-4}$
		β_R	0.1			$0.01\ldots1$
		χ	1			$1\ldots10$
Fabric evolution		N_f	0.12			$10\ldots1000$
		a	3			$1\ldots8$
		F_f	4			$1\ldots20$
		C_f	2			$1\ldots10$
		e_{min0}	0.60	0.61	0.65	$0.3\ldots0.8$
		e_{max0}	0.98	1.03	1.04	$0.6\ldots1.1$

* $a = 6$ (instead of 3) in hardening subfunction $f(e,a) = e^{a(1-e)}$
** stress contours | strain contours

The latter point is particularly difficult if material parameters lack physical meaning and a direct correlation to experimental data is not possible. Concerning routine design, these requirements represent a serious obstacle. Especially, if only a simplified simulation is to be run in order to make a first rough estimation before a full FE analysis with a carefully chosen parameter set is considered, hardly any engineer would face the trouble of taking a model of high complexity. Changing from a once calibrated simpler model to a more sophisticated one, coming along with an extensive calibration procedure, is rather unlikely when taking the next step of refinement.

4.3.1   Conceptual background

Based on the considerations above, the idea arose to create a tool that eases the handling of the new bounding surface model. It is impossible to spare the engineer engaging himself/herself in the theoretical background of a model to use. But it might be a supporting aid to replace certain bounding surface specific input values, which cannot be determined directly, by those that are either known from more popular models or by other physical quantities to be deduced from particular experiments. They are either directly correlated with the bounding surface parameters and can be calculated with little computational effort, or they serve as target values for an optimisation process. The underlying principle is to define a state dedicated to calibration via density and stress level, in combination with the corresponding soil mechanical properties in terms of well-known or easily accessible parameters. But thanks to the state dependent nature of the bounding surface concept the resulting related parameters are theoretically valid for any arbitrary state (practically speaking: a large range of states). Therefore, the internally determined bounding surface parameters are used for the subsequent element test calculation of a state independent from the calibration state.

The optimisation routine, the heart piece of the calibration tool, consists of two successive iterative loops: an isotropic and a drained triaxial compression test. The advantage of these two tests is that they allow for calibrating both yield surfaces independently. The cap is practically made inactive by its hardening modulus if shear (triaxial compression) is applied and the cone is generally not violated if the element is compressed isotropically. Consequently, one surface and its hardening properties do not influence the calibration procedure of the second and the optimisation can be carried out independently.

The strategy used for optimising the bounding surface parameters is a derivative free evolutionary algorithm, the so called particle swarm optimisation (PSO) algorithm, which will be described in detail later on. Starting with an arbitrary set of start values for the respective bounding surface parameters to be determined, the first test is run once, resulting in a soil response reflected by stress-strain curves. From those the quantities defined as target values by the user are deduced and compared to the reference value. Depending on the divergence, a new set of start values is computed on the basis of the PSO algorithm and the element test is run anew, repeating this procedure until a tolerated error is satisfied.

Table 4.7: Internal determination of model parameters based on user input

	model parameter	test	boundary conditions	input parameter
CAP	M_{cap}	OED (analyt.)		E^{ref} (or G^{ref}), E_{oed}^{ref}, ν, K_0
	LCC: ρ_c, p_r	ISO (simul.)	e_0, p_0, p_{fin}	ε_v^{iso}
CONE	m_b	TXD (analyt.)	e_0, p_0	ε_v^{peak}, φ^{peak}
	H_0, A_d, m_d	TXD (simul.)	e_0, p_0	E_{50}, ψ^{peak}, ε_v^{peak}, ε_1^{PT}

The input that needs to be provided by the user can be divided into cap and cone specific parameters and is summarised in Table 4.7. Starting with the cap, the cap steepness M_{cap} is determined analytically in a first step according to the approach described in Sect. 3.2: an oedometric load increment induces a certain elastoplastic strain increment whose direction is dependent on the parameter M_{cap} due to the associated flow rule of the cap ($f(M_{cap}) = g(M_{cap})$), and results in a p-q stress path along the K_0-line. The analytical solution for M_{cap} given in Eq. (3.31) requires the input of the reference stiffness moduli for elasticity (E^{ref} or G^{ref}) and oedometric loading (E_{oed}^{ref}) as well as the Poisson's ratio (ν) and the coefficient of lateral earth pressure at rest (K_0). It has to be noted that M_{cap} is not a constant but a variable due to the stress dependence of the stiffness moduli, which needs to be computed anew in each integration step. Thus, its determination is in fact not part of the calibration procedure but belongs to the parameter update introducing each integration step.

Depending on the chosen definition of the state dependent variable H_0^{cap} for the cap's hardening modulus H^{cap} (Sect. 3.2.3), there are two options for the remaining cap parameter calibration. If Eq. (3.38) applies, there are

no further parameters left to determine since $H_0^{cap} = f(E,\nu,E_{oed},K_0,M_{cap})$. If the hardening modulus is a function of the limiting compression curve (Eq. (3.37)), the three LCC parameters – ρ_c, p_r and ω – remain to be calibrated in order to calculate H_0^{cap}. The idea behind the determination of these parameters is that an isotropic compression starting from a defined initial state (e_0, p_0) results in a certain volumetric deformation, which is controlled by the location of the LCC. Consequently, the target value for optimisation is the total volumetric strain ε_v^{iso} after an isotropic compression up to a certain mean pressure p_{fin} (given by the user). This quantity is mainly influenced by the two LCC parameters ρ_c and p_r. The exponent ω controlling the shape of the stress strain curve has been set to a default value of 0.2^6 for simplicity, since its impact on the final volumetric strain is minor. One could include this parameter into the optimisation procedure by correlating a volumetric target strain with a certain stage of the test in order to capture the curve's non-linearity. But since its meaning is considered to be of little importance for an automatised calibration, which is not supposed to fully replace the manual adjustment, ω is neglected in the calibration process.

Having completed the calibration of the cap parameters, the optimisation routine continues with the triaxial parameters characterising the cone. Similarly, the parameter determination starts with an analytical calculation of the bounding surface parameter m_b, which follows the procedure described in Sect. 4.2.2 and is hence not repeated here.

The second part of the cone calibration consists of a similar optimisation loop as in the isotropic case. Here, a drained triaxial compression test is carried out on a dense soil, resulting in a typical contractive-dilative deformation path (ε_1-ε_v) and a stress-strain curve (ε_1-q) with a pronounced peak before descending to the critical state value of deviatoric stress, as depicted in Fig. 4.27. The parameters primarily controlling the shape of these curves are the bounding surface specific hardening and dilatancy constants, namely h_0, A_d and m_d. They influence the steepness of the pre-peak branch of the stress-strain curve, the location of the phase transition point in strain space or the maximum dilatancy angle, attained approximately at peak state. Therefore, the corresponding quantities for indicating these shape characteristics are used as target values for the optimisation pro-

---

[6]Numerical investigations by Taiebat and Dafalias [TD08] have shown that for two of the three previously introduced sands 0.2 is a good approximation.

cedure: E_{50}, the triaxial secant stiffness modulus for primary loading (at 50 % of deviatoric peak stress); ε_1^{PT}, the axial strain at the phase transition point; ε_v^{peak}, the volumetric strain at peak state and the corresponding dilatancy angle Ψ^{peak}. Experimental quantities like the two strain values (in conjunction with the initial test conditions) are easily available test data. The other soil properties can also be deduced with little effort from triaxial curves and are either basic soil mechanical parameters (φ^{peak}, Ψ^{peak}) or well-known due to their use in other popular material models, such as E_{50} from the Hardening Soil model by Schanz et al. [SVB99].
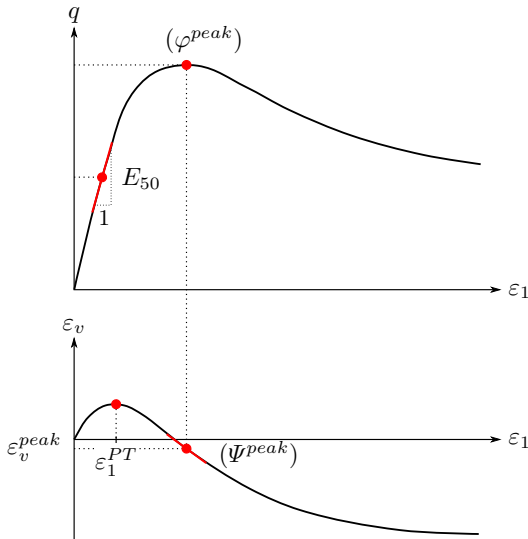
Figure 4.27: Input values for the calibration of the bounding surface specific parameters

4.3.2   Optimisation algorithm

Proceeding to the technical details of the optimisation procedure, it is worth mentioning that both laboratory tests are implemented as explicitly integrated element tests with stress controlled load application. In case of the drained triaxial compression test, based on the user-defined peak state quantities the peak stress can be calculated analytically and serves as terminal point of the test (which is obligatory in stress controlled test simulations anyway).

As introduced earlier, after having tested a Newton method based optimisation algorithm, the calibration routine now works with a particle swarm optimisation (PSO) scheme. In contrast to Newton's method, the evolutionary PSO algorithm requires no derivatives of the objective function f for finding the solution of the optimisation problem[7]. In this population based search algorithm, so called particles (a set of possible solutions = candidate solution) are moved around in search space with the aim of making them swarm towards the best solution (Fig. 4.28 a). They iteratively improve their position through a social learning process: the comparison with previously attained private results and those of other particles as well as the imitation of better individuals are the key to optimisation.
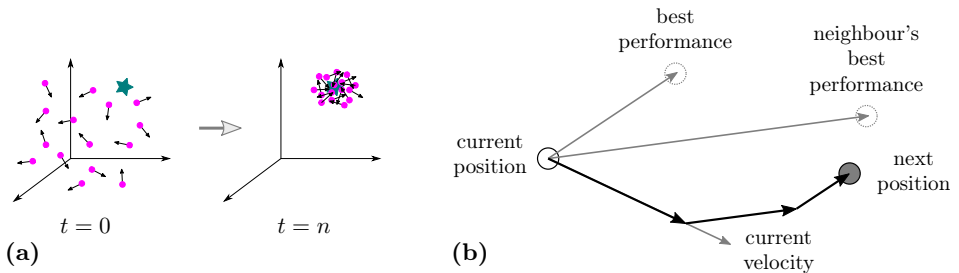
Figure 4.28: (a) Conceptual idea of PSO, (b) visualisation of the calculation principle of the particle's next position based on three contributions

In each iteration step t, a particle i can be described by its position $\boldsymbol{x_{i,t}}$, a fitness value $FV_{i,t} = f(\boldsymbol{x_{i,t}})$ quantifying its success and the velocity $\boldsymbol{v_{i,t}}$ it moves through search space with. In addition, its best search space position until the current iteration t is stored as so called private guide $\boldsymbol{p_{i,t}}$ and the best private guide of all directly neighbouring particles of the swarm is memorised as local guide $\boldsymbol{l_{i,t}}$. The aim of the optimisation process is to minimise the fitness value ($FV \to 0$). The applied learning procedure is based on a mathematical relation transforming the named properties into a new moving direction and velocity according to:

$$\boldsymbol{v_{i,t}} = \omega \cdot \boldsymbol{v_{i,t-1}} + c_1 \cdot \boldsymbol{r_{1,i,t}} \cdot (\boldsymbol{p_{i,t-1}} - \boldsymbol{x_{i,t-1}}) + c_2 \cdot \boldsymbol{r_{2,i,t}} \cdot (\boldsymbol{l_{i,t-1}} - \boldsymbol{x_{i,t-1}})$$
$$(4.19)$$

---

[7]There is no guarantee that the global optimum is found, but the solution is sufficiently good for the expected accuracy. See App. B for more information.

$$x_{i,t} = x_{i,t-1} + v_{i,t} \qquad\qquad (4.20)$$

The parameters ω, c_1 and c_2 are predefinded numerical constants and $\boldsymbol{r_{1,i,t}}$ and $\boldsymbol{r_{2,i,t}}$ are vectors of randomly chosen components between 0 and 1. Thus, a particle's new velocity is composed of three linearly combined components: its own velocity, its best performance and the best performance of its best neighbour, weighed by so called confidential coefficients (Fig. 4.28 b). In case a new position violates the specified search space, its position and velocity are corrected (e. g. by reflection at the boundary). Once the new positions are correctly computed, all private guides are updated by evaluating the objective function for each particle and checking whether $f(\boldsymbol{x_{i,t}}) < f(\boldsymbol{p_{i,t-1}})$. The particle's local guide is determined by checking the new adjacent private guides accordingly. By comparing the fitness values of all local guides, finally the global best position $\boldsymbol{g_t}$ of the iteration step is found.

The optimisation loop is repeated until the defined termination criterion is met, which might be a maximum number of iterations or a minimum improvement from one step to the next that must not be exceeded or undercut, respectively. The algorithm of the optimisation routine can be summarised by the pseudo code in the algorithm box 1. More information on the choice of parameters, the neighbourhood topology referring to the arrangement of particles within the swarm, the formulation of objective functions and correction strategies of particles' positions are given in App. B.

Algorithm 1   Pseudo code of the PSO algorithm

Input: Objective function f, search space $\mathcal{S}$, PSO parameters
  1: **for** each particle i **do**
  2:     Initialisation of position $\boldsymbol{x_{i,0}}$ and velocity $\boldsymbol{v_{i,0}}$
  3: **end for**
  4: Initialisation of fitness values FV_i^p, FV_i^l, $FV^g \leftarrow \infty$
  5: $t \leftarrow 0$
  6: **repeat**
  7:     $t \leftarrow t+1$
  8:     **for** each particle i **do**
  9:         Velocity update $\boldsymbol{v_{i,t}}$ (Eq. (4.19))
10:         Position update $\boldsymbol{x_{i,t}}$ (Eq. (4.20))
11:         **if** $\boldsymbol{x_{i,t}} \notin \mathcal{S}$ **then**
12:            Bound handling strategy for $\boldsymbol{v_{i,t}}$ and $\boldsymbol{x_{i,t}}$
13:         **end if**
14:         Determination of fitness value $FV_{i,t} = f(\boldsymbol{x_{i,t}})$
15:         **if** $FV_{i,t} < FV_i^p$ **then**
16:            Private guide update $\boldsymbol{p_i} \leftarrow \boldsymbol{x_{i,t}}$, $FV_i^p \leftarrow FV_{i,t}$
17:         **end if**
18:     **end for**
19:     **for** each particle i **do**
20:         **if** $FV_i^p < FV_i^l$ **then**
21:            Local guide update $\boldsymbol{l_i} \leftarrow \boldsymbol{p_i}$, $FV_i^l \leftarrow FV_i^p$
22:         **end if**
23:         **for** each neighbour j **do**
24:            **if** $FV_j^p < FV_i^l$ **then**
25:               Local guide update $\boldsymbol{l_i} \leftarrow \boldsymbol{p_j}$, $FV_i^l \leftarrow FV_j^p$
26:            **end if**
27:         **end for**
28:     **end for**
29:     **if** $FV_i^l < FV^g$ **then**
30:         Global best update $\boldsymbol{g} \leftarrow \boldsymbol{l_i}$, $FV^g \leftarrow FV_i^l$
31:     **end if**
32: **until** termination criterion fulfilled
Output: $\boldsymbol{g}$

---

5 Performance of the extended bounding surface model

The performance of the extended bounding surface model presented in the previous chapters is analysed and documented in the following sections. The simulation of various monotonic element tests allows to assess the model's ability of reproducing basic soil behavioural patterns. The subsequent section is dedicated to unconventional laboratory tests, including non-standard monotonic triaxial testing, and loading cases of higher complexity, such as cyclic element tests and combined stress paths.

5.1 Model performance in element tests

In this section, monotonic element tests are simulated with the extended bounding surface model and compared to data obtained in standard laboratory tests documented in literature. All simulation results are based on the parameter sets of the three sands given in Table 4.6. However, simulations will mostly only be shown exemplarily for one of the sands, depending on the intended statement with respect to abilities and limitations of the proposed model. Supplemental simulation results are graphically compiled in App. C.

The produced simulative test data is compared to its experimental counterpart, drawing conclusions on the power of the constitutive model. Deviations between simulation and reality are pointed out and explained on the basis of the model formulation. Potential remedies or proposals, how to handle these issues, are given.

Aside from model deficiencies, another aspect, which should not be left out of consideration, is experimental uncertainty. The soil response's sensitivity to technical influences of the testing equipment, measurement errors

and also insufficiently documented boundary conditions of laboratory experiments (requiring the assumption of missing information) are possible disturbing factors that can cause a deviation of the experimental data from the expected soil behaviour. Thus, provided that these discrepancies are not systematically present in all soil tests of the same kind (independent from the type of sand and the executing laboratory), the inability to reproduce the soil response might not only be due to deficient model formulations. This potential source of error is discussed as well.

5.1.1   Monotonic drained triaxial compression test

Using the example of Toyoura sand, the diagrams in Figs. 5.1 and 5.2 support the state dependent nature of the bounding surface concept as it was described in detail in Sect. 3.1: with a unique set of parameters, different initial states with respect to stress level and void ratio can be modelled, resulting in dramatically different soil responses. The test data by Sun et al. [SHS^{+}07] in Fig. 5.1 provides a large variety of confining pressures, ranging from 200 to 8000 kPa at an initial void ratio of $e_0 = 0.68$, which covers a spectrum of the initial state parameter ψ_0 of -0.223 to 0.154. Consequently, the soil exhibits volumetric behaviour from purely contractant to primarily dilatant (b) and the strength evolution varies from pure hardening to softening behaviour after achievement of peak (a,c). The latter can be detected even more clearly in Fig. 5.2 for two different confining pressures of 100 kPa (a) and 500 kPa (b) at three different initial void ratios each, showing the comparison of simulations with experimental data by Verdugo and Ishihara [VI96]. Their extensive database on Toyoura sand for both drained and undrained triaxial tests is excellent, fulfilling the requirement for a particular combination of initial states recommended in the calibration Sect. (4.2.2). The corresponding void ratio development with mean stress is given in subfigures c and d.

The basic parameter set for Toyoura sand has been calibrated by means of these two data sources, covering a very wide range of densities ($0.68 \leq e_0 \leq 0.996$) and stress states ($100\,\text{kPa} \leq p_0 \leq 8000\,\text{kPa}$) and hence representing a remarkable challenge for the constitutive model. Since the highest premise of the present calibration was to address the complete test domain, compromises had to be made in order to meet all experimental curves with a tolerable deviation. For this purpose, the hardening mechanism

with respect to void ratio was modified slightly[1] as described in Sect. 4.2.2 in order to achieve a wider spread of the curves with respect to different initial densities.

One might raise the objection against this calibration strategy that covering a stress range of such an extent is of little use since pressures exceeding engineering application ranges ($\approx 1\,\mathrm{MPa}$) are out of interest. Furthermore, as described in the context of the LCC concept for compression, the rearrangement of the soil particles is gradually superseded by grain crushing as the
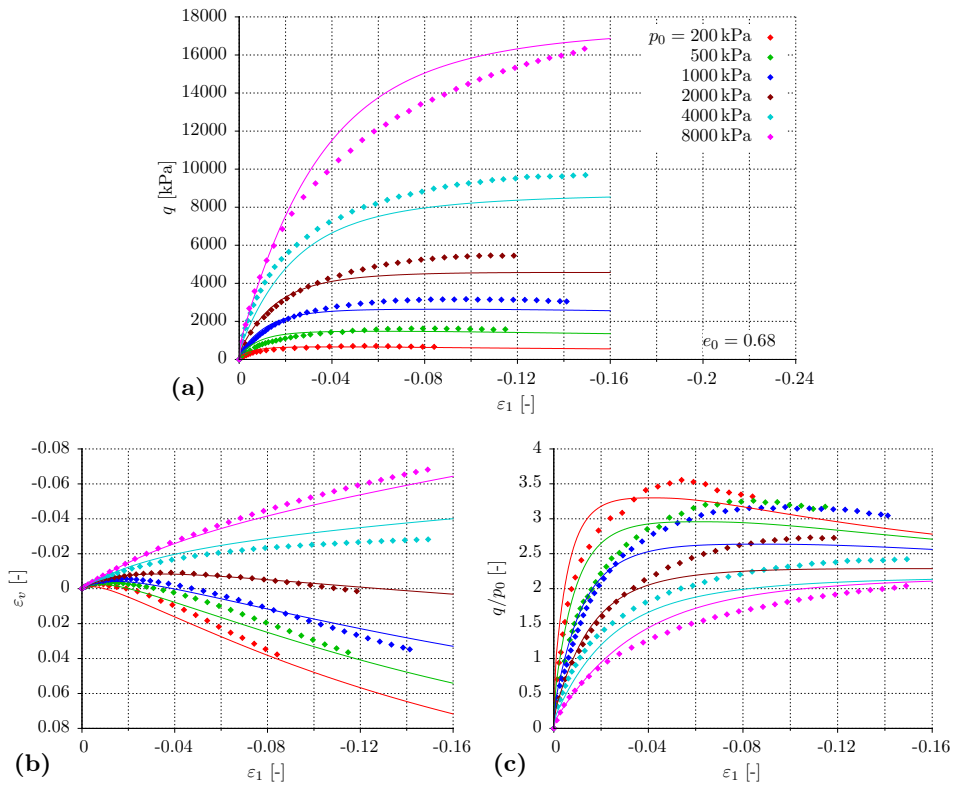
Figure 5.1: Simulation (——) of drained triaxial compression tests on Toyoura sand ($e_0 = 0.68$) compared to test data by Sun et al. [SHS$^+$07] ($\blacklozenge$): (a) ε_1-q, (b) ε_1-ε_v, (c) ε_1-q/p_0

---

[1]The void ratio dependent subfunction in Eq. (3.9) was changed into $f(e) = e^{6(1-e)}$, increasing the exponential parameter from 3 to 6 and hence allowing for a higher stiffness in denser initial configurations.
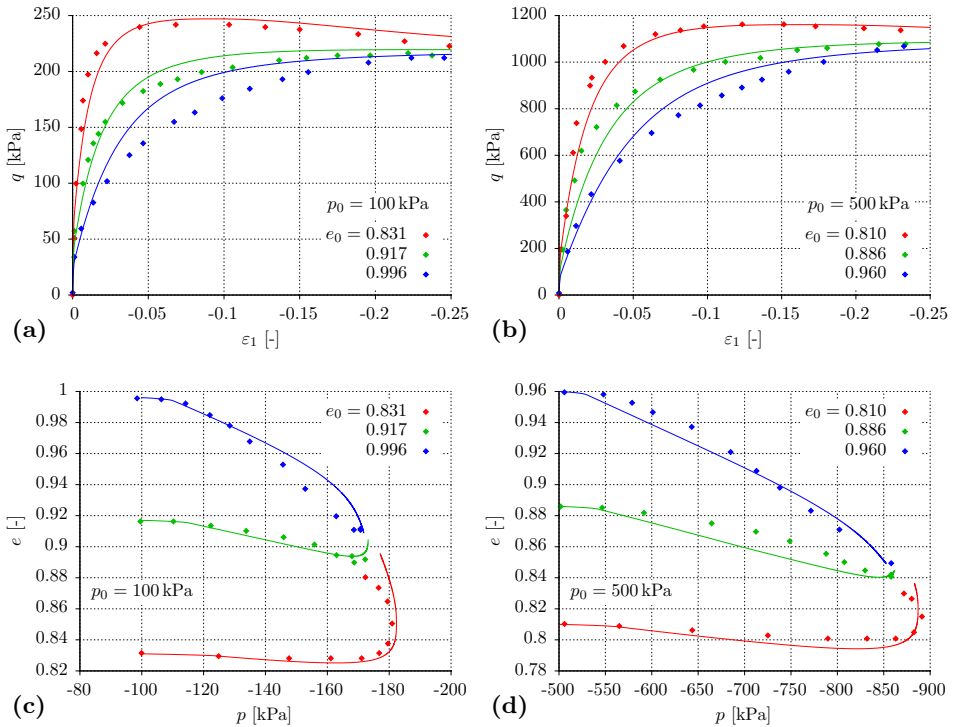
Figure 5.2: Simulation (—) of drained triaxial compression tests on Toyoura sand ($p_0 = 100\,\mathrm{kPa}$ and $500\,\mathrm{kPa}$) compared to test data by Verdugo and Ishihara [VI96] (◆): (a, b) ε_1-q, (c, d) p-e

dominant deformation mechanism within the stress range of 1 to $10\,\mathrm{MPa}$. As a consequence, with the alteration of the grain size distribution due to crushing the soil's mechanical properties change, which is not considered by the model. This might impair the simulated soil response at later stages of loading and also after changes in the stress path. It might hence be more expedient to improve the performance of the model in a certain (relevant) stress and strain range. The aim of the present calibration was, however, to demonstrate the ability of the model to cover a wide stress range.

Even though not all experiments are reproduced equally well, the overall performance is very promising: the model succeeds in capturing the state dependent soil characteristics with respect to strength and deformational behaviour qualitatively and also (with a certain tolerance) quantitatively for a rather large range of different initial states with only one parameter set. The importance of dealing with soil models is the capability to identify

the constitutive components that are responsible for potential deviations and to judge on the severity of the consequences. Of course, in this context a sound knowledge of the model is mandatory, but the aid given in Fig. 4.14 can support the causal investigation. In order to give an example, the most obvious deficiency in the simulated Toyoura sand experiments is the rather large difference of peak stresses particularly at higher stresses. Taking a closer look at Fig. 4.9 b, it is obvious that the chosen value for the bounding surface parameter m_b, controlling the deviatoric stress at peak, can never fit all experimental data. The value of m_b picked for the simulations discussed above is most suitable for tests at lower confining pressures up to $500\,\mathrm{kPa}$ and medium densities (medium green labels in Fig. 4.9 b), but too low for the remaining experiments (light green labels). That is the reason why the simulated stress-strain curves in Fig. 5.1 a for initial states of higher density ($e_0 = 0.68$) and stresses ($p_0 = 1000, 2000\,\mathrm{kPa}$) fail at reproducing the experimentally observed higher peak stresses, whereas the conformity of computed results and test data in Figs. 5.2 a and b is very good.

This discrepancy can be interpreted as a shortcoming of the model: it obviously does not capture the void ratio and/or mean stress dependence of strength properly. This could be remedied by adjusting the corresponding constitutive equations – in this exemplary case by modifying the boundary surface formulation, e. g. via a stress/void ratio dependent m_b –, potentially introducing new model constants. But in order to keep the model's complexity within reason, this insufficiency is accepted. In engineering practice however, the geotechnical problem at stake is usually concerned with a certain range of soil states. Thus, depending on occurring stresses and soil densities, the parameters (particularly those of hardening and dilatancy) can be chosen according to the stress/void ratio range of interest, producing a better image of a limited extract of test data.

Referring to the issue of ill-fitting simulations and possible explanations on the modelling side, it is worth pointing out that the critical state concept and hence the definition of the critical state line is one of the central elements in the bounding surface environment. The distance of the current state's void ratio to the CSL determines whether the soil behaves contractant or dilatant, hardening or softening and via the model surface formulations also the respective magnitude of stiffness and strength. Of course, the CSL is only an assumption for approximating real soil behaviour. Consequently, the match of the simulative response largely depends on the accuracy of the CSL's mathematical expression with respect to its "true" position, especi-

ally if initial soil states lie within the close vicinity of the critical state locus. Aside from theoretical inaccuracies, it can also be an erroneous experimental determination of the initial void ratio and hence of the initial state's position relative to the CSL, which causes a deviation from the expected soil response.

One last aspect linking up with experimental inaccuracies is the effect of membrane penetration on the test results. The penetration of the membrane into the peripheral voids of the specimen due to increasing confining stress affects the volumetric strains in drained triaxial tests or the pore pressure evolution in undrained tests (see also 5.1.2). In the former case, the change of confining pressure causes a change in measured volume, which is attributed not only to the deformation of the soil skeleton, but also to the volume of the water pressed out of the specimen due to the penetrating membrane [NA59, LH77]. The measured change in sample volume plays a key role when it comes to the assessment of the soil's volumetric behaviour, responding contractant or dilative under triaxial compression. Consequently, either experimental or theoretical methods need to be applied in order to compensate for the membrane penetration effect. These include counterbalancing the portion of volume change due to membrane penetration [e. g. NSA89] or modifying the membrane's properties to make it more resistant to penetration [e. g. KS77] on the one hand, and analytical prediction or approximation of the volume change due to membrane penetration and correction of the measured data [e. g. NA59, LH77, BN84] on the other hand.

It should be noted that the impact of membrane penetration on the volume change depends mostly on the average grain size (d_{50}), the geometry of the soil sample, the flexibility of the membrane and the effective confining pressure. Since in case of fine sands the membrane can hardly penetrate into the tiny peripheral voids, the effect of membrane penetration is much more significant for medium and coarse sands [e. g. FZA73], as confirmed by several investigations compiled by Baldi and Nova [BN84] in Fig. 5.3. Consequently, the impact of membrane penetration should be most relevant for Hostun sand and less for the other two investigated finer sands. Moreover, the same authors established a semi-logarithmic relationship for describing the increase of volume change due to membrane penetration with confining pressure (within conventional stress ranges up to $\approx 1\,\mathrm{MPa}$) [BN84]. Bopp and Lade [BL97] complemented this finding with the observation that at high stresses ($> 8\,\mathrm{MPa}$) with a further increase in confining pressure the ef-
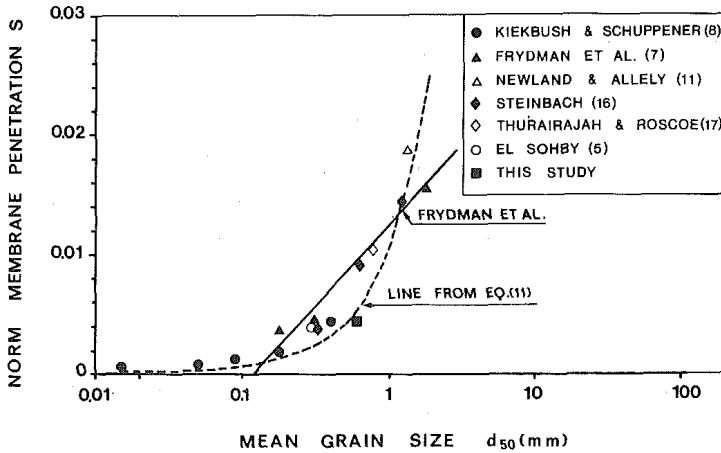
Figure 5.3: Influence of the grain size on the membrane penetration effect [BN84]

fect of membrane penetration decreases, presumably due to grain crushing.

From these considerations follows that volumetric strain data needs to be interpreted with care: if erroneous volume data is not corrected for membrane penetration (which is not necessarily documented), resulting (absolute) volumetric strains and consequently the intensity of dilatancy (and contractancy) are potentially overestimated. Furthermore, wrong conclusions may be drawn from an incorrect void ratio evolution under triaxial compression with respect to the soil's state and its location relative to the CSL in e-p space. However, the influence of membrane penetration on volumetric changes diminishes at high stress levels, which is balanced by problems arising from particle crushing.

5.1.2   Monotonic undrained triaxial compression test

Having obtained a very good match for drained triaxial test data with the parameter set listed in Table 4.6, the simulation of undrained triaxial compression tests gives rather unsatisfactory results: the development of pore water pressures is strongly overpredicted, leading to overly flat effective stress paths in p-q space. Consequently, the estimated undrained strength is too low and although safety considerations based thereon lie on the safe side, they result in a very conservative design. This issue has already been discussed in Sect. 3.2.2 and is not a singular phenomenon particular to

Toyoura sand. It has also been reported by Taiebat and Dafalias [TD08] and is hence not caused by the modifications introduced by the advanced model.

The reason for this phenomenon is a too soft soil response in the initial part of undrained loading. It can also be interpreted as an exaggerated contractancy at early loading stages, being caused by a too large dilatancy ratio $D = \dot{\varepsilon}_p^{pl}/\dot{\varepsilon}_q^{pl}$. Looking at Eq. (3.12) and considering the required changes in the elastic and plastic contributions to volumetric deformation, potential remedies for this problem can be identified. In the undrained case, the elastic and plastic portions are of the same magnitude in order to result in a zero change of volume ($\dot{\varepsilon}_v^{pl} = -\dot{\varepsilon}_v^{el}$). Demanding a steeper undrained stress path calls for either a larger change of deviatoric stress ratio $\dot{\eta}$ or a smaller increment in mean effective stress $\dot{p}$, as depicted in Fig. 5.4 a and b, respectively. Consequently, demanding that $\dot{\eta}$ does not change while the rate of effective mean pressure $\dot{p}$ is reduced (case b), has to result in an adequate increase of the elastic bulk modulus K in order not to alter the elastic volumetric strain portion:

$$\dot{\varepsilon}_v^{el}(\dot{p}) = \dot{\varepsilon}_v^{el}(\dot{p}^*) = -\dot{\varepsilon}_v^{pl}(\dot{\eta} = \dot{\eta}^*) = \frac{\dot{p}}{K} = \frac{\dot{p}^*}{K^*} \quad \rightarrow \quad \text{for} \quad \dot{p}^* < \dot{p}: \quad K^* < K \tag{5.1}$$

Analogously, if $\dot{p}$ and hence $\dot{\varepsilon}_v^{el}$ remain untouched and $\dot{\eta}$ is raised in order to produce a steeper stress path (case a), it follows:

$$\dot{\varepsilon}_v^{pl}(\dot{\eta}) = \dot{\varepsilon}_v^{pl}(\dot{\eta}^*) = -\dot{\varepsilon}_v^{el}(\dot{p} = \dot{p}^*) \quad \rightarrow \quad \text{for} \quad \dot{\eta}^* > \dot{\eta}: \quad \begin{cases} h^* > h \\ A_d^* < A_d \end{cases} \tag{5.2}$$

Focusing on the elastic parameters, it can be deduced from Eq. (5.1) in conjunction with Eq. (3.6) that K reduces by decreasing the reference
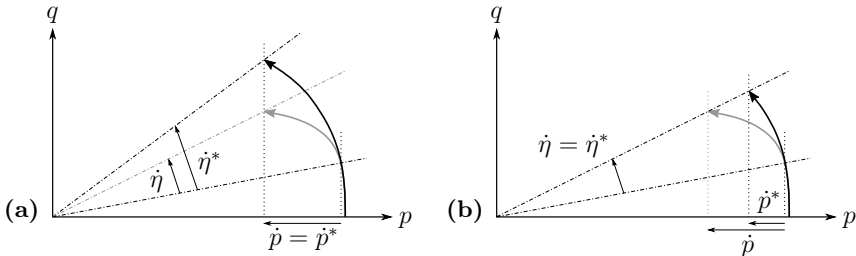

Figure 5.4: Options for improving simulated undrained triaxial compression tests

shear modulus G_0^{ref} and/or the Poisson's ratio ν. On the other hand, Eq. (5.2) indicates that by increasing the hardening parameter h or by reducing the dilatancy parameter A_d, a similar effect can be achieved on the plastic side. In addition, the inclinations of the dilatancy and bounding surface (M^d and M^b) can be modified by changing the contributing parameters ($m_d \uparrow$, $m_b \uparrow$) in order to enhance the effect of A_d and h, respectively.

Concerning the advancement of h (or rather H^{cone}) within Sect. 3.2, up-scaling of the hardening modulus can not only be done by increasing the bounding surface related h_0, but also by specifically adjusting the additional influences, namely small strain stiffness (h_{ss}), fabric evolution (h_{fab}) or minimum void ratio (h_{min}). Here, the small strain stiffness, which intrinsically concerns deformation processes in the initial part of loading, seems particularly appealing: by enlarging the strain range and/or the magnitude of increased (plastic) small strain stiffness (γ_{lim}, m_R), the plastic hardening modulus remains at high values and consequently, the evolution of pore water pressures is slowed down.

Moving the focus to dilatancy instead of hardening, besides a general decrease of the parameter A_d, an initial reduction of A_d has already been proposed in the context of possible modifications on the dilatancy formulation in Sect. 3.2.2. Instead of the bounding surface, which was used as a reference in Eq. (3.25) according to a proposal by Søreide [Sør03], M^d could be used in order to limit the influence of a diminished A_d to the contractant part of a stress path that becomes dilative after phase transition. Of course, this applies to purely contractant stress paths of loose soil as well. Since in that case there is no phase transformation point, the reduction levels out only at critical state, which might be an undesired side effect with respect to drained loading. As mentioned above, aside from A_d, the dilatancy surface parameter m_d can be altered, too. Taking a look at Fig. 4.9 a, it is obvious that the value for drained tests differs considerably from the one for undrained tests. Increasing m_d to 0.7 or larger will clearly improve the undrained simulations, but will simultaneously impair the drained results.

Regarding the fact that modifications on the cited parameters do not only have an impact on the undrained soil behaviour but will equally affect the soil response in drained triaxial loading (or under different loading conditions), changes in the plastic hardening and dilatancy parameters will necessarily have a negative influence on the once perfectly simulated drained triaxial compression tests. On the contrary, the effect of the elastic stiffness parameters is hardly visible in drained calculations due to the dominant

role of plastic strains. Thus, it sounds more promising to alter G_0^{ref} and/or ν, although an unrealistic modification might contradict experimental evidence with respect to soil behaviour in the elastic range, particularly noticeable in unloading situations. But at the same time, it could considerably improve undrained simulations whereas the overall drained soil response remains almost unaffected. As long as the influence of measures on the plastic parameters remains restricted to the pre-phase transition domain or, generally speaking, to relatively small strains, their success with respect to both drained and undrained soil behaviour ought to be comparable.

Based on a small parametric study, it was decided that an increase of the plastic small strain domain or the reduction of the elastic stiffness parameters are the two preferred solutions to the problem. In reference to drained triaxial compression, the former results in a generally stiffer soil response, the latter causes a softer overall deformation behaviour, including swelling in unloading. Of course, the smaller the elastic region (parameter m_{cone}), the less the influence of the elastic parameters on the drained deformational behaviour. The simulations presented in Fig. 5.5 of undrained compression tests were carried out with considerably reduced elastic stiffness parameters ($G_0^{ref} = 15\,000\,\text{kPa}$, $\nu = 0.05$).

Therewith, the reference value of the elastic shear modulus is actually not far from the value of $G_0^{ref} = 125 \cdot p_{at} = 12\,500\,\text{kPa}$ chosen by Dafalias and Manzari [DM04] as well as Taiebat and Dafalias [TD08] on the basis of drained triaxial compression test data on Toyoura sand by Verdugo and Ishihara [VI96]. Not neglecting the fact that they used a slightly different formulation for the void ratio dependency of the elastic shear modulus (2.97 instead of 2.17 in the nominator – according to Richart et al. [RHW70]) this is still far less than investigations compiled by Benz [Ben07] revealed, ranging from 71 up to 104 MPa, which were the basis for the chosen value in Table 4.6. The explanation for this difference is most likely the strain range of 0 to about $3 \cdot 10^{-4}$ evaluated by the two named research groups. As stated earlier in Chap. 3, according to several studies, deformations can be considered to be fully reversible and hence elastic up to strains of maximum 10^{-5}. This is confirmed by experimental data on Hostun sand by Goudarzy [Gou15] cited in the context of parameter calibration. According to his G/G_{max}-database, at strains of $3 \cdot 10^{-4}$ the shear modulus already dropped to approximately 80 % of its elastic value (Fig. 4.22 b).

However, the results based on the not fully realistic elastic parameters show an astonishing improvement compared to the "drained" parameter set, fol-
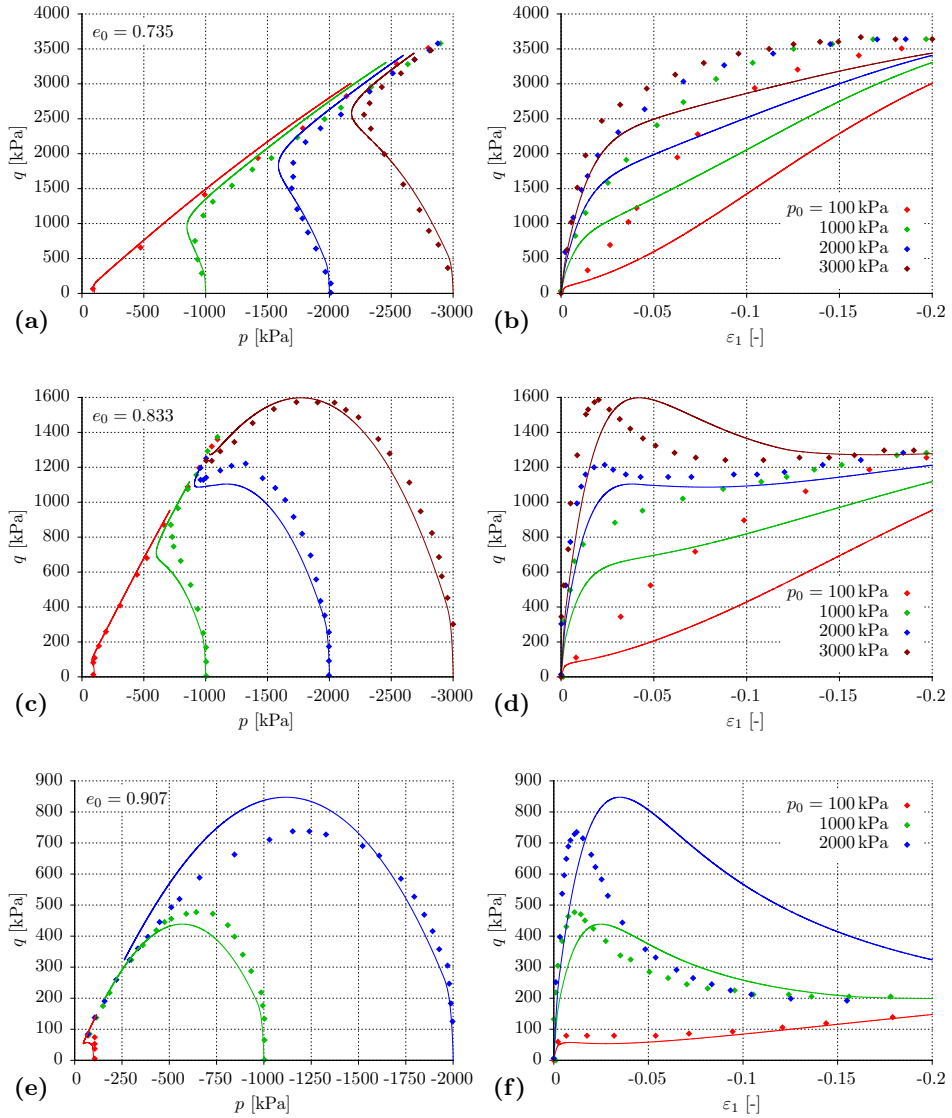
Figure 5.5: Simulation (—) of undrained triaxial compression tests on Toyoura sand ($e_0 = 0.735$, 0.833, 0.907) compared to test data by Verdugo and Ishihara [VI96] (♦): (a, c, e) p-q, (b, d, f) ε_1-q

lowing the experimental stress paths with an acceptable deviation. Nevertheless, the soil response is too soft in the overall axial deformation, clearly visible in the strong shift of the peak in the ε_1-q curves in Figs. 5.5 b, d and f with reference to the laboratory test data by Verdugo and Ishihara [VI96]. For comparison, the drained tests have been repeated with the altered parameters and their visualisation can be found in App. C. Due to the strong reduction in the elastic stiffness, the impact on the results in both stress-strain and strain-strain space is non-negligible.

To conclude on the discussion above, the original as well as the extended model of bounding surface plasticity are not capable of satisfactorily reproducing both drained and undrained triaxial tests with the same set of physically sound parameters. One strategy to cope with this deficiency is to follow the presented way of calibrating a "drained" set of parameters with respect to dilatancy and hardening and finally reduce the elastic stiffness values in order to fit the undrained simulations. Alternatively, the calibration procedure can be executed for an optimal fit of undrained triaxial compression test data, which will most likely result in exaggerated plastic hardening and an underestimation of dilatancy in drained experiments. Depending on the boundary conditions of the geotechnical problem (drainage, loading conditions, density, stress and strain ranges) and its focus with respect to bearing capacity or serviceability, it has to be weighed which way to choose. In the present case, the preference has clearly been to capture the drained soil response, particularly with respect to deformations on a larger scale. The undrained behaviour was secondary, whereas the correct modelling of strength was more important than strains.

If, on the other hand, the liquefaction risk has to be assessed in the context of earthquake engineering for example, the opposite calibration strategy would be more appropriate. Moreover, if the focus lies on loadings in the small strain range, the manipulation of the elastic stiffness might not be a good tactic either. Particularly, if small loading cycles need to be considered, the extra deformations caused by the choice of a lower elastic stiffness will accumulate over the cycles, leading to an overly soft soil response.

Possible sources of discrepancies

Having found a possibility to deal with this modelling issue, it is still debatable, which part of the model formulation exactly contradicts behavioural mechanisms of soil or simplifies them too much. From a micromechanical point of view, one could suspect that rearrangements within the soil ske-

leton have a much higher effect on the soil response in terms of strength and stiffness, if the soil body cannot drain and hence volumetric changes are inadmissible (compared to drained conditions). Consequently, the impact of a finite internal redistribution causes a more pronounced reaction of pore pressure (TXU) than what might be notable as plastic volumetric deformation externally (TXD). This is not considered in the model.

Not directly linked to the material model itself but to the computational framework is the following aspect: while the state dependence of soil stiffness is considered via the bounding surface concept of the constitutive soil model, a potential change of fluid stiffness with loading is not taken into account. In the calculation environment of the used constitutive driver, the pore fluid is assumed to be quasi incompressible in relation to the soil, not varying throughout the whole simulation. For understanding the consequences of this simplification, one has to look at the physical background of pore pressure evolution, going back to the foundations laid by Biot and Skempton.

Assuming that shear has no significant impact on the excess pore pressure development[2], the pore pressure depends solely on the mean stress:

$$\Delta u = B \cdot \Delta p \tag{5.3}$$

This proportional dependence of the pore pressure reaction on an applied increment of total stress is deduced from the Biot formulation of the poroelastic constitutive equations for a fluid-infiltrated porous material [Bio41]. It results from the soil's volumetric response assuming undrained conditions, i. e. no change in water content. The proportionality factor B, the so called B-value introduced by Skempton [Ske54] that is related to the degree of saturation, is correlated with the ratio of the stiffnesses of soil skeleton and pore fluid, K_{soil} and K_{fluid}, respectively:

$$B = \frac{\Delta u}{\Delta p} = \frac{1}{1 + n \frac{K_{soil}}{K_{fluid}}} \tag{5.4}$$

The additional n denotes the soil's porosity[3]. In the constitutive driver the simplifying assumption is made that the fluid stiffness K_{fluid} is as large as

---

[2]This simplifying assumption is only true for an elastic material. For inelastic conditions the pore pressure change ought to be calculated according to Skempton [Ske54]. This issue is commented on at the end of this subsection.

[3]Equation (5.4) is valid for the simplifying assumption that the solid grains within the soil matrix are incompressible.

the bulk stiffness of pure water, which can be considered infinite in comparison to the low soil stiffness K_{soil}, so that the ratio in the denominator of Eq. (5.4) becomes 0 and hence B is at a constant value of 1 (full saturation). However, throughout an undrained triaxial test the B-value does not remain constant: B is a function of the soil's state in terms of density and stress level with regard to its porosity n and the state dependent soil stiffness K_{soil}. From Eq. (5.3) one can conclude that a lower B-value inhibits the pore pressure development and hence results in higher effective (mean) stresses. This variation is not taken into account in the used calculation environment, which might explain the overly flat effective stress paths at least to a certain extent.

Aside from the varying soil properties there is a third and probably the most important factor affecting the B-value: the actual compressibility of the pore fluid K_{fluid}. The saturation of the pore fluid plays a key role in this context. Small gas entrapments inside the pore water reduce the degree of saturation, which can cause a strong variation in the resulting fluid stiffness. This correlation has been identified by Koning [Kon63], who considered the air-water mixture to be an immiscible fluid (disregarding solubility of air in water[4]) and determined its compressibility using Boyle's law in the following form:

$$C_{fluid} = \frac{1}{K_{fluid}} = \frac{S_r}{K_{water}} + \frac{1 - S_r}{K_{air}} \qquad (5.5)$$

K_{water} and K_{air} are the bulk moduli of the water and air inside the pores, respectively, and can alternatively be expressed by the term compressibility, corresponding to the bulk modulus' inverse ($C = 1/K$). The former, although dependent on stress level and temperature, can be assumed to be $K_{water} \approx 2.2 \cdot 10^6$ kPa. The air's bulk modulus equals the total gas pressure within the pores, which corresponds to atmospheric pressure under standard conditions ($K_{air} = p_{at} = 100$ kPa). However, if the pore water is under pressure as well, e. g. due to the phreatic level acting on the soil body, the gas pressure is increased by the water head in the relevant depth, so that $K_{air} = u_{tot} = p_{at} + u_{water}$.

Equation (5.5) is visualised by the diagram in Fig. 5.6: if all voids are entirely filled with water ($S_r = 1$), the pore fluid's compressibility is at its

---

[4]In accordance with Henry's law, the air dissolved in the pore fluid also contributes to the compressibility of the latter, increasing it at low air contents. For further reading the interested reader is advised to Fredlund [Fre76].

Figure 5.6: Variation of fluid compressibility C_{fluid} depending on the degree of saturation S_r for different pore pressure levels u_{tot} $(= u_{air} + u_{water})$

minimum corresponding to C_{water}. Contrarily, if the soil is completely dry $(S_r = 0)$, the high compressibility of air (C_{air}) applies. For any intermediate degree of saturation, the compressibility of the pore fluid ranges between these two extremes, increasing very quickly once the first air bubbles appear. Assuming atmospheric air pressure (red curve), with only $1\,\%$ entrapped gas the pore fluid's compressibility increases by a factor of 220 (with reference to the saturated state)! However, with increasing gas pressure level (green and blue curves), the loss of the pore fluid's bulk stiffness is attenuated, when considering the same reduction in degree of saturation.

The last aspect can also be considered in the light of pore pressure dependency of the fluid stiffness: the increase in pore water pressure in a conventional undrained triaxial compression test induces a reduction of fluid compressibility (or a rise in fluid stiffness) and hence, according to Eq. (5.4), the B-value tends towards 1, which can be translated into a stronger pore pressure response. Consequently, the pore pressure increase has an amplifying effect on itself.

According to Eqs. (5.3) to (5.5), the severe rise in compressibility due to small amounts of air inside the pore fluid significantly influences the pore pressure response of soils under undrained conditions. This mathematical correlation is depicted in Fig. 5.7. For the three previously introduced stress levels the drop in B-value is shown with respect to a reduction in

the degree of saturation of $10\,\%$[5]. The solid lines correspond to a rather soft, the broken lines to a distinctly stiffer soil. As long as the soil is fully saturated, the soil's stiffness is comparably low in relation with the high fluid stiffness, so that the ratio in the denominator of Eq. (5.4) becomes approximately 0 and hence $B = 1$. But with the increasing portion of air, the B-value drops dramatically, with a higher pace for stiff soils. As already stated above, these conditions lead to an inhibited pore pressure development and consequently to larger effective stresses and hence steeper effective stress paths.
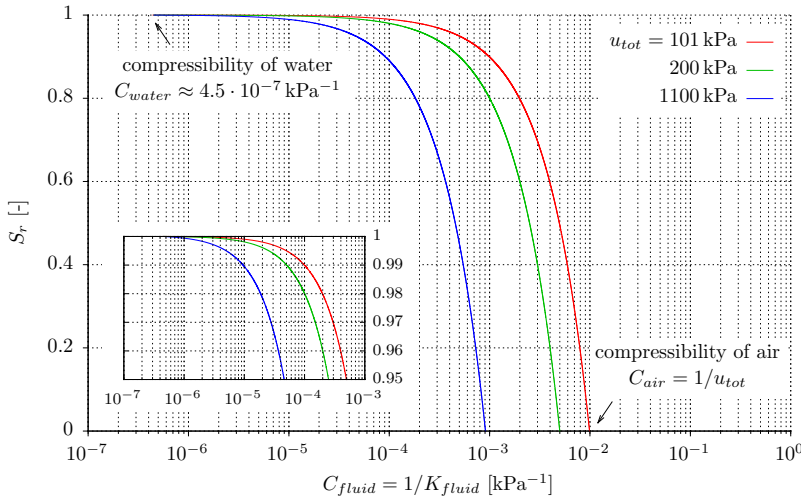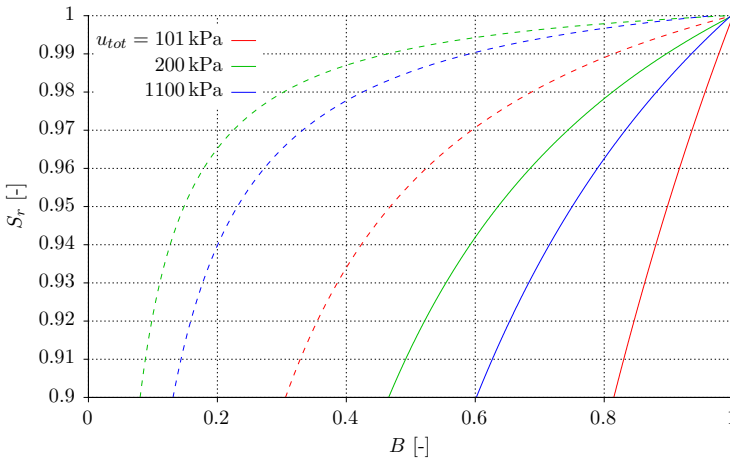

Figure 5.7: Variation of B-value depending on the degree of saturation S_r for different pore pressure levels u_{tot}, with respect to a soft ($G_0^{ref} = 4000\,\text{kPa}$, ——) and a stiff soil ($G_0^{ref} = 40\,000\,\text{kPa}$, - - - -)

Aside from the previous reflections on modelling aspects, potential experimental sources of error come into play in the context of fluid compressibility and saturation. Prior to undrained triaxial test, the successful execution of a B-check ensures the full saturation of the specimen to be sheared: it evidences the direct transfer of a change in cell pressure $\Delta\sigma_3$ onto the

---

[5]It might be surprising at first glance that the three curves in Fig. 5.7 do not respect the order of their respective stress level (referring to B). This is due to the ratio $\frac{K_{soil}}{K_{fluid}}$ in Eq. (5.4), where both stiffnesses, K_{soil} and K_{fluid}, increase with growing pore pressure u_{tot}, but at a different pace. Consequently, up to a pore pressure of $u_{tot} \approx 200\,\text{kPa}$ ($u_{water} \approx 100\,\text{kPa}$) the drop of the B-value with decreasing degree of saturation intensifies, but with a further increase in pore pressure it slowly recovers.

closed pore pressure system, if the increment Δu is of the same size, and hence $B = \Delta u / \Delta \sigma_3 = 1$ (see Eq. (5.4)). By applying a sufficiently high back pressure to the soil sample, air bubbles within the system can be brought into solution in order to reach full saturation. The minimum level of back stress as a function of the initial state of saturation and the type of soil can be determined according to Black and Lee [BL73]. Reaching $B = 1$ is though not self-evident. On the one hand, Black and Lee [BL73] found out that particularly in case of very stiff and/or cohesive soils, even for $100\,\%$ saturation the B-check will not deliver $B = 1$, no matter how high the back pressure. This is also expressed by the stiffness ratio in Eq. (5.4). Thus, due to its comparably high stiffness, the Toyoura sand examined in this work is prone to not reaching full saturation. On the other hand, under standard laboratory conditions it is often not possible to apply a back pressure according to the mentioned recommendations by Black and Lee [BL73] due to technical limitations. The target level of effective stress and the maximum pressure to be generated by the cell pressure controller determine the initial pore pressures and hence limit the maximum possible back pressure. Consequently, B-values usually do not reach 1 but rather values ranging from 0.95 to 0.97[6], confirming insufficient saturation. If, on the contrary, full saturation is assumed for numerical modelling, the simulations will necessarily deviate from the experimental results: based on a theoretical degree of saturation of 1, the simulation will deliver higher pore pressures and hence flatter effective stress paths than the experiment reveals.

This hypothesis was investigated numerically by Tang and Hededal [TH14] using a model formulation for two-phase porous media based on Biot's theory [Bio41], implemented for application of the finite volume method. The implementation is coupled to a constitutive model for soil, which in this case was the bounding surface model according to Manzari and Dafalias [MD97], in order to account for the soil-pore fluid interaction in conjunction with the specific mechanical behaviour of sand. Figure 5.8 shows the results of a simulation of undrained triaxial compression tests on a Nevada sand sample with varying degree of saturation. It can be seen that the impact of the enclosed water in the pore fluid on the pore pressure evolution is

---

[6]The quoted interval corresponds to an average range determined by a non-representative survey in a few selected laboratories with respect to fine sand. The indicated minimum values were around 0.9. The success of saturation depends on the measures taken (level of back pressure, CO_2 flushing,...).
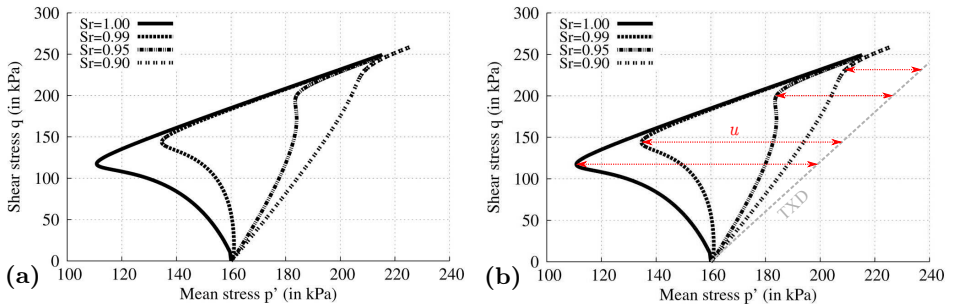
Figure 5.8: Simulated variation of the degree of saturation S_r of a Nevada sand sample ($e_0 = 0.79$, $p_0 = 160\,\text{kPa}$) subject to undrained triaxial compression [TH14]: (a) original diagram, (b) labelling of pore water pressure at phase transition

remarkable: for a partial saturation of a few degrees less than full saturation, which corresponds to realistic laboratory conditions as stated above, the pore pressure at phase transition drops from $\approx 88\,\text{kPa}$ ($S_r = 100\,\%$) to $\approx 73\,\text{kPa}$ for $S_r = 99\,\%$ or even $\approx 42\,\text{kPa}$ for $S_r = 95\,\%$ (marked in subfigure b). Consequently, modelling the fully saturated case and comparing it to an experiment carried out at $S_r = 97\,\%$ might cause a considerable deviation of the resulting stress paths.

Whether the issue of too high simulative pore pressures observed in several sands is indeed due to systematic undersaturation of soil specimens, is open to speculation, unfortunately, since B-checks are seldomly documented in scientific papers. However, it might be part of the explanation for the existing deviation between undrained soil response and simulation. Taking the saturation and stress dependent behaviour numerically into consideration, would result in a steeper stress path in p-q space and hence (at least) partly relieve the described difficulties with regard to undrained loading. If this effect is sufficient to cover the observed discrepancy between simulated drained and undrained soil behaviour, is worth being investigated in more detail.

Having come to experimental sources of error, the effect of membrane penetration and membrane compliance on the soil response under undrained triaxial compression should be concerned (see also Sec. 5.1.1). When applying the confining stress to a soil sample confined by a thin rubber membrane, the specimen is forced into the surface voids between the grains (membrane penetration). As the sample is sheared, pore pressures increase

inside the soil body and tend to push the membrane outwards (membrane compliance). This allows pore water to move from the centre towards the sample edges, resulting in a relaxation of pore pressures [NSA89]. Consequently, the measured effective stresses are higher than the actual stresses inside the specimen, which might lead to an overestimation of the strength particularly for loose soils [HG52, LH77]. It follows that the stress paths resulting from the lab data are potentially steeper compared to simulated curves. Since the effect of membrane penetration is much more significant for medium and coarse sands than for fine sands (see Sec. 5.1.1), mainly Hostun sand might be concerned. However, it cannot be ruled out that the membrane compliance contributes to the simulation problem in all three considered sands.

While there are methods for correcting errors in volume changes due to membrane penetration in drained tests, it is difficult to impossible to retrospectively correct for erroneous pore pressure messurements of undrained tests [Lad16]. That is why there are various proposals on how to experimentally reduce the membrane penetration/compliance effect in undrained tests, e. g. by coating the membrane with liquid rubber[7], as recommended by Kiekbusch and Schuppener [KS77]. But since these measures are seldom well-documented in scientific papers, it is difficult to assess the influence the membrane penetration effect might actually have on the observed deviation of experimental and simulated test results.

Aside from the membrane effects, the technique for preparing laboratory specimens plays an important role with respect to its mechanical behaviour. The same way as different sedimentation histories result in varying bedding angles, different preparation methods lead to contrasting initial fabrics (inherent anisotropy). Elongated particles, for example, tend to orient their long axes along the horizontal plane when being air-pluviated, whereas the orientation of these grains is rather random when moist tamping is applied [NT84]. It has been recognized that these differences in soil fabric due to the preparation method result in different stress-strain characteristics of reconstituted soil samples [e. g. Oda72, AM72, Lad74, MSC$^+$77, NT84]. By means of cyclic undrained triaxial tests, for example, several researchers [e. g. Lad74, MSC$^+$77] have demonstrated that depending on the

---

[7]The liquid rubber is pressed into the interstices between the outer particles, where it stiffens. This way it offers more resistance to penetration and succeeds in reducing the effect by about 85 %.
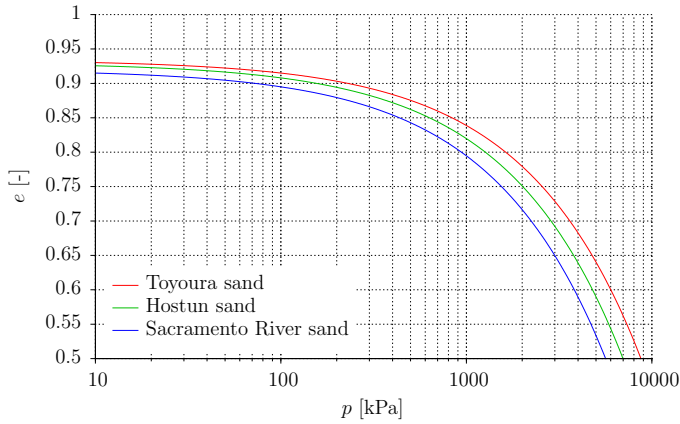
Figure 5.9: Critical state lines of the three model sands in $\log p$-e space

preparation technique the accumulation rates of excess pore pressure differ, leading to different liquefaction resistances. Consequently, various preparation method used within cited experimental studies should also be taken into consideration as a potential source of deviation between simulations and test results.

Concluding on the previously quoted possible reasons for the deficient simulation results in undrained triaxial testing, it is the pore pressure evolution of stiff and dilative soils in particular that is overpredicted. This is due to simplifications in modelling with respect to soil state (pressure, density), saturation of the pore fluid and deviatoric stress changes. Thus, it is especially Toyoura sand with its relatively high stiffness and its strong dilative tendency (in comparison to the two other considered sands, see Fig. 5.9) that suffers from the simplifying presumptions: the results in undrained triaxial loading cases when using the parameter set calibrated for drained conditions are particularly disappointing.

A last comment shall be made in view of the described difficulties concerning the proper calibration of the model for its intended field of application. They clearly illustrate the challenge to automatise this process. The calibration routine introduced in Sect. 4.3 follows the strategy of a "drained" parameter set and considers only one single drained triaxial experiment of a dense specimen. It is a rather simple auxiliary mean to facilitate a quick first application of the model for a rough assessment. Consequently, the user cannot expect to obtain a well-balanced set of parameters, suitable for all loading cases. It is hence indispensable to carry out a sound calibration on

the basis of a comprehensive series of laboratory experiments, keeping an eye on potential experimental disturbing factors and their impact on the soil response.

5.1.3 Monotonic η-constant tests

Having incorporated a cap yield surface allows to capture the plastic deformation along proportional stress (η = const.) and strain paths ($\dot{\varepsilon}_p/\dot{\varepsilon}_q$ = const.), such as isotropic or oedometric compression, which would otherwise induce only elastic strains. As presented in Sect. 3.2.3 the cap's geometry (M_{cap}) and plastic stiffness (H^{cap}) is controlled via the oedometer stiffness, which is an elastoplastic stiffness measure for the overall stress-strain evolution in oedometric loading ($\varepsilon_2 = \varepsilon_3 = 0$). The stress dependence allows to capture the stiffening process in cap loading. Due to its void ratio dependent formulation, the model is also capable of reproducing the stiffening soil response with increasing initial density, as can be seen in Fig. 5.10 a, showing the simulation of isotropic compression tests on Sacramento River sand of four different initial void ratios. The parameter set has been chosen in order to also fit the available oedometer test data[8], provided in subfigure b. Thus, particularly at very large mean pressures of 5 MPa and more,
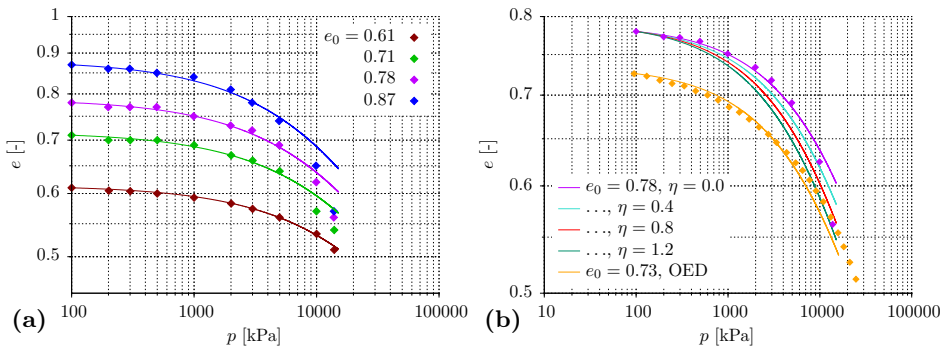
Figure 5.10: Simulation (——) of (a) isotropic compression tests on Sacramento River sand compared to test data (♦) by Lee and Seed [LS67] and (b) an oedometric compression test ($e_0 = 0.726$, data by Lade and Yamamuro [LY93]), complemented with simulations of different η-constant tests with $e_0 = 0.78$

---

[8]The mean pressure has been determined from the recorded axial stress by assuming a K_0-value of 0.455 according to Eq. (4.18).
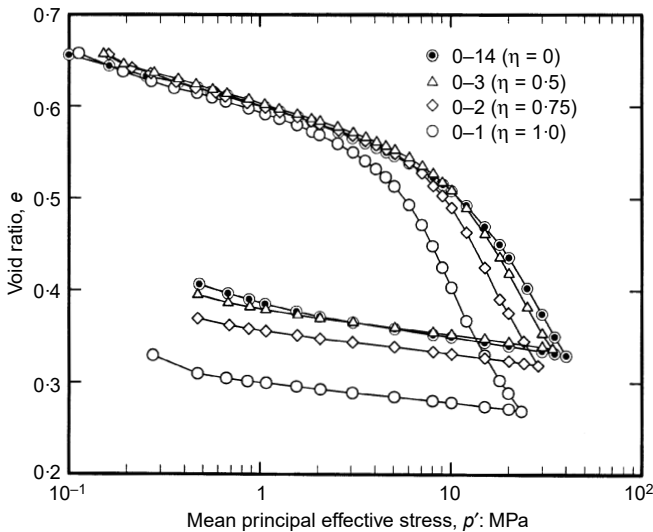
Figure 5.11: Critical state lines of the three model sands in $\log p$-e space [MNH02]

the simulation starts deviating from the experimental results: the isotropic tests tend to be too stiff (at least the looser ones), the oedometer response is slightly too soft. However, it was considered more beneficial to calibrate the involved parameters for the soil behaviour at geotechnically relevant stresses. In addition, since loading is dominated by grain crushing in high stress ranges, altering the soil's grain size distribution and hence also its mechanical properties, the validity of simulation results at high stresses is questionable (see Sec. 3.3).

Aside from the test data of isotropic ($e_0 = 0.78$) and oedometric compression ($e_0 = 0.726$), Fig. 5.10 b also provides simulations of additional constant stress ratio tests of $\eta \neq 0$. Qualitatively, the stress-strain curves (p-e) of these radial consolidations reflect the loss of stiffness with larger stress path inclinations and hence confirm experimental observations made by McDowell et al. [MNH02] on silica sand, see Fig. 5.11.

Unfortunately, regarding anisotropic consolidation ($\eta = \text{const.} \neq 0$) there is no experimental data available on any of the three chosen sands to compare the simulative response with real soil behaviour. However, El-Sohby [ElS69] published quite detailed data of experiments carried out on fine sand in a modified conventional triaxial apparatus, able to load soil specimens along constant stress ratio stress paths. Figure 5.12 presents the results

of these test, which were run at different initial densities ($e_0 = 0.64, 0.86$) and varying constant stress ratios ($\eta = 0 \ldots 1.65$). Subfigure a, showing the resulting radial strain paths in terms of volumetric and axial strain, reveals a clear tendency: with an increase in stress ratio η, the strain ratio $\varepsilon_v/\varepsilon_1$ drops, leading to a clockwise rotation of the corresponding strain paths. This effect intensifies at lower initial densities.

El-Sohby [ElS69] explains the observed deformation characteristic with progressive sliding of the grains, which is induced by the increasing shear stresses, and corresponds to dilation observed in triaxial shear. In his experiments, the strain paths of the denser samples even exhibit dilative behaviour at large stress ratios. However, it has to be noted that particularly these strain paths are not proportional, suggesting that the corresponding stress paths were not perfectly radial and hence experienced stress ratio changes.

Simulations were carried out under similar conditions using the Hostun parameter set in order to qualitatively reproduce the soil behaviour described by El-Sohby [ElS69]. Samples of different initial void ratio ($e_0 = 0.65, 0.85$) were loaded along constant stress ratio paths of different inclinations ($\eta = 0 \ldots 1.5$) up to a maximum vertical stress of $\sigma_1 = 1000\,\text{kPa}$. As Fig. 5.13 a shows, the strain paths trace very similar lines as the experiments: the paths of both densities are congruent under isotropic conditions (with an inclination of 3:1) and turning clockwise with increasing stress anisotropy which is more intense for looser initial states. However, the dilative tendency observed in Fig. 5.12 does not appear. This is not due to testing conditions but is an intrinsic feature of the model. Based on its shape, the cap allows for
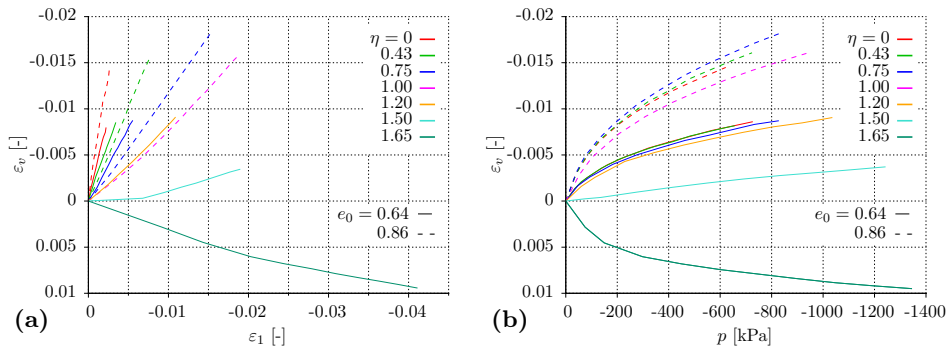
Figure 5.12: Constant stress ratio tests on dense ($e_0 = 0.64$) and loose ($e_0 = 0.86$) fine sand carried out by El-Sohby [ElS69]: volumetric strain ε_v over (a) axial strain ε_1 and (b) mean stress p
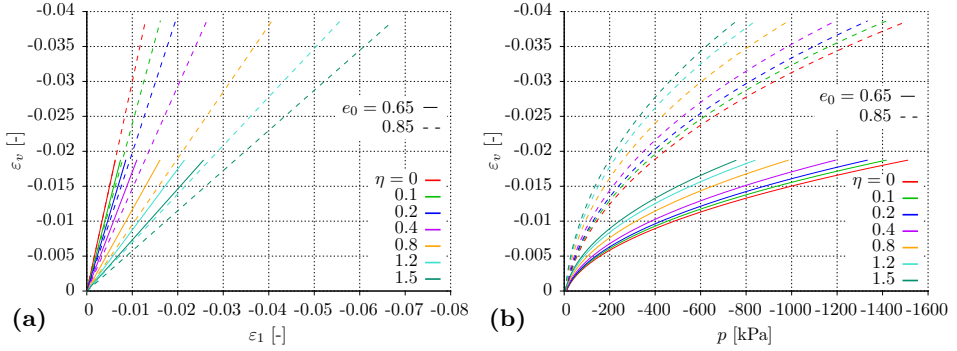
Figure 5.13: Anisotropic consolidation test simulations on dense ($e_0 = 0.65$) and loose ($e_0 = 0.85$) sand (using the Hostun parameter set): volumetric strain ε_v over (a) axial strain ε_1 and (b) mean stress p

compressive volumetric and deviatoric strains only (provided that loading occurs in compression). At isotropic states strain increments are purely volumetric, hence $\dot{\varepsilon}_v : \dot{\varepsilon}_1 = 3 : 1$. With increasing stress ratio shear strains evolve whereas volumetric strains reduce until $\dot{\varepsilon}_v = 0$ and $\dot{\varepsilon}_s = \max$ at the cap's apex. Thus, volumetric strains cannot become positive and cause the soil to dilate. The only source for dilative volumetric strains in the model is the cone, which is almost deactivated in case of constant stress ratio loading. Consequently, disregarding potential errors in the execution of the experiments by El-Sohby [ElS69] mentioned above, his test data could not be fully reproduced.

The changing composition of strains with increasing anisotropy in consolidation also explains what can be seen in Fig. 5.13 b. In addition to the obvious fact that the looser samples compress more under constant stress ratio loading than the denser ones, it shows that the volumetric compaction intensifies with increasing stress path inclination. The growing shear stress component enhances the rearrangement and packing of grains and hence causes a stronger volumetric compression. This is in alignment with the findings of McDowell et al. [MNH02] (Fig. 5.11), but does not completely conform with El-Sohby's [ElS69] results (Fig. 5.12 b). Only up to $\eta = 0.75$ for loose states the latter experimental stress-strain data is in accordance with the simulated trend. For larger stress ratios or higher densities this development is reversed and compressibility decreases, until it finally turns into softening.

Changing the reference value for representing the strain evolution from mean
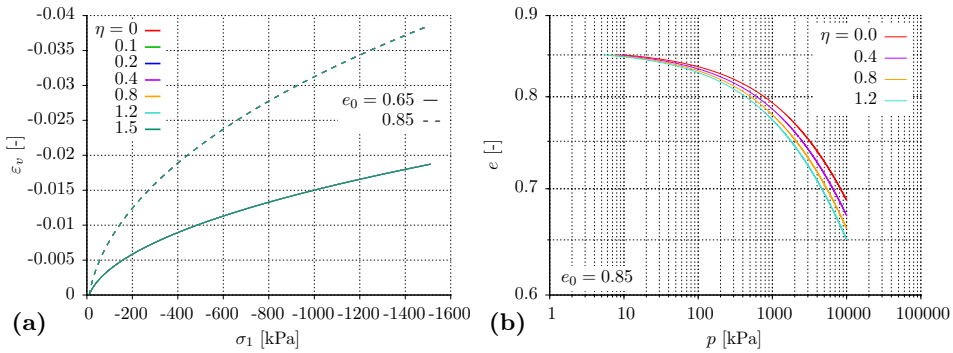
Figure 5.14: Anisotropic consolidation test simulations (continued): (a) represented in σ_1-ε_v space, (b) tests on loose samples up to high stresses (p-e)

stress p to vertical stress σ_1 results in Fig. 5.14 a: for one particular inital density, all curves of different degrees of consolidation anisotropy fall onto one. This outcome is in line with the so called Rutledge hypothesis, which was originally formulated for clay soils. Rutledge [Rut47] concluded from his experiments that the occurring volume changes in radial consolidation are a function of the major principal stress only. This hypothesis became popular for clays and was confirmed for some granular soils, too [e. g. LF67], but is not fully acknowledged though [e. g. PW99]. Lade et al. [LYB05] supported the validity of the Rutledge hypothesis for sand experimentally, but restricted it to high stresses in conjunction with grain crushing.

Continuing the radial consolidation up to high stress ranges of 10 MPa as McDowell et al. [MNH02] did, results in p-e curves presented in Fig. 5.14 b, which are similar to those shown in Fig. 5.10 b. However, the difference between the curves is less pronounced than experiments by McDowell et al. [MNH02] indicate.

Concerning the latter feature, the LCC concept offers better means to control the cap stiffness with variation in the deviatoric stress ratio. See App. C.2 for a comparison of simulations.

Figure 5.15 presents a comparative plot of isotropic and oedometric compression tests on Toyoura sand and therewith gives a summarising illustration of the cap performance for different η-constant stress paths of various initial states. The insufficient stiffness variation for different initial densities can be confirmed in this simulation: the isotropic stress-strain response for

$e_0 = 0.59$ is too soft, whereas the two tests on looser samples are reproduced perfectly. It has to be noted that this property can be controlled by the user-defined exponent of the void ratio dependent factor within the oedometer stiffness function (Eq. (3.30)), n_{oed}, and by simultaneously adjusting the reference value E_{oed}^{ref} and the stress dependency exponent m_{oed}[9]. But since the parameter set was supposed to match both, the isotropic (solid lines) and oedometric data (broken lines), the final choice for the E_{oed}-evolution gives satisfactory simulative results for most test cases up to high stress ranges.
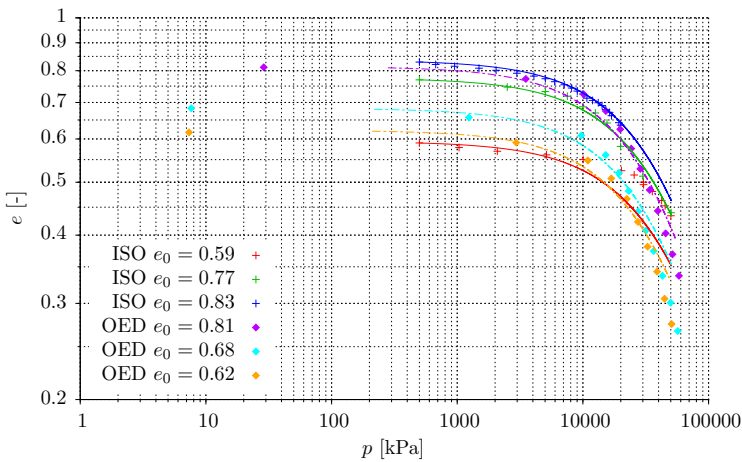
Figure 5.15: Simulation (——/ ····) of isotropic and oedometric compression tests on Toyoura sand compared to test data by Miura [Miu79], Miura et al. [MMY84] and Nakata et al. [NKH+01] (+/◆)

One additional comment has to be made with respect to the initial stresses of the simulated oedometer test in Fig. 5.15. Toyoura sand deforms very little up to relatively high mean pressures and hence requires the cap part of the model to be very stiff at low stresses. In the sense of the constitutive idea, a M_{cap} has to be found that results in a very flat cap in order to produce as little volumetric strain as possible (associativity!). But of course, there are geometric limits, which might become a problem in particular for small

---

[9]A parametric study revealed that many sands demand a rather strong dependency of the oedometer stiffness on the initial void ratio ($n_{oed} > 3$). In order to take account of the stiffness development during loading, which is already driven by the evolving void ratio, it might be required to reduce m_{oed} considerably, even below zero.

stress path inclinations. Transferring this finding into the mathematical context, by looking at Eqs. (3.31) and (3.38), defining M_{cap} and H_0^{cap}, one will acknowledge that the terms in the denominator demand a particular ratio of E/E_{oed} as function of K_0 and ν in order to remain larger than zero. Due to the square root in Eq. (3.31) this also applies to the numerator. Consequently, one has to respect the following condition[10]:

$$\frac{E}{E_{oed}} > (1 + 2K_0)(1 - 2\nu) \qquad (5.6)$$

This requirement limits the size of the oedometer stiffness with respect to the Young's modulus. In case of Toyoura sand this became an issue at very low stresses due to different stress dependencies for E and E_{oed} ($m \neq m_{oed}$), but improved as the stress level increased. Thus, the initial stress was raised, so that the experimental curve could not be simulated to its full extent. Since the deformation caused at low stresses is very small, the error made is negligible. Since this problem would have been even more serious with a reduced Young's modulus as used for the simulation of undrained triaxial loading cases, for all η-constant tests the experimentally indicated elastic parameters have been employed.

5.2 Model performance in non-standard triaxial testing

When focussing on monotonic loadings along conventional triaxial stress paths as well as those evolving at constant stress ratios, only a fractional amount of all possible stress paths starting from a certain point in stress space is considered. In order to capture the behaviour of soil on the complete triaxial plane, it is crucial to also examine the soil response to incremental stress paths of arbitrary inclinations. A very useful tool supporting these investigations is the concept of stress or strain response envelops which will be presented and employed in the following.

5.2.1 Concept of response envelopes

Correctly predicting the soil response in terms of straining (direction and amount) to a certain applied increment of stress (or vice versa) is the pri-

---

[10]In Eqs. (3.30) and (5.6), for η-constant stress paths different from K_0-conditions, K_0 substitutes by the corresponding $K = f(\eta)$.

mary objective in constitutive modelling. Hence, when studying the behaviour of underlying complex constitutive equations and also for the validation of soil models, it can be very instructive to graphically compile computed strain responses to systematically applied stress increments of equal size but varying directions. Connecting the resulting strain paths' end points, shapes an envelope in strain space – the so called strain response envelope. Comparing these numerical outcomes to either experimental data or the simulation results of other constitutive models, allows to assess the performance of the model in question.

The technique of response envelopes was introduced in the 1970s: building on the fundamental idea by Lewin and Burland [LB70], Gudehus [Gud79] developed this method as a useful complementary tool for constitutive modelling. Being restricted to axisymmetric triaxial conditions, the change in principal stresses σ_1 and σ_3 corresponds to a stress increment $\Delta\sigma$ defined as:

$$\Delta\sigma = \sqrt{\Delta\sigma_1^2 + 2\Delta\sigma_3^2} \tag{5.7}$$

Varying the stress components while keeping the stress increment at a constant value results in different loading directions α, which can be computed by:

$$\tan\alpha = \frac{\Delta\sigma_1}{\sqrt{2}\Delta\sigma_3} \tag{5.8}$$

Presented in the Rendulic plane with the axes $\sqrt{2}\sigma_3$ and σ_1, these stress paths form a circular stress envelope (see inset in Fig. 5.16 a): a stress path with an angle of $\alpha = 90°$ ($\Delta\sigma_3 = 0$), for example, corresponds to conventional triaxial compression (light green line), pure radial extension ($\Delta\sigma_1 = 0$) is achieved at an angle of $\alpha = 180°$ (blue line). Figure 5.16 b shows the equivalent representation in p-q space, where the circle turns into an ellipse.

The corresponding strain responses in terms of principal strains ε_1 and ε_3 are also presented in the Rendulic plane and the strain increment analogously amounts to:

$$\Delta\varepsilon = \sqrt{\Delta\varepsilon_1^2 + 2\Delta\varepsilon_3^2} \tag{5.9}$$

Unfortunately, due to the required non-standard triaxial loading conditions, experimental data for verification and validation is not inexhaustible and the method of response envelopes has been mainly used as a numerical tool for classifying constitutive models so far. However, after the initiating investigations by Lewin and Burland [LB70] on clay, a few experimental

studies have been carried out particularly within the last two decades, e. g. by Anandarajah et al. [ASK95] (sand), Doanh [Doa00] (sand), Costanzo et al. [CVT06] (clay) and Danne and Hettler [DH13, DH15, DH16] (sand). These unconventional laboratory investigations provide a database that can serve for qualitative comparisons.

An extensive laboratory study on fine sand has been executed by Danne and Hettler [e. g. DH15]. They systematically investigated the influence of initial stress conditions, loading history and stress increment size on the resulting strain response envelopes. Part of their lab programme is de-
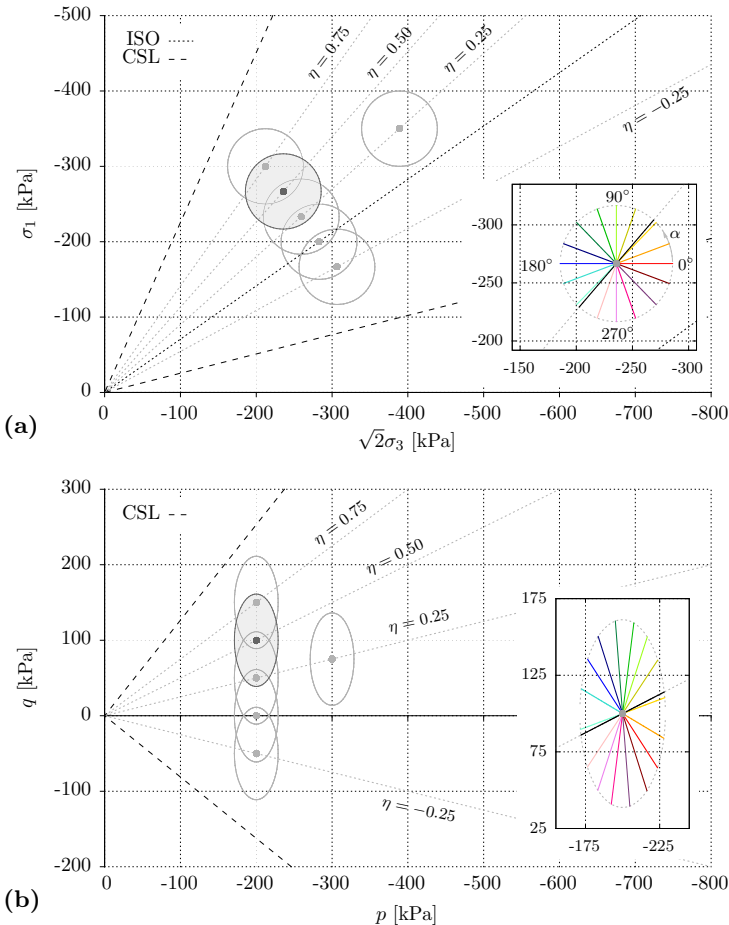
Figure 5.16: Representation of incremental stress paths of different directions in (a) Rendulic plane and (b) triaxial p-q plane
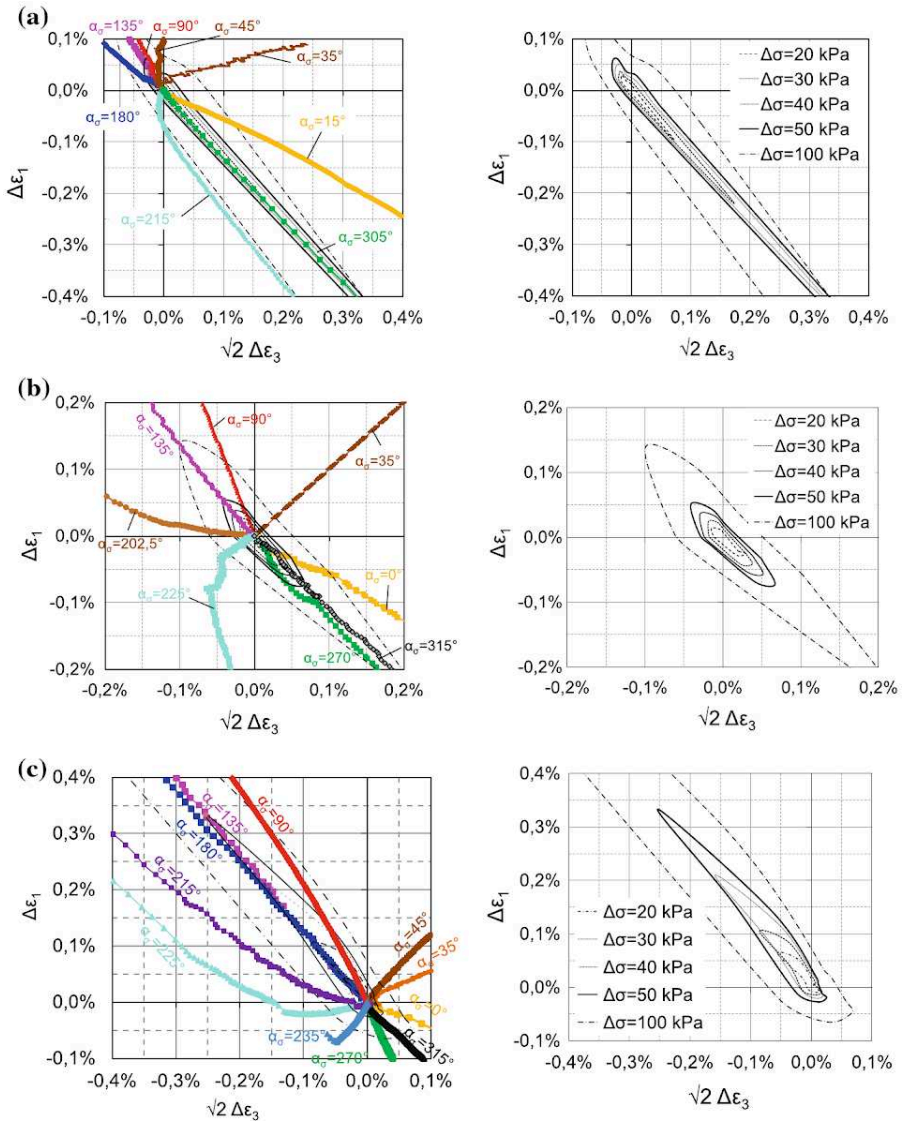
Figure 5.17: Exemplary strain responses of stress probe test by Danne and Hettler [DH16] with initial conditions of $p_0 = 200\,\text{kPa}$ and (a) $\eta_0 = -0.5$, (b) $\eta_0 = 0$ and (c) $\eta_0 = 0.75$

picted in Fig. 5.16: various stress probe tests were run at different initial stress ratios η_0 by keeping the initial mean stress constant at $p_0 = 200\,\text{kPa}$ and varying the corresponding deviatoric stress accordingly. Furthermore, the initial stress ratio was kept constant while the mean and deviatoric stresses were varied. From these starting points (amongst others), stress increments of up to $\Delta\sigma = 100\,\text{kPa}$ were applied in eight different directions ($\alpha = 0, 45, \ldots 315°$) and the strain response was recorded. Exemplary experimental strain responses and the resulting envelopes for three different initial stress conditions ($p_0 = 200\,\text{kPa}$ and $\eta_0 = 0.75, 0.0, -0.5$) are depicted in Fig. 5.17. It can be clearly stated that in contrast to the circularly arranged applied stress increments, the strain envelopes take an elliptical shape, elongated in the direction of deviatoric loading and unloading, corresponding to $\alpha \approx 125°$ and $305°$. Furthermore, the size and orientation of the envelope's elongation (for a constant stress increment $\Delta\sigma$) depends on the initial stress state: the larger its anisotropy, the stronger the straining in the direction of the closest failure line and hence the stronger the strain envelope's geometrical asymmetry. Thus, the stress probe test at $\eta_0 = 0.75$ (subfigure c) exhibits the largest deformations roughly in direction of deviatoric loading, whereas at an initial stress ratio of $\eta_0 = -0.5$ (subfigure a) strains are maximal in deviatoric unloading.

Concerning the straining direction, it can be observed, that in case of the stress probe starting from the isotropic stress state (subfigure b), the
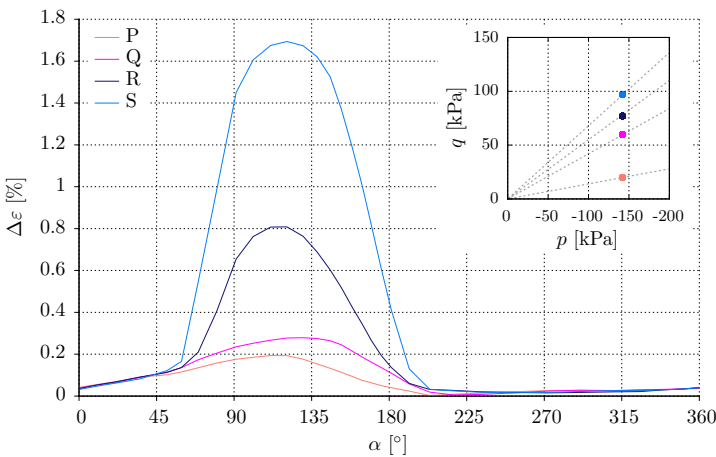
Figure 5.18: Strain evolution with applied direction of stress for stress probe tests of different initial anisotropy, test data by Lewin and Burland [LB70]

coloured strain paths depart almost radially (up to stress increments of $\Delta\sigma = 100$ kPa). But the more anisotropic the initial stress state, the stronger the deflection of the strain paths towards either deviatoric loading or unloading. Consequently, the same direction of stress increment can result in a distinctly different orientation of the resulting strain path depending on the initial stress state (e. g. path "225°").

A similar study carried out by Lewin and Burland [LB70] on Kaolin clay gives reason to assume that the point of maximum total strain is not static with respect to the direction of applied stress. In Fig. 5.18, it seems to move from purely deviatoric loading ($\alpha \approx 125°$) at (almost) isotropic initial states towards larger angles α with increasing anisotropy.

5.2.2   Simulation of response envelopes

Following the layout of the experimental study by Danne and Hettler [e. g. DH15], the observed characteristics of strain paths resulting from stress probe tests are numerically investigated in the following. In order to analyse the influence of the initial stress state on the extent and orientation of the strain response envelopes, stress probe tests were run at five different initial deviatoric stress ratios η_0 with a common mean stress of $p_0 = 200$ kPa. Additionally, keeping $\eta_0 = 0.25$, but increasing the initial mean stress to 300 kPa (and the deviatoric stress accordingly) allows a direct comparison of the deformational responses at different mean stress levels. All initial stress states are plotted in Fig. 5.16. The simulations were carried out using the strain contour concept regarding the stiffness at small strains and the parameter set of Toyoura sand was used, with an initial void ratio of 0.8. Since this study aims for qualitatively analysing the soil response to stress probe tests, the initial loading paths for reaching the respective starting point (isotropic consolidation, triaxial compression) have not been simulated – the anisotropic stress state has been initialised "wished in place". Consequently, each stress probe test is numerically treated as a primary loading, the initial conical yield surface being centred around the starting point and the first strain contour being initiated when loading starts.

Figures 5.19 b to d show the strain paths resulting from multi-directional stress increments of $\Delta\sigma = 50$ kPa as depicted in subfigure a: the soil response is the stiffest when loadings occur close to the initial stress ratio and softens on stress paths in the vicinity of purely deviatoric (un-)loading. Hence, the computed strain response envelopes generally reproduce the elliptical shape, stretching from deviatoric loading to unloading. As observed
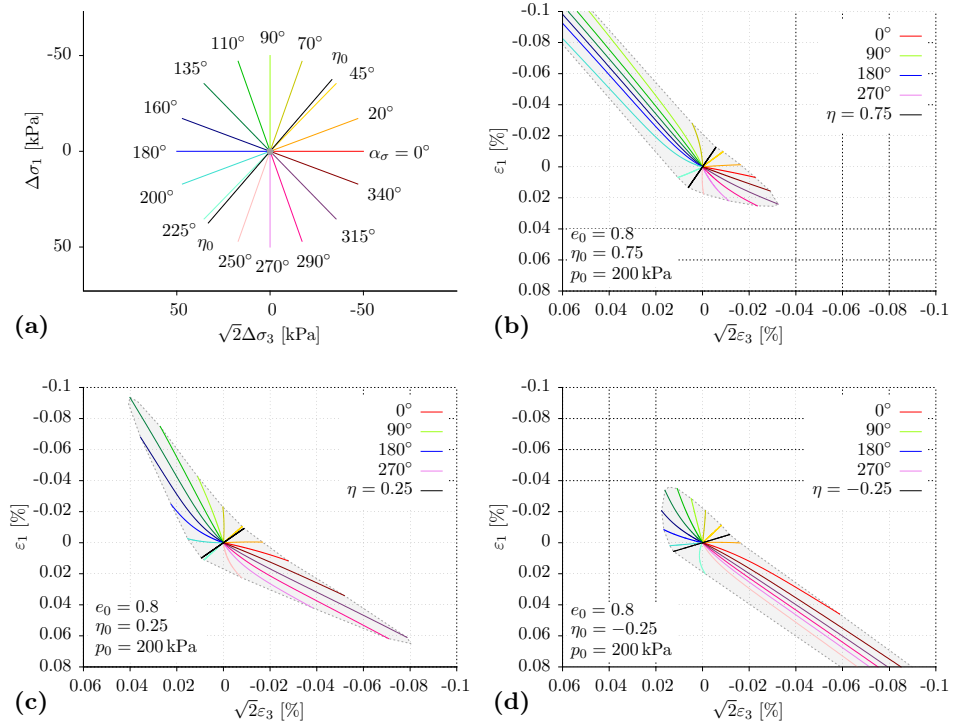
Figure 5.19: (a) Simulated loading directions; resulting strain paths and envelopes for $e_0 = 0.8$, $p_0 = 200\,\text{kPa}$ and (b) $\eta_0 = 0.75$, (c) $\eta_0 = 0.25$ and (d) $\eta_0 = -0.25$

in the experiments, with decreasing initial stress ratio η_0 through subfigures b to d, the largest deformations are shifted from deviatoric loading to unloading. This variation of η_0 illustrates the previously mentioned effect of anisotropy on the strain response envelope. On the constitutive level this behaviour is caused by the distance of the actual stress state to its attributed failure surface in compression or extension: as the initial stress ratio drops, the distance measure d^b with reference to the compressive side increases, causing the response to become stiffer, while it decreases on the extension side, resulting in larger strains.

When looking closely at subfigure c, the response envelope is rather symmetrical. In contrast to the experimental results, this almost balanced lookout does not appear in case of the initially isotropic sample (as one might expect), but for $\eta_0 = 0.25$. This is due to the choice of the critical state angles in compression and extension, which cause the failure envelope in extension

to be considerably closer to the isotropic state than in compression. Since the distance of the actual stress state to the failure surfaces M_c^b and M_e^b, respectively, controls the evolution of strains, the "neutral" position with respect to the response envelope's shape is shifted into the compression domain.

As observed previously, it is not only the amount of straining that changes with anisotropy, but also the strain path's orientation. Considering the same loading direction as before, $\alpha_\sigma = 225°$, the strain path's directional development changes with the initial stress ratio, being gradually pulled towards the main straining direction.

In Fig. 5.20 the numerical variation of three important influencing factors is documented. Subfigure a shows the obvious increase of the strain envelope's size with doubling of the applied stress increment. However, the enlarge-
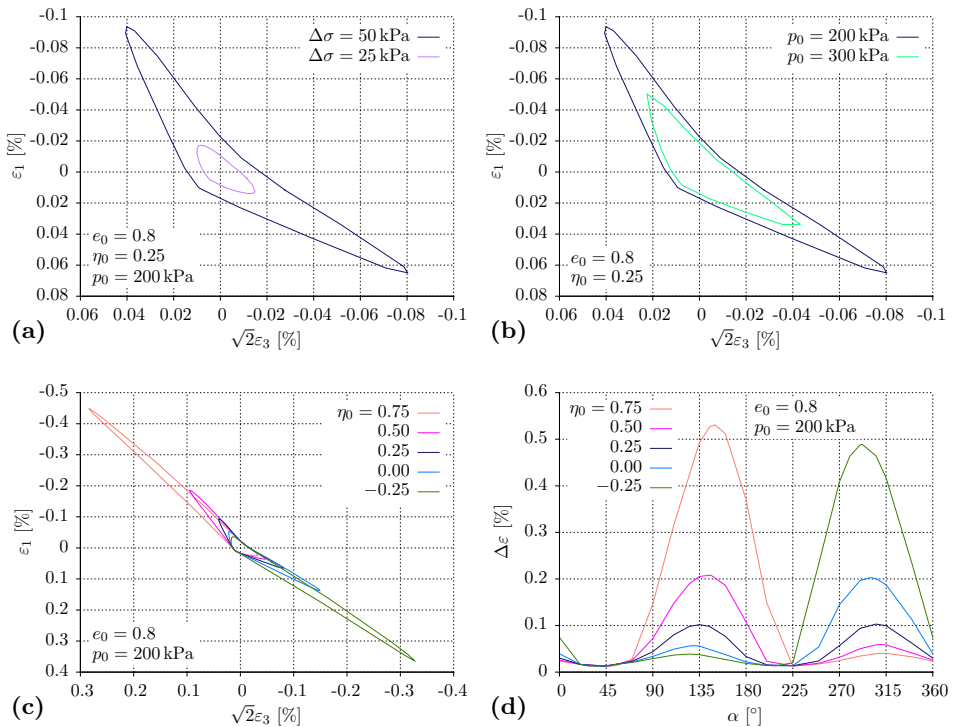
Figure 5.20: Comparative simulation of response envelopes with respect to varying testing conditions: (a) $\Delta\sigma$, (b) p_0 and (c) η_0, (d) variation of resulting strain $\Delta\varepsilon$ with loading direction α_σ for different η_0

ment is not proportional in all directions due to the non-linear development of plastic strains. Similarly, if probe tests are run at the same initial stress ratio but an increased mean stress level stress (subfigure b), the resulting strain response envelope shrinks equally, mainly along its main axis.

Subfigures c and d depict the variation of η_0 over the whole range of examined stress ratios and confirm the statements with respect to anisotropy and its effect on the orientation and amount of resulting strains made in the context of Fig. 5.19. One aspect, which is well documented by the graphical representation in subfigure d, is the shift of loading direction for maximum straining with increasing anisotropy. If the initial state is (about) isotropic, the strain increment $\Delta\varepsilon$ reaches its maximum when purely deviatoric loading occurs ($\Delta p = 0 \rightarrow \alpha_\sigma \approx 125°$ in loading or $\alpha_\sigma \approx 305°$ in unloading). The more anisotropic the initial stress state, the more the stress probe direction at maximum strain moves away from this angle towards higher (loading) or lower (unloading) angles. This would be in accordance with the observation made with respect to experimental data by Lewin and Burland [LB70] in the previous section (Fig. 5.18).

One aspect that might be worth mentioning is the shape of the response envelope, which exhibits a slight bending in the simulations (e.g. Fig. 5.19 c) in contrast to the rather balanced ellipse of the experimental results by Danne and Hettler in Fig. 5.17. Transferring the deformational data of Fig. 5.19 c into the more familiar ε_1 -ε_v representation (see Fig. 5.21 a), reveals a strong contractant tendency in strain paths that correspond to loadings, which involve an increase of mean pressure. Considering the re-
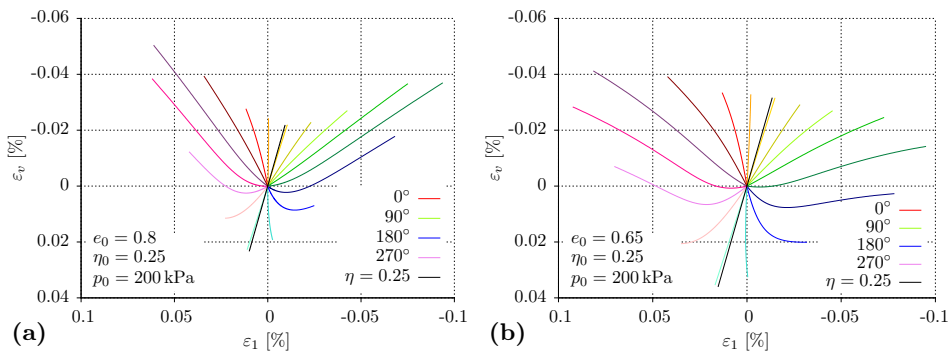
Figure 5.21: Simulated strain paths for $p_0 = 200\,\text{kPa}$, $\eta_0 = 0.25$ and (a) $e_0 = 0.8$, (b) $e_0 = 0.65$
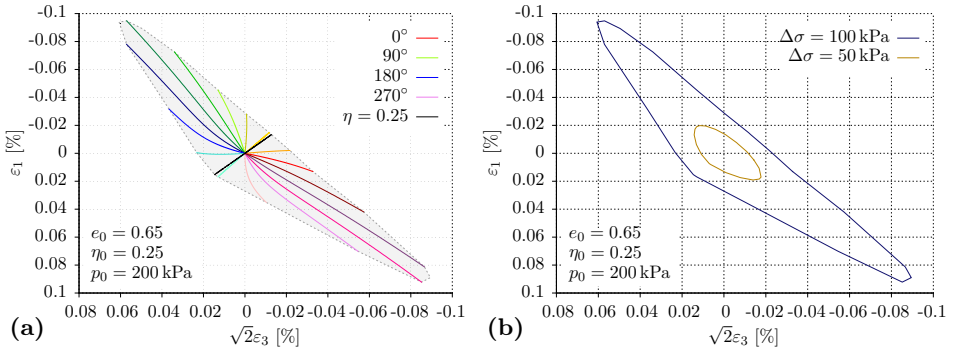
Figure 5.22: Simulated strain paths and resulting response envelope for $e_0 = 0.65$, $p_0 = 200\,\text{kPa}$ and $\eta_0 = 0.25$

latively loose initial state of the soil specimen ($e_0 = 0.8$), the tendency of being compacted is not surprising. This leads to the conclusion that at higher densities the contractant behaviour will become more dilatant (see Fig. 5.21 b) and hence the banana shape of the envelope should turn into a well-formed ellipse. The simulation of an equivalent stress probe test starting from an initial void ratio of $e_0 = 0.65$ in Fig. 5.22 confirms this assumption.

Consequently, not only the initial stress state, but also the initial density of the soil has an influence on the shape of the resulting strain envelope. The question is, whether the distortion in shape with varying void ratio is a numerical effect or a feature of soil behaviour. Comparing Danne's results with alternative experimental data, such as the strain response envelopes derived by Costanzo et al. [CVT06] (Fig. 5.23), the following can be observed: aside from the effect of initial anisotropy on the elongation of the strain response envelope, a distinct bending of the loops can be recognised. The clearly deviating strain paths along the respective semi-major axes of the "ellipse" ($\alpha_\sigma = 126° \rightarrow 305°$) confirm the distorted shape produced by the simulations on looser sand (Fig. 5.19).

As initially mentioned, for this numerical study the specimen's loading history experienced in the laboratory test (isotropic loading, triaxial compression to the anisotropic stress state) was neglected for the sake of simplicity in view of a better comparability of the simulation results. Had the preloading been taken into account, particularly the initial part of stress probe loading would have lead to slightly different response envelopes. Due to the preceding shearing path the cone would actually be displaced in a way that the starting point of the stress probe test was located on the yield sur-
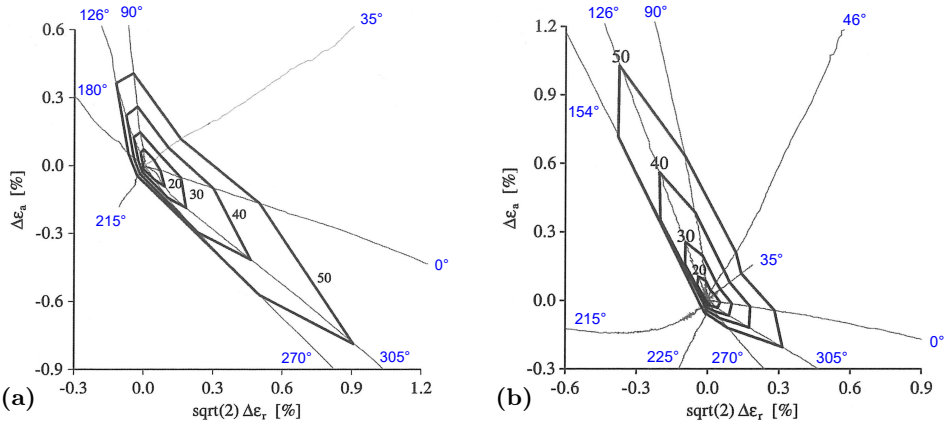
Figure 5.23: Strain response envelopes of stress probe test with $\Delta\sigma = 20\ldots50\,\text{kPa}$ on a low plasticity silty clay by Costanzo et al. [CVT06] with initial conditions of $e_0 \approx 0.75$, $p_0 = 150\,\text{kPa}$ and (a) $\eta_0 = 0$ and (b) $\eta_0 = 0.4$ (blue α_σ values added)

face. Any stress probe test departing with little change in loading direction (more or less perpendicular to the yield surface) would directly cause plastic strains, whereas $\approx 180°$-reversals would exhibit elastic strains at first (having to cross the complete elastic domain). In addition, depending on the size of directional change, the small strain hardening mechanism would influence the plastic stiffness. Consequently, the response envelope in Fig. 5.19 c, to give an example, would lose its geometrical balance and be more elongated along the 135°-axis and shorter on the opposite side, when respecting the specimen's loading history.

A last comment shall be made on the consistency of strain paths predominantly created by violating the cap or the cone yield criterion. Considering all simulated response envelopes presented in this chapter, the η-constant stress paths are in very good agreement with adjacent stress paths, which slightly deviate from the constant value of the deviatoric stress ratio. Due to the two-part yield surface with two different hardening mechanisms for $\eta = \text{const.}$ and $\eta \neq \text{const.}$ this is not necessarily the case and depends on the parameter choice for the cap. Since Toyoura sand is very stiff in compression, the small stress increments along the η-constant stress paths inside the conical yield surface caused deformations close to elastic. If the examined material behaves softer, such as Hostun sand for example, it is the cap parameter C that determines the contribution of the cap along stress

paths drifting away from constant stress ratios. Thus, with an inappropri-
ate choice of C, a distinct discontinuity might appear in the strain response
envelope in the direction of cap loading.

5.3   Model performance on general stress paths

The previous section dealt with the reproduction of monotonic loadings,
represented by a single branch stress path in stress space. With the objective
of analysing practical geotechnical problems, the next step is to proceed to
more complex loading cases. Typical applications in geotechnical routine are
rarely restricted to one-way loadings, but are composed of several branches.
One might think in long lapse of time, referring to the formation history
of a soil from sedimentation and consolidation (stress path along K_0-line)
to geological transformations by pressure (e. g. overburden by glacier) or
temperature to erosion or weathering. It is a long chain of events influencing
the soil mechanical properties considerably, which is often reduced to an in-
situ stress and density state and by defining a corresponding K_0-value or
overconsolidation ratio (OCR). However, if the genesis of the soil profile in
question is too intricate, it might be worth considering the simulation of
the full history, resulting in a rather complex stress path.
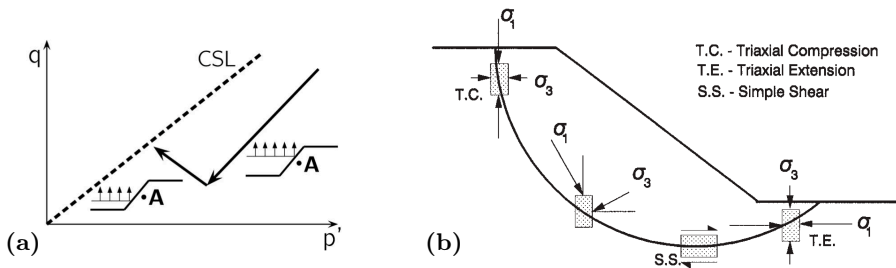
Figure 5.24: (a) Stress path of a point A inside a slope during excavation
[NH14], (b) reorientation of principal stresses along a slip surface beneath
an embankment [UV98]

When focusing on limited periods, construction processes come into play.
In less complex staged constructions as a plain excavation in layers, the
stress path of a soil element right next to the emerging slope describes
an unloading in triaxial extension $(-\Delta\sigma_1)$, followed by an unloading in
triaxial compression $(-\Delta\sigma_3)$, see Fig. 5.24 a. Similarly, in the simple case of
ground failure, principal stresses rotate from triaxial compression to simple

shear mode and further to triaxial extension along the slip surface (5.24 b). Increasing complexity, the setting up of a construction pit offers various changes of soil states, including for example the excavation of ground, the stepwise installation of anchors or struts, the increase of foundation loads by advancing construction or even an unexpected flooding of the excavation pit. When considering a particular soil element in the vicinity of the site, it experiences numerous loading situations regarding orientation and size of the acting principal stresses (Fig. 5.25).
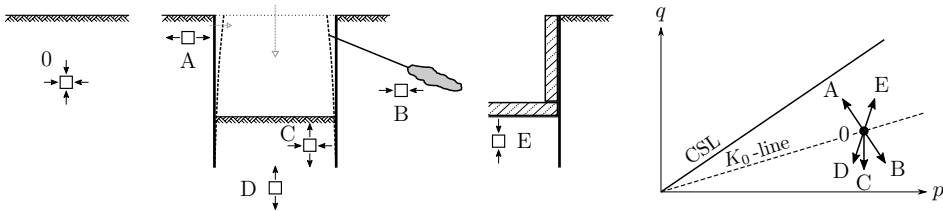
Figure 5.25: Possible changes of stress states in various points in the vicinity of a construction pit and their representation as stress paths in p-q stress space

Moving on to a third category of non-monotonic cases, attention is paid to repetitive loadings. They typically occur during operation of infrastructural buildings due to cyclically recurring traffic loads, such as passing trains or vehicles (which might even have a dynamic influence). Alternatively, quasi-static load reversals due to up- and downstream locking of ships can be mentioned, which act on the surrounding soil via the water level induced deformations of the lock. Another example for repetitive loadings at a quasi-static pace is the stepwise installation of anchors with the progressing excavation of a construction pit. Furthermore, repetitive variations in the (free) water table can cause pore pressure changes and hence an alteration of effective stresses. Depending on the speed of the water level drop in relation to the permeability of the soil, excess pore water pressures can emerge (Fig. 5.26). If the soil is rather permeable and/or the water table changes occur very slowly (e. g. due to precipitation and natural run-off or storage level control), stationary conditions can be assumed, resulting only in an adjustment of effective stresses due to the hydrostatic pore water change. If these fluctuations of the water level occur within short stretches of time and in rather fine grained and hence impermeable soils, the reduction in hydrostatic pore water pressure lags behind the drop of the water table,
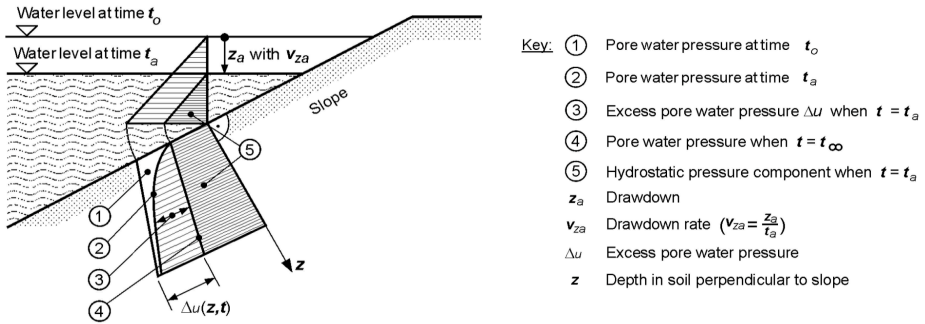
Figure 5.26: Hydrostatic pore water pressure and excess pore water pressure during a quick water level drop [Bun11]

so that excess pore pressures build up[11]. They might lead to a considerable reduction in effective stresses, which disappear with time and rerise of the water table, resulting in an oscillating horizontal q-constant stress path with an alternate stabilising/destabilising effect on the soil body. This phenomenon can be observed, for instance, along embankments of waterways as a consequence of waves, induced by passing ships, high and low tide, wind or lock and weir operation [Bun11].

It is hence interesting to know, how the model responds to elementary composed stress paths in order to extrapolate its behaviour with respect to loading cases of higher complexity. Non-monotonic stress paths automatically include changes in loading direction, which can appear as full reversals (180°) or be of any other size. In this context, it is the small strain stiffness as well as the fabric evolution mechanism that are of particular importance and will hence be examined in the following.

5.3.1 Triaxial compression at small strains

Since the small strain extension of the present model applies to the conical yield surface and its hardening mechanism, triaxial compression tests are simulated in order to present the capabilities and limitations of the three implemented procedures: strain contours, stress contours and intergranular strain.

---

[11]This phenomenon is strongly linked to the existence of gas inclusions in the pore fluid: gas bubbles increase in size with reduction of the hydrostatic water pressure and delay the pressure compensation. Further reading in Köhler [Köh97].

Considering monotonic triaxial compression tests first, due to the very similar calibration results for the three small strain options (see Sect. 4.2.3), no significant differences are to be expected for the stiffness and hence stress-strain evolution in virgin loading. If, on the contrary, stress paths are taken into account that include partial stress (or strain) reversals ($90° \leq \alpha \leq 180°$), only models with a corresponding stiffness interpolation mechanism are capable of delivering differing soil responses. In order to analyse the capabilities and potential limitations of the implemented mechanisms, in Fig. 5.27, the simulative results of four distinct loading paths are shown, modelled with the two directionally dependent models: strain contours and intergranular strain. The evaluated p-constant stress path (starting from an isotropic stress state) was preceded by an isotropic compression path (a: $\alpha = 90°$), an opposed p-constant path (b: $\alpha = 180°$) and a p-constant stress path of the same orientation, departing in the extension regime (c: $\alpha = 0°$). In addition, a reference path (0), starting directly from the isotropic stress state without any precedent loading, has been simulated. The stiffness degradation curves of the latter path are almost congruent for the two small strain options, which confirms the adequacy of the calibrated parameter sets. Another general observation is that all graphs join at roughly the same shear strain level: $2 \cdot 10^{-3}$, corresponding to the chosen limit strain γ_{lim}, where most of the additional small strain stiffness has decayed.

Besides these similarities, there are obvious distinctions. Depending on the previous directional change, the graphs depart from different stiffness
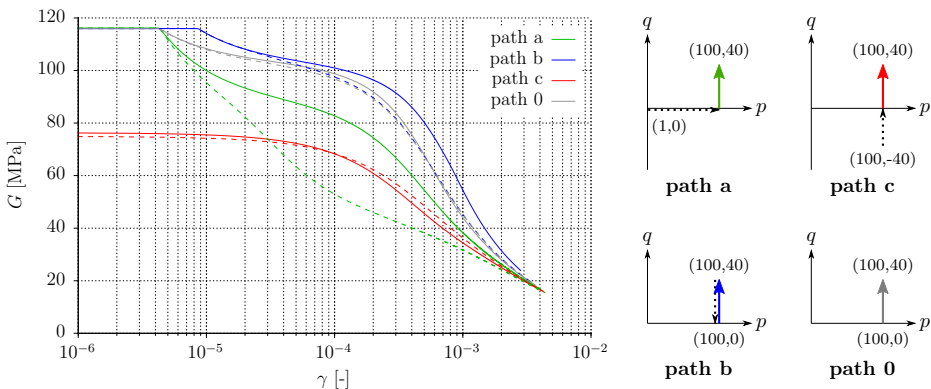
Figure 5.27: Simulated evolution of secant shear modulus G with shear strain γ for four stress paths partly including changes in loading direction: ── strain contours, --- intergranular strain

levels: paths a and b ($\alpha \geq 90°$) both start from the elastic stiffness since the stress reversals force them back into the elastic domain. But due to the full reversal, path b has to cross the complete elastic cone, whereas path a departs from the yield surface's median and hence crosses only half of it. Consequently, the transition to plasticity is slightly shifted towards higher shear strains in case of the 180°-turn.

On the contrary, the stiffness of path c when trespassing the isotropic stress state is considerably lower. Since this stress path does not include any directional change, the previously reached plastic (small strain) stiffness is transferred to the beginning of the second part of loading and keeps on decreasing steadily. Because of the generally very similar response of all small strain models in monotonic loading, the solid and the broken G-γ curves hardly deviate from another.

After leaving the elastic domain, the results for path a and b deviate from another, which is attributed to the stiffness interpolation function. Due to the 90°-turn, the reduced plastic stiffness factor $h_{ss} = m_T = 0.4 \cdot m_R$ is applied to path a and hence the secant shear stiffness degrades more quickly than in case of path b ($h_{ss} \approx m_R$). But not only the paths vary, the performance of the two small strain stiffness options also does. The strain contour model only applies the mentioned interpolation with respect to the change in direction. The intergranular strain concept, on the other hand, also takes account of the previously developed intergranular strain via its specific length ρ and a function of the angle between intergranular strain and actual strain increment, $\boldsymbol{\delta} \cdot \dot{\boldsymbol{\varepsilon}}$ (see Eq. (3.44) and Fig. 3.24). Consequently, the hardening factor h_{ss} decreases at a faster pace and hence the stiffness degradation curve of path a, calculated with the intergranular strain model, lies below the strain contour model's response. This also means that the intergranular strain evolves, no matter how the soil is loaded. However, it is only activated, when the conical yield surface is violated by deviatoric loading. This way on the isotropic part of stress path a ρ grew from 0 to almost 1 and affected the further stiffness decrease as described above.

Another interesting aspect worth mentioning is that in case of the intergranular strain overlay, although the stiffness degradation curves of path b and reference path 0 depart from different shear strain levels, after a certain amount of straining they rejoin and remain congruent until the end of the loading path. On the contrary, the strain contour model clearly produces two distinct curves, the unloading curve (b) being stiffer than the one of first loading (0). This reflects the provision for the first Masing rule, deman-

ding the scaling of the backbone curve by a factor of 2 for unloading and reloading and hence the increase in secant shear stiffness. This mechanism works whenever deviatoric strain is reversed, for any change of direction $90° < \alpha \leq 180°$ departing from a virgin loading path. Only the initial value of h_{ss} will be reduced if $\alpha < 180°$. Simultaneously, the intergranular strain concept takes account of the directional change additionally and hence a deviation from a truly full shear reversal (in terms of strain) causes the intergranular strain evolution to follow scheme (b) instead of (a) shown in Fig. 3.23. Consequently, ρ does not decrease down to 0 but only to an intermediate value before reincreasing to 1. Following the evolution rule of Eq. (3.49), this causes the reduction of h_{ss} to be much faster and finally the stiffness degradation curve to be flatter compared to a full $180°$-turn. Returning to the initially considered path b, the full stress reversal does not result in a full reversion of strains (only $\approx 168°$), so that the shear stiffness decreases more quickly than in case of the strain contour model.

The observation described above can be investigated by the simple example of triaxial compression and its reversal. The essential point is that this stress path reversal induces a full reversion of strains only in seldom cases. The direction of elastic straining after turning in terms of volumetric over deviatoric strain rate is defined by $\frac{\dot{\varepsilon}_p^{el}}{\dot{\varepsilon}_q^{el}} = \frac{\dot{p}}{K} \cdot \frac{3G}{\dot{q}}$, reducing to $\frac{\dot{\varepsilon}_p^{el}}{\dot{\varepsilon}_q^{el}} = \frac{G}{K} = \frac{3(1-2\nu)}{2(1+\nu)}$ due to the stress path inclination of 3 in the particular case of triaxial compression/extension. Generally speaking, the elastic straining direction is predetermined by the choice of ν (for straight stress paths and according to the definitions for shear and bulk modulus applied). From this follows that only if the triaxial stress path, along which the elastoplastic strain direction changes steadily, is reversed in the exact moment where $\frac{\dot{\varepsilon}_p}{\dot{\varepsilon}_q} \approx D = \frac{3(1-2\nu)}{2(1+\nu)}$, strains turn by $180°$. Alternatively, if triaxial compressive loading is stopped precisely at phase transition, where $\dot{\varepsilon}_p = 0$, and continued by an unloading along a p-constant stress path ($\dot{p} = 0 \rightarrow \dot{\varepsilon}_p^{el} = 0$), a full strain reversal can be detected. This latter option is compared to a regular full stress reversal at the moment of phase transition along a triaxial path (resulting in $\alpha \approx 157°$) in Fig. 5.28. Analysing the evolution of h_{ss} in subfigure a, it is clearly visible that the triaxial unloading (1) causes a reduced post-reversal plastic stiffness and a faster decay with reference to the full strain reversal along the p-constant path (2). The impact on the secant stiffness degradation (Fig. 5.28 b) within the range of small strains is almost negligible. The deviation growing at large strains ($> 10^{-3}$), visible in the secant stiffness evolution (b) as well as the unloading branch of the stress-strain curve (c), is
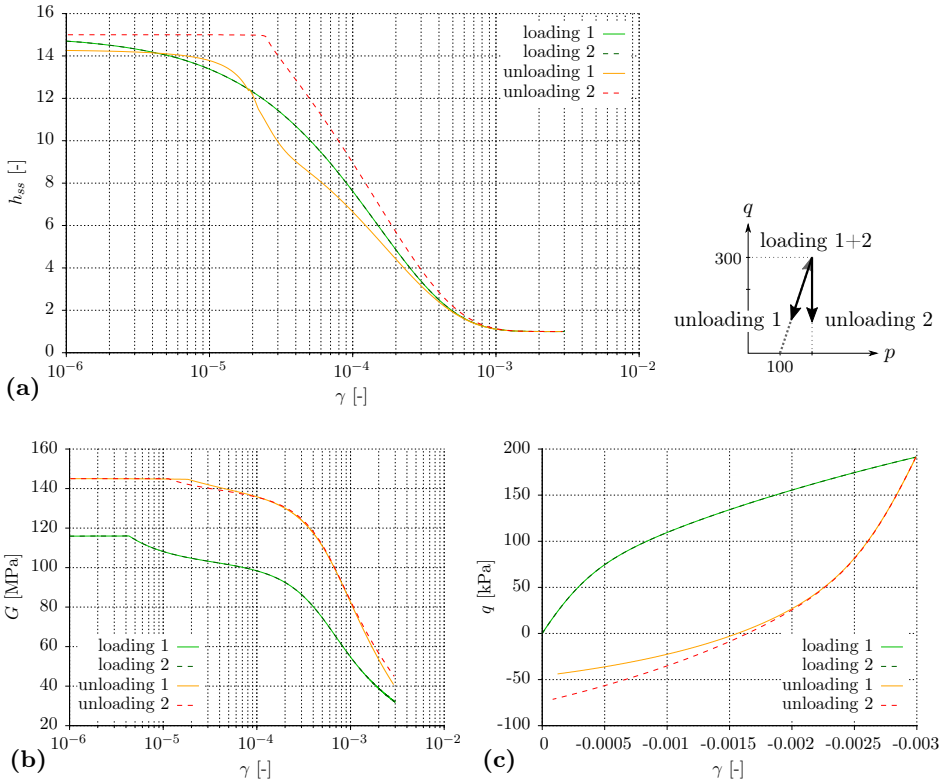
Figure 5.28: Simulation of a triaxial compressive loading path up to phase transition followed by (1) triaxial unloading and (2) p-constant unloading: evolution of (a) hardening factor h_{ss}, (b) secant shear modulus G and (c) deviatoric stress q (intergranular strain overlay)

not linked to the intergranular strain mechanism any longer but originating from the bounding surface formulation and is due to the different types of unloading stress paths.

From the previous considerations and the started discussion on the fulfilment of the first Masing rule, one can conclude that the intergranular strain overlay is not conceptualised for producing a perfectly double magnified backbone curve in unloading. Its evolution equation basically mimics the underlying idea, which is particularly visible in case of a full strain reversal with the complete degeneration and redevelopment of intergranular strain $(-R \rightarrow 0 \rightarrow R)$. Though, the resulting shape of the backbone curve only approximates the first Masing rule's postulation. Figure 5.29 visualises
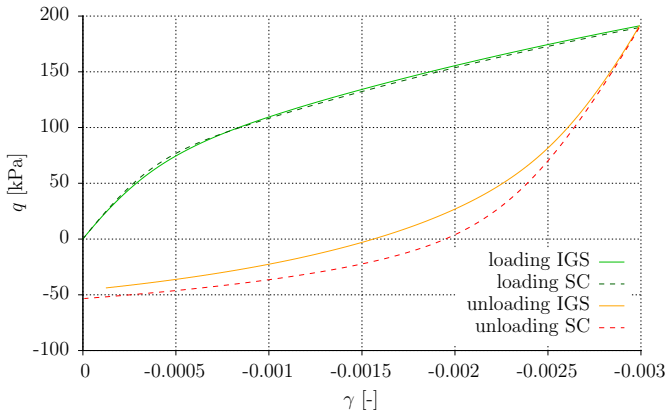
Figure 5.29: Stress-strain evolution of a triaxial compressive loading path and its reversal, simulated with the intergranular strain overlay (——) and the strain contour model (---)

the consequence of this conceptual difference, comparing the reversal of a triaxial compression path modelled with the intergranular strain concept and the strain contours, respectively.

5.3.2   Cyclic triaxial loading

Effect of small strain stiffness

Having analysed the different small strain mechanisms in detail, it is worth pointing out the benefits of the strain dependent stiffness degradation at smaller strains. Of course, as long as only a single cycle is modelled, small inaccuracies with respect to the soil's stress-strain response might be negligible. But as soon as loading direction changes more often, staying in the small strain domain, small errors sum up to larger deviations, which can severely distort the final result. Particularly in case of drained cyclic loading with numerous load reversals, this ratcheting effect is a serious problem, which can be solved by respecting stiffness evolution at small strains. An exemplary comparative simulation for showing the impact of the small strain stiffness on the deformational behaviour is given in Fig. 5.30.

Transferring the issue of volumetric deformation behaviour in drained cyclic shearing to undrained loading cases, the pore pressure evolution substitutes for void ratio related aspects. The overshoot in volumetric strains translates into an exaggerated pore pressure evolution, if the strain dependent stiffness
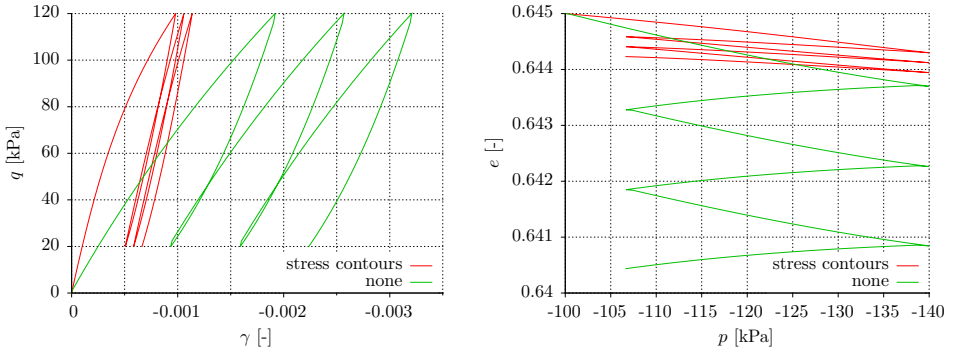
Figure 5.30: Simulation of the stress-strain evolution in cyclic loading, modelled with stress contours and without any small strain option

in the small strain range is neglected. Consequently, taking small strain stiffness into account improves the formation of pore pressures towards a more realistic (slower) development. On the one hand, this partly remedies the problem of too flat stress paths, as discussed in Sect. 3.2.4. On the other hand, in the context of liquefaction analyses the correct capture of cyclically accumulating pore water pressures ensures a reliable failure prediction. In analogy to Fig. 5.30, Fig. 5.31 presents the simulation of an undrained triaxial test with several load reversals, with and without using a small strain stiffness option. In subfigure b it is clearly visible that the initial stress path branch departs distinctly steeper when taking account of an increased stiffness at small strains, and consequently, a cycling stress path
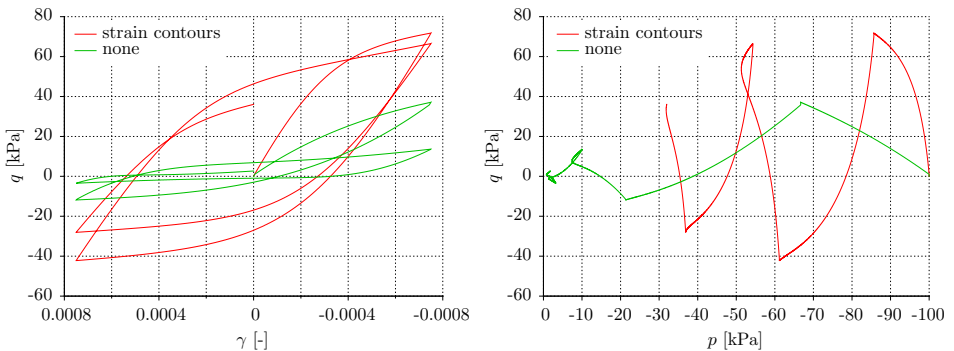
Figure 5.31: Simulation of the stress-strain evolution in strain-controlled undrained cyclic loading, modelled with strain contours and without any small strain option, respectively

approaches liquefaction state ($p' = 0\,\mathrm{kPa}$) more slowly.

It might be worth mentioning that the choice of stress and strain contours, respectively, for the simulation of the two previous cyclic triaxial loadings was made in view of the type of load control. Using stress contours in case of constant stress cycle amplitudes (stress controlled drained cyclic test: $\eta_{max} = $ const., $\eta_{min} = $ const.), cycling will take place inside one contour. This avoids undesirable stiffness changes due to the resumption of old contours, which would occur due to the permanently changing limits of shear strain (see Fig. 5.30 a), if strain contours were used. In order to remain consistent, for the simulation of the strain controlled undrained cycles the strain contours have been used. As mentioned in Sect. 4.2.3, the exponent ζ takes different values for stress and strain contours, but has been chosen so that the resulting stress-strain responses are comparable ($\zeta^{strain} = 10$, $\zeta^{stress} = 7$). Consequently, modelling the undrained cycles with stress contours instead, leads to almost the same stress path.

The combined effect of small strain stiffness and fabric evolution

In addition to the higher stiffness at small strains, the fabric evolution mechanism ensures that the accumulation of strains and pore pressures, respectively, decelerates with progressive cyclic loading (within the contractant domain) and hence the soil's stiffening tendency (shake down phenomenon). At the same time, the increasing compliance associated to (partly) dilative cycles is taken into account, as mentioned above, which is important in the context of liquefaction and cyclic mobility.

The combined effect of small strain stiffness and fabric evolution is visualised by means of a drained cyclic triaxial p-constant test on loose Toyoura sand (see Fig. 5.32). The broken green line corresponds to a simulation without activating any of the two options. In subfigures a and c, it reveals that the volumetric behaviour in the contractant regime is clearly too soft compared to experiments carried out by Pradhan et al. [PTS89]. Accounting for the increased stiffness at small strains after shear reversals already improves the soil response considerably (broken blue line). However, once dilation occurs, the following contractant branch contributes too little deformation, resulting in an overall soil response that is too stiff.

After the third shear reversal, a third solid red curve starts deviating from the path of the blue curve, representing the simulative soil response accounting for small strains and fabric evolution simultaneously. Due to a
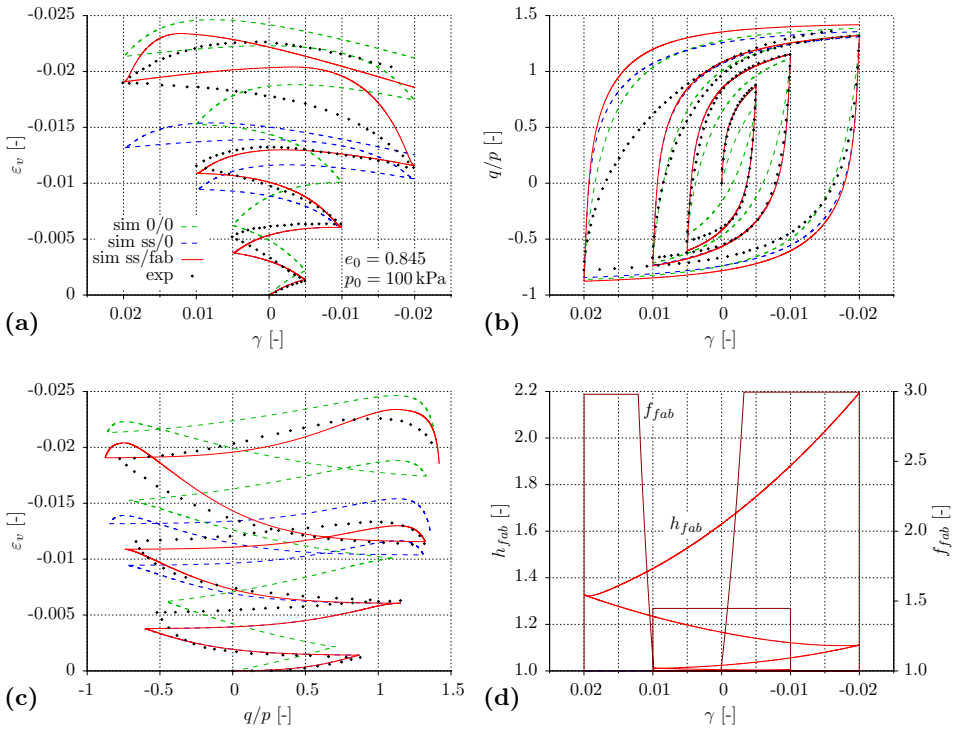
Figure 5.32: Simulation of a drained triaxial p-constant test with increasing shear strain cycles on loose Toyoura sand ($e_0 = 0.845$, $p = 100\,\text{kPa}$), with and without accounting for small strain stiffness (ss: stress contours) and fabric evolution (fab), respectively, compared to test data ($\bullet$) by Pradhan et al. [PTS89]

small, hardly visible portion of dilative volumetric deformation just before the third reversal, the fabric tensor $\boldsymbol{f}$ starts evolving according to Eq. (3.51) in the opposite direction along $-\boldsymbol{n}$, so that $\boldsymbol{f} \uparrow\downarrow \boldsymbol{n}$. At shear reversal ($\gamma = -0.01$), $\boldsymbol{n}$ changes sign ($\boldsymbol{f} \uparrow\uparrow \boldsymbol{n}$) and activates the Macauley brackets in Eq. (3.53), so that the dilatancy scaling factor f_{fab} jumps up from its initial value of 1 (Fig. 5.32 d). Consequently, the dilatancy ratio D is enlarged by the factor of $f_{fab} \approx 1.45$, resulting in a slightly stronger contractive effect. The value of f_{fab} remains constant until by shearing either the phase transition point or the next shear reversal is reached. In the present example, the latter case applies, so that at $\gamma = 0.01$, $\boldsymbol{n}$ changes orientation and f_{fab} instantly drops to 1. Only at the subsequent onset of dilation $\boldsymbol{f}$ changes again, continuing in the previously followed direction.

But since $\boldsymbol{f} \uparrow\downarrow \boldsymbol{n}$ still, its evolution only traces to f_{fab} at the next shear reversal ($\gamma = -0.02$). Comparing the red and the blue curve in subfigures a and c, the compliance after this load reversal is even more intense than the previous one, caused by a larger f_{fab}, being very close to the possible maximum of $1 + C_f = 3$. It should be noted that in the simulation the admittedly overly contractive phase is followed by a dilative one, which is not the case in the experimental data. This is due to the parameter choice, resulting in a rather high magnification factor of 3, which leaves room for optimisation. However, the overall soil response is very satisfying.

The initial loading branches up to the third load reversal comprise merely contractant behaviour, hence a decelerating accumulation tendency of the volumetric deformation should be observable when comparing the broken blue to the red solid line in Fig. 5.32 a and c (with and without fabric evolution, respectively). Due to the parameter choice (low F_f, high a) this effect is rather weak, which can be understood by looking at subfigure d: only after the fifth reversal the plastic stiffness enhancing factor h_{fab} takes values distinctly different from 1.

Inferring from the comparison of the final results of the simulations – with both small strain stiffness and fabric evolution mechanism, and without any of the two options – one could state that the two effects cancel out: the increased compliance at shear reversal after a dilative phase counteracts the increased small strain stiffness. However, the two mechanisms describe two distinct phenomena resulting in qualitatively different responses, which do not necessarily occur at the same time and overlap as they do in the present example. They are hence worth being considered separately in the form of the two model extensions.

Another remark has to be made with respect to the γ-q/p plot in Fig. 5.32 b: with increasing number of cycles, the reloadings starting in the extension domain ($-q/p \rightarrow q/p$) become softer, being considerably less stiff than the loadings departing on the compression side of stress space ($q/p \rightarrow -q/p$). However, this effect can only be observed in the experimental data, the simulations do not show a similar trend – on the contrary: the simulated load cycles appear as rather symmetric stress-strain hysteresis loops. Due to the nature of p-constant stress paths, it is not a varying mean stress level that might be responsible for different soil stiffnesses (as in conventional triaxial compression/extension). In addition, the distance d^b from the reversal point to the bounding surface remains approximately of the same size (disregarding compaction and hence change of the state parameter),

no matter if the load is reversed on the compression or the extension side. Consequently, there is no constitutive element that would account for the observed difference in stiffness.

Although not explicitly stated by the authors of the experimental investigation, a possible explanation for this phenomenon might be a structural anisotropy of the examined soil. The alternating loading in compression and extension causes the principal stress directions to rotate by 90° every time (induced stress anisotropy). Assuming the stiffness of the soil sample is higher in one direction than the other due to sample preparation or loading/deposition history, the variation in the deformational response would be a logical consequence. By gravitational preparation techniques, such as sedimentation under water or air pluviation, the mechanical characteristics in the direction of deposition (vertical) become stronger than in the horizontal direction. Loading with a vertically oriented principal stress as in triaxial compression consequently results in a stiffer soil response than in extension, where the principal stress acts in the radial direction and hence in parallel to the bedding plane. Similar findings have been reported by numerous researchers, such as Yamada and Ishihara [YI79] and Vaid et al. [VCK90] (water-deposited) as well as Arthur and Menzies [AM72] and de Gennaro et al. [dGCD$^+$04] (air-pluviated), confirming inherently anisotropic deformation properties due to sample preparation.

In the light of these former experimental observations, the strong contraction in extension opposed to the dilative tendency in compression (Fig. 5.32 b) can be attributed to the inherent anisotropy of the soil structure. The higher stiffness in vertical direction as a consequence of the preparation procedure leads to a greater compaction in extension than in compression. These peculiarities with respect to stiffness and volumetric behaviour caused by the initial soil fabric's orientation and its evolution cannot be taken into account by the presented bounding surface model, since it lacks a mean for tracing three-dimensional soil structural conditions. There is no so called fabric tensor as established by Oda [Oda99], introduced into the bounding surface model of Li and Dafalias [LD02], which stores information on the soil fabric in view of mechanical properties such as stiffness and dilatancy. The fabric evolution variable h_{fab} as an empirical scalar, based on the directional quantity $\boldsymbol{f}$ at least, remedies part of this issue. But since this mechanism does not consider the degree of anisotropy (which is in any way not easy to determine), it is obvious that the weaker reloading in extension cannot be captured.
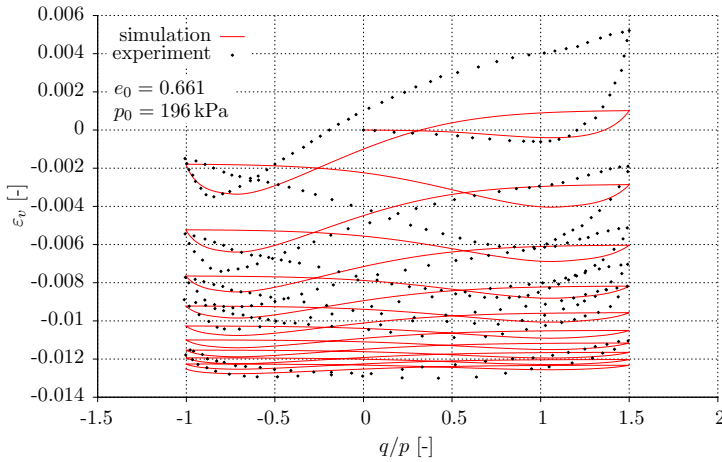
Figure 5.33: Simulation (——) of a cyclic drained triaxial p-constant test (10 cycles) on dense Toyoura sand ($e_0 = 0.661$, $p = 196\,\text{kPa}$) compared to test data ($\bullet$) by Hinokio et al. [HNH$^+$01]

Transferring this conclusion to undrained triaxial tests, one can infer that an anisotropic state as described above (stiffer behaviour in direction of deposition) leads to stronger contraction in extension, accompanied by higher excess pore pressures and hence a greater susceptibility to liquefaction. Consequently, a disregarded inherent anisotropy might cause unexpected soil liquefaction.

Figure 5.32 has shown the mechanism's behaviour with respect to its impact on dilatancy for a limited amount of cycles. In order to assess its stiffening effect with continuous cyclic loading, experimental data by Hinokio et al. [HNH$^+$01] with ten cycles serves as reference; the simulation result is presented in Fig. 5.33. Admittedly, the first cycle does not properly meet the monotonic soil behaviour: the experimental basis exhibits more dilatancy than the model response, which is due to the different source of data used for calibration of the monotonic part of the model parameters (see Fig. 5.1). But although the volumetric deformation is not captured perfectly in detail, the overall evolution of the cycles and the clear stiffening tendency is reflected satisfyingly.

The application of the fabric evolution mechanism (in combination with small strain stiffness) to undrained triaxial loading conditions is presented in the following. First of all, the suitability of the chosen parameters responsible for the dilatancy part of the fabric mechanism (C_f, F_f) is checked

using the example of a simple undrained triaxial loading-unloading cycle on rather dense Toyoura sand (see Fig. 5.34). The simulation results are compared to extracted data by Verdugo and Ishihara [VI96], which has already been used in Fig. 5.5. It has to be noted that, on the one hand, the same reduction of elastic parameters has been applied as for the equivalent monotonic tests (see Sect. 5.1.2 for details). On the other hand, for this purpose the hardening part of the fabric mechanism was deactivated by setting $N_f = 0$. Due to the high level of stress and the large strains generated in these experiments ($\varepsilon_{1,max} = 25\%$), the parameter picked previously for a completely different stress-strain-range (dissipating a considerably higher amount of energy dW) will cause an exaggerated stiffening already along the first loading branch. Thus, it can be stated that the value of N_f is not generally valid when it comes to large differences in stress or strain. However, the fit for the dilatancy related parameters is rather satisfying.

Cyclic experiments on medium dense Toyoura sand by Zhang et al. [ZJY10] are used for assessing the performance of the model with respect to a larger number of cycles (see Fig. 5.35). The simulation results are depicted in Fig. 5.36. The initial states with respect to stress and density were approximately equivalent in all three cyclic tests ($p_0 = 100\,\text{kPa}$, $e_0 \approx 0.75$); the varying quantity is the applied deviatoric stress amplitude Δq. Although the simulation deviates from the experimental outcome especially
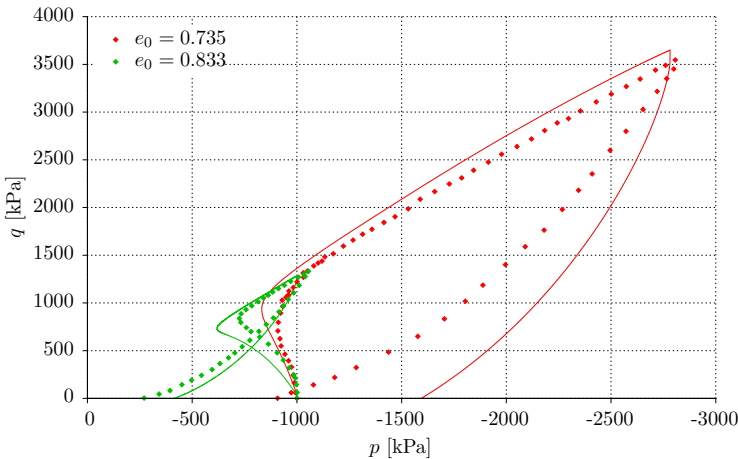
Figure 5.34: Simulation (——) of two undrained triaxial tests (including unloading) on Toyoura sand ($e_0 = 0.735, 0.833$, $p_0 = 1000\,\text{kPa}$) compared to test data (♦) by Verdugo and Ishihara [VI96]
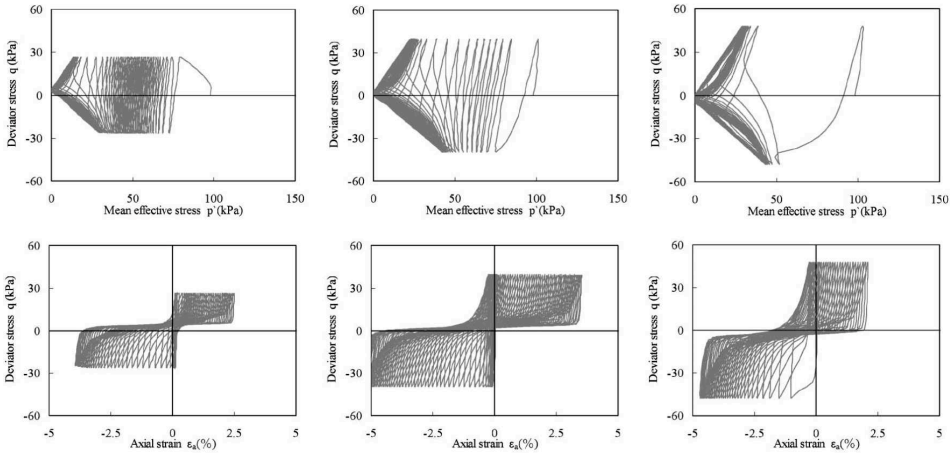
Figure 5.35: Cyclic undrained triaxial tests on medium dense Toyoura sand with an initial isotropic stress state of $p_0 = 96$ kPa for three different deviatoric stress amplitudes (30, 40, 50 kPa), data provided by Zhang et al. [ZJY10]

regarding the amount of cycles needed for reaching its final stable state, the qualitative response is captured well by the model. With increasing stress amplitude the effective stress paths approach liquefaction increasingly fast. However, it is not liquefaction that is finally reached, but the soil stabilises in a butterfly shape – a similar phenomenon called cyclic mobility. Every time the phase transformation point is passed, the soil regains strength due to the reduction of pore pressures, which built up in the preceding contractant phase of loading. Thus, the soil keeps on cycling without liquefying. Casting an eye on the deformation caused by the described loading scheme (Fig. 5.36 d-f), an enhanced straining accompanies the stronger tendency towards cyclic mobility. It can also be observed that the deformation develops mostly on the extension side. This trend resembles the one shown in the experimental results, though it is overly strong due to the comparably stiff response in compressive loading. The reason for this behaviour can be found in the choice of the critical state friction angle in extension, or more precisely, the ratio $c = {}^{M_e^c}/{}_{M_c^c}$, which is also applied to the dilatancy and bounding surface. Since the inclination of the latter two is considerably steeper in compression than in extension, which is in accordance with experimental evidence, the dilative phase of compressive loading takes place at larger values of mean pressure and stress ratio. Hence, the elastoplastic stiffness matrix D^{ep} according to Eq. (A.8) takes higher values than on the
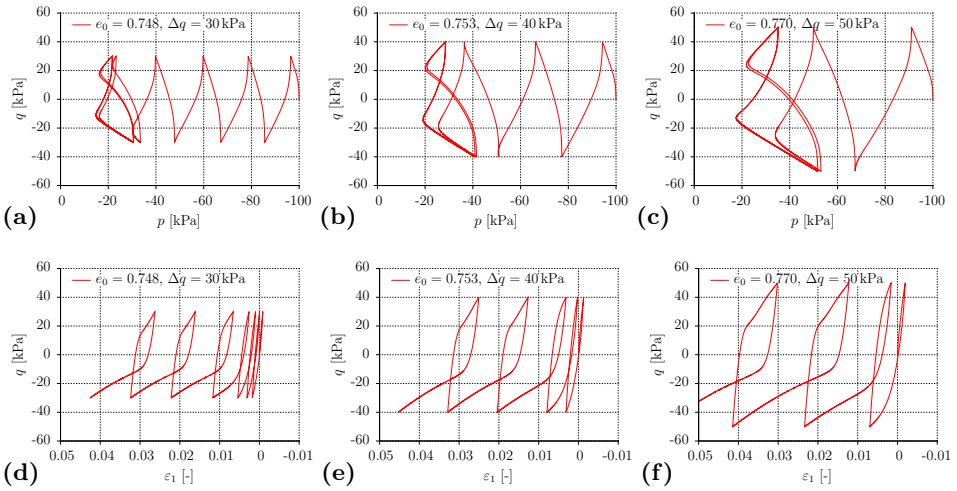
Figure 5.36:   Simulation of cyclic undrained triaxial tests on medium dense Toyoura sand with varying deviatoric stress amplitudes (Δq = 30, 40, 50 kPa), according to test data in Fig. 5.35

extension side, causing the soil response to be stiffer – in the present case obviously too stiff. According to the constitutive formulation, the stress-strain cycles could only be approximately symmetric if $M_e^c = M_c^c$, resulting in a friction angle in extension considerably larger than in compression, which is highly unrealistic.

In the simulations in Fig. 5.37 the initial density is varied instead of the cyclic stress amplitude. The effect is very similar: with rising initial void ratio, the effective stress state reaches cyclic mobility increasingly fast and the simultaneous growth in axial deformation is even more intense. In case of the loosest sample ($e_0 = 0.95$) the effective stresses even tend to zero on the unloading branch, striving towards liquefaction instead of cyclic mobility. In its initial state the soil's state parameter amounts to a positive value ($\psi_0 = 0.035$), which remains positive until the first and only load reversal. Consequently, the dilatancy surface is placed outside the critical state surface and can hence never be crossed. Thus, the contractant soil response cannot turn into dilation, which would otherwise create stabilising negative pore pressures and hence initiate cyclic mobility. One can conclude that only truly loose soil ($\psi_0 > 0$) is prone to liquefy. If a dense state in terms of state parameter ψ is attained within the first loading, the model is very likely to produce the butterfly shaped stress path typical of cyclic
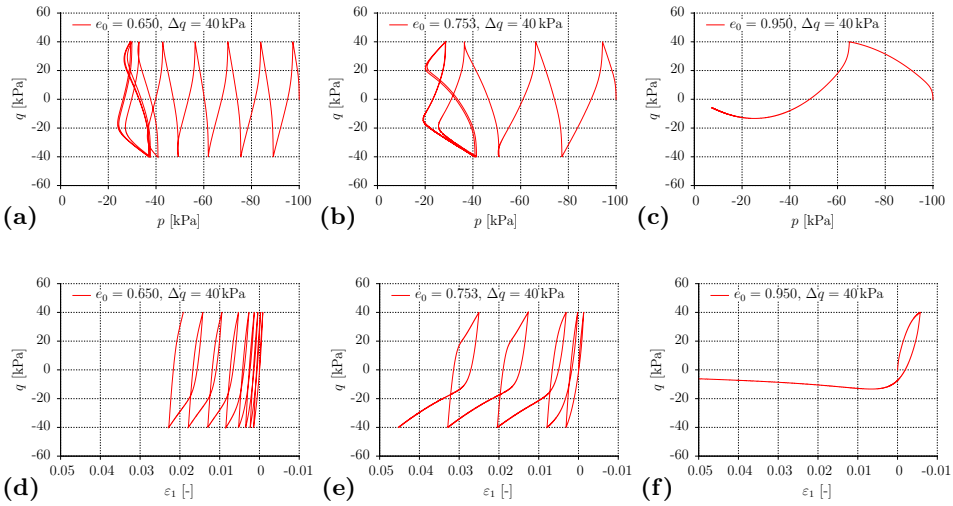
Figure 5.37: Simulation of cyclic undrained triaxial tests on Toyoura sand of varying density ($e_0 = 0.65$, 0.753, 0.95) with a deviatoric stress amplitudes of $\Delta q = 40\,\text{kPa}$

mobility. It can also be inferred from the simulations that the denser the soil, the farther from zero effective stress cyclic mobility is attained and the smaller the resulting strains. Consequently, the risk for reaching liquefaction decreases with higher densities and the deformations occurring also remain in a limited range.

Considering the comparably low number of cycles that suffices for reaching cyclic mobility, the conclusion could be drawn that the simulated pore pressure development is too strong. This is partly attributed to the general issue regarding drained/undrained simulations, potentially linked to disregarded gas inclusions as discussed in the context of monotonic undrained loadings. This effect has been slightly relieved by choosing lower elastic stiffness parameters, as mentioned earlier. In addition, the previously discussed potential anisotropy of test samples, which is not taken into account by the constitutive law, can cause the simulated loading branch from extension towards compression to be stiffer than experimentally observed. A possibility to deal with this problem is to increase the parameters of the hardening component of the fabric mechanism (N_f, a) in order to obtain a better fit. This fact confirms that at least this part of the mechanism, captured by the state variable h_{fab}, does not meet the requirements of unified modelling due to its sensitivity to different testing conditions.

A generalising explanation for this problem could be the mentioned simple approach of covering three-dimensional rearrangements within the soil skeleton by a scalar affecting plastic stiffness and dilatancy, respectively. The definition of the evolution variables h_{fab} and f_{fab} reflects the attempt to capture qualitative characteristics observed in cyclic loading processes. The problem is that due to the highly complex nature of structural changes resulting from outer impacts, there are numerous influencing factors, partly not even known, which might cause the soil response under certain boundary conditions to deviate from the investigated standard case. Taking the entirety of influences into account by a single scalar variable is apparently not possible. Recalling the impact of anisotropy, for example, which has been discussed earlier and is not considered in the model formulation, parameters calibrated for a particular initial configuration will inevitably produce a poor match for different inherent material anisotropies.

Aside from this, due to the repetitive character of cyclic loadings, the final result is susceptible to small deviations in the single loading branches, which can lead to considerable errors. The calibrated parameter set (for monotonic loadings) usually represents an optimal choice for a certain bandwidth of soil states. This automatically implies that there are initial states that are less well reproduced than others, particularly in the outer limits of the considered range of soil states. Thus, if already the first loading differs from the monotonic soil response as it does in the example of dense sand in Fig. 5.33, the overall result is likely to not fully satisfy the expectations.

To conclude on the performance of the fabric evolution mechanism, the demonstrated test cases confirmed the capability of the model overlay to reproduce the soil behaviour due to several load cycles. However, one has to admit the model feature's limitation with respect to its application to different boundary conditions because of its conceptual simplicity. Consequently, it offers a valuable mean to assess the evolution of deformations and pore pressures, respectively, but only if the case to be studied does not differ too much from the calibrated test configuration. Thus, the term unified modelling, which applies to the presented bounding surface model under monotonic loading conditions, cannot be transferred to cyclic loadings without restrictions.

6 Conclusions and perspectives

6.1 Conclusions

The present work is concerned with a new material model based on the principles of bounding surface plasticity. With the primary aim to establish a constitutive law suitable for application in engineering practice, an existing modelling framework was adapted to the defined needs. One of the key components of the strategy followed was to build upon well-known concepts and accepted models. Thus, first of all, the theory of elastoplasticity was chosen, offering a modelling approach that is widespread in the geotechnical community and easily understood due to the separation of reversible (elastic) and irreversible (plastic) behaviour, which is a widely used modelling assumption. Fundamental soil mechanical observations are directly transferred to constitutive elements in the shape of limit surfaces, which mostly are of a geometrical nature and hence easier to grasp than abstract constitutive equations. Along these lines, the distinction of elastic and plastic deformations, for example, is translated into the yield surface, bounding the elastic regime in stress space. Evolution rules for describing the change of soil properties such as strength, stiffness or dilatancy are usually linked to the position and/or extent of these constitutive items. Starting from such a popular modelling platform enhances the likelihood of being noticed and taken into consideration when it comes to testing a new material model for routine design.

On the foundations of elastoplasticity, the next essential ingredient is the ability for modelling all the basic features of soil behaviour with respect to the engineer's requirements. This aspect implies that the model necessarily has a certain complexity, but the crucial point is to keep it within reasonable limits. A highly sophisticated model might cope with a wide range of soil mechanical challenges, but on the other hand bear the risk of discoura-

ging potential users due to the lack of transparency. In order to find the good proportions, the fundamental patterns of soil behaviour to be modelled were listed and the corresponding constitutive ingredients were added to the model accordingly. This way the concept of critical states and the principle of state dependence became the heart pieces of the present modelling framework, allowing for phenomena such as dilatancy/contractancy, hardening/softening and attainment of critical state, to name only the elementary ones. In addition, the state parameter accounting for different soil states with respect to density and stress is the key to unified modelling – the simulation of soil responses for a wide range of different initial states with only one parameter set. On this basis, bounding surface plasticity was identified as an appropriate member of the large family of elastoplastic models, meeting the most important demands and having the potential for further development.

It is the formulation by Manzari and Dafalias [MD97] that is called the "original" version of the bounding surface model in the present work and served as prototype for the extended new variant. In order to improve the model with respect to certain additional features, which are considered to be imperative in view of engineering needs, such as a strain dependence of stiffness (in the small strain range) as well as a directional dependence of stiffness (shear/compression), a number of extensions have been incorporated into the original formulation: a cap serves as second yield surface in the compressive regime, using the well-known cap formulation of the hardening soil model [SVB99]; a small strain mechanism allows for an increased stiffness after shear reversals and its subsequent strain dependent degradation; modifications in the hardening law and the flow rule improve the deformational behaviour. The evolution of fabric due to the rearrangement of grains within the soil skeleton and its consequences on stiffness and dilatancy can be taken into account with an additional mechanism.

Most of the listed extensions of the model are implemented in a modular fashion, so that the user is able to activate and deactivate certain model features according to his/her needs. This way the complexity of the model can be reduced by switching off specific options if the boundary conditions do not necessitate their application in order to save computing time and avoid the needless determination of associated model constants. Alternatively, the modular structure allows for analysing the impact of considering a particular behavioural pattern on the final result by comparative studies.

The first implementation of the model has been realised on a rather low level

of computational complexity by using an explicitly integrating constitutive driver for the simulation of element tests. It is particularly advantageous in the process of constitutive modelling, allowing for a direct access to all model components, including the influence of numerical factors. In this programming environment the mentioned modular concept can be incorporated easily and the condensed structure focusing on simple element tests is most suitable for model calibration. So, even if the transformation into an implicit user-defined soil model for the application in a finite element software is intended (see Sect. 6.2), the constitutive driver might remain a helpful tool for parameter optimisation purposes.

Having set up the constitutive model successfully within a predefined network of requirements, a strategy is needed for paving its way into application. Since the underlying bounding surface plasticity does not yet belong to the circle of widely-used soil models, particularly the bounding surface specific parameters are less easy to access. Thus, the implementation is completed with an auxiliary mean to find a satisfying first fit for a handful of model constants, which are not self-explanatory or straightforward to determine. It consists of an optional routine, which calibrates a number of parameters on the basis of alternative input data directly related to elementary laboratory tests. It should be pointed out that this tool is not supposed to replace a sound parameter calibration for the solution of boundary value problems. For adapting the parameter set to a wide range of soil states in view of more complex loading situations, the optimisation process inevitably involves the careful examination of the full expanse of the considered range. The calibration routine delivers the best parameter combination for the calibrated state, which might however not be the optimum for a whole spectrum of states within particular limits. Nevertheless, the best fit of the integrated calibration tool can help to get an access to the model by allowing to run first test calculations. This routine primarily aims for enabling the potential user to get a feeling for the behaviour of the model and overcome reservations concerning new and unfamiliar models. It is not supposed to spare the engineer the profound engagement with the theoretical background.

The aforementioned calibration tool goes hand in hand with the provision of an extensive documentation of the constitutive model. This work can be considered as a compendium with a listing of all constitutive equations, a thorough description of all included features and with directions for the "manual" calibration procedure. Aside from this, numerous simple test cases

show the elementary model behaviour and document the quality of the model performance. An integral part of this documentation is a critical examination of both capabilities and limitations of the proposed model in order to offer a sound basis for deciding on the qualification of the model for a certain case of application.

To take up the previous aspect of potentials and restrictions, reflections on the initial intentions and their degree of fulfilment should be given. The chosen constitutive framework of bounding surface plasticity has proven to meet the expectations: most of the basic features of soil behaviour as listed in Sect. 3.1 can be qualitatively and quantitatively captured satisfactorily, which is particularly valuable in the light of state dependence. The additional cap yield surface delivers good results with regard to constant stress ratio loadings and is automatically (virtually) disabled if stress ratio changes are detected. Consequently, the dependence of stiffness on the straining direction is taken into account (compression vs. shear). The initially too soft behaviour in repetitive shear loadings has been partly remedied by the incorporation of an additional dependence of stiffness with respect to the amount of straining – with an increased stiffness at very small strains, followed by a gradual reduction towards larger strains. This feature is complemented with another mechanism for cyclic loadings, taking fabric restructuration and resulting changes in stiffness and dilatancy into consideration. With this combination of constitutive ingredients a large variety of engineering problems can be considered: starting from simple monotonic loadings such as consolidation processes, to more complex stress paths as in staged constructions (excavation – installation of anchors – application of foundation loads – . . .), to cyclic impacts due to operation of infrastructural buildings (continuous quasi-static un- and reloading).

Besides the highlighted capabilities, two major restrictions have to be pointed out. Comparing the model performance regarding drained monotonic loading conditions to undrained simulations (when using the same parameter set, calibrated for the drained case), the accordance with laboratory test results is less good in the latter case: the pore pressure evolution is too strong compared to experimental soil responses, leading to overly flat effective stress paths in p-q space, concerning the initial loading branch in particular. This problem can be partly remedied by choosing unrealistically low elastic stiffness parameters and/or by activating the small strain stiffness option. Either way, the pore pressure evolution is inhibited. The former measure is the most efficient one, but the manipulation of soil pro-

perties for the sake of numerical fitting is clearly undesirable. In addition, although its influence is almost negligible in conventional drained loading cases, it impairs drained calculations at small to medium strains. Considering solely the small strain stiffness option within a reasonable strain range, its effect is not sufficient for improving the simulative result. A potential explanation for this issue was found in the disregarded influence of the gas portion within the pore fluid, resulting in a lower pore fluid compressibility and consequently a weaker pore pressure development. This reflects both an apparently inappropriate simplification of the constitutive law and a potentially not fully saturated state within the soil sample, contradicting the computational assumptions. Further possible reasons for the deviation between simulations and experiments were found in the impact of the rubber membrane or the applied sample preparation method, potentially inhibiting the pore pressure evolution, which cannot be taken into account numerically.

The second challenge is the fabric mechanism, which is supposed to take structural rearrangements due to cyclic loadings and their impact on the soil response into account. According to its conceptual background it captures the experimentally observed soil behaviour qualitatively with respect to the deceleration or acceleration of the pore pressure and deformation evolution, respectively. The enhanced compliance resulting from a shear reversal after a dilative loading is translated into a stronger contraction by means of a dilatancy related mechanism, which has proven to work well. The second, hardening related mechanism, increasing the stiffness with continuous cycling, seems to be very sensitive to changes in loading conditions with respect to the stress and strain range and the consequential amount of dissipated energy. The reason is most likely a combination of several factors, which could be summarised as the attempt to reduce a three-dimensional process to a scalar: the description of the reorganisation of grains in space without a tensorial quantity seems to be inappropriate, but was considered a necessary simplification in order to retain a manageable model. However, this issue might not only be attributed to constitutive deficiencies: repetitive loadings represent one of the most complex problems in soil mechanics, combining the already challenging monotonic behaviour with additional cyclic effects. Even small deviations in the monotonic response, which might result from model shortcomings or faulty assumptions regarding the initial soil state, accumulate to considerable errors. Consequently, the term unified modelling cannot be transferred to the fabric mechanism without restrictions, since a modification of the calibrated state puts the validity of the

parameter set into question. From this follows, that the fabric mechanism in its present form is an auxiliary mean for examining the qualitative effect of certain loading schemes on the soil response and perhaps even quantitatively, if comparable lab data is available. Though, the extrapolation of simulative soil responses to different in-situ conditions has to be done with very good care and requires experience in dealing with the model in general and the fabric mechanism in particular.

In the context of repetitive loadings it should be pointed out that one of the main aims of the present extended bounding surface model is to enable the reproduction of stress paths of higher complexity. This primarily concerns stress paths composed of different loading branches with respect to direction and size of applied stresses as well as drainage conditions, as for example occurring in staged construction processes. It can also be interpreted in the sense of cyclic loading, meaning continuously recurring loading schemes of the same pattern, particularly appearing in the phase of operation. The model is basically able to capture the soil mechanical peculiarities of repeated load cycles. But one has to acknowledge that the calculation time jumps up with an increase in the number of cycles. Consequently, the model in its present form is not suitable for high-cyclic problems. The following section gives an outlook on how to potentially handle this shortcoming.

Concluding from the aforementioned summarising words, it can be stated that the extended bounding surface model offers a powerful tool to numerically assess the soil's behaviour in a wide field of geotechnical engineering applications. Different from most existing models used in routine design, the foundation of bounding surface plasticity allows for unified modelling due to its state dependent nature, which is a clear advantage in boundary value problems with more intricate boundary conditions and more complex stress paths. The constitutive ingredient small strain stiffness is particularly valuable for rather stiff soils and structures in combination with comparably small to medium loads, where expected deformations will remain in the (very) small strain range. Especially if load reversals come into play, the overall soil response will be much more realistic when accounting for the increased stiffness at small strains. The cap, on the other hand, predominantly enhances settlement predictions, where the compressive stiffness of the soil – normally or overconsolidated, under either isotropic or oedometric conditions – determines the soil behaviour. The improvements in the flow rule and hardening law formulations ensure that the behaviour under monotonic shear is well captured. All these individual aspects contribute to a

good performance in monotonic loading situations, which is an indispensable prerequisite for the successful reproduction of cyclic loadings, responding particularly sensitively to perturbations in the single loading branches.

Apart from these clear benefits arising from the model's capabilities, the user has to be aware of its limitations, too. No constitutive model will invariably reproduce all characteristics of soil behaviour. In Sect. 3.3 the applications, which the model is not intended for, are listed, such as rate-dependent loadings, cementation and degradation processes or unsaturated states. In addition, there are features that perform less well, as to name triaxial shear in undrained loading or cyclic loading. Certain deficiencies, as those in the former group, are accepted in favour of manageability and accessibility of the model. Others, as the latter examples, are undesired and mainly due to unwanted constitutive inadequacies. It is subject of the following section to give an insight into possible strategies to solve or handle these problems.

The same way it is obvious for any other constitutive model, the geotechnical engineer is expected to acquaint oneself with the extended bounding surface model before use: its underlying theory, its capabilities and limitations. In this regard, the present work offers a scholarly basis for making a reasonable model choice for the intended field of application in view of a credible outcome. Despite the incorporated state dependence, the user is advised to make sure that the chosen parameter set is appropriate and balanced for the boundary conditions to be investigated, which refers to drainage as well as to the range of soil states to be expected. Small adjustments on a generally acceptable configuration of parameters can allow for improving the quality of the predictions and optimising the final design. The use of the model for cyclic loadings is recommended for qualitative statements or if the calibration data is compatible and reliable with respect to the case to be simulated. For an outlook on further developments or possible alternatives, the reader is referred to the following section.

The author greatly appreciates spreading of the model, its wide use and any critical considerations.

6.2   Future perspectives

The current evolution stage of the extended bounding surface model on the constitutive level and also with regard to its implementation environment offers a sound basis for the model's application on an element test scale. Ho-

wever, for its establishment in geotechnical routine design, it is mandatory to provide the engineer with a user defined soil model for the use in relevant finite element software in order to allow for the solution of boundary value problems. In this context, the conversion from the current explicit integration scheme to a more efficient implicit one is to be considered. This step is planned for the near future.

An important aspect concerning the model implementation is the modular structure, which is considered particularly beneficial in view of comparative analyses or the adjustment of model complexity depending on the problem in question, as mentioned above. With regard to the intended provision of the model in an open source environment the modular character also eases further development: a clear coding structure allows for a direct access to specific constitutive components for potential corrections or improvements or even for the supplement of new features in the form of an additional module.

Along the lines of model development, it might be a valuable improvement to extend the existing calibration routine. Instead of an integrated calculation loop a more complex sub-programme could offer a more comfortable and powerful optimisation tool for parameter determination. A conceivable modification would be the consideration of two different soil states (e.g. loose and dense) instead of only one for a better fit over a defined range of densities and stresses (according to Fig. 4.16). One could also consider to feed the calibration routine with experimental curves in the form of data files instead of a set of target values. This would, of course, escalate the programme's complexity considerably, but might increase the model's acceptance at the same time. However, this idea for further development is linked to the software environment rather than the constitutive content, since this approach can be used for any model, irrespective of its constitutive background.

As mentioned above and explained earlier, the model is not intended for use in high-cyclic loadings. For accessing this field of application the calculation strategy would need to be altered from expensively calculating each single cycle implicitly (not referring to the integration scheme here) to a partly explicit algorithm. Approaches exist that use a small amount of implicit cycles – calculated with the underlying constitutive model – for extrapolating the accumulated deformation of the following ones, occasionally checking the result with interposed control cycles [NWT05]. This could be a conceivable way to enter the high-cyclic domain with this model.

One modification, that does not concern the constitutive equations themselves but the implementation environment, could be the provision for a varying fluid stiffness with its dependence on the degree of saturation and the pressure level. This rather simple alteration would have a visible impact on undrained simulations, which is particularly beneficial for partially saturated conditions.

Leaving the general ground of improvements, a potential enhancement on the constitutive level should be addressed. As mentioned in the precedent conclusions, the one-dimensional consideration of the spatial restructuring of fabric is a simplification possibly leading to severe inaccuracies – particularly when it comes to repetitive loadings. A logical escape from this inconsistency would be to raise the model's dimension to a full multiaxial formulation. This would allow to map fabric rearrangements to tensorial quantities in order to capture interparticle changes and their impact on the soil mechanical behaviour. Even the conventionally formulated flow rule or hardening law could potentially be transferred to more fabric related expressions of dilatancy and hardening mechanisms, respectively.

However, before fabric tensors can be used for tracing three-dimensional processes, the necessary micromechanical background needs to be explored in much more depth than it is today. The essential premise for making good predictions is a sound knowledge about the interparticle processes and all influencing factors, to be acquired by systematic investigations. Of course, simplifying assumptions are indispensable when it comes to constitutive modelling, aiming for obtaining a manageable tool. But in order to come by satisfying approximations, simplifications should ideally be abstracted from complex situations, which requires a reliable scientific foundation. Certain approaches for translating the soil structure into a mathematical context exist. Even its evolution with respect to external impacts is under investigation and specific proposals have been made (although by far not all phenomena of soil behaviour can be explained on a micromechanical scale).

In this context, a central problem is, how to define the initial state of fabric. A sophisticated evolution law is of little use, if the soil's configuration prior to loading is unknown. Thus aside from exploring fundamental aspects of soil behaviour on a micromechanical scale, (experimental) methods for defining the soil's initial state and properties need improvement, so that initialisation data and material parameters can be determined with reasonable effort.

Bibliography

[Al 97]   M. Al Mahmoud: *Étude en laboratoire du comportement des sables sous faibles contraintes*. PhD thesis, École Centrale de Lille, Lille, 1997.

[AGJ90]   E. E. Alonso, A. Gens, and A. Josa: A constitutive model for partially saturated soils. *Géotechnique*, 40(3):405–430, 1990. DOI: `10.1680/geot.1990.40.3.405`.

[Alt18]   H. Altenbach: *Kontinuumsmechanik*. Springer Berlin Heidelberg, Berlin, Heidelberg, 2018. DOI: `10.1007/978-3-662-57504-8`.

[ASK95]   A. Anandarajah, K. Sobhan, and N. Kuganenthira: Incremental stress-strain behavior of granular soil. *Journal of Geotechnical Engineering*, 121(1):57–68, 1995. DOI: `10.1061/(ASCE)0733-9410(1995)121:1(57)`.

[APB05]   K. I. Andrianopoulos, A. G. Papadimitriou, and G. D. Bouckovalas: Bounding surface models of sands – Pitfalls of mapping rules for cyclic loading. In: G. Barla, editor, *11th International Conference of IACMAG – Proceedings*, Bologna. Pàtron Ed, 2005.

[AFS⁺74]   J. H. Argyris, G. Faust, J. Szimmat, E. P. Warnke, and K. J. Willam: Recent developments in the finite element analysis of prestressed concrete reactor vessels. *Nuclear Engineering and Design*, 28(1):42–75, 1974. DOI: `10.1016/0029-5493(74)90088-0`.

[AM72]   J. R. F. Arthur and B. K. Menzies: Inherent anisotropy in a sand. *Géotechnique*, 22(1):115–128, 1972. DOI: `10.1680/geot.1972.22.1.115`.

[AF85]   J. H. Atkinson and D. M. Farrar: Stress path tests to measure soil strength parameters for shallow landslips. In: ISSMFE, editor, *11th International Conference on Soil Mechanics and Foundation Engineering – Proceedings*, pp. 983–986, Rotterdam. Balkema, 1985.

[AS91]   J. H. Atkinson and G. Sällfors: Experimental determination of soil properties. In: *10th European Conference on Soil Mechanics and Foundation Engineering – 10th ECSMFE – Proceedings*, vol. 3, pp. 915–956, 1991.

[ACT⁺17] R. J. N. Azeiteiro, P. A. L. F. Coelho, D. M. G. Taborda, and J. C. D. Grazina: Critical state-based interpretation of the monotonic behavior of Hostun sand. *Journal of Geotechnical and Geoenvironmental Engineering*, 143(5):04017004(1–14), 2017. DOI: `10.1061/(ASCE)GT.1943-5606.0001659`.

[BFM97]   T. Bäck, D. B. Fogel, and Z. Michalewicz: *Handbook of evolutionary computation*. Institute of Physics Pub. and Oxford University Press, Bristol, Philadelphia, and New York, 1997.

[Bai11]   L. Bairstow: The elastic limits of iron and steel under cyclical variations of stress. *Philosophical Transactions of the Royal Society A: Mathematical, Physical and Engineering Sciences*, 210(460):35–55, 1911. DOI: `10.1098/rsta.1911.0002`.

[Bak04]   R. Baker: Nonlinear Mohr envelopes based on triaxial data. *Journal of Geotechnical and Geoenvironmental Engineering*, 130(5):498–506, 2004. DOI: `10.1061/(ASCE)1090-0241(2004)130:5(498)`.

[BN84]   G. Baldi and R. Nova: Membrane penetration effects in triaxial testing. *Journal of Geotechnical Engineering*, 110(3):403–420, 1984. DOI: `10.1061/(ASCE)0733-9410(1984)110:3(403)`.

[Bar84]   J. P. Bardet: *Application of plasticity theory to soil behavior: a new sand model*. PhD thesis, California Institute of Technology, Pasadena, 1984.

[Bar90]   J. P. Bardet: Lode dependences for isotropic pressure-sensitive elastoplastic materials. *Journal of Applied Mechanics*, 57(3):498–506, 1990. DOI: `10.1115/1.2897051`.

[BC91]   J. P. Bardet and W. Choucair: A linearized integration technique for incremental constitutive equations. *International Journal for Numerical and Analytical Methods in Geomechanics*, 15(1):1–19, 1991. DOI: `10.1002/nag.1610150102`.

[BS04]   B. Baudet and S. Stallebrass: A constitutive model for structured clays. *Géotechnique*, 54(4):269–278, 2004. DOI: `10.1680/geot.2004.54.4.269`.

[Bau96]   E. Bauer: Calibration of a comprehensive hypoplastic model for granular materials. *Soils and Foundations*, 36(1):13–26, 1996.

[BJ85]   K. Been and M. G. Jefferies: A state parameter for sands. *Géotechnique*, 35(2):99–112, 1985. DOI: `10.1680/geot.1985.35.2.99`.

[BJ04]   K. Been and M. Jefferies: Stress dilatancy in very loose sand. *Canadian Geotechnical Journal*, 41(5):972–989, 2004. DOI: `10.1139/t04-038`.

[BSV05]   T. Benz, R. Schwab, and P. A. Vermeer: On the numerical modelling of quasi-static cyclic problems. In: G. Barla, editor, *11th International Conference of IACMAG – Proceedings*, Bologna. Pàtron Ed, 2005.

[Ben03]   T. Benz: Bounding surface plasticity for cyclic loaded sand and its implementation. In: K.-J. Bathe, editor, *2nd MIT Conference on Computational Fluid and Solid Mechanics – Proceedings*, vol. 1, pp. 95–98, Amsterdam and Boston. Elsevier, 2003.

[Ben07]   T. Benz: *Small-strain stiffness of soils and its numerical consequences*. PhD thesis, University of Stuttgart, Stuttgart, 2007.

[BH17]   K. Bergholz and I. Herle: Experimentelle Bestimmung der Nichtlinearität von Spannungsgrenzbedingungen im Bereich geringer Spannungen. *geotechnik*, 40(2):119–125, 2017. DOI: `10.1002/gete.201600008`.

[Bio41]   M. A. Biot: General theory of three-dimensional consolidation. *Journal of Applied Physics*, 12(2):155–164, 1941.

[Bis59]   A. W. Bishop: The principle of effective stress. *Teknisk uke-blad*, 39:859–863, 1959.

[BB63]   A. W. Bishop and G. E. Blight: Some aspects of effective stress in saturated and partly saturated soils. *Géotechnique*, 13(3):177–197, 1963. DOI: `10.1680/geot.1963.13.3.177`.

[BL73]   D. K. Black and K. L. Lee: Saturating laboratory samples by back pressure. *Journal of the Soil Mechanics and Foundations Division*, 99(SM 1):75–93, 1973.

[Bol86]   M. D. Bolton: The strength and dilatancy of sands. *Géotechnique*, 36(1):65–78, 1986. DOI: `10.1680/geot.1986.36.1.65`.

[BL97]   P. A. Bopp and P. V. Lade: Membrane penetration in granular materials at high pressures. *Geotechnical Testing Journal*, 20(3):272–278, 1997. DOI: `10.1520/GTJ19970002`.

[BK07]   D. Bratton and J. Kennedy: Defining a standard for particle swarm optimization. In: *Swarm Intelligence Symposium 2007 – Proceedings*, pp. 120–127, 2007. DOI: `10.1109/SIS.2007.368035`.

[BS60]   R. Brewer and J. R. Sleeman: Soil structure and fabric. *Journal of Soil Science*, 11(1):172–185, 1960. DOI: `10.1111/j.1365-2389.1960.tb02213.x`.

[Bun11]   Bundesanstalt für Wasserbau: BAW Code of practice: Principles for the design of bank and bottom protection for inland waterways – GBB, 2011.

[Bur89]   J. B. Burland: Ninth Laurits Bjerrum Memorial Lecture – Small is beautiful - the stiffness of soils at small strains. *Canadian Geotechnical Journal*, 26(4):499–516, 1989. DOI: `10.1139/t89-064`.

[CDH$^+$96] R. C. Chaney, K. R. Demars, E. Hoque, F. Tatsuoka, and T. Sato: Measuring anisotropic elastic properties of sand using a large triaxial specimen. *Geotechnical Testing Journal*, 19(4):411, 1996. DOI: `10.1520/GTJ10718J`.

[CDH$^+$97] R. C. Chaney, K. Demars, E. Hoque, T. Sato, and F. Tatsuoka: Performance evaluation of LDTs for use in triaxial

tests. *Geotechnical Testing Journal*, 20(2):149–167, 1997. DOI: `10.1520/GTJ10735J`.

[CK02]   M. Clerc and J. Kennedy: The particle swarm - explosion, stability, and convergence in a multidimensional complex space. *IEEE Transactions on Evolutionary Computation*, 6(1):58–73, 2002. DOI: `10.1109/4235.985692`.

[Cle06]   M. Clerc: *Particle swarm optimization*. ISTE, London and Newport Beach, 2006.

[Cor16]   R. Corti: *Hardening memory surface constitutive model for granular soils under cyclic loading conditions*. PhD thesis, University of Bristol, Bristol, 2016.

[CDM+16] R. Corti, A. Diambra, D. Muir Wood, D. E. Escribano, and D. F. T. Nash: Memory surface hardening model for granular soils under repeated loading conditions. *Journal of Engineering Mechanics*, 142(12), 2016. DOI: `10.1061/(ASCE)EM.1943-7889.0001174`.

[CVT06]   D. Costanzo, G. Viggiani, and C. Tamagnini: Directional response of a reconstituted fine-grained soil, Part I – Experimental investigation. *International Journal for Numerical and Analytical Methods in Geomechanics*, 30(13):1283–1301, 2006. DOI: `10.1002/nag.526`.

[Daf81]   Y. F. Dafalias: A novel bounding surface constitutive law for the monotonic and cyclic hardening response of metals. In: *6th International Conference on Structural Mechanics in Reactor Technology – Proceedings*, vol. 1, pp. L 3/4, Amsterdam. North-Holland, 1981.

[DH80]   Y. F. Dafalias and H. J. Herrmann: A bounding surface soil plasticity model. In: G. N. Pande and O. C. Zienkiewicz, editors, *Soils under cyclic and transient loading – Proceedings*, pp. 335–345, Rotterdam. Balkema, 1980.

[DM99]   Y. F. Dafalias and M. T. Manzari: Modeling of fabric effect on the cyclic loading response of granular soils. In: *13th ASCE Engineering Mechanics Conference – Proceedings*, 1999.

[DP75]   Y. F. Dafalias and E. P. Popov: A model of nonlinearly
           hardening materials for complex loading. *Acta Mechanica*,
           21(3):173–192, 1975. DOI: `10.1007/BF01181053`.

[DT16]   Y. F. Dafalias and M. Taiebat: SANISAND-Z – Zero elastic
           range sand plasticity model. *Géotechnique*, 66(12):999–1013,
           2016. DOI: `10.1680/jgeot.15.P.271`.

[DM04]   Y. F. Dafalias and M. T. Manzari: Simple Plasticity Sand
           Model Accounting for Fabric Change Effects. *Journal of En-
           gineering Mechanics*, 130(6):622–634, 2004. DOI: `10.1061/`
           `(ASCE)0733-9399(2004)130:6(622)`.

[DMP06]   Y. F. Dafalias, M. T. Manzari, and A. G. Papadimitriou: SA-
           NICLAY – Simple anisotropic clay plasticity model. *Interna-
           tional Journal for Numerical and Analytical Methods in Geo-
           mechanics*, 30(12):1231–1257, 2006. DOI: `10.1002/nag.524`.

[DPL04]   Y. F. Dafalias, A. G. Papadimitriou, and X. S. Li: Sand plas-
           ticity model accounting for inherent fabric anisotropy. *Jour-
           nal of Engineering Mechanics*, 130(11):1319–1333, 2004. DOI:
           `10.1061/(ASCE)0733-9399(2004)130:11(1319)`.

[DH15]   S. Danne and A. Hettler: Experimental strain response-
           envelopes of granular materials for monotonous and low-cycle
           loading processes. In: T. Triantafyllidis, editor, *Holistic Si-
           mulation of Geotechnical Installation Processes – Numerical
           and physical modelling*, Lecture notes in applied and compu-
           tational mechanics. Springer International Publishing, Cham,
           2015.

[DH13]   S. Danne and A. Hettler: Verhalten von nichtbindigen Böden
           bei niederzyklischer Belastung. *geotechnik*, 36(1):19–29, 2013.
           DOI: `10.1002/gete.201200010`.

[DH16]   S. Danne and A. Hettler: Experimental and numerical element
           tests for granulr soils – Performance of different constitutive
           models for monotonous and low-cycle loading. In: T. Trianta-
           fyllidis, editor, *Holistic simulation of geotechnical installation
           processes – Benchmarks and simulations*, Lecture notes in ap-
           plied and computational mechanics. Springer, Cham, 2016.

[DH10]   A. Daouadji and P.-Y. Hicher: An enhanced constitutive model for crushable granular materials. *International Journal for Numerical and Analytical Methods in Geomechanics*, 34(6):555–580, 2010. DOI: `10.1002/nag.815`.

[dBee66]   E. E. de Beer: Influence of the mean normal stress on the shearing strength of sand. In: ISSMFE, editor, *6th International Conference on Soil Mechanics and Foundation Engineering – Proceedings*, vol. 1, pp. 165–169. University of Toronto Press, 1966.

[dBor87]   R. de Borst: Integration of plasticity equations for singular yield functions. *Computers & Structures*, 26(5):823–829, 1987. DOI: `10.1016/0045-7949(87)90032-0`.

[dGCD+04]   V. de Gennaro, J. Canou, J. C. Dupla, and N. Benahmed: Influence of loading path on the undrained behaviour of a medium loose sand. *Canadian Geotechnical Journal*, 41(1):166–180, 2004. DOI: `10.1139/t03-082`.

[dMel77]   V. F. B. de Mello: Reflections on design decisions of practical significance to embankment dams. *Géotechnique*, 27(3):281–355, 1977. DOI: `10.1680/geot.1977.27.3.281`.

[Des13]   J. Desrues: ALERT 2007 database on strain localization in tests on Hostun sand – Full experimental data sets of biaxial and triaxial tests, 2013.

[Doa00]   T. Doanh: Strain response envelope: a complementary tool for evaluating hypoplastic constitutive equations. In: D. Kolymbas, editor, *Constitutive modelling of granular materials*, pp. 375–396. Springer, Berlin, Heidelberg, 2000.

[DIM97]   T. Doanh, E. Ibraim, and R. Matiotti: Undrained instability of very loose Hostun sand in triaxial compression and extension. Part 1 – Experimental observations. *Mechanics of Cohesive-frictional Materials*, 2(1):47–70, 1997. DOI: `10.1002/(SICI)1099-1484(199701)2:1<47::AID-CFM26>3.0.CO;2-9`.

[DC70]   J. M. Duncan and C.-Y. Chang: Nonlinear analysis of stress and strain in soils. *Journal of the Soil Mechanics and Foundations Division*, 96(5):1629–1653, 1970.

[FDD06]   Z. Finge, T. Doanh, and P. Dubujet: Undrained anisotropy of Hostun RF loose sand – New experimental investigations. *Canadian Geotechnical Journal*, 43(11):1195–1212, 2006. DOI: `10.1139/t06-068`.

[FDP90]   E. Flavigny, J. Desrues, and B. Palayer: Note technique – Le sable d'Hostun 'RF'. *Revue Française de Géotechnique*, 1990(53):67–70, 1990.

[FGM^{+}00]   R. Foerch, V. Gros, V. Mounoury, S. Quilici, and G. Cailletaud: Cyclic calculations and life prediction in thermomechanical fatique using the Zmat library. In: *ABAQUS Users' Conference – Proceedings*, pp. 289–303, 2000.

[Fre76]   D. G. Fredlund: Density and compressibility characteristics of air–water mixtures. *Canadian Geotechnical Journal*, 13(4):386–396, 1976. DOI: `10.1139/t76-040`.

[FZA73]   S. Frydman, J. G. Zeitlen, and I. Alpan: The membrane effect in triaxial testing of granular soils. *Journal of Testing and Evaluation*, 1(1):37–41, 1973. DOI: `10.1520/JTE11599J`.

[GW99]   A. Gajo and D. M. Wood: A kinematic hardening constitutive model for sands: the multiaxial formulation. *International Journal for Numerical and Analytical Methods in Geomechanics*, 23(9):925–965, 1999.

[GN93]   A. Gens and R. Nova: Conceptual bases for a constitutive model for bonded soils and weak rocks. In: A. Anagnostopoulos, R. Frank, N. Kalteziotis, and F. Schlosser, editors, *Geotechnical engineering of hards soils - soft rocks – Proceedings*, pp. 485–494, Rotterdam. CRC Press, 1993.

[GSD14]   M. Ghafghazi, D. A. Shuttle, and J. T. DeJong: Particle breakage and the critical state of sand. *Soils and Foundations*, 54(3):451–461, 2014. DOI: `10.1016/j.sandf.2014.04.016`.

[GB90]   J. D. Goddard and Y. M. Bashir: On Reynold's dilatancy. In: D. de Kee and P. N. Kaloni, editors, *Recent developments in structured continua*, pp. 23–35. Longman Scientific & Technical, Harlow, 1990.

[Gol76]   M. Goldscheider: Grenzbedingung und Fliessregel von Sand. *Mechanics Research Communications*, 3(6):463–468, 1976. DOI: `10.1016/0093-6413(76)90037-9`.

[Gou15]   M. Goudarzy: *Micro and macro mechanical assessment of small and intermediate strain properties of granular material.* PhD thesis, Ruhr-University Bochum, Bochum, 2015.

[Gud79]   G. Gudehus: A comparison of some constitutive laws for soils under radially symmetric loading and unloading. In: W. Wittke, editor, *3rd International Conference on Numerical Methods in Geomechanics – Proceedings*, pp. 1309–1323, Rotterdam. Balkema, 1979.

[Gud96]   G. Gudehus: A comprehensive constitutive equation for granular materials. *Soils and Foundations*, 36(1):1–12, 1996.

[GAG+08]   G. Gudehus, A. Amorosi, A. Gens, I. Herle, D. Kolymbas, D. Mašín, D. Muir Wood, A. Niemunis, R. Nova, M. Pastor, C. Tamagnini, and G. Viggiani: The soilmodels.info project. *International Journal for Numerical and Analytical Methods in Geomechanics*, 32(12):1571–1572, 2008. DOI: `10.1002/nag.675`.

[Guo00]   P. Guo: *Modelling granular materials with respect to stress-dilatancy and fabric – A fundamental approach.* PhD thesis, University of Calgary, Ottawa, 2000.

[Han47]   R. F. Hanstock: Damping capacity, strain hardening and fatigue. *Proceedings of the Physical Society*, 59(2):275–287, 1947. DOI: `10.1088/0959-5309/59/2/311`.

[Har78]   B. O. Hardin: The nature of stress-strain behavior of soils – State-of-the-art report. In: *Specialty Conference on Earthquake Engineering and Soil Dynamics – Proceedings*, pp. 3–90, 1978.

[HB66]   B. O. Hardin and W. L. Black: Sand stiffness under various triaxial stresses. *Journal of the Soil Mechanics and Foundations Division*, 92(SM 2):27–42, 1966.

[HB68]   B. O. Hardin and W. L. Black: Vibration modulus of normally consolidated clay. *Journal of the Soil Mechanics and Foundations Division*, 94(SM 2):353–369, 1968.

[HR63]   B. O. Hardin and F. E. Richart: Elastic wave velocities in granular soils. *Journal of the Soil Mechanics and Foundations Division*, 89(SM 1):33–65, 1963.

[HD72a]   B. O. Hardin and V. P. Drnevich: Shear modulus and damping in soils – Design equations and curves. *Journal of the Soil Mechanics and Foundations Division*, 98(SM 7):667–692, 1972.

[HD72b]   B. O. Hardin and V. P. Drnevich: Shear modulus and damping in soils: Measurement and parameter effects. *Journal of the Soil Mechanics and Foundations Division*, 98(SM 6):603–624, 1972.

[Hau93]   P. Haupt: On the mathematical modelling of material behavior in continuum mechanics. *Acta Mechanica*, 100(3-4):129–154, 1993. DOI: `10.1007/BF01174786`.

[Hau02]   P. Haupt: *Continuum mechanics and theory of materials.* Springer, Berlin, Heidelberg, 2002. DOI: `10.1007/978-3-662-04775-0`.

[Hel10]   S. Helwig: *Particle swarms for constrained optimization – Partikelschwärme für Optimierungsprobleme mit Nebenbedingungen.* PhD thesis, Universität Erlangen-Nürnberg, Erlangen, 2010.

[HNW09]   S. Helwig, F. Neumann, and R. Wanka: Particle Swarm Optimization with Velocity Adaptation. In: A. Bouchachia, N. Nedjah, L. Mourelle, and W. Pedrycz, editors, *International Conference on Adaptive and Intelligent Systems – ICAIS – Proceedings*, pp. 146–151, 2009. DOI: `10.1109/ICAIS.2009.32`.

[HG52]   D. J. Henkel and G. D. Gilbert: The effect of the rubber membrane on the measured triaxial compression strength of clay samples. *Géotechnique*, 3(1):20–29, 1952. DOI: `10.1680/geot.1952.3.1.20`.

[HEH87]   P.-Y. Hicher, M. S. El Hosri, and M. Homsi: Cyclic properties of soils within a large range of strain amplitude. In: A. S. Cakmak, editor, *3rd International Conference on Soil Dynamics and Earthquake Engineering – Proceedings*, vol. Soil Dynamics

and Liquefaction of *Developments in Geotechnical Engineering*, pp. 365–378, Burlington. Elsevier Science, 1987.

[HNH+01]   M. Hinokio, T. Nakai, T. Hoshikawa, and H. Yoshida: Dilatancy characteristic and anisotropy of sand under monotonic and cyclic loading. *Soils and Foundations*, 41(3):107–124, 2001.

[HK81]   R. D. Holtz and W. D. Kovacs: *An introduction to geotechnical engineering*. Prentice-Hall, Englewood Cliffs, N.J., 1981.

[HKZ+17]   Y. Hong, C. H. Koo, C. Zhou, C. W. W. Ng, and L. Z. Wang: Small strain path-dependent stiffness of Toyoura sand – Laboratory measurement and numerical implementation. *International Journal of Geomechanics*, 17(1):04016036(1–10), 2017. DOI: `10.1061/(ASCE)GM.1943-5622.0000664`.

[HT00]   E. Hoque and F. Tatsuoka: Kinematic elasticity of a granular material. In: ISRM, editor, *ISRM International symposium – Proceedings*. International Society for Rock Mechanics, 2000.

[Hor11]   E.-D. Hornig: *Eindimensionale Kompression überkonsolidierter bindiger Böden am Beispiel des Gipskeupers*. PhD thesis, Technische Universität Bergakademie Freiberg, Freiberg, 2011.

[Hou81]   G. T. Houlsby: *A study of plasticity theories and their applicability to soils*. PhD thesis, University of Cambridge, Cambridge, 1981.

[HN79]   T. Hueckel and R. Nova: Some hysteresis effects of the behaviour of geologic media. *International Journal of Solids and Structures*, 15(8):625–642, 1979. DOI: `10.1016/0020-7683(79)90076-3`.

[Hvo37]   M. J. Hvorslev: Über die Festigkeitseigenschaften gestörter bindiger Böden. In: Danmarks Naturvidenskabelige Samfund, editor, *Ingeniørvidenskabelige Skrifter*. Vol. A45, Ingeniørvidenskabelige Skrifter. Kopenhagen, 1937.

[Ish93]   K. Ishihara: Liquefaction and flow failure during earthquakes. *Géotechnique*, 43(3):351–451, 1993. DOI: `10.1680/geot.1993.43.3.351`.

[ITY75]   K. Ishihara, F. Tatsuoka, and S. Yasuda: Undrained deforma-
            tion and liquefaction of sand under cyclic stresses. *Soils and
            Foundations*, 15(1):29–44, 1975.

[Isr11]   J. N. Israelachvili: *Intermolecular and surface forces*. Acade-
            mic Press, Burlington, MA, 3rd ed. Edition, 2011.

[Ják44]   J. Jáky: The coefficient of earth pressure at rest – (in Hun-
            garian: A nyugalmi nyomas tenyezoje). *Journal for Society of
            Hungarian Architects and Engineers*, 78(22):355–358, 1944.

[Ják48]   J. Jáky: Pressure in silos. In: ISSMFE, editor, *2nd Internatio-
            nal Conference on Soil Mechanics and Foundation Engineer-
            ing – Proceedings*, vol. 1, pp. 103–107, 1948.

[Jan63]   N. Janbu: Soil compressibility as determined by oedometer
            and triaxial tests. In: *2nd European Conference on Soil Me-
            chanics and Foundation Engineering – Proceedings*, vol. 1,
            pp. 19–25, 1963.

[JPF$^+$86] R. J. Jardine, D. M. Potts, A. B. Fourie, and J. B. Burland:
            Studies of the influence of non-linear stress–strain characte-
            ristics in soil–structure interaction. *Géotechnique*, 36(3):377–
            396, 1986. DOI: `10.1680/geot.1986.36.3.377`.

[JSB84]   R. J. Jardine, M. J. Symes, and J. B. Burland: The measure-
            ment of soil stiffness in the triaxial apparatus. *Géotechnique*,
            34(3):323–340, 1984. DOI: `10.1680/geot.1984.34.3.323`.

[Jov97]   V. Jovičić: *The measurement and interpretation of small
            strain stiffness of soils*. PhD thesis, City University, London,
            1997.

[KE95]   J. Kennedy and R. Eberhart: Particle swarm optimization.
            In: *International Conference on Neural Networks – ICNN'95
            – Proceedings*, pp. 1942–1948, 1995. DOI: `10.1109/ICNN.
            1995.488968`.

[KHV05]   N. Khalili, M. A. Habte, and S. Valliappan: A bounding sur-
            face plasticity model for cyclic loading of granular soils. *In-
            ternational Journal for Numerical Methods in Engineering*,
            63(14):1939–1960, 2005. DOI: `10.1002/nme.1351`.

[KS77]   M. Kiekbusch and B. Schuppener: Membrane penetration and
            its effect on pore pressures. *Journal of the Geotechnical Engi-
            neering Division*, 103(11):1267–1279, 1977.

[KS67]   H.-Y. L. Ko and F. Scott: Deformation of sand in hydrostatic
            compression. *Journal of the Soil Mechanics and Foundations
            Division*, 93(SM 3):137–156, 1967.

[KS68]   H.-Y. L. Ko and R. F. Scott: Deformation of sand at fai-
            lure. *Journal of the Soil Mechanics and Foundations Division*,
            94(4):883–898, 1968.

[Koe70]   R. M. Koerner: Behavior of single mineral soils in triaxial
            shear. *Journal of the Soil Mechanics and Foundations Divi-
            sion*, 96(SM 4):1373–1390, 1970.

[Köh97]   H.-J. Köhler: Porenwasserdruckausbreitung im Boden – Mess-
            verfahren und Berechnungsansätze. In: Bundesanstalt für
            Wasserbau, editor, *Mitteilungsblatt der Bundesanstalt für
            Wasserbau*, pp. 95–108. Karlsruhe, 1997.

[Koi53]   W. T. Koiter: Stress-strain relations, uniqueness and varia-
            tional theorems for elastic-plastic materials with a singular
            yield surface. *Quarterly of Applied Mathematics*, 11(3):350–
            354, 1953. DOI: 10.1090/qam/59769.

[Kok80]   T. Kokusho: Cyclic triaxial test of dynamic soil properties for
            wide strain range. *Soils and Foundations*, 20(2):45–60, 1980.

[Kol88]   D. Kolymbas: *A constitutive theory for soils and other granu-
            lar materials*. Habilitation dissertation, University of Karls-
            ruhe, Karlsruhe, 1988.

[KB93]   D. Kolymbas and E. Bauer: Soft oedometer – A new testing
            device and its application for the calibration of hypoplastic
            constitutive laws. *Geotechnical Testing Journal*, 16(2):263–
            270, 1993. DOI: 10.1520/GTJ10044J.

[KW90]   D. Kolymbas and W. Wu: Recent results of triaxial tests with
            granular materials. *Powder Technology*, 60(2):99–119, 1990.
            DOI: 10.1016/0032-5910(90)80136-M.

[Kol91]   D. Kolymbas: An outline of hypoplasticity. *Archive of Applied
            Mechanics*, 61(3):143–151, 1991.

[Kol16]   D. Kolymbas: *Geotechnik – Bodenmechanik, Grundbau und Tunnelbau*. Springer, Berlin, Heidelberg, 2016. DOI: `10.1007/978-3-662-53593-6`.

[Kon63]   H. L. Koning: Some observations on the modulus of compressibility of water. In: *2nd European Conference on Soil Mechanics and Foundation Engineering – Proceedings*, pp. 33–36, 1963.

[Kon78]   J. Konishi: *Microscopic studies on the deformation and strength behavior of granular materials like sand*. PhD thesis, Kyoto University, Kyoto, 1978.

[Kre00]   S. Krenk: Characteristic state plasticity for granular materials – Part I: Basic theory. *International Journal of Solids and Structures*, 37(43):6343–6360, 2000. DOI: `10.1016/S0020-7683(99)00278-4`.

[Kri75]   R. D. Krieg: A practical two surface plasticity theory. *Journal of Applied Mechanics*, 42(3):641–646, 1975. DOI: `10.1115/1.3423656`.

[KJ02]   R. Kuwano and R. J. Jardine: On the applicability of cross-anisotropic elasticity to granular materials at very small strains. *Géotechnique*, 52(10):727–749, 2002. DOI: `10.1680/geot.2002.52.10.727`.

[Kuw99]   R. Kuwano: *The stiffness and yielding anisotropy of sand*. PhD thesis, University of London, Imperial College, London, 1999.

[LFI+77]   C. C. Ladd, R. Foott, K. Ishihara, F. Schlosser, and H. G. Poulos: Stress-deformation and strength characteristics – State-of-the-art reports. In: ISSMFE, editor, *9th International Conference on Soil Mechanics and Foundation Engineering – Proceedings*, pp. 421–494, 1977.

[Lad74]   R. S. Ladd: Specimen preparation and liquefaction of sands. *Journal of the Geotechnical Engineering Division*, 100(10):1180–1184, 1974.

[Lad77]   P. V. Lade: Elasto-plastic stress-strain theory for cohesionless soil with curved yield surfaces. *International Journal of Solids*

and Structures, 13(11):1019–1035, 1977. DOI: 10.1016/0020-7683(77)90073-7.

[Lad16]   P. V. Lade: *Triaxial testing of soils*. John Wiley & Sons Inc, Hoboken, 2016.

[LA05]   P. V. Lade and A. V. Abelev: Characterization of cross-anisotropic soil deposits from isotropic compression tests. *Soils and Foundations*, 45(5):89–102, 2005.

[LD73]   P. V. Lade and J. M. Duncan: Cubical triaxial tests on cohesionless soil. *Journal of the Soil Mechanics and Foundations Division*, 99(10):793–812, 1973.

[LD75]   P. V. Lade and J. M. Duncan: Elastoplastic stress-strain theory for cohesionless soil. *Journal of the Geotechnical Engineering Division*, 101(10):1037–1053, 1975.

[LH77]   P. V. Lade and S. B. Hernandez: Membrane penetration effects in undrained tests. *Journal of the Geotechnical Engineering Division*, 103(2):109–125, 1977.

[LY93]   P. V. Lade and J. A. Yamamuro: Instablility and behavior of granular materials at high pressures – Report to the air force office of scientific research, Los Angeles, 1993.

[LYB05]   P. V. Lade, J. A. Yamamuro, and P. A. Bopp: Relative density effects on drained and undrained strengths of sand at high pressures. In: ISSMGE, editor, *16th International Conference on Soil Mechanics and Geotechnical Engineering – Proceedings*, pp. 537–541, Rotterdam. Millpress, 2005.

[Län99]   T. Länsivaara: *A study of the mechanical behavior of soft clay*. PhD thesis, Norwegian University of Science and Technology, Trondheim, 1999. DOI: 10.13140/RG.2.1.2842.0641.

[LE05]   C. Lauer and J. Engel: A triaxial device for unsaturated sand - new developments. In: T. Schanz, editor, *Unsaturated soils – Proceedings*, vol. 93 of *Springer proceedings in physics*, pp. 301–314, Berlin and New York. Springer, 2005. DOI: 10.1007/3-540-26736-0_23.

[LHI08]   C. LeBlanc, O. Hededal, and L. B. Ibsen: A modified criti-
            cal state two-surface plasticity model for sand - theory and
            implementation, Aalborg, 2008.

[Lee66]   I. K. Lee: Stress-dilatancy performance of feldspar. *Journal of
            the Soil Mechanics and Foundations Division*, 92(SM 2):79–
            103, 1966.

[LPK+13]   J. Lee, D. Park, D. Kyung, and D. Lee: Effect of particle
            characteristics on K_0 behavior for granular materials. In: P.
            Delage, editor, *18th International Conference on Soil Mecha-
            nics and Geotechnical Engineering – Proceedings*, pp. 377–380,
            Paris. Presses des Ponts, 2013.

[Lee65]   K. L. Lee: *Triaxial compressive strength of saturated sand un-
            der seismic loading conditions*. PhD thesis, University of Ca-
            lifornia, Berkeley, 1965.

[LF67]   K. L. Lee and I. Farhoomand: Compressibility and crushing
            of granular soil in anisotropic triaxial compression. *Canadian
            Geotechnical Journal*, 4(1):68–86, 1967. DOI: `10.1139/t67-
            012`.

[LS67]   K. L. Lee and H. B. Seed: Drained strength characteristics of
            sands. *Journal of the Soil Mechanics and Foundations Divi-
            sion*, 93(SM 6):117–141, 1967.

[Len09]   S. Lenart: The use of dissipated energy loaded saturated soils.
            In: T. Miura and Y. Ikeda, editors, *Earthquake engineering
            – New research*, pp. 295–321. Nova Science Publishers, New
            York, 2009.

[LB70]   P. I. Lewin and J. B. Burland: Stress-probe experiments on
            saturated normally consolidated clay. *Géotechnique*, 20(1):38–
            56, 1970. DOI: `10.1680/geot.1970.20.1.38`.

[LD00]   X. S. Li and Y. F. Dafalias: Dilatancy for cohesionless soils.
            Géotechnique, 50(4):449–460, 2000. DOI: `10.1680/geot.2000
            .50.4.449`.

[LD04]   X. S. Li and Y. F. Dafalias: A constitutive framework for ani-
            sotropic sand including non-proportional loading. *Géotechni-
            que*, 54(1):41–55, 2004.

[LW98]   X. S. Li and Y. Wang: Linear representation of steady-state line for sand. *Journal of Geotechnical and Geoenvironmental Engineering*, 124(12):1215–1217, 1998. DOI: `10.1061/(ASCE) 1090-0241(1998)124:12(1215)`.

[LD02]   X. S. Li and Y. F. Dafalias: Constitutive modeling of inherently anisotropic sand behavior. *Journal of Geotechnical and Geoenvironmental Engineering*, 128(10):868–880, 2002. DOI: `10.1061/(ASCE)1090-0241(2002)128:10(868)`.

[LDW99]   X.-S. Li, Y. F. Dafalias, and Z.-L. Wang: State-dependant dilatancy in critical-state constitutive modelling of sand. *Canadian Geotechnical Journal*, 36(4):599–611, 1999. DOI: `10. 1139/t99-029`.

[Lo 95]   D. C. F. Lo Presti: General report: Measurement of shear deformation of geomaterials in the laboratory. In: S. Shibuya, T. Mitachi, and S. Miura, editors, *International Symposium on Pre-Failure Deformation Characteristics of Geomaterials – Proceedings*, pp. 1067–1088, Rotterdam. Balkema, 1995.

[Mai93]   R. J. Mair: Developments in geotechnical engineering research: application to tunnels and deep excavations – Unwin memorial lecture. *Proceedings of the Institution of Civil Engineers - Civil Engineering*, 97(1):27–41, 1993. DOI: `10.1680/ icien.1993.22378`.

[MD97]   M. T. Manzari and Y. F. Dafalias: A critical state two-surface plasticity model for sands. *Géotechnique*, 47(2):255–272, 1997. DOI: `10.1680/geot.1997.47.2.255`.

[Mar85]   S. Marchetti: On the field determination of K_0 in sand. In: ISSMFE, editor, *11th International Conference on Soil Mechanics and Foundation Engineering – Proceedings*, vol. 5, pp. 2667–2672, Rotterdam. Balkema, 1985.

[Mas26]   G. Masing: Eigenspannungen und Verfestigung beim Messing. In: *2nd International Congress of Applied Mechanics – Proceedings*, pp. 332–335, 1926.

[Mat74]   H. Matsuoka: Dilatancy characteristics of soil. *Soils and Foundations*, 14(3):13–24, 1974.

[MN74]   H. Matsuoka and T. Nakai: Stress-deformation and strength
           characteristics of soil under three different principal stresses.
           In: *Conference of Japan Society of Civil Engineering – Pro-
           ceedings*, pp. 59–70, 1974.

[Mat99]   H. Mattsson: *On a mathematical basis for constitutive drivers
           in soil plasticity*. PhD thesis, Luleå University of Technology,
           Luleå, 1999.

[MAK97]   H. Mattsson, K. Axelsson, and M. Klisinski: A method to cor-
           rect yield surface drift in soil plasticity under mixed control
           and explicit integration. *International Journal for Numeri-
           cal and Analytical Methods in Geomechanics*, 21(3):175–197,
           1997. DOI: `10.1002/(SICI)1096-9853(199703)21:3<175::
           AID-NAG864>3.0.CO;2-2`.

[MK82]   P. W. Mayne and F. H. Kulhawy: K_0-OCR relationships
           in soil. *Journal of the Geotechnical Engineering Division*,
           108(GT6):851–872, 1982.

[MNH02]   G. R. McDowell, Y. Nakata, and M. Hyodo: On the plastic
           hardening of sand. *Géotechnique*, 52(5):349–358, 2002. DOI:
           `10.1680/geot.2002.52.5.349`.

[MD53]   R. D. Mindlin and H. Deresiewicz: Elastic spheres in contact
           under vyrying oblique forces. *Journal of Applied Mechanics*,
           20(3):327–344, 1953.

[Miu79]   N. Miura: A consideration on the stress–strain relation of a
           sand under high pressures. *Proceedings of the Japan Society
           of Civil Engineers*, 1979(282):127–130, 1979. DOI: `10.2208/
           jscej1969.1979.282_127`.

[MMY84]   N. Miura, H. Murata, and N. Yasufuku: Stress-strain cha-
           racteristics of sand in a particle-crushing region. *Soils and
           Foundations*, 24(1):77–89, 1984.

[MY75]   N. Miura and T. Yamanouchi: Effect of water on the behavior
           of a quartz-rich sand under high stresses. *Soils and Foundati-
           ons*, 15(4):23–34, 1975.

[Mró67]   Z. Mróz: On the description of anisotropic workhardening.
           Journal of the Mechanics and Physics of Solids, 15(3):163–
           175, 1967. DOI: `10.1016/0022-5096(67)90030-0`.

[MNZ78]   Z. Mróz, V. A. Norris, and O. C. Zienkiewicz: An anisotropic
           hardening model for soils and its application to cyclic loading.
           *International Journal for Numerical and Analytical Methods
           in Geomechanics*, 2(3):203–221, 1978. DOI: `10.1002/nag.
           1610020303`.

[MNZ79]   Z. Mróz, V. A. Norris, and O. C. Zienkiewicz: Application
           of an anisotropic hardening model in the analysis of elasto–
           plastic deformation of soils. *Géotechnique*, 29(1):1–34, 1979.
           DOI: `10.1680/geot.1979.29.1.1`.

[Mui90]   D. Muir Wood: *Soil behaviour and critical state soil mecha-
           nics.* Cambridge University Press, Cambridge [England] and
           New York, 1990.

[MM08]   D. Muir Wood and K. Maeda: Changing grading of soil –
           Effect on critical states. *Acta Geotechnica*, 3(1):3–14, 2008.
           DOI: `10.1007/s11440-007-0041-0`.

[MSC⁺77]   J. P. Mulilis, H. B. Seed, C. K. Chan, J. K. Mitchell, and
           K. Arulanandan: Effects of sample preparation on sand li-
           quefaction. *Journal of the Geotechnical Engineering Division*,
           103(2):91–109, 1977.

[NHH⁺01]   Y. Nakata, M. Hyodo, A. F. HYDE, Y. Kato, and H. Mu-
           rata: Microscopic particle crushing of sand subjected to high
           pressure one-dimensional compression. *Soils and Foundations*,
           41(1):69–82, 2001. DOI: `10.3208/sandf.41.69`.

[NKH⁺01]   Y. Nakata, Y. Kato, M. Hyodo, A. F. L. Hyde, and H. Murata:
           One-dimensional compression behaviour of uniformly graded
           sand related to single particle crushing strength. *Soils and
           Foundations*, 41(2):39–51, 2001.

[NT84]   S. Nemat–Nasser and K. Takahashi: Liquefaction and fabric of
           sand. *Journal of Geotechnical Engineering*, 110(9):1291–1306,
           1984. DOI: `10.1061/(ASCE)0733-9410(1984)110:9(1291)`.

[NS79]   S. Nemat-Nasser and A. Shokooh: A unified approach to den-
           sification and liquefaction of cohesionless sand in cyclic she-
           aring. *Canadian Geotechnical Journal*, 16(4):659–678, 1979.
           DOI: `10.1139/t79-076`.

[NT82]   S. Nemat-Nasser and Y. Tobita: Influence of fabric on lique-
           faction and densification potential of cohesionless sand. *Me-
           chanics of Materials*, 1(1):43–62, 1982. DOI: `10.1016/0167-
           6636(82)90023-0`.

[NA59]   P. L. Newland and B. H. Allely: Volume changes during un-
           drained triaxial tests on saturated dilatant granular materials.
           Géotechnique, 9(4):174–182, 1959. DOI: `10.1680/geot.1959.
           9.4.174`.

[NSA89]   P. G. Nicholson, R. B. Seed, and H. Anwar: Measurement
           and elimination of membrane compliance effects in undrained
           triaxial testing, Berkeley, 1989.

[Nie02]   A. Niemunis: *Extended hypoplasticity models for soils*. Habili-
           tation dissertation, Ruhr-University Bochum, Bochum, 2002.

[NH97]   A. Niemunis and I. Herle: Hypoplastic model for cohesion-
           less soils with elastic strain range. *Mechanics of Cohesive-
           frictional Materials*, 2(4):279–299, 1997.

[NWP$^+$05] A. Niemunis, T. Wichtmann, Y. Petryna, and T. Triantafylli-
           dis: Stochastic modelling of settlements due to cyclic loading.
           In: G. Augusti, G. I. Schuëller, and M. Ciampoli, editors, *9th
           International Conference on Structural Safety and Reliability
           – ICOSSAR'05 – Proceedings*, Rotterdam. Millpress, 2005.

[NWT05]   A. Niemunis, T. Wichtmann, and T. Triantafyllidis: A high-
           cycle accumulation model for sand. *Computers and Geo-
           technics*, 32(4):245–263, 2005. DOI: `10.1016/j.compgeo.
           2005.03.002`.

[NH14]   K. Nitzsche and I. Herle: Analysis of displacement patterns
           during an excavation using different constitutive models. In:
           M. A. Hicks, R. B. J. Brinkgreve, and A. Rohe, editors, *8th
           European Conference on Numerical Methods in Geotechni-
           cal Engineering – NUMGE 2014 – Proceedings*, pp. 777–782,
           2014.

[NW79]   R. Nova and D. M. Wood: A constitutive model for sand in
           triaxial compression. *International Journal for Numerical and
           Analytical Methods in Geomechanics*, 3(3):255–278, 1979. DOI:
           `10.1002/nag.1610030305`.

[Oda99]   M. Oda: Fabric tensor and its geometrical meaning. In: M. Oda and K. Iwashita, editors, *Mechanics of granular materials – An introduction*, pp. 27–34. Balkema, 1999.

[OKH78]   M. Oda, I. Koishikawa, and T. Higuchi: Experimental study of anisotropic shear strength of sand by plane strain test. *Soils and Foundations*, 18(1):25–38, 1978.

[OKN80]   M. Oda, J. Konishi, and S. Nemat-Nasser: Some experimentally based fundamental results on the mechanical behaviour of granular materials. *Géotechnique*, 30(4):479–495, 1980. DOI: `10.1680/geot.1980.30.4.479`.

[Oda72]   M. Oda: Initial fabrics and their relation to mechanical properties of granular material. *Soils and Foundations*, 12(1):17–36, 1972.

[Oda82]   M. Oda: Fabric tensor for discontinious geological materials. *Soils and Foundations*, 22(4):96–108, 1982.

[ONK85]   M. Oda, S. Nemat-Nasser, and J. Konishi: Stress-induced anisotropy in granular masses. *Soils and Foundations*, 25(3):85–97, 1985.

[Ohd39]   J. Ohde: Zur Theorie der Druckverteilung im Baugrund. *Der Bauingenieur*, 20(33/34):451–459, 1939.

[PB02]   A. G. Papadimitriou and G. D. Bouckovalas: Plasticity model for sand under small and large cyclic strains: a multiaxial formulation. *Soil Dynamics and Earthquake Engineering*, 22(3):191–204, 2002. DOI: `10.1016/S0267-7261(02)00009-X`.

[PW95]   J. M. Pestana and A. J. Whittle: Compression model for cohesionless soils. *Géotechnique*, 45(4):611–631, 1995.

[PW99]   J. M. Pestana and A. J. Whittle: Formulation of a unified constitutive model for clays and sands. *International Journal for Numerical and Analytical Methods in Geomechanics*, 23(12):1215–1243, 1999. DOI: `10.1002/(SICI)1096-9853(1999910)23:12<1215::AID-NAG29>3.0.CO;2-F`.

[PG85]   D. M. Potts and A. Gens: A critical assessment of methods of correcting for drift from the yield surface in elasto-plastic finite element analysis. *International Journal for Numerical*

and Analytical Methods in Geomechanics, 9(2):149–159, 1985. DOI: `10.1002/nag.1610090204`.

[PTS89]   T. B. S. Pradhan, F. Tatsuoka, and Y. Sato: Experimental stress-dilatancy relations of sand subjected to cyclic loading. *Soils and Foundations*, 29(1):45–64, 1989.

[PB69]   D. C. Procter and L. Barden: A note on the drained strength of sand under generalized strain conditions. *Géotechnique*, 19(3):424–426, 1969.

[PB98]   A. M. Puzrin and J. B. Burland: Non-linear model of small-strain behaviour of soils. *Géotechnique*, 48(2):217–233, 1998. DOI: `10.1680/geot.1998.48.2.217`.

[Pyk79]   R. M. Pyke: Nonlinear soil models for irregular cyclic loadings. *Journal of the Geotechnical Engineering Division*, 105(6):715–726, 1979.

[Raf12]   A. Rafiee: LMGC90 Software – Force chain, 14.01.2012.

[RO43]   W. Ramberg and W. R. Osgood: Description of stress-strain curves by three parameters – Technical Note 902. National Advisory Committee for Aeronautics, editor, Washington, D.C., 1943.

[RHW70]   F. E. Richart, J. R. Hall, and R. D. Woods: *Vibrations of soils and foundations*. Prentice-Hall international series in theoretical and applied mechanics. Prentice-Hall, Englewood Cliffs, N.J., 1970.

[RdS58]   J. E. Roberts and J. M. de Souza: The compressibility of sands. In: ASTM, editor, *Annual meeting of the American Society for Testing and Materials – Proceedings*, pp. 1269–1277, Philadelphia, 1958.

[RS63]   K. H. Roscoe and A. N. Schofield: Mechanical behaviour of an idealized 'wet' clay. In: *2nd European Conference on Soil Mechanics and Foundation Engineering – Proceedings*, 1963.

[RST63]   K. H. Roscoe, A. N. Schofield, and A. Thurairajah: Yielding of clays in states wetter than critical. *Géotechnique*, 13(3):211–240, 1963. DOI: `10.1680/geot.1963.13.3.211`.

[RSW58]   K. H. Roscoe, A. N. Schofield, and C. P. Wroth: On the yiel-
          ding of soils. *Géotechnique*, 8(1):22–53, 1958. DOI: `10.1680/`
          `geot.1958.8.1.22`.

[Row62]   P. W. Rowe: The stress-dilatancy relation for static equili-
          brium of an assembly of particles in contact. *Proceedings of
          the Royal Society A - Mathematical, Physical and Engineer-
          ing Sciences*, 269(1339):500–527, 1962. DOI: `10.1098/rspa.`
          `1962.0193`.

[Row72]   P. W. Rowe: Theoretical meaning and observed values of de-
          formation parameters for soil. In: R. H. G. Parry, editor,
          *Roscoe Memorial Symposium – Stress-strain behaviour of soils
          – Proceedings*, pp. 143–194, 1972.

[Rut47]   P. C. Rutledge: Cooperative triaxial shear research program.
          Corps of Engineers, US Department of the Army, editor, 1947.

[Sat82]   M. Satake: Fabric tensor in granular materials. In: P. A. Ver-
          meer and H. J. Luger, editors, *Deformation and failure of
          granular materials – Proceedings*, pp. 63–68, Rotterdam. Bal-
          kema, 1982.

[Sch12]   B. Schädlich: *A multilaminate constitutive model for stiff soils.*
          PhD thesis, Technische Universität Graz, Graz, 2012.

[SV96]   T. Schanz and P. A. Vermeer: Angles of friction and dilatancy
          of sand. *Géotechnique*, 46(1):145–151, 1996. DOI: `10.1680/`
          `geot.1996.46.1.145`.

[SVB99]   T. Schanz, P. A. Vermeer, and P. G. Bonnier: The hardening
          soil model: Formulation and verification. In: R. B. J. Brink-
          greve, editor, *Beyond 2000 in Computational Geotechnics –
          10 years of PLAXIS International – Proceedings*, Rotterdam.
          Balkema, 1999.

[Sch07]   F. Scharinger: *A multilaminate model for soil incorporating
          small strain stiffness.* PhD thesis, Technische Universität
          Graz, Graz, 2007.

[SW68]   A. N. Schofield and P. Wroth: *Critical state soil mechanics.*
          European civil engineering series. McGraw-Hill, London and
          New York, 1968.

[Sed00]   K. Sedlan: *Viskoelastisches Materialverhalten von Elasto-merwerkstoffen – Experimentelle Untersuchung und Modell-lbildung.* PhD thesis, Universität Gesamthochschule Kassel, Kassel, 2000.

[SL67]   H. B. Seed and K. L. Lee: Undrained strength characteristics of cohesionless soils. *Journal of the Soil Mechanics and Foundations Division*, 93(SM 6):333–360, 1967.

[ST14]   G. Seidalinov and M. Taiebat: Bounding surface SANICLAY plasticity model for cyclic clay behavior. *International Journal for Numerical and Analytical Methods in Geomechanics*, 38(7):702–724, 2014. DOI: `10.1002/nag.2229`.

[SDD⁺05]   G. Servant, F. Darve, J. Desrues, and I. O. Georgopoulos: Diffuse modes of failure in geomaterials. In: H. DiBenedetto, T. Doanh, H. Geoffroy, and C. Sauzéat, editors, *Deformation characteristics of geomaterials – Recent investigations and prospects*, pp. 181–200. Taylor & Francis, 2005.

[Sim92]   B. Simpson: Retaining structures – displacement and design. *Géotechnique*, 42(4):541–576, 1992. DOI: `10.1680/geot.1992.42.4.541`.

[SOC79]   B. Simpson, N. J. O'Riordan, and D. D. Croft: A computer model for the analysis of ground movements in London Clay. *Géotechnique*, 29(2):149–175, 1979. DOI: `10.1680/geot.1979.29.2.149`.

[Ske54]   A. W. Skempton: The Pore-Pressure Coefficients A and B. *Géotechnique*, 4(4):143–147, 1954. DOI: `10.1680/geot.1954.4.4.143`.

[Slo87]   S. W. Sloan: Substepping schemes for the numerical integration of elastoplastic stress-strain relations. *International Journal for Numerical Methods in Engineering*, 24(5):893–911, 1987. DOI: `10.1002/nme.1620240505`.

[SJH92]   P. R. Smith, R. J. Jardine, and D. W. Hight: The yielding of Bothkennar clay. *Géotechnique*, 42(2):257–274, 1992. DOI: `10.1680/geot.1992.42.2.257`.

[ElS69]   M. A. El-Sohby: Deformation of sands under constant stress ratios. In: ISSMFE, editor, *7th International Conference on*

Soil Mechanics and Foundation Engineering – Proceedings, vol. 1, pp. 111–119. Sociedad Mexicana de Mecanica, 1969.

[Sør03]   O. K. Søreide: *Mixed hardening models for frictional soils.* PhD thesis, NTNU, Trondheim, 2003.

[Sta90]   S. E. Stallebrass: *Modelling the effect of recent stress history on the deformation of overconsolidated soils.* PhD thesis, City University, London, 1990.

[SHS⁺07]   D. A. Sun, W. X. Huang, D. C. Sheng, and H. Yamamoto: An elastoplastic model for granular materials exhibiting particle crushing. *Key Engineering Materials*, 340-341:1273–1278, 2007. DOI: `10.4028/www.scientific.net/KEM.340-341.1273`.

[SM69]   H. B. Sutherland and M. S. Mesdary: The influence of the intermediate principal stress on the strength of sand. In: IS-SMFE, editor, *7th International Conference on Soil Mechanics and Foundation Engineering – Proceedings*, pp. 391–399. Sociedad Mexicana de Mecanica, 1969.

[SK12]   L. P. Suwal and R. Kuwano: Poisson's ratio evaluation on silty and clayey sands on laboratory speicmens by flat disk shaped piezo-ceramic transducer. *Bulletin of ERS*, 45:141–158, 2012.

[AlT87]   A. Al-Tabbaa: *Permeability and stress-strain response of speswhite kaolin.* PhD thesis, University of Cambridge, Cambridge, 1987.

[AM89]   A. Al-Tabbaa and D. Muir Wood: An experimentally based 'bubble' model for clay. In: S. Pietruszczak and G. N. Pande, editors, *3rd International Symposium on Numerical Models in Geomechanics – NUMOG III – Proceedings*, pp. 91–99, London and New York. Elsevier Applied Science, 1989.

[TPZ16]   D. Taborda, D. M. Potts, and L. Zdravković: On the assessment of energy dissipated through hysteresis in finite element analysis. *Computers and Geotechnics*, 71:180–194, 2016. DOI: `10.1016/j.compgeo.2015.09.001`.

[Tai09]   M. Taiebat: *Advanced elastic-plastic constitutive and numerical modeling in geomechanics.* PhD thesis, University of California Davis, Davis, 2009.

[TD08]   M. Taiebat and Y. F. Dafalias: SANISAND – Simple anisotro-
            pic sand plasticity model. *International Journal for Numeri-
            cal and Analytical Methods in Geomechanics*, 32(8):915–948,
            2008. DOI: `10.1002/nag.651`.

[TDP10]   M. Taiebat, Y. F. Dafalias, and R. Peek: A destructuration
            theory and its application to SANICLAY model. *International
            Journal for Numerical and Analytical Methods in Geomecha-
            nics*, 34(10):1009–1040, 2010. DOI: `10.1002/nag.841`.

[Tam12]   C. Tamagnini: Numerical implementation of constitutive mo-
            dels. ALERT Olek Zienkiewicz School, TU Dresden, 17-21
            September 2012.

[TH14]   T. Tang and O. Hededal: Simulation of pore pressure accu-
            mulation under cyclic loading using finite volume method. In:
            M. A. Hicks, R. B. J. Brinkgreve, and A. Rohe, editors, *8th
            European Conference on Numerical Methods in Geotechnical
            Engineering – NUMGE 2014 – Proceedings*, pp. 1301–1306,
            2014.

[Tay48]   D. W. Taylor: *Fundamentals of soil mechanics*. J. Wiley &
            sons, New York, 1948.

[Tob89]   Y. Tobita: Fabric tensors in constitutive equations for granu-
            lar materials. *Soils and Foundations*, 29(4):91–104, 1989.

[Tri16]   T. Triantafyllidis: Zyklische Belastung von Boden – Attrakto-
            renzustände, Historiotropie und Fraktalität. In: F. Rackwitz,
            editor, *12. Hans Lorenz Symposium – Proceedings*, Veröffentli-
            chungen des Grundbauinstitutes der Technischen Universität
            Berlin, pp. 11–50, Herzogenrath. Shaker, 2016.

[Tse09]   A. B. Tsegaye: *Evaluation of material models for liquefaction*.
            Master's thesis, Delft University of Technology, Delft, 2009.

[TYB13]   A. B. Tsegaye, B. W. Ygzaw, and T. Benz: Stress-dependency
            of intergranular strain. In: Q. Yang, J.-M. Zhang, H. Zheng,
            and Y. Yao, editors, *Constitutive modeling of geomateri-
            als*, Springer Series in Geomechanics and Geoengineer-
            ing, pp. 483–490. Springer, Berlin, Heidelberg, 2013. DOI:
            `10.1007/978-3-642-32814-5_66`.

[Tse14]   A. B. Tsegaye: *On the modelling of state-dilatancy and mecha-nical behaviour of frictional material.* PhD thesis, Norwegian University of Science and Technology, Trondheim, 2014.

[TNB13]   A. B. Tsegaye, S. Nordal, and T. Benz: On shear-volume cou-pling in deformation of soils. In: Q. Yang, J.-M. Zhang, H. Zheng, and Y. Yao, editors, *Constitutive modeling of geoma-terials*, Springer Series in Geomechanics and Geoengineering, pp. 491–500. Springer, Berlin, Heidelberg, 2013.

[UV98]   M. Uthayakumar and Y. P. Vaid: Static liquefaction of sands under multiaxial loading. *Canadian Geotechnical Journal*, 35(2):273–283, 1998. DOI: `10.1139/t98-007`.

[VCK90]   Y. P. Vaid, E. K. F. Chung, and R. H. Kuerbis: Stress path and steady state. *Canadian Geotechnical Journal*, 27(1):1–7, 1990. DOI: `10.1139/t90-001`.

[VI96]   R. Verdugo and K. Ishihara: The steady state of sandy soils. *Soils and Foundations*, 36(2):81–91, 1996.

[Ver78]   P. A. Vermeer: A double hardening model for sand. *Géotechni-que*, 28(4):413–433, 1978. DOI: `10.1680/geot.1978.28.4.413`.

[VDZ00]   P. A. Vermeer, J. Desrues, and B. Zweschper: Institutsbericht 13 – Database for tests on Hostun RF sand – Report, Stutt-gart, 2000.

[vTer25]   K. von Terzaghi: *Erdbaumechanik auf bodenphysikalischer Grundlage.* Deuticke, Leipzig and Wien, 1925.

[vTer43]   K. von Terzaghi: *Theoretical soil mechanics.* John Wiley & Sons Inc., New York and London, 1943.

[vTPM96]   K. von Terzaghi, R. B. Peck, and G. Mesri: *Soil mechanics in engineering practice.* Wiley, New York, 3rd ed. Edition, 1996.

[Vuc90]   M. Vucetic: Normalized behavior of clay under irregular cyclic loading. *Canadian Geotechnical Journal*, 27(1):29–46, 1990. DOI: `10.1139/t90-004`.

[Vuc94]   M. Vucetic: Cyclic threshold shear strains in soils. *Journal of Geotechnical Engineering*, 120(12):2208–2228, 1994. DOI: `10.1061/(ASCE)0733-9410(1994)120:12(2208)`.

[VD91]   M. Vucetic and R. Dobry: Effect of soil plasticity on cyclic
            response. *Journal of Geotechnical Engineering*, 117(1):89–107,
            1991. DOI: `10.1061/(ASCE)0733-9410(1991)117:1(89)`.

[WG99]   R. G. Wan and P. J. Guo: A pressure and density dependent
            dilatancy model for granular materials. *Soils and Foundations*,
            39(6):1–11, 1999.

[WG98]   R. G. Wan and P. Guo: A simple constitutive model for gra-
            nular soils – Modified stress-dilatancy approach. *Computers
            and Geotechnics*, 22(2):109–133, 1998. DOI: `10.1016/S0266-
            352X(98)00004-4`.

[WG04]   R. G. Wan and P. Guo: Stress dilatancy and fabric depen-
            dencies on sand behavior. *Journal of Engineering Mechanics*,
            130(6):635–645, 2004. DOI: `10.1061/(ASCE)0733-9399(2004
)130:6(635)`.

[WDS90]   Z.-L. Wang, Y. F. Dafalias, and C.-K. Shen: Bounding surface
            hypoplasticity model for sand. *Journal of Engineering Me-
            chanics*, 116(5):983–1001, 1990. DOI: `10.1061/(ASCE)0733-
            9399(1990)116:5(983)`.

[Weh06]   M. Wehnert: *Ein Beitrag zur drainierten und undrainierten
            Analyse in der Geotechnik.* PhD thesis, Universität Stuttgart,
            Stuttgart, 2006.

[WNT09]   T. Wichtmann, A. Niemunis, and T. Triantafyllidis: Valida-
            tion and calibration of a high-cycle accumulation model based
            on cyclic triaxial tests on eight sands. *Soils and Foundations*,
            49(5):711–728, 2009.

[Wic05]   T. Wichtmann: *Explizites Akkumulationsmodell für nichtbin-
            dige Böden unter zyklischer Belastung – Explicit accumulation
            model for non-cohesive soils under cyclic loading.* PhD thesis,
            Ruhr-Universität Bochum, Bochum, 2005.

[WA86]   R. K. S. Wong and J. R. F. Arthur: Sand sheared by stresses
            with cyclic variations in direction. *Géotechnique*, 36(2):215–
            226, 1986. DOI: `10.1680/geot.1986.36.2.215`.

[YI79]   Y. Yamada and K. Ishihara: Anisotropic deforamtion charac-
            teristics of sand under three dimensional stress conditions.
            Soils and Foundations, 19(2):79–94, 1979.

[YBL96]   J. A. Yamamuro, P. A. Bopp, and P. V. Lade: One-dimensional compression of sands at high pressures. *Journal of Geotechnical Engineering*, 122(2):147–154, 1996. DOI: `10.1061/(ASCE)0733-9410(1996)122:2(147)`.

[YDH85]   B.-L. Yang, Y. F. Dafalias, and L. R. Herrmann: A bounding surface plasticity model for concrete. *Journal of Engineering Mechanics*, 111(3):359–380, 1985. DOI: `10.1061/(ASCE)0733-9399(1985)111:3(359)`.

[YHD$^+$16]   Z.-Y. Yin, P.-Y. Hicher, C. Dano, and Y.-F. Jin: Modeling mechanical behavior of very coarse granular materials. *Journal of Engineering Mechanics*:C4016006, 2016. DOI: `10.1061/(ASCE)EM.1943-7889.0001059`.

[YIV98]   M. Yoshimine, K. Ishihara, and W. Vargas: Effects of principal stress direction and intermediate principal stress of undrained shear behavior of sand. *Soils and Foundations*, 38(3):179–188, 1998.

[You72]   T. L. Youd: Compaction of sands by repeated shear straining. *Journal of the Soil Mechanics and Foundations Division*, 98(SM 7):709–725, 1972.

[ZJ97]   L. Zdravkovic and R. J. Jardine: Some anisotropic stiffness characteristics of a silt under general stress conditions. *Géotechnique*, 47(3):407–437, 1997. DOI: `10.1680/geot.1997.47.3.407`.

[ZJY10]   F. Zhang, Y. Jin, and B. Ye: A try to give a unified description of Toyoura sand. *Soils and Foundations*, 50(5):679–693, 2010.

[Zie59]   H. Ziegler: A modification of Prager's hardening rule. *Quarterly of Applied Mathematics*, 17(1):55–65, 1959. DOI: `10.1090/qam/104405`.

[ZI97]   S. Zlatovic and K. Ishihara: Normalized behavior of very loose non-plastic soils – Effects of fabric. *Soils and Foundations*, 37(4):47–56, 1997.

Appendices

The appendix serves as a collection of information, which is not primarily important for a comprehensive reading of this thesis. The first chapter contains additional information on the mathematical background of the model: a compilation of all major constitutive equations as well as derivations of mathematical expressions and correlations used in the model formulation. The second chapter gives a more detailed view on the particle swarm optimisation method, which has been implemented for the parameter calibration subroutine. Finally, supplementary simulation results, which would go beyond the scope of the principal part of this work with respect to a useful and informative visualisation of computational outcomes, are outsourced to the third chapter.

A Mathematical background

A.1 Fundamental equations of elastoplasticity

Consistency condition:

$$\dot{f} = \frac{\partial f}{\partial \boldsymbol{\sigma}} \cdot \dot{\boldsymbol{\sigma}} + \frac{\partial f}{\partial \boldsymbol{\kappa}} \cdot \dot{\boldsymbol{\kappa}} = 0 \tag{A.1}$$

with the rate of stress $\dot{\boldsymbol{\sigma}}$ and the incremental change in hardening variable(s) $\dot{\boldsymbol{\kappa}}$

Decomposition of strain rate:

$$\dot{\boldsymbol{\varepsilon}} = \dot{\boldsymbol{\varepsilon}}^{el} + \dot{\boldsymbol{\varepsilon}}^{pl} \tag{A.2}$$

Flow rule:

$$\dot{\boldsymbol{\varepsilon}}^{pl} = \lambda \frac{\partial g}{\partial \boldsymbol{\sigma}} \tag{A.3}$$

with the gradient of the plastic potential $\frac{\partial g}{\partial \boldsymbol{\sigma}}$ defining the direction of plastic straining and the plastic multiplier λ scaling the magnitude of strains

Hardening rule:

$$\dot{\boldsymbol{\kappa}} = H \dot{\boldsymbol{\varepsilon}}^{pl} \tag{A.4}$$

Stress-strain relation:

$$\dot{\boldsymbol{\sigma}} = \boldsymbol{D}^{ep} \cdot \dot{\boldsymbol{\varepsilon}} = \boldsymbol{D}^{el} \cdot \dot{\boldsymbol{\varepsilon}}^{el} = \boldsymbol{D}^{el} \cdot \left(\dot{\boldsymbol{\varepsilon}} - \lambda \frac{\partial g}{\partial \boldsymbol{\sigma}} \right) \tag{A.5}$$

Based on the consistency condition and with respect to flow rule and hardening rule, the plastic multiplier for an incremental elastoplastic loading step can be derived.

$$\dot{f} = \frac{\partial f}{\partial \boldsymbol{\sigma}} \cdot \dot{\boldsymbol{\sigma}} + \frac{\partial f}{\partial \boldsymbol{\kappa}} \cdot H \dot{\boldsymbol{\varepsilon}}^{pl} = \frac{\partial f}{\partial \boldsymbol{\sigma}} \cdot \boldsymbol{D}^{el} \cdot \left(\dot{\boldsymbol{\varepsilon}} - \lambda \frac{\partial g}{\partial \boldsymbol{\sigma}} \right) + \frac{\partial f}{\partial \boldsymbol{\kappa}} \cdot H \lambda \frac{\partial g}{\partial \boldsymbol{\sigma}} = 0 \tag{A.6}$$

$$\rightarrow \quad \lambda = \frac{\frac{\partial f}{\partial \boldsymbol{\sigma}} \cdot \dot{\boldsymbol{\sigma}}}{-\frac{\partial f}{\partial \boldsymbol{\kappa}} \cdot H \frac{\partial g}{\partial \boldsymbol{\sigma}}} = \frac{\frac{\partial f}{\partial \boldsymbol{\sigma}} \cdot \dot{\boldsymbol{\sigma}}}{K_p} = \frac{\frac{\partial f}{\partial \boldsymbol{\sigma}} \cdot \boldsymbol{D}^{el} \cdot \dot{\boldsymbol{\varepsilon}}}{\frac{\partial f}{\partial \boldsymbol{\sigma}} \cdot \boldsymbol{D}^{el} \cdot \frac{\partial g}{\partial \boldsymbol{\sigma}} - \frac{\partial f}{\partial \boldsymbol{\kappa}} \cdot H \frac{\partial g}{\partial \boldsymbol{\sigma}}} \tag{A.7}$$

$$\text{with } K_p = -\frac{\partial f}{\partial \boldsymbol{\kappa}} \cdot H \frac{\partial g}{\partial \boldsymbol{\sigma}} \text{ being the plastic modulus}$$

Consequently, the elastoplastic stiffness matrix $\boldsymbol{D}^{ep}$ in Eq. (A.5) can be expressed as

$$\boldsymbol{D}^{ep} = \boldsymbol{D}^{el} - \frac{\boldsymbol{D}^{el} \cdot \frac{\partial g}{\partial \boldsymbol{\sigma}} \otimes \frac{\partial f}{\partial \boldsymbol{\sigma}} \cdot \boldsymbol{D}^{el}}{\frac{\partial f}{\partial \boldsymbol{\sigma}} \cdot \boldsymbol{D}^{el} \cdot \frac{\partial g}{\partial \boldsymbol{\sigma}} - \frac{\partial f}{\partial \boldsymbol{\kappa}} \cdot H \frac{\partial g}{\partial \boldsymbol{\sigma}}} \tag{A.8}$$

Finally, based on the applied strain increment $\dot{\boldsymbol{\varepsilon}}$ and the elastoplastic stiffness matrix $\boldsymbol{D}^{ep}$ (Eq. (A.8)), the stress increment $\dot{\boldsymbol{\sigma}}$ can be calculated according to Eq. (A.5) and the corresponding change in hardening variables $\dot{\boldsymbol{\kappa}}$ results from Eqs. (A.3), (A.4) and (A.7):

$$\dot{\boldsymbol{\kappa}} = H \cdot \lambda \frac{\partial g}{\partial \boldsymbol{\sigma}} = H \cdot \frac{\frac{\partial f}{\partial \boldsymbol{\sigma}} \cdot \boldsymbol{D}^{el} \cdot \frac{\partial g}{\partial \boldsymbol{\sigma}}}{\frac{\partial f}{\partial \boldsymbol{\sigma}} \cdot \boldsymbol{D}^{el} \cdot \frac{\partial g}{\partial \boldsymbol{\sigma}} - \frac{\partial f}{\partial \boldsymbol{\kappa}} \cdot H \frac{\partial g}{\partial \boldsymbol{\sigma}}} \cdot \dot{\boldsymbol{\varepsilon}} = \boldsymbol{H}^{ep} \cdot \dot{\boldsymbol{\varepsilon}} \tag{A.9}$$

A.2 Compilation of major constitutive equations (multiaxial formulation)

STATE

Void ratio increment:

$$\dot{e} = (1 + e_0) \cdot \dot{\varepsilon}_p$$

State parameter:

$$\psi = e - e_{cs}$$

Critical state line:

$$e_{cs} = e_{cs0} - \lambda \left(\frac{p}{p_{at}} \right)^{\xi}$$

ELASTICITY

Elastic strain increment:

$$\dot{\boldsymbol{\varepsilon}}^{el} = \frac{\dot{\boldsymbol{s}}}{2G} + \frac{1}{3} \frac{\dot{p}}{K} \boldsymbol{I}$$

Elastic stiffnesses:

$$G = G_0^{ref} \cdot \frac{(2.17 - e)^2}{1 + e} \cdot \left(\frac{p}{p_{ref}} \right)^m$$

$$K = \frac{2(1 + \nu)}{3(1 - 2\nu)} G$$

$$E = 2(1 + \nu) G$$

CONE

Yield surface:

$$f^{cone} = \sqrt{(\boldsymbol{s} - p\boldsymbol{\alpha}) \cdot (\boldsymbol{s} - p\boldsymbol{\alpha})} - \sqrt{\frac{2}{3}} m_{cone} \cdot p = 0$$

$$\frac{\partial f^{cone}}{\partial \boldsymbol{s}} = \frac{\boldsymbol{s} - p\boldsymbol{\alpha}}{\sqrt{(\boldsymbol{s} - p\boldsymbol{\alpha}) \cdot (\boldsymbol{s} - p\boldsymbol{\alpha})}} = \boldsymbol{n} \qquad \frac{\partial f^{cone}}{\partial p} = -\boldsymbol{\alpha} \cdot \boldsymbol{n} - \sqrt{\frac{2}{3}} m_{cone}$$

$$\frac{\partial f^{cone}}{\partial \boldsymbol{\alpha}} = -p \cdot \boldsymbol{n}$$

Flow rule:

$$\dot{\boldsymbol{\varepsilon}}^{pl} = \lambda \left(\frac{\partial g^{cone}}{\partial \boldsymbol{s}} + \frac{1}{3} \frac{\partial g^{cone}}{\partial p} \boldsymbol{I} \right) = \lambda \left(\frac{\partial f^{cone}}{\partial \boldsymbol{s}} + \frac{1}{3} \frac{\partial g^{cone}}{\partial p} \boldsymbol{I} \right)$$

$$= \lambda \left(\boldsymbol{n} + \frac{1}{3} D \boldsymbol{I} \right)$$

$$D = A_d \left(\boldsymbol{\alpha^d} - \boldsymbol{r} \right) \cdot \boldsymbol{n} = A_d \cdot d^d$$

$$\boldsymbol{\alpha^d} = \sqrt{\frac{2}{3}} \cdot g(\theta, c) \cdot M_c^d \cdot \boldsymbol{n}$$

$$g(c, \theta) = \frac{\cos \gamma}{\cos \left(\frac{1}{3} \arccos (\cos 3\gamma \cdot \cos 3\theta) \right)} \quad \text{with} \quad \gamma = \frac{\pi}{3} + \arctan \left(\frac{1 - 2c}{\sqrt{3}} \right)$$

$$M_c^d = \frac{6 f_{sd} \sin \varphi_{cs}}{3 - f_{sd} \sin \varphi_{cs}} \quad \text{with} \quad f_{sd} = \exp(m_d \cdot \text{sgn} \, \psi \cdot \sqrt{|\psi|})$$

$$A_d = A_0 \cdot f_{fab}$$

$$\text{with} \quad f_{fab} = 1 + \langle \boldsymbol{f} \cdot \boldsymbol{n} \rangle \qquad \dot{\boldsymbol{f}} = \begin{cases} -F_f \cdot |\text{d}W_i| \cdot (C_f \boldsymbol{n} + \boldsymbol{f}) & \text{for } D < 0 \\ 0 & \text{for } D \geq 0 \end{cases}$$

Hardening rule:

$$\dot{\boldsymbol{\alpha}} = \lambda \cdot H^{cone} \cdot \frac{\partial g^{cone}}{\partial \boldsymbol{s}} = \lambda \cdot H^{cone} \cdot \frac{\partial f^{cone}}{\partial \boldsymbol{s}} = \lambda \cdot H^{cone} \cdot \boldsymbol{n}$$

$$H^{cone} = H_0^{cone} \cdot h_{ss} \cdot h_{fab} \cdot h_{min}$$

$$H_0^{cone} = h \cdot \left(\boldsymbol{\alpha^b} - \boldsymbol{r} \right) \cdot \boldsymbol{n} = h \cdot d^b$$

$$\boldsymbol{\alpha^b} = \sqrt{\frac{2}{3}} \cdot g(\theta,c) \cdot M_c^b \cdot \boldsymbol{n}$$

$$M_c^b = \exp(m_b \cdot \langle -\psi \rangle) \cdot M_c^c$$

$$h = h_0 \cdot \sqrt{\frac{|d^b|}{d_{ref}^b - |d^b|}} \cdot \exp(3(1-e)) \cdot \sqrt{\frac{p_{at}}{p}} \qquad d_{ref}^b = \sqrt{\frac{2}{3}} \left(M_c^b + M_e^b \right)$$

SC: $h_{ss} = 1 + (m_R - 1) \left(1 - \min \left(\frac{\Delta \eta^{SR}}{\eta_{lim}}, 1 \right) \right)^{\zeta}$ with $\eta_{lim} \approx G_{SR} \frac{\gamma_{lim}}{p_{SR}}$

$$h_{fab} = 1 + \langle f_p \rangle^a \quad \text{with} \quad \dot{f}_p = N_f \cdot \mathrm{d}W_i$$

$$h_{min} = 1 + 100 \cdot \left(\frac{e_{cs} - e}{e_{cs} - e_{min}} \right)^{100b} \quad \text{with} \quad e_{min} = e_{min0} - \lambda \left(\frac{p}{p_{at}} \right)^{\xi}$$

CAP

Yield surface:

$$f^{cap} = \frac{3}{2} \frac{\boldsymbol{s} \cdot \boldsymbol{s}}{M_{cap}^2} + p^2 - p_c^2 = 0$$

$$\frac{\partial f^{cap}}{\partial \boldsymbol{s}} = \frac{3\boldsymbol{s}}{M_{cap}^2} \qquad \frac{\partial f^{cap}}{\partial p} = 2p \qquad \frac{\partial f^{cap}}{\partial p_c} = -2p_c$$

Flow rule:

$$\dot{\boldsymbol{\varepsilon}}^{pl} = \lambda \left(\frac{\partial g^{cap}}{\partial \boldsymbol{s}} + \frac{1}{3} \frac{\partial g^{cap}}{\partial p} \boldsymbol{I} \right) = \lambda \left(\frac{\partial f^{cap}}{\partial \boldsymbol{s}} + \frac{1}{3} \frac{\partial f^{cap}}{\partial p} \boldsymbol{I} \right)$$

$$= \lambda \left(\frac{3\boldsymbol{s}}{M_{cap}^2} + \frac{1}{3} \cdot 2p \cdot \boldsymbol{I} \right)$$

Hardening rule:

$$\dot{p}_c = \lambda \cdot H^{cap} \cdot \frac{\partial g^{cap}}{\partial p} = \lambda \cdot H^{cap} \cdot \frac{\partial f^{cap}}{\partial p} = \lambda \cdot H^{cap} \cdot 2p$$

$$H^{cap} = H_0^{cap} \cdot h\left(\dot{\eta}, \dot{\varepsilon}_p, \dot{\varepsilon}_q\right)$$

$$H_0^{cap} = \frac{\sqrt{\left(\frac{1-K_0}{M_{cap}}\right)^2 + \left(\frac{1+2K_0}{3}\right)^2} \cdot E_{oed} \cdot E}{E - (1+2K_0)(1-2\nu) \cdot E_{oed}}$$

$$h\left(\dot{\eta}, \dot{\varepsilon}_p, \dot{\varepsilon}_q\right) = C^{\alpha \cdot (\beta + \gamma)}$$

$$\alpha = 1 - \exp(-V\,|\dot{\eta}|) \qquad \beta = 1 - \exp\left(-V\left|\Delta\frac{\dot{\varepsilon}_p}{\dot{\varepsilon}_q + a}\right|\right) \qquad \gamma = \exp(-V\,|\dot{\varepsilon}_p|)$$

$$E_{oed} = E_{oed}^{ref} \cdot \left(\frac{e}{e+1}\right)^{-n_{oed}} \cdot \left(\frac{\sigma_1'}{p^{ref}}\right)^{m_{oed}}$$

$$M_{cap} = \frac{3}{\sqrt{2}}\sqrt{\frac{(E - E_{oed} \cdot (1+2K_0) \cdot (1-2\nu)) \cdot (1-K_0)}{(E - E_{oed} \cdot (1-K_0) \cdot (1+\nu)) \cdot (1+2K_0)}}$$

A.3   Elastoplastic stiffness matrix for singular yield surfaces

The stress-strain relation according to Eq. (A.5) requires the determination of an elastoplastic stiffness matrix $\boldsymbol{D^{ep}}$. The usual case of a single yield surface $\boldsymbol{D^{ep}}$ can be calculated according to Eq. (A.8). However, it takes a particular form if two yield surfaces are active simultaneously. The numerical treatment of this special case has been investigated by de Borst [dBor87] and the derivation of $\boldsymbol{D^{ep}}$ is summarised in the following.

Based on Koiter's rule (Eq. (4.3)), the consistency conditions for the two intersecting yield surfaces according to Eq. (A.1) can be reformulated:

$$\begin{cases} \dot{f}_1 = \dfrac{\partial f_1}{\partial \boldsymbol{\sigma}} \cdot \dot{\boldsymbol{\sigma}} + \dfrac{\partial f_1}{\partial \boldsymbol{\kappa}} \cdot \dfrac{\partial \boldsymbol{\kappa}}{\partial \boldsymbol{\varepsilon^{pl}}} \cdot \left(\lambda_1 \dfrac{\partial g_1}{\partial \boldsymbol{\sigma}} + \lambda_2 \dfrac{\partial g_2}{\partial \boldsymbol{\sigma}}\right) = 0 \\[3mm] \dot{f}_2 = \dfrac{\partial f_2}{\partial \boldsymbol{\sigma}} \cdot \dot{\boldsymbol{\sigma}} + \dfrac{\partial f_2}{\partial \boldsymbol{\kappa}} \cdot \dfrac{\partial \boldsymbol{\kappa}}{\partial \boldsymbol{\varepsilon^{pl}}} \cdot \left(\lambda_1 \dfrac{\partial g_1}{\partial \boldsymbol{\sigma}} + \lambda_2 \dfrac{\partial g_2}{\partial \boldsymbol{\sigma}}\right) = 0 \end{cases} \tag{A.10}$$

$$\text{with} \quad \dot{\boldsymbol{\kappa}} = \frac{\partial \boldsymbol{\kappa}}{\partial \boldsymbol{\varepsilon^{pl}}} \cdot \dot{\boldsymbol{\varepsilon}}^{pl} = H\dot{\boldsymbol{\varepsilon}}^{pl}$$

Substituting Eq. (4.4) for $\dot{\boldsymbol{\sigma}}$ and reorganising Eq. (A.10) gives

$$\begin{cases} \dfrac{\partial f_1}{\partial \boldsymbol{\sigma}} \cdot \boldsymbol{D^{el}} \cdot \dot{\boldsymbol{\varepsilon}} = \mu_1 \lambda_1 + \mu_2 \lambda_2 \\[3mm] \dfrac{\partial f_2}{\partial \boldsymbol{\sigma}} \cdot \boldsymbol{D^{el}} \cdot \dot{\boldsymbol{\varepsilon}} = \mu_3 \lambda_1 + \mu_4 \lambda_2 \end{cases} \tag{A.11}$$

with μ_1 to μ_4 being defined as

$$\mu_1 = \left(-\frac{\partial f_1}{\partial \boldsymbol{\kappa}} \cdot \frac{\partial \boldsymbol{\kappa}}{\partial \boldsymbol{\varepsilon}^{pl}} + \boldsymbol{D}^{el} \cdot \frac{\partial f_1}{\partial \boldsymbol{\sigma}} \right) \cdot \frac{\partial g_1}{\partial \boldsymbol{\sigma}} \tag{A.12}$$

$$\mu_2 = \left(-\frac{\partial f_1}{\partial \boldsymbol{\kappa}} \cdot \frac{\partial \boldsymbol{\kappa}}{\partial \boldsymbol{\varepsilon}^{pl}} + \boldsymbol{D}^{el} \cdot \frac{\partial f_1}{\partial \boldsymbol{\sigma}} \right) \cdot \frac{\partial g_2}{\partial \boldsymbol{\sigma}} \tag{A.13}$$

$$\mu_3 = \left(-\frac{\partial f_2}{\partial \boldsymbol{\kappa}} \cdot \frac{\partial \boldsymbol{\kappa}}{\partial \boldsymbol{\varepsilon}^{pl}} + \boldsymbol{D}^{el} \cdot \frac{\partial f_2}{\partial \boldsymbol{\sigma}} \right) \cdot \frac{\partial g_1}{\partial \boldsymbol{\sigma}} \tag{A.14}$$

$$\mu_4 = \left(-\frac{\partial f_2}{\partial \boldsymbol{\kappa}} \cdot \frac{\partial \boldsymbol{\kappa}}{\partial \boldsymbol{\varepsilon}^{pl}} + \boldsymbol{D}^{el} \cdot \frac{\partial f_2}{\partial \boldsymbol{\sigma}} \right) \cdot \frac{\partial g_2}{\partial \boldsymbol{\sigma}} \tag{A.15}$$

REMARK: If the hardening parameters are clearly associated to only one of the two surfaces, the "mixed" contributions $-\frac{\partial f_1}{\partial \boldsymbol{\kappa}} \cdot \frac{\partial \boldsymbol{\kappa}}{\partial \boldsymbol{\varepsilon}^{pl}} \cdot \frac{\partial g_2}{\partial \boldsymbol{\sigma}}$ in μ_2 and $-\frac{\partial f_2}{\partial \boldsymbol{\kappa}} \cdot \frac{\partial \boldsymbol{\kappa}}{\partial \boldsymbol{\varepsilon}^{pl}} \cdot \frac{\partial g_1}{\partial \boldsymbol{\sigma}}$ in μ_3 vanish, since $\boldsymbol{\kappa}$ refers to the corresponding plastic potential and hence $\frac{\partial f_1}{\partial \kappa_2} = \frac{\partial f_2}{\partial \kappa_1} = 0$.

The system of Eqs. (A.11) can be solved for λ_1 and λ_2 :

$$\lambda_1 = \frac{\mu_4 \frac{\partial f_1}{\partial \boldsymbol{\sigma}} \cdot \boldsymbol{D}^{el} \cdot \dot{\boldsymbol{\varepsilon}} - \mu_2 \frac{\partial f_2}{\partial \boldsymbol{\sigma}} \cdot \boldsymbol{D}^{el} \cdot \dot{\boldsymbol{\varepsilon}}}{\mu_1 \mu_4 - \mu_2 \mu_3} \tag{A.16}$$

$$\lambda_2 = \frac{\mu_1 \frac{\partial f_2}{\partial \boldsymbol{\sigma}} \cdot \boldsymbol{D}^{el} \cdot \dot{\boldsymbol{\varepsilon}} - \mu_3 \frac{\partial f_1}{\partial \boldsymbol{\sigma}} \cdot \boldsymbol{D}^{el} \cdot \dot{\boldsymbol{\varepsilon}}}{\mu_1 \mu_4 - \mu_2 \mu_3} \tag{A.17}$$

Finally, the elastoplastic stiffness matrix $\boldsymbol{D}^{ep}$ for two intersecting yield surfaces can be determined according to

$$
\begin{aligned}
\boldsymbol{D}^{ep} = \boldsymbol{D}^{el} &- \frac{\boldsymbol{D}^{el} \cdot \left(\mu_1 \frac{\partial g_2}{\partial \boldsymbol{\sigma}} \cdot \frac{\partial f_2}{\partial \boldsymbol{\sigma}} + \mu_4 \frac{\partial g_1}{\partial \boldsymbol{\sigma}} \cdot \frac{\partial f_1}{\partial \boldsymbol{\sigma}} \right) \cdot \boldsymbol{D}^{el}}{\mu_1 \mu_4 - \mu_2 \mu_3} \\
&+ \frac{\boldsymbol{D}^{el} \cdot \left(\mu_2 \frac{\partial g_1}{\partial \boldsymbol{\sigma}} \cdot \frac{\partial f_2}{\partial \boldsymbol{\sigma}} + \mu_3 \frac{\partial g_2}{\partial \boldsymbol{\sigma}} \cdot \frac{\partial f_1}{\partial \boldsymbol{\sigma}} \right) \cdot \boldsymbol{D}^{el}}{\mu_1 \mu_4 - \mu_2 \mu_3}
\end{aligned}
\tag{A.18}
$$

In analogy to Eq. (A.9) the change in hardening variables can be determined from the total strain rate via the elastoplastic hardening matrix $\boldsymbol{H}^{ep}$. Assuming the hardening variables are each clearly associated to one of the two active surfaces, their increment can be derived by

$$
\begin{cases}
\dot{\kappa}_1 = H_1 \cdot \lambda_1 \dfrac{\partial g_1}{\partial \boldsymbol{\sigma}} = H_1 \cdot \dfrac{\left(\mu_4 \frac{\partial f_1}{\partial \boldsymbol{\sigma}} - \mu_2 \frac{\partial f_2}{\partial \boldsymbol{\sigma}} \right) \cdot \boldsymbol{D}^{el} \cdot \frac{\partial g_1}{\partial \boldsymbol{\sigma}}}{\mu_1 \mu_4 - \mu_2 \mu_3} \cdot \dot{\boldsymbol{\varepsilon}} = \boldsymbol{H}_1^{ep} \cdot \dot{\boldsymbol{\varepsilon}} \\[4mm]
\dot{\kappa}_2 = H_2 \cdot \lambda_2 \dfrac{\partial g_2}{\partial \boldsymbol{\sigma}} = H_2 \cdot \dfrac{\left(\mu_1 \frac{\partial f_2}{\partial \boldsymbol{\sigma}} - \mu_3 \frac{\partial f_1}{\partial \boldsymbol{\sigma}} \right) \cdot \boldsymbol{D}^{el} \cdot \frac{\partial g_2}{\partial \boldsymbol{\sigma}}}{\mu_1 \mu_4 - \mu_2 \mu_3} \cdot \dot{\boldsymbol{\varepsilon}} = \boldsymbol{H}_2^{ep} \cdot \dot{\boldsymbol{\varepsilon}}
\end{cases}
\tag{A.19}
$$

A.4 Coefficient matrices S and E for loading constraints

The numerical integration technique according to Bardet and Choucair [BC91] requires the definition of the constraint matrices S and E, which contain the stress and strain dependent loading conditions respectively, and the loading vector $\dot{V}$. Since the Voigt notation is applied, $\dot{V}$ reduces to 6 elements and the two matrices to dimensions 6×6. Equation (4.1) results in:

$$
\underbrace{\begin{bmatrix} \cdots & \cdots & \cdots & \cdots & \cdots & \cdots \\ \cdots & \cdots & \cdots & \cdots & \cdots & \cdots \\ \cdots & \cdots & \cdots & \cdots & \cdots & \cdots \\ \cdots & \cdots & \cdots & \cdots & \cdots & \cdots \\ \cdots & \cdots & \cdots & \cdots & \cdots & \cdots \\ \cdots & \cdots & \cdots & \cdots & \cdots & \cdots \end{bmatrix}}_{S} \underbrace{\begin{bmatrix} \dot{\sigma}_1 \\ \dot{\sigma}_2 \\ \dot{\sigma}_3 \\ \dot{\sigma}_4 \\ \dot{\sigma}_5 \\ \dot{\sigma}_6 \end{bmatrix}}_{\dot{\sigma}} + \underbrace{\begin{bmatrix} \cdots & \cdots & \cdots & \cdots & \cdots & \cdots \\ \cdots & \cdots & \cdots & \cdots & \cdots & \cdots \\ \cdots & \cdots & \cdots & \cdots & \cdots & \cdots \\ \cdots & \cdots & \cdots & \cdots & \cdots & \cdots \\ \cdots & \cdots & \cdots & \cdots & \cdots & \cdots \\ \cdots & \cdots & \cdots & \cdots & \cdots & \cdots \end{bmatrix}}_{E} \underbrace{\begin{bmatrix} \dot{\varepsilon}_1 \\ \dot{\varepsilon}_2 \\ \dot{\varepsilon}_3 \\ \dot{\varepsilon}_4 \\ \dot{\varepsilon}_5 \\ \dot{\varepsilon}_6 \end{bmatrix}}_{\dot{\varepsilon}} = \underbrace{\begin{bmatrix} 0 \\ 0 \\ 0 \\ 0 \\ 0 \\ \dot{x} \end{bmatrix}}_{\dot{V}}
$$

$$\text{(A.20)}$$

$\dot{x}$ in the loading vector $\dot{V}$ corresponds to the actual load increment (in terms of stress or strain). Matrices S and E need to be filled accordingly so that Eq. (A.20) describes the loading conditions correctly. Giving a simple example, Eq. (A.20) for a **stress controlled drained triaxial compression test** is constructed as follows:

$$
\underbrace{\begin{bmatrix} 1 & 0 & 0 & 0 & 0 & 0 \\ 0 & 1 & 0 & 0 & 0 & 0 \\ 0 & 0 & 0 & 1 & 0 & 0 \\ 0 & 0 & 0 & 0 & 1 & 0 \\ 0 & 0 & 0 & 0 & 0 & 1 \\ 0 & 0 & 1 & 0 & 0 & 0 \end{bmatrix}}_{S} \underbrace{\begin{bmatrix} \dot{\sigma}_1 \\ \dot{\sigma}_2 \\ \dot{\sigma}_3 \\ \dot{\sigma}_4 \\ \dot{\sigma}_5 \\ \dot{\sigma}_6 \end{bmatrix}}_{\dot{\sigma}} + \underbrace{\begin{bmatrix} 0 & 0 & 0 & 0 & 0 & 0 \\ 0 & 0 & 0 & 0 & 0 & 0 \\ 0 & 0 & 0 & 0 & 0 & 0 \\ 0 & 0 & 0 & 0 & 0 & 0 \\ 0 & 0 & 0 & 0 & 0 & 0 \\ 0 & 0 & 0 & 0 & 0 & 0 \end{bmatrix}}_{E} \underbrace{\begin{bmatrix} \dot{\varepsilon}_1 \\ \dot{\varepsilon}_2 \\ \dot{\varepsilon}_3 \\ \dot{\varepsilon}_4 \\ \dot{\varepsilon}_5 \\ \dot{\varepsilon}_6 \end{bmatrix}}_{\dot{\varepsilon}} = \underbrace{\begin{bmatrix} 0 \\ 0 \\ 0 \\ 0 \\ 0 \\ \Delta\sigma \end{bmatrix}}_{\dot{V}}
$$

$$\text{(A.21)}$$

CAUTION: The vertical loading direction is defined along the 3-axis!

In case of **strain controlled undrained triaxial compression** the S and E matrices need to be adapted to the fact that the total volume remains constant, hence $\dot{\varepsilon}_v = \dot{\varepsilon}_1 + \dot{\varepsilon}_2 + \dot{\varepsilon}_3 = 0$. In addition, the lateral strains are of equal size and consequently $\dot{\varepsilon}_1 = \dot{\varepsilon}_2 = -0.5\dot{\varepsilon}_3$. This results in the following

lookout of Eq. (A.20):

$$
\begin{bmatrix} 0 & 0 & 0 & 0 & 0 & 0 \\ 0 & 0 & 0 & 0 & 0 & 0 \\ 0 & 0 & 0 & 0 & 0 & 0 \\ 0 & 0 & 0 & 0 & 0 & 0 \\ 0 & 0 & 0 & 0 & 0 & 0 \\ 0 & 0 & 0 & 0 & 0 & 0 \end{bmatrix}
\begin{bmatrix} \dot{\sigma}_1 \\ \dot{\sigma}_2 \\ \dot{\sigma}_3 \\ \dot{\sigma}_4 \\ \dot{\sigma}_5 \\ \dot{\sigma}_6 \end{bmatrix}
+
\begin{bmatrix} 1 & 0 & 0.5 & 0 & 0 & 0 \\ 0 & 1 & 0.5 & 0 & 0 & 0 \\ 0 & 0 & 0 & 1 & 0 & 0 \\ 0 & 0 & 0 & 0 & 1 & 0 \\ 0 & 0 & 0 & 0 & 0 & 1 \\ 0 & 0 & 1 & 0 & 0 & 0 \end{bmatrix}
\begin{bmatrix} \dot{\varepsilon}_1 \\ \dot{\varepsilon}_2 \\ \dot{\varepsilon}_3 \\ \dot{\varepsilon}_4 \\ \dot{\varepsilon}_5 \\ \dot{\varepsilon}_6 \end{bmatrix}
=
\begin{bmatrix} 0 \\ 0 \\ 0 \\ 0 \\ 0 \\ \Delta\varepsilon \end{bmatrix}
$$

$$
\boldsymbol{S} \qquad\quad \dot{\boldsymbol{\sigma}} \quad + \qquad\qquad \boldsymbol{E} \qquad\qquad \dot{\boldsymbol{\varepsilon}} \quad = \quad \dot{\boldsymbol{V}}
$$

$$\text{(A.22)}$$

Analogously, the constraint matrices can be set up for many other loading cases, including so called mixed control conditions with both stress and strain constraints. In the following, $\boldsymbol{S}$ and $\boldsymbol{E}$ are given for all implemented test conditions.

mixed control
drained triaxial
compression

$$
\boldsymbol{S} =
\begin{bmatrix} 1 & 0 & 0 & 0 & 0 & 0 \\ 0 & 1 & 0 & 0 & 0 & 0 \\ 0 & 0 & 0 & 0 & 0 & 0 \\ 0 & 0 & 0 & 1 & 0 & 0 \\ 0 & 0 & 0 & 0 & 1 & 0 \\ 0 & 0 & 0 & 0 & 0 & 0 \end{bmatrix}
\qquad
\boldsymbol{E} =
\begin{bmatrix} 0 & 0 & 0 & 0 & 0 & 0 \\ 0 & 0 & 0 & 0 & 0 & 0 \\ 0 & 0 & 0 & 0 & 0 & 0 \\ 0 & 0 & 0 & 0 & 0 & 0 \\ 0 & 0 & 0 & 0 & 0 & 0 \\ 0 & 0 & 1 & 0 & 0 & 0 \end{bmatrix}
$$

$$\text{(A.23)}$$

strain controlled
1D compression

$$
\boldsymbol{S} =
\begin{bmatrix} 0 & 0 & 0 & 0 & 0 & 0 \\ 0 & 0 & 0 & 0 & 0 & 0 \\ 0 & 0 & 0 & 0 & 0 & 0 \\ 0 & 0 & 0 & 0 & 0 & 0 \\ 0 & 0 & 0 & 0 & 0 & 0 \\ 0 & 0 & 0 & 0 & 0 & 0 \end{bmatrix}
\qquad
\boldsymbol{E} =
\begin{bmatrix} 1 & 0 & 0 & 0 & 0 & 0 \\ 0 & 1 & 0 & 0 & 0 & 0 \\ 0 & 0 & 0 & 1 & 0 & 0 \\ 0 & 0 & 0 & 0 & 1 & 0 \\ 0 & 0 & 0 & 0 & 0 & 1 \\ 0 & 0 & 1 & 0 & 0 & 0 \end{bmatrix}
$$

$$\text{(A.24)}$$

mixed control
1D compression

$$
\boldsymbol{S} =
\begin{bmatrix} 0 & 0 & 0 & 0 & 0 & 0 \\ 0 & 0 & 0 & 0 & 0 & 0 \\ 0 & 0 & 0 & 0 & 0 & 0 \\ 0 & 0 & 0 & 0 & 0 & 0 \\ 0 & 0 & 0 & 0 & 0 & 0 \\ 0 & 0 & 1 & 0 & 0 & 0 \end{bmatrix}
\qquad
\boldsymbol{E} =
\begin{bmatrix} 1 & 0 & 0 & 0 & 0 & 0 \\ 0 & 1 & 0 & 0 & 0 & 0 \\ 0 & 0 & 0 & 0 & 0 & 0 \\ 0 & 0 & 0 & 1 & 0 & 0 \\ 0 & 0 & 0 & 0 & 1 & 0 \\ 0 & 0 & 0 & 0 & 0 & 0 \end{bmatrix}
$$

$$\text{(A.25)}$$

stress controlled
isotropic
compression
(*exchange* $\boldsymbol{S}$ *and*
$\boldsymbol{E}$ *for strain*
control)

$$
\boldsymbol{S} = \begin{bmatrix} 1 & 0 & -1 & 0 & 0 & 0 \\ 0 & 1 & -1 & 0 & 0 & 0 \\ 0 & 0 & 0 & 1 & 0 & 0 \\ 0 & 0 & 0 & 0 & 1 & 0 \\ 0 & 0 & 0 & 0 & 0 & 1 \\ 0 & 0 & 1 & 0 & 0 & 0 \end{bmatrix} \qquad \boldsymbol{E} = \begin{bmatrix} 0 & 0 & 0 & 0 & 0 & 0 \\ 0 & 0 & 0 & 0 & 0 & 0 \\ 0 & 0 & 0 & 0 & 0 & 0 \\ 0 & 0 & 0 & 0 & 0 & 0 \\ 0 & 0 & 0 & 0 & 0 & 0 \\ 0 & 0 & 0 & 0 & 0 & 0 \end{bmatrix}
$$

(A.26)

stress controlled
compression
with arbitrary
constant stress
path inclination
($\tan\alpha = \frac{\dot{q}}{\dot{p}}$)

$$
\boldsymbol{S} = \begin{bmatrix} 1 & 0 & \frac{\tan\alpha-3}{2\tan\alpha+3} & 0 & 0 & 0 \\ 0 & 1 & \frac{\tan\alpha-3}{2\tan\alpha+3} & 0 & 0 & 0 \\ 0 & 0 & 0 & 1 & 0 & 0 \\ 0 & 0 & 0 & 0 & 1 & 0 \\ 0 & 0 & 0 & 0 & 0 & 1 \\ 0 & 0 & 1 & 0 & 0 & 0 \end{bmatrix} \qquad \boldsymbol{E} = \begin{bmatrix} 0 & 0 & 0 & 0 & 0 & 0 \\ 0 & 0 & 0 & 0 & 0 & 0 \\ 0 & 0 & 0 & 0 & 0 & 0 \\ 0 & 0 & 0 & 0 & 0 & 0 \\ 0 & 0 & 0 & 0 & 0 & 0 \\ 0 & 0 & 0 & 0 & 0 & 0 \end{bmatrix}
$$

(A.27)

mixed control
drained simple
shear

$$
\boldsymbol{S} = \begin{bmatrix} 0 & 0 & 0 & 0 & 0 & 0 \\ 0 & 0 & 0 & 0 & 0 & 0 \\ 0 & 0 & 1 & 0 & 0 & 0 \\ 0 & 0 & 0 & 1 & 0 & 0 \\ 0 & 0 & 0 & 0 & 1 & 0 \\ 0 & 0 & 0 & 0 & 0 & 1 \end{bmatrix} \qquad \boldsymbol{E} = \begin{bmatrix} 1 & 0 & 0 & 0 & 0 & 0 \\ 0 & 1 & 0 & 0 & 0 & 0 \\ 0 & 0 & 0 & 0 & 0 & 0 \\ 0 & 0 & 0 & 0 & 0 & 0 \\ 0 & 0 & 0 & 0 & 0 & 0 \\ 0 & 0 & 0 & 0 & 0 & 0 \end{bmatrix}
$$

(A.28)

mixed control
plane strain
compression

$$
\boldsymbol{S} = \begin{bmatrix} 1 & 0 & 0 & 0 & 0 & 0 \\ 0 & 0 & 0 & 0 & 0 & 0 \\ 0 & 0 & 0 & 1 & 0 & 0 \\ 0 & 0 & 0 & 0 & 1 & 0 \\ 0 & 0 & 0 & 0 & 0 & 1 \\ 0 & 0 & 0 & 0 & 0 & 0 \end{bmatrix} \qquad \boldsymbol{E} = \begin{bmatrix} 0 & 0 & 0 & 0 & 0 & 0 \\ 0 & 1 & 0 & 0 & 0 & 0 \\ 0 & 0 & 0 & 0 & 0 & 0 \\ 0 & 0 & 0 & 0 & 0 & 0 \\ 0 & 0 & 0 & 0 & 0 & 0 \\ 0 & 0 & 1 & 0 & 0 & 0 \end{bmatrix}
$$

(A.29)

A.5   Derivation of $\boldsymbol{M_{cap}}$ and $\boldsymbol{H^{cap}}$

The shape of the cap surface f^{cap} is mainly based on the factor M_{cap}, controlling the steepness of the cap. Since the cap is associated ($f^{cap} = g^{cap}$),

the direction of plastic straining is also linked to M_{cap} via the flow rule. In the context of one-dimensional compression, which can be executed conventionally in an oedometer test device or alternatively in a K_0-triaxial compression test, the aim is to reproduce a K_0-stress path in p-q space with the corresponding inclination $\eta = \frac{3(1-K_0)}{1+2K_0}$ (Fig. A.1 a). Due to the surface's associated nature, this can be achieved by adjusting the cap's shape to the applied stress increment $(\dot{q}, \dot{p})$ and resulting strain rate direction $(\dot{\varepsilon}_p, \dot{\varepsilon}_q)$ (Fig. A.1 b), taking into account the boundary conditions of one-dimensional compression with lateral constraint with respect to stress and strain.
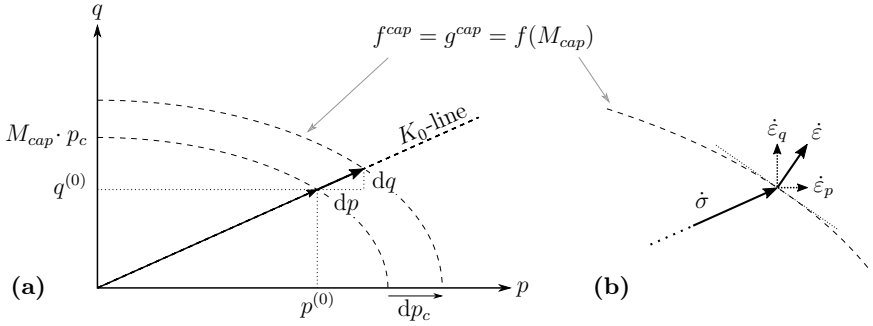
Figure A.1: (a) Load increment along the K_0-line, (b) direction of resulting plastic strain increment

Oedometric loading is defined as loading along the vertical axis, resulting in purely axial deformation, whereas radial strains are constrained:

$$\dot{\varepsilon}_2 = \dot{\varepsilon}_3 = 0 \tag{A.30}$$

In triaxial terms, this results in

$$\dot{\varepsilon}_q = \frac{2}{3}(\dot{\varepsilon}_1 - \dot{\varepsilon}_3) = \frac{2}{3}\dot{\varepsilon}_1 \quad \text{and} \quad \dot{\varepsilon}_p = \dot{\varepsilon}_1 + 2\dot{\varepsilon}_3 = \dot{\varepsilon}_1 \tag{A.31}$$

In order to determine the lateral stresses – in the following σ_3 representative for both σ_2 and σ_3 – the assumption is made that K_0 conditions apply, so that

$$\sigma_3 = K_0 \cdot \sigma_1 \tag{A.32}$$

and hence a particular triaxial stress state is defined through

$$p = \frac{1 + 2K_0}{3} \cdot \sigma_1 \quad \text{and} \quad q = (1 - K_0) \cdot \sigma_1 \tag{A.33}$$

The stiffness of an elastoplastic load step can be characterised by the stress and void ratio dependent oedometer stiffness E_{oed} according to Eq. (3.30):

$$\dot{\sigma}_1 = \dot{\varepsilon}_1 \cdot E_{oed} \tag{A.34}$$

The strain increment resulting from this load step decomposes into an elastic and a plastic contribution in both deviatoric and volumetric direction. The elastic portion follows from general elasticity:

$$\dot{\varepsilon}^{el} = \dot{\varepsilon}_q^{el} + \dot{\varepsilon}_p^{el} = \frac{\dot{q}}{3G} + \frac{\dot{p}}{K} \tag{A.35}$$

The plastic strain rate is defined by the flow rule according to

$$\dot{\varepsilon}^{pl} = \lambda \cdot \frac{\partial g}{\partial \sigma} = \lambda \cdot \left(\frac{\partial g}{\partial q} + \frac{\partial g}{\partial p} \right) \tag{A.36}$$

The required flow direction $\frac{\partial g}{\partial \sigma}$ is deduced from the cap's plastic potential

$$g^{cap} = f^{cap} = \frac{q^2}{M_{cap}^2} + p^2 - p_c^2 \tag{A.37}$$

leading to the gradients

$$\frac{\partial g}{\partial q} = \frac{2q}{M_{cap}^2} \quad \text{and} \quad \frac{\partial g}{\partial p} = 2p \tag{A.38}$$

Finally, the elastoplastic deviatoric and volumetric strain rates can be expressed as follows and linked to the boundary conditions according to Eq. (A.31):

$$\dot{\varepsilon}_q = \dot{\varepsilon}_q^{el} + \dot{\varepsilon}_q^{pl} = \frac{\dot{q}}{3G} + \lambda \cdot \frac{2q}{M_{cap}^2} \overset{!}{=} \frac{2}{3}\dot{\varepsilon}_1 \tag{A.39}$$

$$\dot{\varepsilon}_p = \dot{\varepsilon}_p^{el} + \dot{\varepsilon}_p^{pl} = \frac{\dot{p}}{K} + \lambda \cdot 2p \overset{!}{=} \dot{\varepsilon}_1 \tag{A.40}$$

Equations (A.39) and (A.40) build a system of equations that can be solved for M_{cap} by eliminating λ:

$$M_{cap}^2 = \frac{3q \cdot \left(\dot{\varepsilon}_1 - \frac{\dot{p}}{K} \right)}{2p \cdot \left(\dot{\varepsilon}_1 - \frac{\dot{q}}{2G} \right)} \tag{A.41}$$

Incorporating Eqs. (A.33) and (A.34) results in

$$M_{cap}^2 = \frac{3\left(1 - K_0\right)\cancel{\sigma_1} \cdot \left(1 - \frac{1+2K_0}{3}\frac{E_{oed}}{K}\right)\cancel{\dot{\varepsilon}_1}}{2\left(\frac{1+2K_0}{3}\right)\cancel{\sigma_1} \cdot \left(1 - \left(1 - K_0\right)\frac{E_{oed}}{2G}\right)\cancel{\dot{\varepsilon}_1}} \tag{A.42}$$

and replacing the bulk modulus K and the shear modulus G by the Young's modulus E and the Poisson's ratio ν according to Eq. (3.6) finally leads to M_{cap} in the following form:

$$M_{cap} = \frac{3}{\sqrt{2}} \sqrt{\frac{(1 - K_0)(E - (1 + 2K_0)(1 - 2\nu) E_{oed})}{(1 + 2K_0)(E - (1 - K_0)(1 + \nu) E_{oed})}} \qquad \text{(A.43)}$$

It should be noted that M_{cap} is derived assuming a load step that is large enough to cause plastic strains. Hence E and E_{oed} are independent quantities. In purely elastic oedometric loading cases M_{cap} has no direct impact on the stress-strain response, since in elasticity the inclination of the stress path is directly linked to the straining direction (and vice versa): $\dot{\varepsilon}_q^{el} = \frac{\dot{q}}{3G} = \frac{2}{3}\dot{\varepsilon}_1$ and $\dot{\varepsilon}_p^{el} = \frac{\dot{p}}{K} = \dot{\varepsilon}_1$, so that $\frac{\dot{q}}{\dot{p}} = \frac{2G}{K} = 3\frac{1-2\nu}{1+\nu}$.

The corresponding hardening modulus H_0^{cap}, completing the requirements for producing an η_{K_0}-inclined stress path under oedometric loading conditions ($\varepsilon_2 = \varepsilon_3 = 0$), can be deduced from the general elastoplastic expressions of hardening and flow rule (Eqs. (A.3) and (A.4)) and the cap's plastic potential (Eq. (A.37)):

$$\dot{p}_c = \lambda \cdot H^{cap} \cdot \frac{\partial g^{cap}}{\partial p} = \lambda \cdot H^{cap} \cdot 2p \qquad \text{(A.44)}$$

In conjunction with the volumetric strain rate condition (Eq. (A.40)), the cap hardening modulus can be extracted as:

$$H^{cap} = \frac{\dot{p}_c}{\dot{\varepsilon}_1 - \frac{\dot{p}}{K}} \qquad \text{(A.45)}$$

Basing the initial cap size p_c^0 as well as the determination of the increment Δp_c of a load step on the initial state (explicit approach), the calculation of the hardening rate $\dot{p}_c$ reduces to the following expression, resulting from the corresponding yield surface definition (Eq. (A.37)) and the oedometric stress conditions (Eqs. (A.33) and (A.34)):

$$\dot{p}_c = \sqrt{\left(\frac{\dot{q}}{M_{cap}}\right)^2 + \dot{p}^2} = \sqrt{\left(\frac{1 - K_0}{M_{cap}}\right)^2 + \left(\frac{1 + 2K_0}{3}\right)^2} \cdot \dot{\varepsilon}_1 E_{oed} \qquad \text{(A.46)}$$

Returning to Eq. (A.45), substituting the derived expression of Eq. (A.46)

for $\dot{p}_c$, the formula for the cap hardening modulus H^{cap} finally is:

$$H^{cap} = \frac{\sqrt{\left(\frac{1-K_0}{M_{cap}}\right)^2 + \left(\frac{1+2K_0}{3}\right)^2} \cdot \cancel{\dot{s}}E_{oed}}{\cancel{\dot{s}}1 - \frac{1+2K_0}{3} \cdot \cancel{\dot{s}}1 \cdot \frac{E_{oed}}{K}} = \frac{\sqrt{\left(\frac{1-K_0}{M_{cap}}\right)^2 + \left(\frac{1+2K_0}{3}\right)^2} \cdot E_{oed}}{1 - \frac{1+2K_0}{\cancel{3}} \cdot \frac{E_{oed}\cdot\cancel{3}(1-2\nu)}{E}}$$

$$= \frac{\sqrt{\left(\frac{1-K_0}{M_{cap}}\right)^2 + \left(\frac{1+2K_0}{3}\right)^2} \cdot E_{oed} \cdot E}{E - \left(1 + 2K_0\right)\left(1 - 2\nu\right) \cdot E_{oed}} \tag{A.47}$$

A.6 Intergranular strain adjustment

The evolution law for the intergranular strain $\dot{\boldsymbol{\delta}}$, given in Eq. (3.47), distinguishes two cases depending on the initial angle between the current intergranular strain $\boldsymbol{\delta}$ and the strain rate $\dot{\boldsymbol{\varepsilon}}$. In case the two vectors enclose an acute angle ($\alpha < 90°$) and the length of the intergranular strain vector has already reached its maximum ($|\boldsymbol{\delta}| = R$), Eq. (3.47) has to ensure a pure rotation of $\boldsymbol{\delta}$ towards $\dot{\boldsymbol{\varepsilon}}$ without any further change in its length. This is realised by a small correction x, which originates from the geometry of a segment of a circle as depicted in Fig. A.2 a. The sagitta h of the arc corresponds to the required correction x, the radius r of the associated circle is the length of the intergranular strain vector $|\boldsymbol{\delta}|$ and half the chord length s can be determined by applying the Pythagorean theorem to the geometry in Fig. A.2 b:

$$\left(\frac{s}{2}\right)^2 = |\dot{\boldsymbol{\varepsilon}}|^2 - \left(|\dot{\boldsymbol{\varepsilon}}|\left(\hat{\boldsymbol{\delta}}^T \cdot \hat{\dot{\boldsymbol{\varepsilon}}}\right)\right)^2 \tag{A.48}$$

(a) $h = r - \sqrt{r^2 - \left(\frac{s}{2}\right)^2}$ (b)
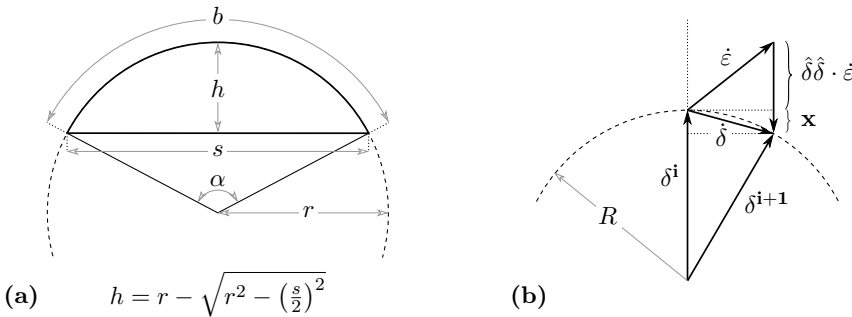
Figure A.2: (a) Geometry of the segment of a circle, (b) transfer to the intergranular strain evolution

The resulting expression for x is:

$$x = \left(|\boldsymbol{\delta}| - \sqrt{|\boldsymbol{\delta}|^2 - |\dot{\boldsymbol{\varepsilon}}|^2 \cdot \left(1 - \left(\hat{\boldsymbol{\delta}}^T \cdot \hat{\dot{\boldsymbol{\varepsilon}}} \right)^2 \right)} \right) \cdot \hat{\boldsymbol{\delta}} \qquad \text{(A.49)}$$

A.7   Intergranular strain correlation

The correlation for the strain ratio γ_{lim}/R and the two degradation parameters β_R and χ is based on the consideration of a monotonic simple shear path. This allows simplifying the multiaxial intergranular strain evolution Eq. (3.47) in analogy to the one-dimensional case as follows:

$$\dot{\delta} = \left(1 - \rho^{\beta_R} \right) \dot{\gamma} \quad \text{for } \delta \cdot \dot{\gamma} > 0 \qquad \text{(A.50)}$$

In its rate-type form the strain ratio $\rho = \frac{|\delta|}{R}$ can be substituted into Eq. (A.50) and finally gives:

$$\frac{\dot{\gamma}}{R} = \frac{\dot{\rho}}{1 - \rho^{\beta_R}} \qquad \text{(A.51)}$$

The integration of both sides leads to the following correlation [Tse09]:

$$\frac{\gamma}{R} = 1 + \rho \cdot \left(1 + \sum_{i=1}^{\infty} \frac{\rho^{i \cdot \beta_R}}{i \cdot \beta_R + 1} \right) \qquad \text{(A.52)}$$

Assuming that the intergranular hardening factor h_{ss} decreases from its maximum value m_R to 1 as the intergranular strain δ tends towards R, the evolution of the former can be related to ρ with an additional parameter χ accounting for non-linearity:

$$\rho^{\chi} = \frac{m_R - h_{ss}}{m_R - 1} \qquad \text{(A.53)}$$

Equation (A.52) can be solved for $\gamma = \gamma_{lim}$ by taking the boundary condition $\rho^{\chi}\left(\gamma = \gamma_{lim}\right) = 0.95$ into account, which has been postulated in Sect. 4.2.3. This leads to the final relation:

$$\frac{\gamma_{lim}}{R} = 1 + \rho \cdot \left(1 + \sum_{i=1}^{\infty} \frac{\rho^{i \cdot \beta_R}}{i \cdot \beta_R + 1} \right) \quad \text{with} \quad \rho = 0.95^{\frac{1}{\chi}} \qquad \text{(A.54)}$$

The graphical representation of this correlation can be found in Fig. 4.23 in Sect. 4.2.3. It allows estimating β_R or χ, knowing the ratio γ_{lim}/R and the respective second shape parameter.

B Details on particle swarm optimisation

The particle swarm optimisation algorithm used in the calibration routine for the bounding surface specific parameters and shortly presented in Sect. 4.3.2 is explained in more detail in the following article.

PSO was originally developed by Kennedy and Eberhart [KE95] and published in 1995. This optimisation method belongs to the metaheuristics – search algorithms that purposefully sample a set of solutions and that are particularly interesting if the optimisation problem is poorly defined in mathematical terms. A functional representation of the objective function f is not taken into account in PSO algorithms, since f is evaluated in black box style (Fig. B.1). By searching over a large range of feasible solutions instead of expensively assessing information on the optimisation problem (such as gradients of highly non-linear objective functions), these algorithms often find satisfactory results at comparably little computational costs. Consequently, the optimisation problem does not need to be differentiable as classical optimisation methods such as the Newton method require. However, PSO does not guarantee that the globally optimal solution is ever detected.
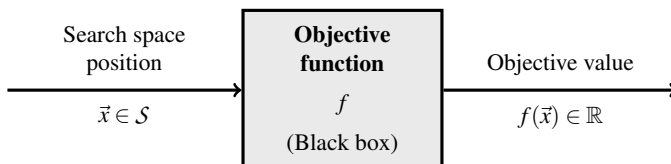
Figure B.1: Black box priciple of PSO [Hel10]

The underlying concept of PSO has been derived from social science, where the intention had been to investigate and simulate social behaviour such as the movement of individuals in a bird flock or a fish school. Existing methods have been reduced to a very simple optimisation rule combining two search strategies, based on each individual's autobiographical memory and public standards, which all individuals of a group try to attain. Iteratively, the swarm of individuals is moved through search space, improving its position in each iteration step by evaluating the local and global best places.

The formulae for deriving each particle's velocity and new position were given in Sect. 4.2 and are repeated here for convenience:

$$\boldsymbol{v_{i,t}} = \omega \cdot \boldsymbol{v_{i,t-1}} + c_1 \cdot \boldsymbol{r_{1,i,t}} \cdot (\boldsymbol{p_{i,t-1}} - \boldsymbol{x_{i,t-1}}) + c_2 \cdot \boldsymbol{r_{2,i,t}} \cdot (\boldsymbol{l_{i,t-1}} - \boldsymbol{x_{i,t-1}}) \tag{B.1}$$

$$\boldsymbol{x_{i,t}} = \boldsymbol{x_{i,t-1}} + \boldsymbol{v_{i,t}} \tag{B.2}$$

What has not been discussed there, are particular features such as the arrangement of particles within the swarm and the definition of neighbourhood, the choice of parameters for Eq. (B.1) or possible strategies for handling search space violations. These will be presented in extracts in the following – without being exhaustive – and reference is made to the options implemented in the new calibration routine. The compiled information is mainly based on the work by Clerc [Cle06], Bratton and Kennedy [BK07], and Helwig [Hel10].

Particle topology

The arrangement of the particles within the swarm can have many different forms. In the first versions of PSO, the organisation of the individuals in search space has been fixed and regular (same amount of links for each particle) in the shape of a circle, the so called ring topology [KE95], Fig. B.2 a. Another static topology is the fully connected circle, where all particles are connected, which is supposed to increase the speed of convergence, but might lead to a premature detection of local minima (Fig. B.2 b). Alternatively, the two-dimensional grid with wrapped around edges, the so called Neumann topology, can be applied, where the neighbourhood is set to four adjacent particles. This arrangement has been chosen for the optimisation routine of this work.

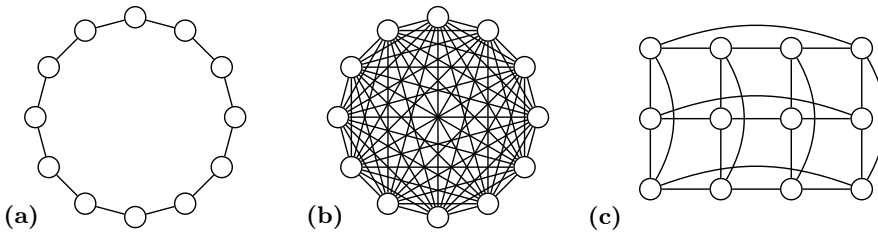(a)   (b)   (c)

Figure B.2: (a) Ring topology, (b) fully connected, (c) Neumann topology [Hel10]

Besides the presented regular topologies, there are irregular fixed arrangements, which occasionally give better results due to their randomness, whereas regular topologies are said to be more robust and reliable on average [Cle06]. In addition, the static topologies have been modified to dynamic particle arrangements, where interparticle links vary throughout the optimisation process with or without a dependence on the particle swarm performance. For more varieties of topologies the interested reader is advised to Helwig [Hel10], for example. The size of the applied topology in terms of the number of particles is a measure for the speed and reliability of convergence: the more particles, the better the performance, but also the higher the computational effort. Therefore, a compromise has to be found. Bratton and Kennedy [BK07] recommended a number of 50 particles. This quantity is supported by a benchmark test analysing the performance of population sizes of 20 to 100, although the result was not evident and the influence of the particle number seemed to be rather small. Clerc [Cle06] summarised empirical findings with 20 to 30. A swarm of 20 in the shape of a 4 by 5 grid has been implemented in the optimisation algorithm.

Parameter setting

In order to control the impact of the three influencing directions of the new particle's velocity, the weighting factors ω, c_1 and c_2 have been introduced. The first parameter ω is also called inertia weight, adjusting the influence of the previous particle velocity on the new velocity. It can be set to a constant value or even decrease from a high to a low value in order to encourage the exploration of the search space in early optimisation stages and slow it down later on for focusing the swarm on the detected potentially best area.

The learning or acceleration coefficients c_1 and c_2 are mostly chosen to be constants of the same size for simplicity, resulting in equal contributi-

ons of the private and the local guide to the new velocity. Referring to a slightly modified velocity update equation, Bratton and Kennedy [BK07] recommend the following empirical relation (adapted for the velocity update according to Eq. (4.19)):

$$\omega = \frac{2}{\left| 2 - \varphi - \sqrt{\varphi^2 - 4\varphi} \right|} \quad \text{with} \quad \varphi = \frac{c_1 + c_2}{\omega} \quad \text{and} \quad \varphi > 4 \qquad \text{(B.3)}$$

The proposal for the choice of φ is linked to the convergence behaviour, which was found to be optimal with respect to speed and reliability for values larger than 4 [CK02]. Choosing $\varphi = 4.1$ results in a constant value of $\omega \approx 0.73$ and values of $c_1 = c_2 \approx 1.5$, which have been chosen in the optimisation routine. Concerning the inertia weight, in the present work a varying value with a linear interpolation rule has been applied, using a maximum of $\omega_{max} = 0.9$ and a minimum of $\omega_{min} = 0.4$.

Constraint handling strategies

Most optimisation problems are constrained: either the parameter values are limited to a certain range, so that the search space is bounded (box constraints), or inequality/equality constraints apply, referring to dependencies among parameters. Violating one of these constraints, results in an infeasible solution. For instance, when computing the new particle velocity, the boundaries may be exceeded by the updated position of the particle. Furthermore, taking the example of the present application, if the target value $g_i(\boldsymbol{x})$ (e.g. E_{50}, ψ ...) resulting from an element test simulation with a particular $\boldsymbol{x}$ (e.g. H_0, m_d ...) violates predefined limits (such as negative stiffness values or negative peak dilatancy angles), the solution $\boldsymbol{x}$ is inadmissible. These infeasible solutions have to be corrected applying a certain constraint handling technique. There are numerous strategies, whereas penalty functions and repair algorithms are the most common ones.

The idea of a penalty function is to modify the objective function f and hence the fitness value $f(\boldsymbol{x})$ in order to penalise the infeasible solution and distract the exploration from the actual position in search space. According to Bäck et al. [BFM97] the penalised objective function can be expressed as:

$$f_p(\boldsymbol{x}) = f(\boldsymbol{x}) + \sum_{i=0}^{m} C_i \cdot \delta_i \quad \text{with} \quad \begin{cases} \delta_i > 0 & \text{if constraint is violated} \\ \delta_i = 0 & \text{if constraint is satisfied} \end{cases}$$
$$\text{(B.4)}$$

In its simplest form, the parameters in this static penalty function are constants, increasing the objective function by a certain amount if the constraint is violated ($\delta_i = 1$) and leaving it unpenalised if the constraint is satisfied ($\delta_i = 0$). The parameter δ_i can also be made a function of the distance to feasibility, which is supposed to improve the search performance. Moreover, there exist dynamic approaches, which further modify Eq. (B.4) by making C_i an increasing function of the length of search. In the present study, the simple form of static penalty has been implemented.

The second popular constraint handling strategy can be summarised as repair algorithms, which consist of mapping an inadmissible position $\boldsymbol{x}$ back into search space and hence transforming it into a feasible solution or the objective function is repaired accordingly. The former technique is the most common one and is the preferred treatment of boundary constraints. According to Helwig [Hel10], position and velocity handling strategies are distinguished. The first step is to correct the particle's position following one of the methods depicted in Fig. B.3: resetting it to the nearest boundary (a), setting it to the intersection point with the boundary (b) or using the boundary for reflecting it back into search space (d), to only name a few. These are combined with velocity handling strategies, which can consist of leaving it unmodified (keep the velocity of the infeasible particle), adjusting it to the new position so that $\boldsymbol{v_{i,t}} = \boldsymbol{v_{i,t}} - \boldsymbol{v_{i,t-1}}$, setting the new velocity to zero or even inverting it. Helwig [Hel10] has carried out an extensive study on the suitability of different combinations of position and velocity handling strategies and came to the conclusion that the overall performance of "Reflect-Z" – reflection of the infeasible position at the boundary and zero velocity – is superior to most other analysed bound handling methods. Based on these findings, in addition to the static penalty function, this approach has been incorporated into the optimisation routine.

Initialisation of particle positions and velocities

The particles' positions are mostly initialised randomly within the search space, which has also been done in the calibration programme. Concerning their velocity, there are more possible strategies for initialisation: the simplest way is to set velocity to zero, which has been chosen in the optimisation routine. Alternatively, the so called half-diff method can be applied, where additional random positions $\boldsymbol{z_i}$ in search space are drawn and the initial velocity corresponds to $\boldsymbol{v_{i,0}} = \frac{1}{2}\left(\boldsymbol{z_i} - \boldsymbol{x_{i,0}}\right)$. In both cases, although these initialisation methods perform better than others, the probability of
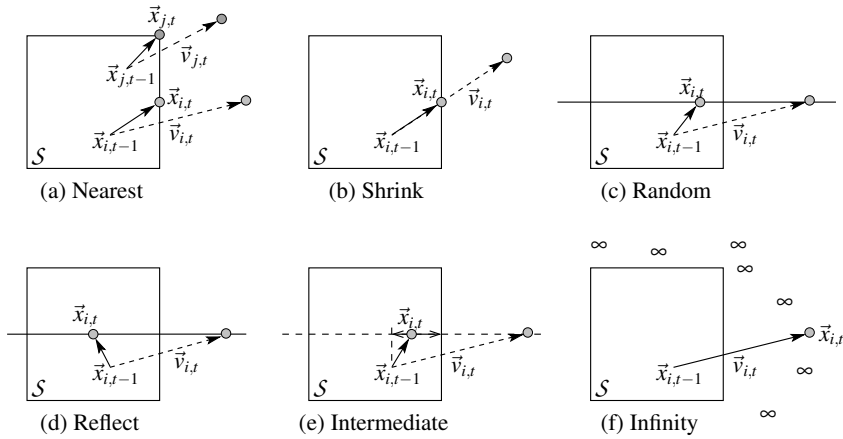
Figure B.3: Boundary handling strategies [Hel10]

the particles leaving search space already within the first iteration steps is
high. Their direct impact on the overall particle swarm performance is neg-
ligible, but the bound handling strategies required for coping with infeasible
solutions do have an influence, as will be explained in the next section.

Velocity adaptation

As noted in the previous section, the initialisation of the particles is no
trivial task to solve. Especially the selected velocity for the first iteration
steps is crucial: If the initial speed is too low, exploration might be inhibited
and hence the global best solution will be missed. If it is too high, particles
tend to leave the search space already within the first iterations and need
to be corrected to feasible positions. However, the mentioned investigation
by Helwig [Hel10] revealed that the chosen bound handling strategy lar-
gely controls the initial swarm behaviour particularly in high-dimensional
optimisation problems and even influences the final solution. In order to re-
medy this weakness, Helwig et al. [HNW09] proposed a velocity adaptation
mechanism that dynamically adapts the velocity to the search progress ac-
cording to the swarm's success. The algorithm increases a particle's velocity
as long as the private guide evolves and decreases its velocity if no impro-
vement is detected. Experimental investigations [Hel10] have shown that
the "Reflect-Z" bound handling method in combination with the velocity
adaptation algorithm considerably improves the search performance. Thus,
it has been implemented in the calibration routine accordingly.

C Compilation of simulation results

C.1 Monotonic triaxial loading

C.1.1 Toyoura sand

In comparison to the simulations based on the experimentally supported elastic stiffness values, the quality of the results for drained triaxial tests on Toyoura sand is less good with respect to the laboratory test data (Figs. C.1 and C.2). This is due to the quite large drop in elastic stiffness in favour of undrained triaxial tests.

C.1.2 Sacramento River sand

Commenting on the drained triaxial compression test simulations of Sacramento River sand shown in Fig. C.3, it can be stated that the computed soil responses match the test data quite well, although a few major deviations can be observed. As in case of Toyoura sand the calibration aimed for covering a possibly large range of initial states. Thus, particularly at low and large stresses, leading to comparably high values of the state parameter, the fit is not satisfactory. Based on the volumetric behaviour depicted in Fig. C.3 a and b, exhibiting too little dilatancy for large negative states ($\psi_0 \ll 0$) and too high contractancy for large positive states ($\psi_0 \gg 0$), it might be concluded that the state function is inappropriate: too high on both its positive and negative extremities. Having a critical view on the experimental data, considering the two curves for confining pressures of 98 and 294 kPa at an initial void ratio of 0.61 (resulting in state parameters of -0.285 and -0.257, respectively), the increase in dilatancy is quite large for the little difference in intial state. On the contrary, looking at the curves for confining pressures of 3932 and 11 768 kPa at an initial void ratio of 0.87 (resulting in state parameters of 0.277 and 0.654, respectively), the
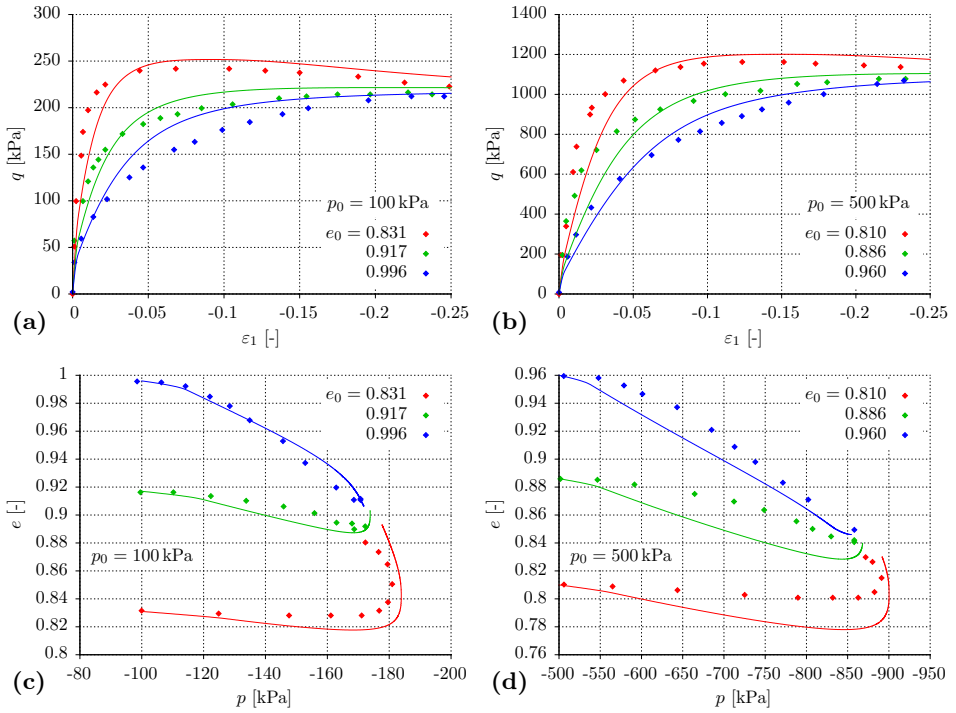
Figure C.1: Simulation (——) of drained triaxial compression tests on Toyoura sand ($p_0 = 100\,\text{kPa}$ and $500\,\text{kPa}$) compared to test data by Verdugo and Ishihara [VI96] (♦): (a, b) ε_1-q, (c, d) p-e – with modified elastic stiffness compared to Fig. 5.2
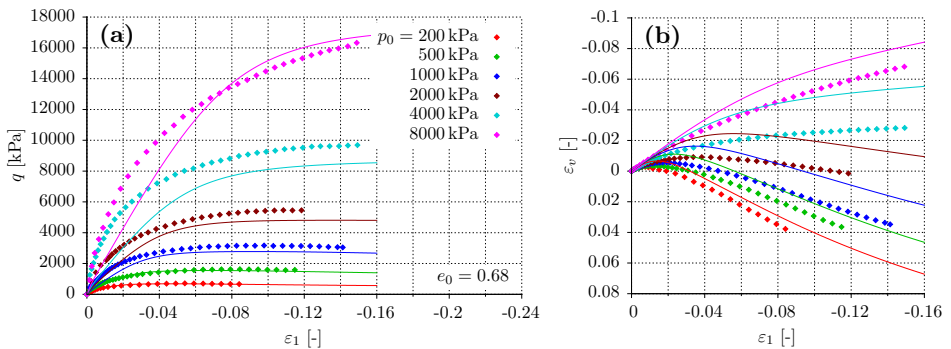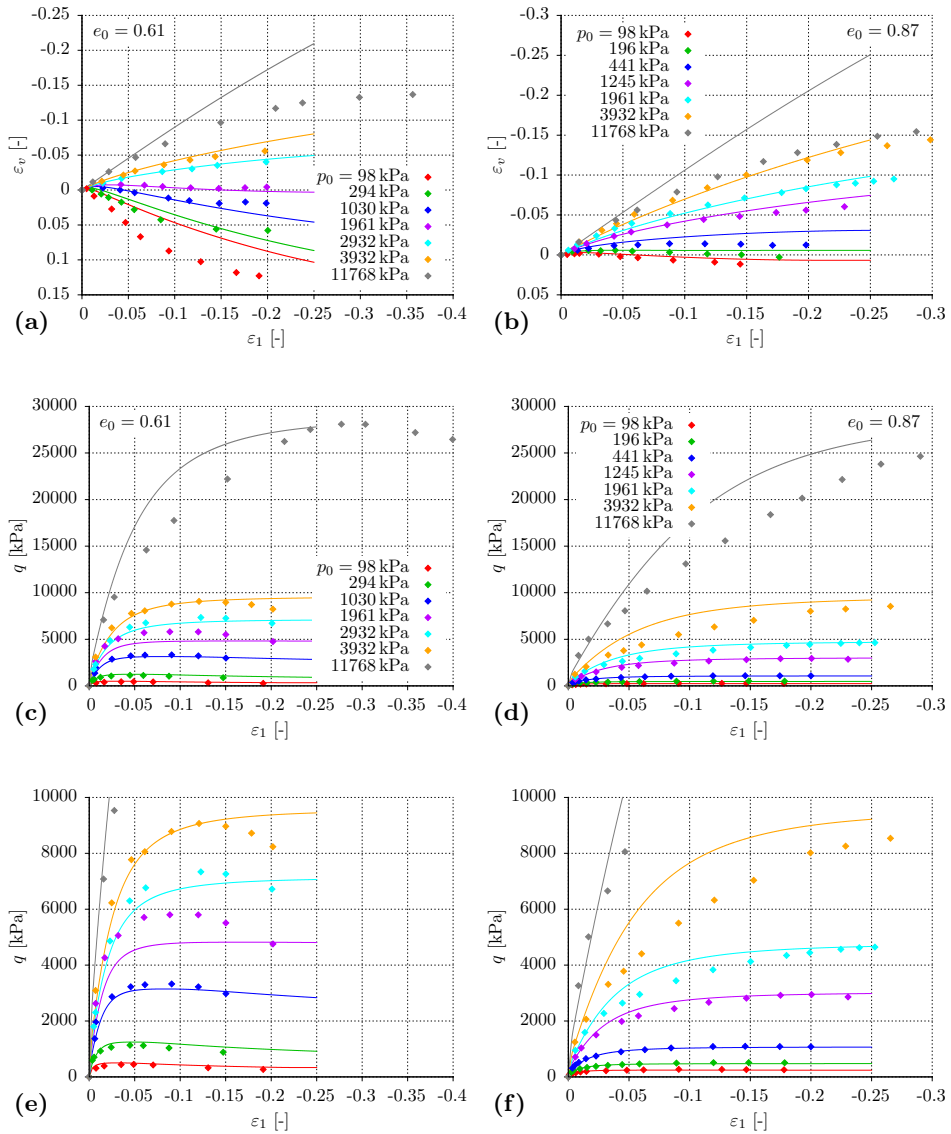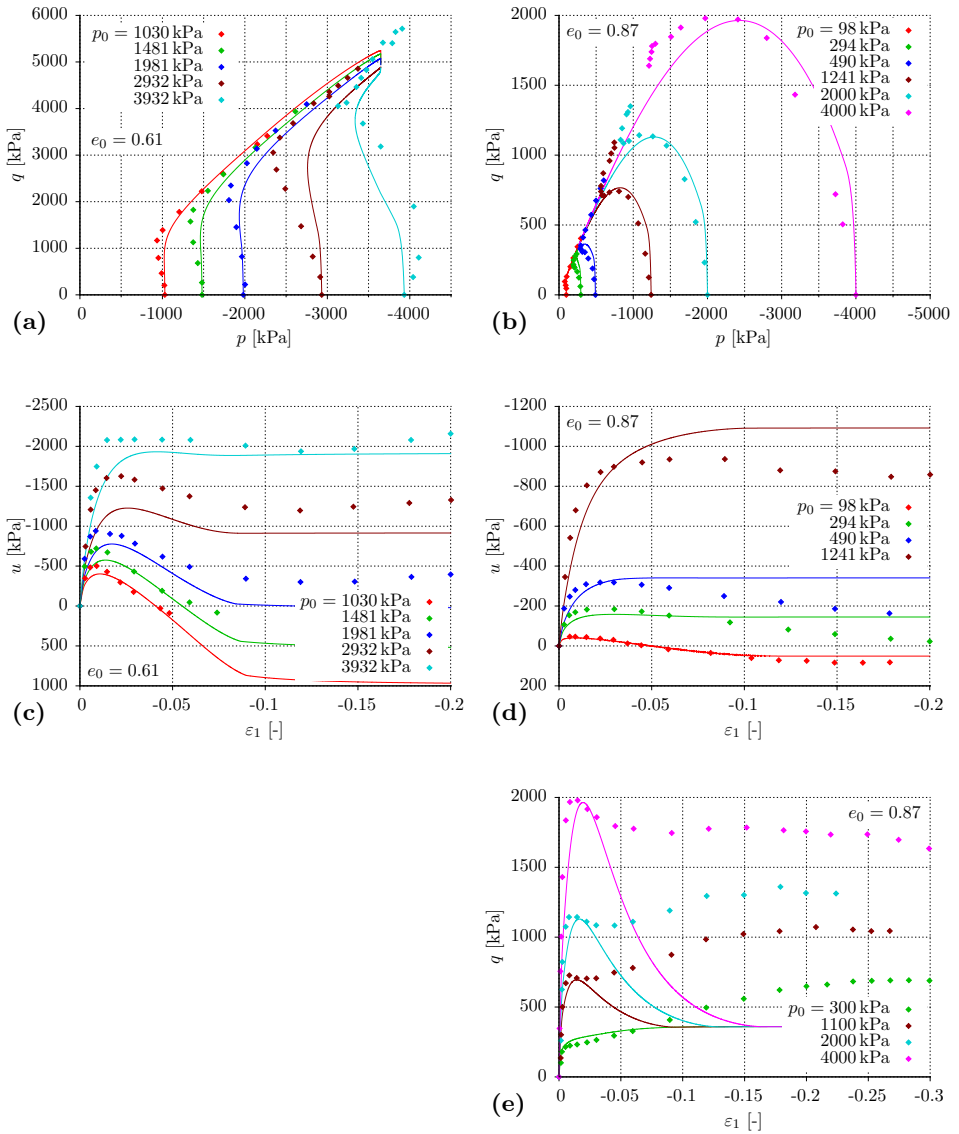

Figure C.2: Simulation (——) of drained triaxial compression tests on Toyoura sand ($e_0 = 0.68$) compared to test data by Sun et al. [SHS$^+$07] (♦): (a) ε_1-q, (b) ε_1-ε_v – with modified elastic stiffness compared to Fig. 5.1

Figure C.3: Simulation (——) of drained triaxial compression tests on Sacramento River sand ($e_0 = 0.61$ and 0.87) compared to test data by Lee and Seed [LS67] (◆): (a, b) ε_1-ε_v, (c, d) ε_1-q, (e, f) detail of (c, d)

Figure C.4: Simulation (—) of undrained triaxial compression tests on Sacramento River sand ($e_0 = 0.61$ and 0.87) compared to test data by Seed and Lee [SL67] and Lee [Lee65] ($\blacklozenge$): (a, b) p-q, (c, d) ε_1-u, (e) ε_1-q

big difference in initial state is not reflected in the volumetric deformations. The intention is not to question the experiments by Lee and Seed [LS67], rather to stress the intricate problem of finding a suitable state function that meets all requirements.

The simulation of the undrained triaxial compression tests carried out by Lee [Lee65] as well as Seed and Lee [SL67] also necessitated the reduction of the stiffness parameters as in case of Toyoura sand, which were used directly for both drained and undrained calculations. In contrast to Toyoura sand the original void ratio function of the cone hardening modulus was used (with an exponential factor of 3), indicating that this dependence is less intense for Sacramento River sand. The agreement of experiments and simulations is generally good, as depicted in Fig. C.4, the stress-strain evolution at low densities ($e_0 = 0.87$) excluded. Subfigure e shows clearly, that the deviatoric stress drops steadily with further axial straining, in opposition to the reascending experimental stress paths in subfigure b. This is an intrinsic problem of the critical state concept: all stress paths with confining pressures of $490\,\mathrm{kPa}$ and larger lie on the loose side of the defined CSL in p-e space ($\psi_0 > 0$). Consequently, they can theoretically not exhibit a phase transition point as visible in Fig. C.4 b. In some cases, where the initial loose state lies rather close to the CSL and/or where the hardening modulus is very low, the state might cross the CSL (Fig. C.5 a). From this follows that the state parameter becomes negative (Fig. C.5 b), the dilatancy line moves below the critical state line (in p-q space) and is crossed by the stress state, which results in phase transition, a decrease in pore water pressure
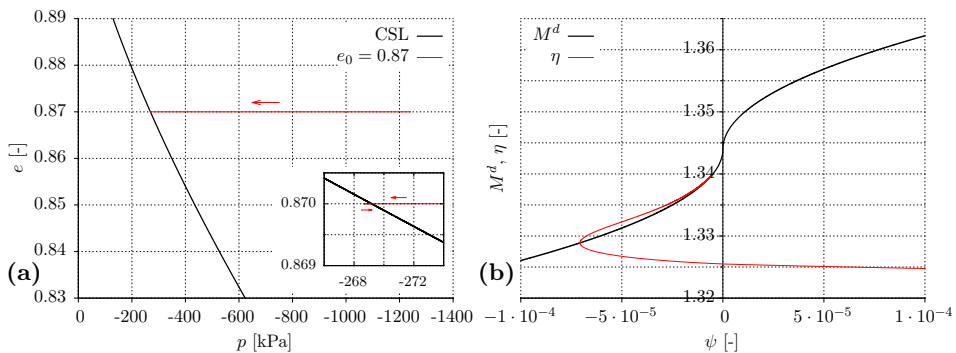

Figure C.5: Evolution of the stress state of an initially dense sample of Sacramento River sand ($e_0 = 0.87$, $p_0 = 1241\,\mathrm{kPa}$) in close proximity to the critical state in an undrained triaxial compression test

and hence a reversion of the undrained stress path. But this turnaround of the stress path occurs only after a rather long descent, almost down to the origin, which is not in accordance with the experimental observation. The only remedy to this problem within the constitutive framework is to redefine the CSL as to make the concerned initial stress states fall onto the dense side. But of cause, this will have an impact on other simulations and might impair the overall performance.

C.1.3   Hostun sand

In analogy to the other two sands, the simulation results for Hostun sand are presented and discussed below. The issue of an appropriate choice of the critical state parameters is even more pronounced than in the previous cases. Looking at Fig. C.6, the graphical summary of exemplary triaxial compression test results at a confining pressure of $300\,\text{kPa}$ for different initial densities, it is evident that it is a difficult, virtually impossible, task to find a critical state line definition in p-q and p-e space, which is fully in accordance with the experimental data. Depending on their initial state, the curves are supposed to approach these lines from above or below, respectively, obeying the underlying theory of the critical state concept. But the experiments show contradictions: in subfigure a the stress-strain path of the initial void ratio $e_0 = 0.819$ (corresponding to a "dense" state of $\psi_0 = -0.064$) exhibits its peak below the slightly looser experiment of $e_0 = 0.868$ – in opposition to the theoretically expected higher peak of a denser sample. The same applies for the two samples with $e_0 = 0.639$ and $e_0 = 0.661$, as well as for the
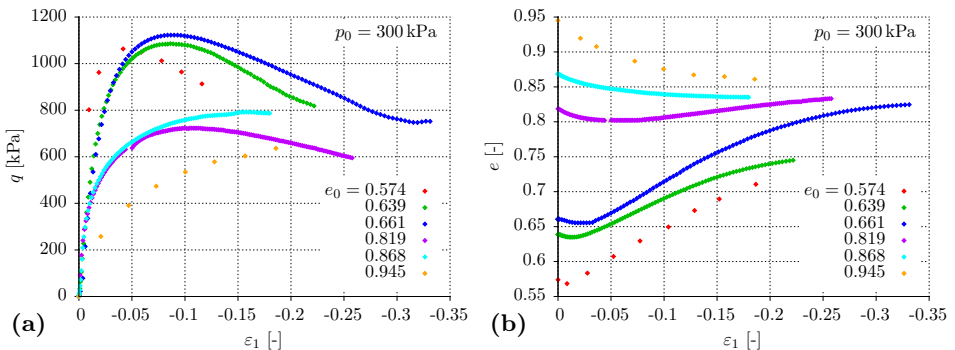

Figure C.6: Experimental data for triaxial compression tests on Hostun sand of different initial void ratios at a confining stress of $p_0 = 300\,\text{kPa}$ in (a) ε_1-q space and (b) ε_1-e space

densest sample of this series ($e_0 = 0.574$), whose peak is supposed to appear at a distinctly higher deviatoric stress according to theory. This behaviour clearly disagrees with the theoretical background and can hence not be captured by the model, independent from the parameter choice. Similarly, in subfigure b all ε_1-e curves tend towards a certain void ratio at critical state. One would expect that the higher the initial density, the stronger the dilative soil response and hence the larger the observed dilatancy angle. But the sample with an initial void ratio of $e_0 = 0.639$ exhibits less dilatancy than the slightly denser one of $e_0 = 0.661$.

The awareness that a certain observed soil response is not in agreement with the soil mechanical theory the applied model is based upon, avoids unavailing calibration attempts. The model is not capable of reproducing behavioural patterns that are contradictory to the fundamentals of critical state theory or bounding surface plasticity, such as the examples given above – no matter which parameters are chosen. In this context possible sources of errors and potential explanations for the deviations might lie in the experimental setup. Particularly, if the test data originates from different research teams and/or several laboratories, as it is the case with Hostun sand, inconsistencies from one test to another are likely to being caused by differences in the execution of experiments (technical equipment, sample preparation method, accuracy in soil classification tests,...). Consequently, besides scrutinizing the numerical model, a critical consideration of the reliability of experimental data is one component in the analysis of divergences between simulative and experimental results.

The simulations of drained and undrained triaxial compression tests based on the chosen parameter set are given in Figs. C.7 and C.8, respectively. Drained tests have been compiled for three different confining stresses ((90) 100, 300 and 600 kPa) and each with various initial void ratios. Strain data is presented in ε_1-e space (instead of ε_1-ε_v) in order to mark the value of e^{cs}, the void ratio at critical state; analogously, q^{cs} is given in ε_1-q plots. The overall performance is satisfying. Nevertheless, as discussed above, certain observed features are not reproduced by the model, but are suspected to be due to different lab testing conditions since they do not represent the expected soil mechanical behaviour with respect to the critical state concept either.

The stress paths of undrained triaxial tests in p-q space look quite promising, but the post-peak stiffness is overestimated in case of dense initial states (Fig. C.8 b). This observation most likely indicates a not fully ap-
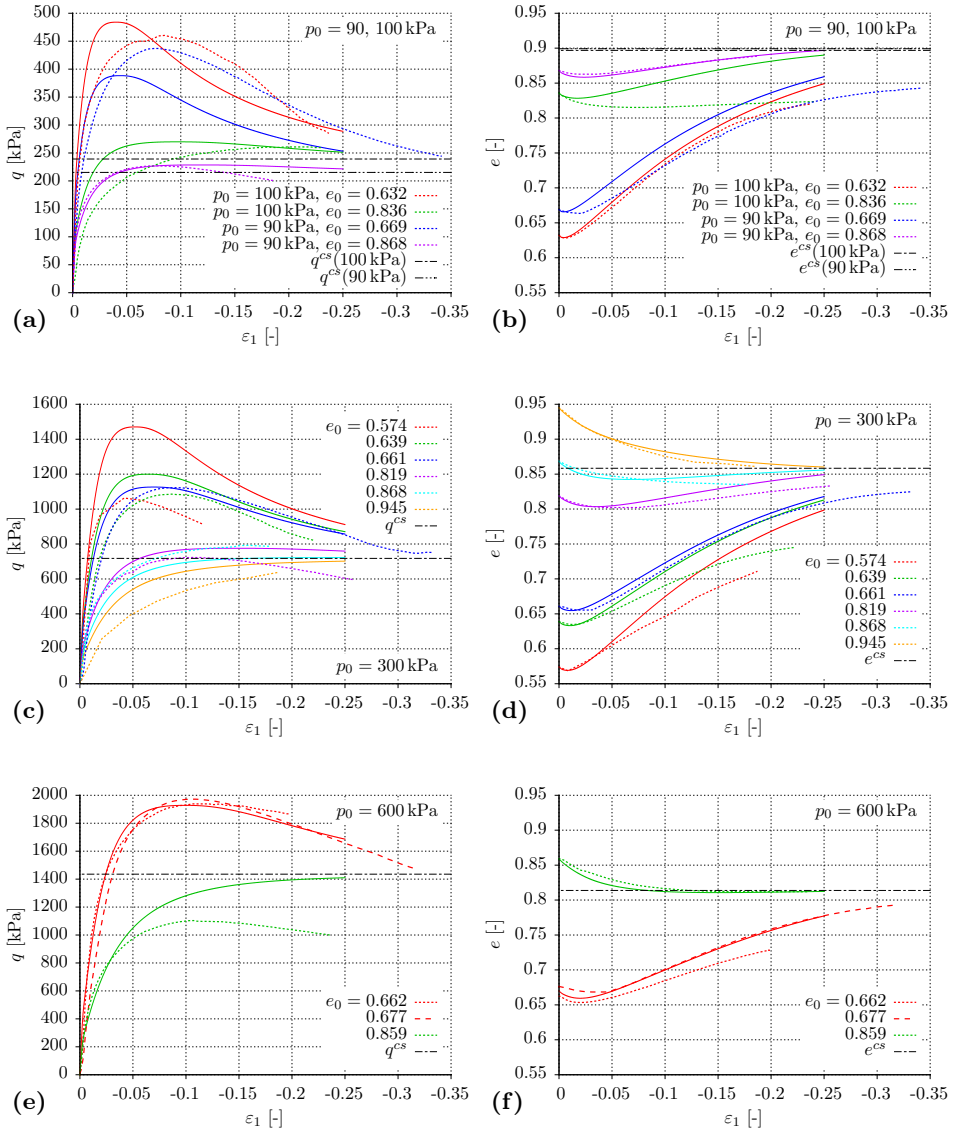
Figure C.7: Simulation (——) of drained triaxial compression tests on Hostun sand ($p_0 = 90(100)$, 300, $600\,\mathrm{kPa}$) compared to test data by Vermeer et al. [VDZ00], Desrues [Des13], and Khalili et al. [KHV05] ($\cdots$ / $---$)): (a, c, e) ε_1-q, (b, d, f) ε_1-e – including critical state values of deviatoric stress and void ratio respectively (according to assumed CSL)
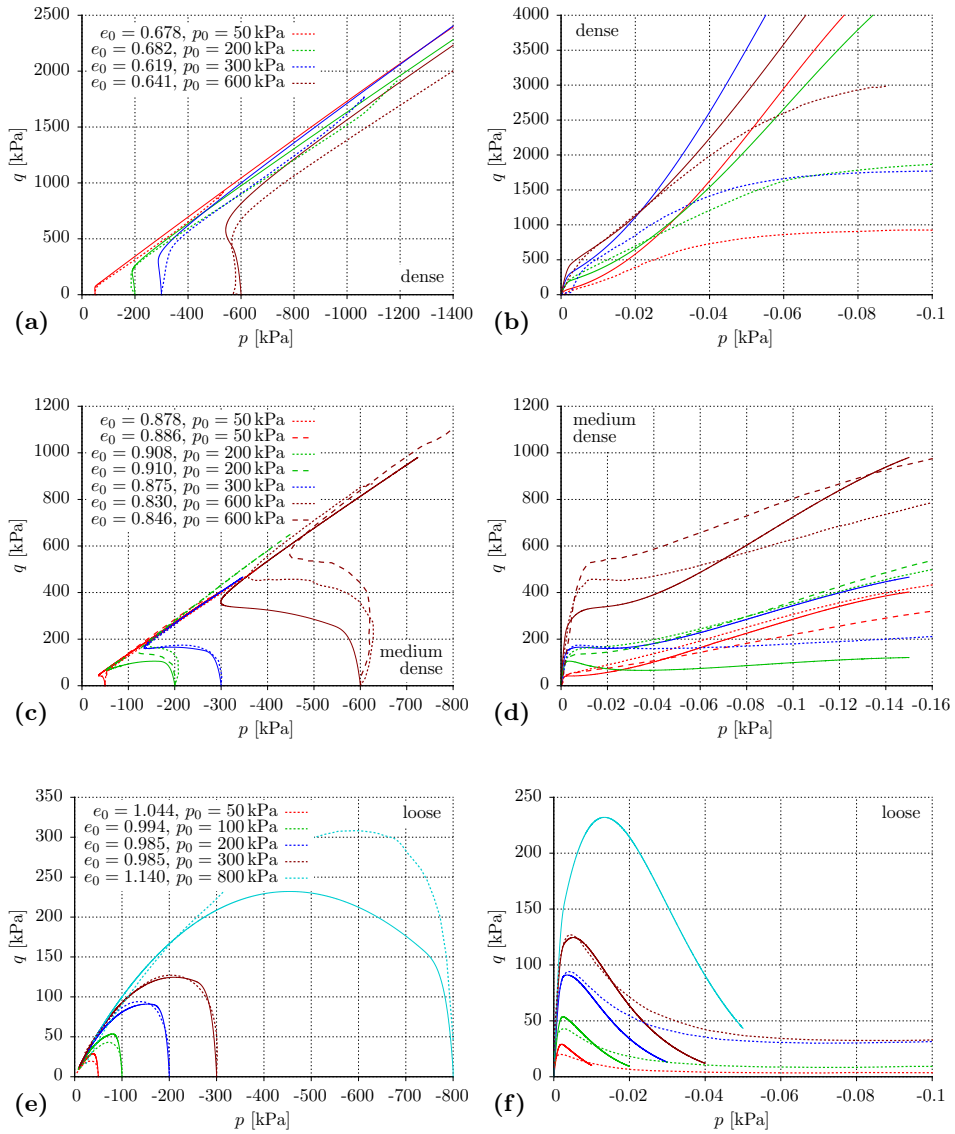
Figure C.8: Simulation (——) of undrained triaxial compression tests on Hostun sand of high, medium and low density compared to test data by Vermeer et al. [VDZ00], Desrues [Des13], Servant et al. [SDD$^+$05], Finge et al. [FDD06], and Doanh et al. [DIM97] ($\cdots\cdots$/ $----$)): (a, c, e) p-q, (b, d, f) ε_1-q

propriate caption of the plastic stiffness evolution with soil density.

The author wants to call the reader's attention to one particular effect that has already been observed in a similar form in the context of undrained Sacramento River sand simulations. Usually, one would neither expect an initially loose sample to exhibit a peak nor a phase transformation with subsequent dilatancy. Though, numerically at least the latter is possible, which is shown in Fig. C.9 for the case of a drained triaxial test with $e_0 = 0.859$ and $p_0 = 600\,\mathrm{kPa}$. If the initial (loose) state lies in close proximity of the critical state line, e.g. resulting in a very small state parameter of $\psi_0 = 0.006$ as in the example, it might cross the CSL after an initial contractant phase, the deviatoric stress ratio keeps on increasing until it exceeds the dilatancy line and consequently dilation is initiated with phase
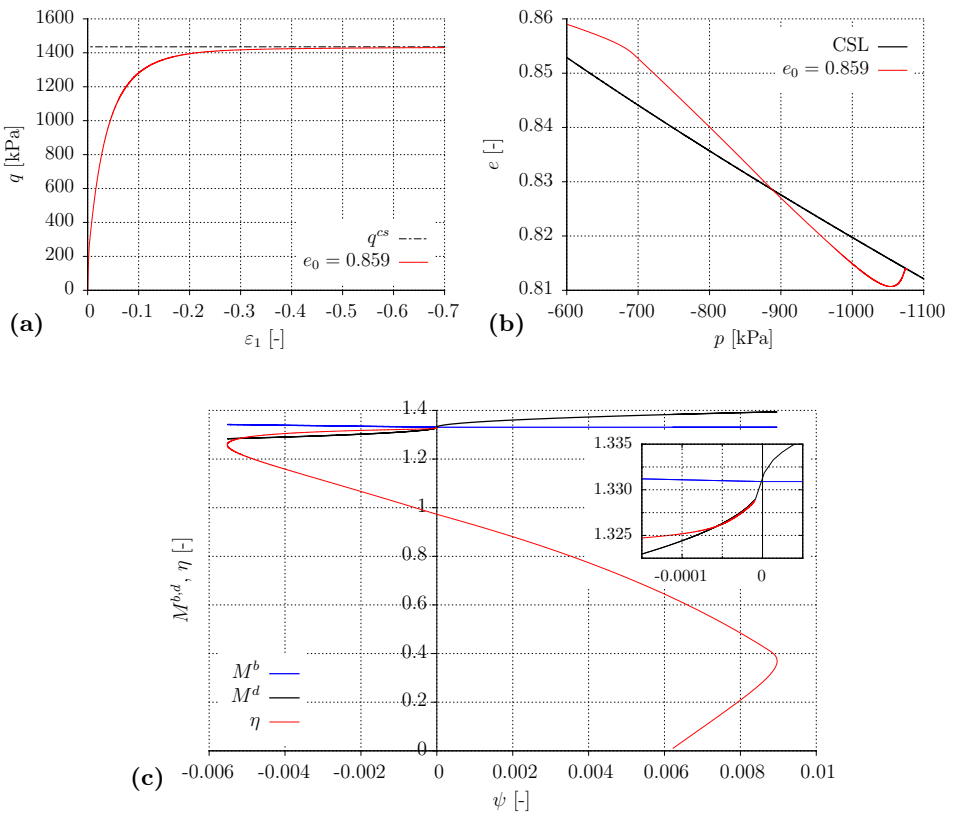
Figure C.9: Triaxial compression test on Hostun sand sample with initial state of $p_0 = 600\,\mathrm{kPa}$ and $e_0 = 0.859$: (a) ε_1-q, (b) p-e and (c) ψ-$M^{b,d}$,η

transition. But since the soil state is already very close to critical state at that stage, the stiffness is too low for the stress ratio η to trespass the bounding surface and redescend. Thus, although a phase transformation point can be identified, there is no peak stress and the stress-strain curve approaches the critical state deviatoric stress from below (Fig. C.9 a).

C.2 Monotonic η-constant loading

As presented in Sects. 3.2.3 and 4.2.3, the model includes a cap yield surface, whose hardening mechanism is based on the oedometer stiffness, but can alternatively be exchanged by a mechanism following the limiting compression curve (LCC) concept. For comparison, a few selected examples are given below for the LCC implementation.

C.2.1 Sacramento River sand

Figure C.10 presents experimental and simulative results of isotropic compression tests on Sacramento River sand. The LCC parameters used are displayed in the respective diagrams. Aside from those, the general parameter set (Tab. 4.6) has been used, resulting in a very good reproduction of the lab data (subfigure a). In subfigure b the reduced elastic stiffness parameters have been applied, which were found to deliver better simulation results for undrained triaxial tests (see previous subsection). The match is satisfying, too, but the elastic stiffness is too low and hence the deformations generally slightly too high, which cannot be overcome by adjusting the
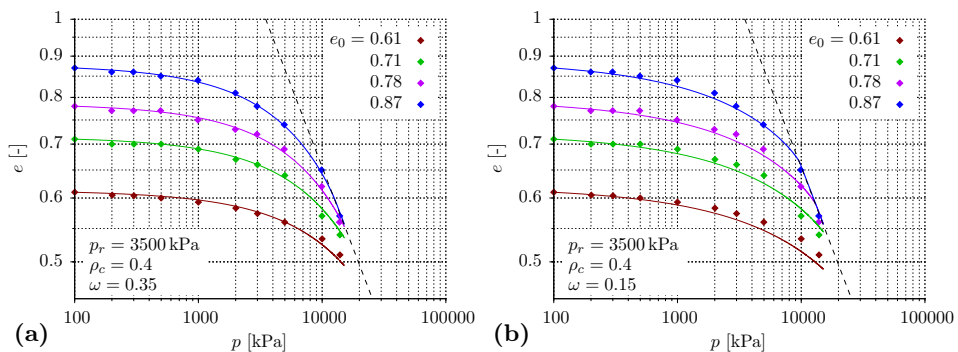

Figure C.10: Simulation (——) of isotropic compression tests on Sacramento River sand compared to test data by Lee and Seed [LS67] (♦): (a) without and (b) with elastic stiffness reduction – LCC mechanism

LCC parameters only.

When taking η-constant stress paths with inclinations different from zero into consideration, Fig. C.11 (the LCC version of Fig. 5.10) clearly depicts the softening effect, which is introduced into the hardening function by the $\boldsymbol{\alpha^c}/\boldsymbol{r}$-extension in Eq. (3.37). In contrast to the M_{cap} mechanism, the intensity could be modified by adjusting the predefined factor 2. However, it should be noted that the simulated oedometric stress-strain curve deviates from the experimental data considerably already at medium stresses. This is due to the η-dependent location of the LCC, which forces the soil response to be markedly softer than in the isotropic compression loading case. The experimentally observed behaviour, where the oedometric path even crosses the isotropic one, cannot be modelled by applying the LCC concept. This possibility is not basically ruled out when applying the M_{cap} mechanism, but depends on the choice of parameters.

It ought to be recalled that, although the LCC concept aims for reproducing the compression behaviour of soils up to very high stresses, where the deformation mechanism is dominated by grain crushing, simulation results in these ranges should generally be interpreted with care.
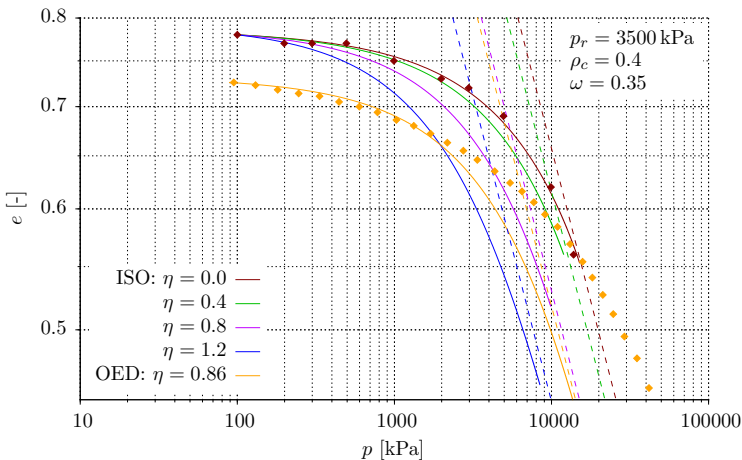

Figure C.11: Simulation (—) of an isotropic and an oedometric compression test on Sacramento River sand ($e_0 = 0.73$) compared to test data by Lee and Seed [LS67] and Lade and Yamamuro [LY93] (♦), complemented with simulations of different η-constant tests with $e_0 = 0.78$ – LCC mechanism

C.2.2   Hostun sand

In analogy to Toyoura and Sacramento River sand, the cap parameters have been determined for Hostun sand primarily based on oedometric compression test data as shown in detail in Sect. 4.2.3. However, since isotropic test data was available, too, the earlier found stiffness was increased slightly to a value of $E_{oed}^{ref} = 350\,\text{kPa}$ in order to get a better fit for both, isotropic and oedometric compressive loading. The calibration has been carried out for the experimentally supported elastic parameters only. Figure C.12 presents the corresponding simulative results for oedometric as well as isotropic compression tests, which attest an optimal parameter choice for all considered loading cases modelled with the M_{cap}-mechanism.

For the sake of completeness the first two loading - unloading - reloading cycles of the one-dimensional compression test in Fig. 4.17 with the initial void ratio of $e_0 = 0.67$ were simulated. The result is presented in Fig. C.13 and shows that the extended bounding surface model with the cap mechanism is capable of reproducing not only loadings, but also unloading - reloading schemes with a relatively good fit. However, the experiment exhibits a stronger hysteresis than the simulation (which could be improved by adapting the small strain stiffness properties). In addition, the unloading - reloading branches of the simulated curve have approximately the same inclination at
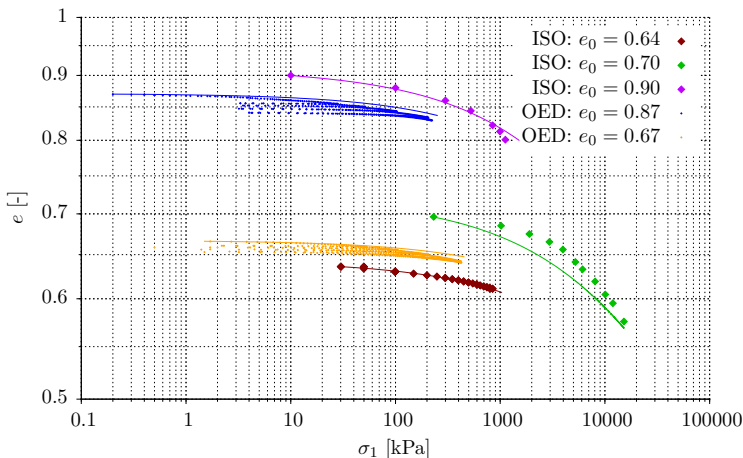

Figure C.12: Simulation (——) of isotropic and oedometric compression tests on Hostun sand compared to test data by Vermeer et al. [VDZ00], Daouadji and Hicher [DH10], and Al Mahmoud [Al 97] ($\bullet$) – M_{cap} mechanism

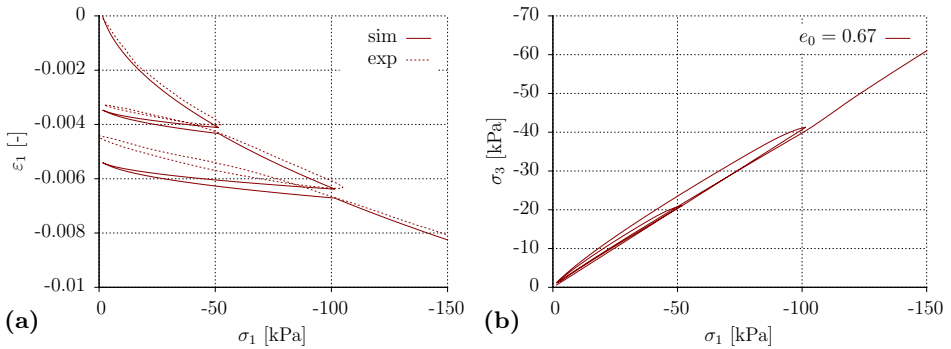**(a)**   **(b)**

Figure C.13: Multi-stage one-dimensional compression test on Hostun sand with an initial void ratio of $e_0 = 0.67$: (a) σ_1 - ε_1 and (b) σ_1 - σ_3

both stress levels (based on the constitutive formulation), which is not the case in the experimental data.

C.3   Cyclic triaxial loading

In addition to the cyclic p-constant test on a loose soil sample ($e_0 = 0.845$), as carried out by Pradhan et al. [PTS89] and presented in Sect. 5.3, the simulative results of an equivalent test on a dense sample ($e_0 = 0.653$) are presented in Fig. C.14. The first cycles of this experiment have been used as reference in the parametric study related to the calibration of the fabric parameters C_f and F_f in Sect. 4.2.3. Apparently, the simulated overall expansive effect, noticeable in subfigures a and c, is not in accordance with the experimental outcome, where expansive and contractive tendencies are in balance. This issue could not have been solved by enhancing the contraction after load reversals via an increase of the parameter C_f. The fact that the simulations without small strain stiffness and/or fabric mechanism qualitatively show the same result after the initial cycles underlines this finding. This strategy might work well as long as the cycles remain comparably small and few, but dilation takes over quickly and the strong expansive tendency impairs the final volumetric response. It is important to note that the experimentally observed dilatancy angle is well captured by the model. The problem lies in the very dense state of the soil: due to the low mean pressure and the high density, the initial state parameter amounts to a relatively high value of -0.262, which causes the dilatancy surface to take a rather shallow initial position in p-q space with a quite large distance

to the critical state line. This geometrical starting situation is responsible for the very short contractive phase and the almost direct transition to dilation. It is an intrinsic model property that can only be influenced to a limited extent by the fabric evolution mechanism. For obtaining extensive contractant phases as visible in Fig. C.14 a the formulation of the CSL in p-e space would need to be modified in order to reduce the initial state parameter and hence change the volumetric behaviour to a more contractive one. Alternatively, one might consider the measured initial void ratio to be defective (due to measuring inaccuracies) and increase its value as to reach a less dilative state.
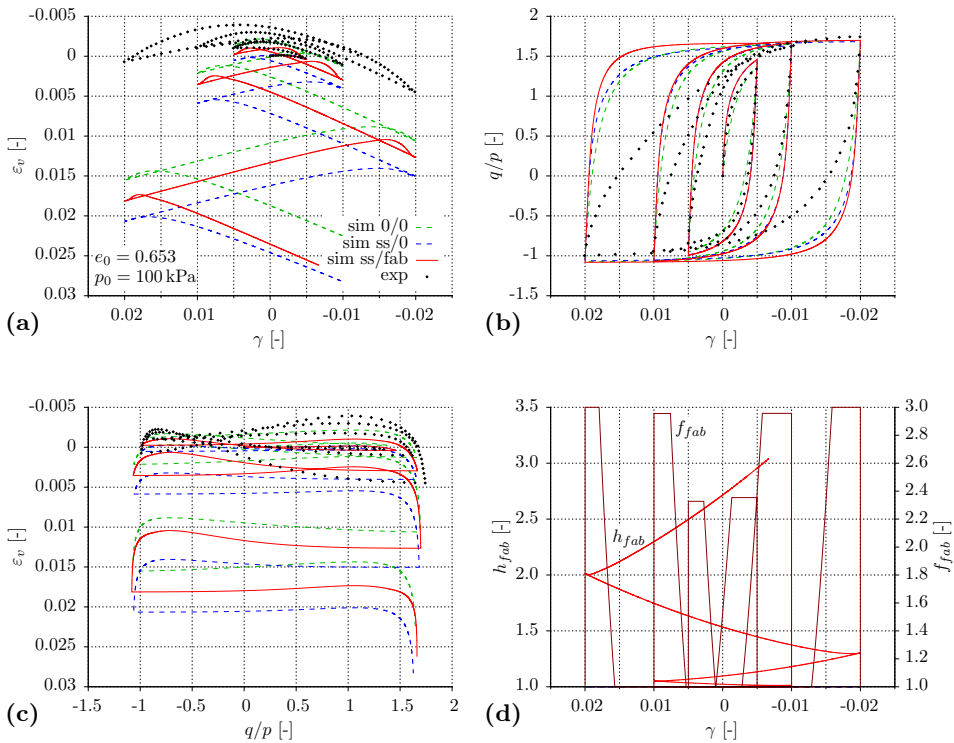
Figure C.14: Simulation of drained triaxial p-constant tests on dense Toyoura sand ($e_0 = 0.653$, $p = 100\,\mathrm{kPa}$) with and without accounting for small strain stiffness (ss: strain contours) and fabric evolution (fab), respectively, compared to test data ($\blacklozenge$) by Pradhan et al. [PTS89]

Herausgeber: Univ.-Prof. Dr.-Ing. habil. Dietrich Franke

Heft 1	Franke, D. (Hrsg.)	1992	Das Institut für Geotechnik an der TU Dresden + Die Veröffentlichungen Johann Ohdes
Heft 2	Franke, D. (Hrsg.)	1995	OHDE-Kolloquium 1993
Heft 3	Franke, D. (Hrsg.)	1995	Festschrift zum 60. Geburtstag von Prof. Dr.-Ing. habil. Dietrich Franke
Heft 4	Franke, D. (Hrsg.)	1997	OHDE-Kolloquium 1997
Heft 5	Engel, J.	1998	Entwicklung von Datenstrukturen für bodenmechanische Anwendungen
Heft 6	Vogt, L.	1998	Untersuchungen zum Tragverhalten und zur Verbesserung der Standsicherheit von Stützmauern
Heft 7	al Diban, I.	2000	Das Tragverhalten horizontal belasteter, in nichtbindigem Boden eingespannter starrer Träger, in ebenem und geböschtem Gelände
Heft 8	Winkler, A.	2001	Ermittlung des Erddrucks im Bruchzustand bei Drehung einer Wand um den Kopfpunkt
Heft 9	Franke, D. (Hrsg.)	2001	OHDE-Kolloquium 2001
Heft 10	Engel, J.	2002	Verfahren zur Festlegung von Kennwerten für bodenmechanische Nachweise
Heft 11	Neuberg, C.	2002	Ein Verfahren zur Berechnung des räumlichen passiven Erddrucks vor parallel verschobenen Trägern

Herausgeber: Univ.-Prof. Dr.-Ing. habil. Ivo Herle

Heft 12	Bartl, U.	2004	Zur Mobilisierung des passiven Erddrucks in kohäsionslosem Boden
Heft 13	Arnold, M.	2004	Zur Berechnung des Erd- und Auflastdrucks auf Winkelstützwände im Gebrauchszustand
Heft 14	Al-Akel, S.	2005	Beitrag zur Berechnung von eingespannten starren Stützkonstruktionen in kohäsionslosem Boden
Heft 15	Herle, I. (Hrsg.)	2005	OHDE-Kolloquium 2005
Heft 16	Herle, I. (Hrsg.)	2009	OHDE-Kolloquium 2009
Heft 17	Wegener, D.	2013	Ermittlung bleibender Bodenverformungen infolge dynamischer Belastung mittels numerischer Verfahren
Heft 18	Gajári, G.	2013	Modellierung bleibender Verformungen des Asphalts mit einem hypoplastischen Stoffmodell der Bodenmechanik
Heft 19	Herle, I. (Hrsg.)	2014	OHDE-Kolloquium 2014
Heft 20	Shi, X.	2016	Verformungsverhalten von Kippenböden mit Multiporosität
Heft 21	Nitzsche, K.	2016	Verschiebungsmuster in Böschungen während Aushubvorgängen
Heft 22	Hleibieh, J.	2017	Anwendung der Hypoplastizität bei numerischen Berechnungen von bodendynamischen Problemen
Heft 23	Schwiteilo, E.	2018	Bestimmung bodenmechanischer Parameter nach fortgeschrittenen Methoden
Heft 24	Herle, I. (Hrsg.)	2018	OHDE-Kolloquium 2018